UNIVERSIDADE DE SÃO PAULO

INSTITUTO DE FÍSICA DE SÃO CARLOS

EDWIN EDUARDO PEDROZO PEÑAFIEL

Production of a Bose-Einstein condensate of sodium atoms and investigation considering non-linear atom-photon interactions

São Carlos

2016

EDWIN EDUARDO PEDROZO PEÑAFIEL

Production of a Bose-Einstein condensate of sodium atoms and investigation considering non-linear atom-photon interaction

Thesis presented to the Graduate Program in Physics at Instituto de Física de São Carlos, Universidade de São Paulo, to obtain the dregree of Doctor of Science.

Concentration area: Basic Physics
Advisor: Prof. Dr. Vanderlei Salvador Bagnato

Reviewed Version

(Original version available on the Program Unit)

São Carlos

2016

AUTHORIZE THE REPRODUCTION AND DISSEMINATION OF TOTAL OR PARTIAL COPIES OF THIS THESIS, BY CONVENCIONAL OR ELECTRONIC MEDIA FOR STUDY OR RESEARCH PURPOSE, SINCE IT IS REFERENCED.

Cataloguing data reviewed by the Library and Information Service
of the IFSC, with information provided by the author

Pedrozo Peñafiel, Edwin Eduardo
Production of a Bose-Einstein condensate of sodium atoms and investigation considering non-linear atom-photon interactions / Edwin Eduardo Pedrozo Peñafiel; advisor Vanderlei Salvador Bagnato - reviewed version -- São Carlos 2016.
175 p.

Thesis (Doctorate - Graduate Program in Basic Physics) -- Instituto de Física de São Carlos, Universidade de São Paulo - Brasil , 2016.

1. Bose-Einstein condensate. 2. Sodium atoms. 3. Optically plugged quadrupole trap. 4. Cooperative absorption of two photons. I. Bagnato, Vanderlei Salvador, advisor. II. Title.

To whom really deserves this thesis: my mother "Alci", my father "Jaso", my sisters Nini and Marlin, my nephew "El gran Daniel", to my grand mother "Tina", and to my great love, my wife Karen. Without you nothing of this could have happened.

Also, in memory to my great cousins (brothers) and friends:
Brayan Rafael Peñafiel Lopez and Edinson Pallares Barranco.
Thanks for all the unforgottable moments we lived together.

ACKNOWLEDGMENTS

I have no words to thanks my supervisor prof. Dr. Vanderlei (Vander) Bagnato. He's one who marked me deeply. Vanderlei is a great example of how to be a great scientist, a wonderful person and a visionary in many aspects. His enthusiasms always cover all the labs, and is extended to the whole hall of the labs, second and first floors of the IFSC-USP. One short discussion about physics with him can change the way you see the world and how to face any new and big challenges; To never give up. I thanks a lot for this! I remember in my first year at IFSC, the dye laser was driving me crazy, and He was there and taught me how to align all the mirrors in the ring cavity and centralize the spots in all the mirrors at the same time for increasing power and cleaning the mode. At that moment I knew it will be great to work with Him as it was and it is!

I want to thanks Kilvia Mayre Farias, who tough me a lot of things and helped me in many aspects. You always were supporting me, specially in the harder moments, that were a lot. There are no word to thanks, and I would need several pages for write this.

I also have no words to thanks our collaborator and kind friend (Caro Amici), Giacomo Roati. You always helped us in the most critical moments, also your leadership mark routes to follows, giving us a light to walk when the road was obscure. I thanks you for any advice and joke, definitively you are a great example and someone whom I want to keep learning.

I want to thanks Rafael Rothganger, for all the help and friendship along this seven years. To Franklin J. Vivanco, who also helped me with several nice figures for this thesis. To Pedro Tavares, who with his deep knowledge about the experimental apparatus of BEC helped us in many times. Also, I want to thank you for being very supportive in difficult moments.

I want to thanks sodium-potassium team. Patricia Castilho deserves a very especial acknowledgment; Her effort in the lab and hard work made possible this thesis, I am sure She will be very successful in the rest of Her PhD and all the futures challenges Her want to face. Thanks to Emmanuel Mercado Gutierrez who made the lab more funny. Long conversations about everything were a good relaxing therapy at the end of every hard days in the lab. To Pedro Mazo and Pablo S. Dias, the new generation of the NaK team. I am sure they will improve a lot the system and will face big challenges with enthusiams. To Vitor Monteiro, who shared a lot of funny moments in the lab.

I want to thanks all the lab people, which were always willing to help and with I shared many moments in the lab and outside, especially at “Rancho da picanha”: Gustavo Telles, Amilson Fritsh, Freddy Jackson Poveda, Jorge Seman, Andres Rodriguez, Arnold García, Emanuel Henn, Daniel Varela, Stella Muller, and Sergio Muniz.

To Brazil, that gave me the opportunity to have a high quality education in science and the opportunity to learn a lot about this wonderful country and its wonderful people. Also, to give me the opportunity to learn about the greatest musician I have ever listened to: The *Maestro* Antonio Carlos “Tom” Jobim. This country also has to be recognizes for many big names as Vital Brazil, Santos Dumont, Carlos Chagas, Cesar Lattes, Oswaldo Cruz, Oscar Niemeyer, and surely others that will enter in this list in few years.

To Bene, Christiane, Adriane, Patricia, Wagner, and Isabel, for all the help and efficiency about solving bureaucratic things.

To all the IFSC library people, especially to Neusa for the all the work in formatting this thesis. To all the people in he machine shop who constructed the sciences chambers. To

Luciano from the cryogenic workshop, who realized leak test in our system many times, and every time with the same disposal. To Leandro and Evaldo from the optic's group workshop. To my good friend Leandro, I hope in brief a new engineer will emerge.

To the Liepo workshop. João Marcelo, Guilherme, Carlos, Rogeiro, Richard, Dennis, Leandro, and Rui, thanks for the help with many complicated circuits we always have to face. To CNpq for the financial support along my graduates studies. To FAFQ for

the financial support in this last year. To ll my friends in São Carlos. Ruben, Oriana,

Thais, Thiago, Alfredo, Rogelio, Rosa, Mary, Camy, Martin, Rodo, Migue, Andres, Maye, Wilson, Eliceo, Jeiny. Of course, among many others. The list is very extensive and it is not possible to continue.

Finally, to all my family. My father and mother, you sacrificed your dreams in change of my dreams, and then I have no way to pay you back. To my sisters, I love you even when you. To my nephew Daniel, who who is the happiness of my house. To my grandmother to whom I debt a lot. To all my family which very numerous and I can't write all your names here ;-). To the love of my life: Karen, my wife, patient, understanding, and all the support in the most difficult moments: I love you.

To god.

Abstract

PEDROZO-PEÑAFIEL, E. *Production of a Bose-Einstein condensate of sodium atoms and investigation considering non-linear atom-photon interactions.* 2016. 175p. Tese (Doctorate in Science) - Instituto de Física de São Carlos, Universidade de São Paulo, São Carlos, 2016.

In this work we constructed an experimental system to realize a BEC of sodium atoms. In the first part of the work, we study two atomic sources in order to choose the most suitable for our system. The comparison between a Zeeman slower and a bidimensional magneto-optical trap (2D-MOT) was performed to evaluate the capacity of producing an appropiate flux of atoms in order to load a tridimensional magneto-optical trap (3D-MOT). The experimental results show that the 2D-MOT is as efficient as the Zeeman slower with the advantage of being more compact and easier to operate, and for these reasons we choose it as our source of cold atoms. After this, the experimental apparatus to produce a Bose-Einstein condensate was constructed and characterized. With this experimental system we realized all the required stages to achieve the Bose-Einstein condensation (BEC). Initially, we characterized and compared the performance between the Bright-MOT and Dark-SPOT MOT of sodium atoms, observing the great advantages this last configuration offers. Afterward, we implemented the experimental sequence for the achivement of the BEC of sodium atoms. After the optical molasses process, the atoms are tranferred to an optically plugged quadrupole trap (OPT) where the process of evaporative cooling is performed. With this setup, we achive a sodium BEC with $\sim 5 \times 10^5$ atoms and a critical temperature of $\sim 1.1\,\mu$K. Finally, with the constructed and characterized machine, we started to perform experiments of cooperative absorption of two photons by two trapped atoms. With the new system, we wanted to take advantage of the higher densities in the magnetic trap and BEC to explore some features of this phenomenon in the classical and quantum regimes. We were interested in exploring some features of this nonlinear light-matter interaction effect. The idea of having two or more photons interacting with two or more atoms is the beginning of a new possible class of phenomena that we could call many photons-many body intercation. In this new possibity, photons and atoms will be fully correlated, introducing new aspects of interactions.

Keywords: Bose-Einstein condensate. Sodium atoms. Optically plugged quadrupole trap. Cooperative absorption of two photons.

Resumo

PEDROZO-PEÑAFIEL, E. *Producção de um Condensado de Bose-Einstein de átomos de sódio e investigação considerando interações não lineares entre átomos e fótons.* 2016. 175p. Tese (Doutorado em Ciências) - Instituto de Física de São Carlos, Universidade de São Paulo, São Carlos, 2016.

Neste trabalho, realizamos a construção de um sistema experimental para a realização de um condensado de Bose-Einstein de átomos de sódio. Na primeira parte do trabalho, realizamos o estudo de duas fontes átomicas com o intuito de escolher a mais adequada para nosso sistema experimental. A comparação foi realizada entre um Zeeman slower e uma armadilha magneto-óptica bidimensional (MOT-2D), que são técnicas usadas para fornecer um grande fluxo de átomos com distribuição de velocidades adequadas para serem capturados numa armadilha magneto-óptica tridimensional (MOT-3D). Os resultados experimentais da caracterização de ambos os sistemas mostra que o MOT-2D oferece um grande fluxo atômico da mesma ordem do Zeeman slower, mas com a vantagem de ser um sistema mais compacto em questão de tamanho, razão pela qual foi escolhido como fonte atômica no nosso sistema. A partir daqui, realizamos a construção do sistema experimental para a realização do condensado de sódio. Inicialmente realizamos o aprisionamento numa MOT-3D, realizando subsequentemente os passos de resfriamento sub-Doppler mediante o processo de molasses ópticas. Depois disto, os átomos são transferidos para uma armadilha magnética, que consiste de um par de bobinas em configuração anti-Helmholtz, as mesmas usadas para a MOT-3D mas com um gradiente de campo magnético ao redor de uma ordem de grandeza maior. Esta armadilha é combinada com um laser com dessintonia para o azul focado a $30\,\mu$m no centro da armadilha, onde o campo magnético é zero com o objetivo de evitar as perdas por majorana que acontecem nessa região. Com esta configuração, um condensado de $\sim 5 \times 10^5$átomos é obtido a uma temperatura crítica de $\sim 1.1\,\mu$K. Por último, com a máquina construída e caracterizada, começamos re-explorar o experimento de absorção cooperativa de dois fótons por dois átomos aprisionados. Com nosso novo sistema, é possível explorar este efeito no regime clássico e quântico. Estamos interessados em explorar algumas características da interação não linear entre luz e matéria. A ideia de ter dois ou mais fótons interagindo com um ou mais átomos, é possivelmente o começo de uma nova classe de fenômenos que poderíamos chamar de interação de muitos fótons com muitos átomos.

Palavras-chave: Condensado de Bose-Einstein. Átomos de sódio. Armadiliha PLUG. Absorção cooperativa de dois fótons.

List of Figures

Figura 2.3.1 – Apparatus constructed to characterize and compare the atomic sources. Left: 2D-MOT. Center: science chamber. Right: Zeeman slower. . . . 32

Figura 2.3.2 – Magnetic field profile of the ZS. Red curve is theoretical curve produced by Equation (2.2.3). Dots: Experimental data. 34

Figura 2.3.3 – Optical setup for the production of the 3D-MOT using the ZS as source of atoms. 35

Figura 2.3.4 – Number of trapped atoms vs the oven$_{ZS}$ temperature and current of the ZS coils. The frequency of the cooling transition was fixed at $-160\,\mathrm{MHz}$ with respect to the cooling transition frequency with an intensity of $\sim 8I_s$, which was the maximum value of the intensity achievable in our system. The linewidth for the D2 line transition of sodium is $\Gamma = 2\pi \times 9.795\,\mathrm{MHz}$. 35

Figura 2.3.5 – Number of atoms vs the Intensity and detuning of the cooling beam of the ZS. 36

Figura 2.3.6 – Number of atoms as a function of the intensity and detuning of the repumper light beam of the ZS. The defuning is measured with respect to the repumper transition. In this case the intensity of the cooling beam of the ZS were maintained fixed at $4.5I_s$ and $-180\,\mathrm{MHz}$. 37

Figura 2.3.7 – 2D-MOT chamber and magnet arrangement to produce the magnetic field gradient to realized the 2D-MOT of sodium atoms. The blue curve represents the measured magnetic field and the red curve the calculated gradient from the blue one. 38

Figura 2.3.8 – Optical setup for the 3D-MOT and 2D-MOT. 38

Figura 2.3.9 – Number of trapped atoms vs the push beam intensity and detuning. . . 39

Figura 2.3.10 – Number of trapped atoms vs the repumper intensity and detuning measured with respect to the repumper transition. 40

Figura 2.3.11 – Number of trapped atoms vs the intensity of the ZS light beam for the 2D-MOT. 40

Figura 3.1.1 – Frontal (a) and perspective (b) views of the machine for producing the BEC of sodium atoms. The components for potassium atoms are present in the picture. 44
Figura 3.1.2 – (a) and (b) show the experimental system with the optical table where the optical components are be placed to produce the 3D-MOT, MT and BEC. 45
Figura 3.1.3 – Complete experimental system is shown from another perspective. 45
Figura 3.1.4 – 2D-MOT chamber. In the picture it is shown the 45° tilted windows with respect to gravity axis. The MOT beams and the magnetic field is also shown. 46
Figura 3.1.5 – Differential pumping tubes placed between the 2D-MOT chambers and the SC. In (a) the length of the canals with diameters $\phi = 1\,\mathrm{mm}$ and $\phi = 2\,\mathrm{mm}$ are the same, $l = 12.7\,\mathrm{mm}$. 47
Figura 3.1.6 – (a) Pressure and temperature of the SC. When the turbo pump is turned on and the ion pump switched on, the pressure fall abruptly to HV conditions. The same effect is observed for the 2D-MOT chambers in (b). (c) shows the decay in pressure, reachin UHV condition when the Ti-sublimation pump is activated with cycles shown in (d). 51
Figura 3.2.1 – Hyperfine level structure of sodium atoms for the $D2$ line. All the frequencies used in the experiment are presented in the diagram. Detunings are lsited in Table 3.1. 53
Figura 3.2.2 – (a) Schematic diagram of the whole laser system. (b) Components of the SHG box, taken from Toptica website. 54
Figura 3.2.3 – (a) Optical setup for generating the frequencies from the solid state laser. (b) Optical setup for the Zeeman slower light, generated fro the dye laser. Before each optical fiber (not shown in the schemes) in order to switch of the light in a fast way. 56
Figura 3.2.4 – Saturated Absorption setup for Lock-In of the solid state laser. . . 59
Figura 3.3.1 – (a) It is shown the SAS signal and the corresponding error signal used to lock the frequency to the zero point. (b) The three peaks of the signal correspond to the transitions $F = 2 \to F' = 3$ (left peak), $F = 1 \to F' = 2$ (right peak), and the crossover (central inverted peak) between these two transitions. 60
Figura 3.3.2 – (a) Setup for the polarization spectroscopy (PE) to lock the dye laser. (b) The red curve is the dispersion signal, obtained directly form the PE scheme. The black curve corresponds to the cooling transition peak. 61

Figura 3.3.3 – Control system logic. It is shown the order in which the communication process between the different programs and components of the control system happen. 61

Figura 3.3.4 – (a) and (c) show the interface of the static and dynamic (sequence) control, respectively. (b) shows the notepad file where the experimental parameters are written, and (d) the Python interface program, where the experimental sequence is coded. 63

Figura 4.2.1 – Schematic diagram showing the Radiative Escape (RE) and FSCC mechanisms. $V(R)$ represents the interaction potential and R the internuclear separation between the atoms. 68

Figura 4.2.2 – Optical setup used for the 3D-MOT. Both configurations are shown, the Bright-MOT and Dark-SPOT MOT configuration. 69

Figura 4.2.3 – (a) Irregular MOT due to interference of the trapping beams. (b) After some fine adjustment the interference pattern is eliminated. . 72

Figura 4.2.4 – (a) Yellow fluorescence from the sodium MOT with around 4×10^9 atoms. (b) Configuration of the MOT. 73

Figura 4.3.1 – (a) The repumper beam with a dark hole in the center. (b) The repumper beam propagating along the optical system for producing the MOT. 74

Figura 4.3.2 – Optimization of the size of the Dark-SPOT. We look at the number of atoms transferred to the MT for each the Dark-SPOT size. In the MT we put a RF “knife” of 30 MHz and $TOF = 10\,\mathrm{ms}$. 76

Figura 4.3.3 – Evaluating the performance of the Bright-MOT. We measure the loading rate as a function of the 2D-MOT intensity cooling light. The intensities of the other beams were: $I_{3D}^{cooling} = 1.67 I_s$ per beam, $I_{3D}^{repumper} = 0.81 I_s$, $I_{push} = 7.32 I_s$, and $I_{ZS} = 25.73 I_s$. 77

Figura 4.3.4 – Evaluating the performance of the Bright-MOT. We measure the loading rate as a function of the 3D-MOT intensity cooling light. The intensities of the other beams were: $I_{2D}^{cooling} = 3.74 I_s$ per beam, $I_{3D}^{repumper} = 0.81 I_s$, $I_{push} = 7.32 I_s$, and $I_{ZS} = 25.73 I_s$. 78

Figura 4.3.5 – Evaluating the performance of the Bright-MOT. We measure the loading rate as a function of the ZS intensity cooling light. The intensities of the other beams were: $I_{3D}^{cooling} = 1.67 I_s$ per beam, $I_{2D}^{cooling} = 3.74 I_s$ per beam, $I_{3D}^{repumper} = 0.81 I_s$, and $I_{push} = 7.32 I_s$. . 79

Figura 4.3.6 – Evaluating the performance of the Dark-SPOT MOT. We measure the loading rate as a function of the 2D-MOT intensity cooling light. The intensities of the other beams were: $I_{3D}^{cooling} = 1.67 I_s$ per beam, $I_{3D}^{repumper} = 0.81 I_s$, $I_{push} = 7.32 I_s$, and $I_{ZS} = 25.73 I_s$. . 80

Figura 4.3.7 – (a) Bright-MOT. The MOT camera is left to saturate just to show the strong fluorescence of the atomic cloud. (b) The Dark-SPOT MOT enormously diminished the fluorescence of the atomic cloud because 99% of the atoms are in the dark state $|F=1\rangle$. The fluorescence seen in the picture is mainly emitted by the atoms in the surface of the MOT, where the atoms interact with the cooling beam. (c) Absorption of the probe beam ($3^2S_{1/2}\,(|F=1\rangle) \rightarrow 3^2P_{3/2}\,(|F'=2\rangle)$). It is very helpful to align the Dark-SPOT looking at this picture, i.e. diminishing the fluorescence while aligning. And (d) shows the normalized absorption image (section 5.4) , clearly shown the high optical density of the Dark-SPOT MOT. . 82

Figura 5.0.1 – Schematic diagram of the stages in the Bose-Einstein condensation process. Figure is not to scale. 83

Figura 5.2.1 – Calibration of the Hall probe used to measured the quadrupole magnetic field. 89

Figura 5.2.2 – Voltage vs current circulating through the quadrupole coils for obtaining the resistance of both coils separately, A and B. A source of precision and a high stable source was used. 90

Figura 5.2.3 – Coils in the holder support and installed on the science chamber. The vertical windows are deeper than the other ones in order to be nearer to the atoms, in this way the needed current to create high the magnetic field gradient is smaller. Also, this setup allows good optical access in the $z-$axis. 91

Figura 5.2.4 – Curves showing the convertion between the values used in the program of the control system the real values of voltage and current provided to the power supply, then to the quadrupole coils. In (c) it is shown the simulated B-field gradient in the z-direction as a function of the current. For the magnetic trap it is used 46.90 A which represents a B-field gradient of 302 G/cm. 92

Figura 5.2.5 – Modulus of the magnetic field generated for the quadrupole coils. Around the center of the trap the $B-$field gradient is constant. . . 93

Figura 5.2.6 – (a) and (b) show the process of switching on the current from the power supply. For different currents it was monitored the time it takes to turn off comparing both situations: when the control is made using IGBT and when it is not. It is possible to see that there is no significative difference when using or not the IGBT when switching on the magnetic current and B-field. In (c) and (d) it is shown the big difference in turning off the current in the coils (consequently the B-field) when the IGBT is used. The corresponding time for the B-field to fall to the value $1/e$ is $\tau \sim 1\,\mathrm{ms}$, which is fast enough for this setup. 94

Figura 5.2.7 – Test of the cooling system of the coils. In (a) we can see the variation of the voltage through the coils as a function of time for different currents. The variation of the voltage is due to the variation of the resistance as a consequence of the heating. In (b) the variation in the resistance is calculated from (a) using the Ohm law. Then in (c), it is plotted the variation in temperature of the Nylon case. 95

Figura 5.2.8 – Test of the cooling system of the coils simulating an experimental sequence. The current is made to circulate during 1 min and then switched off for other 1 min. This this very similar o the real experimental sequence, and give information about the capacity to maintain the temperature at a constant value, which is very important to hold the resistance of the coils the same, then the B-field is always the same. 96

Figura 5.2.9 – OPT potential along the three axis. 99

Figura 5.2.10 – The plug beam is focused in the center of the chamber and the center of the MT. The plug beam propagates along the same path the image beam, being possible to obtain the image of the plug in the CCD camera. This helps in the alignment of the plug. 100

Figura 5.2.11 – Principle of the optically plugged quadrupole trap. The plug beam propagates along the x-direction. 101

Figura 5.2.12 – Image of the plug beam in the CCD camera. It is clearly visible the hole produced by the plug beam. (a) When the plug beam is misaligned (out of the Majorana hole) the cloud is very dilute due to the great loss of atoms by Majorana losses. (b) When the plug beam is correctly aligned the atoms are kept in the trap and the cloud become very dense. 103

Figura 5.2.13–(a) plug beam profile showing the slightly elliptical mode with radius $a = 43.47\,\mu$m and $b = 36.09\,\mu$m. (b) Because of the symmetry broken due to the slightly elliptical shape of the plug, the atomic cloud separate in two (double well potential), instead of a ring shape. This image correspond a evaporation until 1.3 MHz with a $t_{TOF} = 10\,$ms. (c) It is shown that the most of the atoms can be transferred to a single well potential when the plug beam is slightly misaligned. Here, BEC of sodium atoms showing the bimodal fit. Inside the red circle in the top right of the picture it is possible to see the remaining atoms at one of the potential wells. (e) BEC of sodium atoms with all the atoms transferred to a single potential well. 104

Figura 5.3.1–Working principle of evaporation by Radio frequency (RF). Atoms are transferred from the trappable state $m_F = -1$ to the untrappable $m_F = 1$, where they see a repulsive potential and then are expelled from the trap. 107

Figura 5.3.2–Measurement of the reflected power by the antenna in series with a resistor of $50\,\Omega$(red circles). In black squares and blue triangles are the measurements of power without antenna and only the resistor, respectively. 108

Figura 5.4.1– (a) Normalized image in the LabView program used to process the image, which send the normalized image to a program in Python that finally process the absorption image (b), given ll the parameters needed for the analysis. The image in (a) and (b) does not correspond to the same atomic cloud, which were put here just for illustration. 113

Figura 5.4.2–Temporal sequence for the TOF imaging beam to produce a normalized image. Not to scale. 114

Figura 5.4.3– Optimization of the probe beam frequency. All frequencies used in the experiment are calculated relative to this. The value of the linewidth obtained from the curve deviate just 9% of the exact value ($\Gamma_{exact}/2\pi = 9.795\,$MHz). This curve was realized taking images of an atomic cloud evaporated until 8 MHz with $t_{TOF} = 10\,$ms. $f_{probe} = 0$ in the Curve, corresponds to a value of 1.62 V in the control program system, driving the frequency of the double-pass AOM, and corresponds to a frequency of $-36.80\,$MHz with respect to the frequency obtained when $V_{program} = 0$. This is the frequency taken as reference, $\delta_{lock} = -36.80\,$MHz, because the probe beam has to exactly tuned to the transition $F = 2 \rightarrow F' = 3$. 114

Figura 6.1.1 – Schematic diagram (Not to scale) for the temporal sequence taken into account only the parameters involved in the processes between MOT loading and pre-pumping to the $F = 1$ stage. This last stage is realized in order to send most the atoms to the ground state $F = 1$. The detuning of the repumper light (*) is calculated with respect to the repumper transition. 118

Figura 6.1.2 – Schematic diagram for the temporal sequence of the magnetic field gradient, plug intensity, and RF frequency. Not to scale. 118

Figura 6.2.1 – (a) Optimized Evaporation ramp for sodium atoms. The evaporation ramp is divided in five steps, each step is a linear ramp. At the final value of the ramp, 0.65 MHz, the BEC of sodium atoms is achieved. (b) Absorption images of the atoms in each step of the evaporation process. 119

Figura 6.2.2 – Lifetime of the atoms in the MT. The number of atoms was measured in the magnetic trap, using a knife of 30 MHz, and using TOF imaging with $t_{TOF} = 6\,\mathrm{ms}$ 120

Figura 6.2.3 – Evaporation ramp for sodium atoms. The black dots are the points of in the MT with the plug beam, and the red points represents evaporation without plug beam. From this, we can observe the importance of the plug beam in avoiding the Majorana losses in the MT. 122

Figura 6.2.4 – The lifetime of the BEC is measured keeping the atoms in the OPT for different times after the BEC is reached. The curve is made for different final evaporation RF. The lifetime for the final RF (0.65 MHz) used in the subsequent experiments is $\tau = 636\,\mathrm{ms}$, enough for the the realization of the experiments of interest. . . . 123

Figura 6.2.5 – Tentative to measure the aspect ration of the condensate. It is hard for this system to measure the aspect ration because the change occurs in the initial milliseconds of the expansion, making the BEC very dense and dense the image inaccurate due to saturation. (b) Images of the BEC for different t_{TOF}. From this picture, it is possible to note that the aspect ration is not completely evident as we would like. Thus, it is concluded, that before $t_{TOF} = 4\,\mathrm{ms}$ the cloud was tightly confined in the y direction because this is the axis with strongest frequency. . . . 124

Figura 6.3.1 – BEC of sodium atoms in an OPT configuration. The two BECs corresponds to atoms in the two potential wells created by the plug beam. 125

Figura 6.3.2 – Single BEC in a OPT configuration. The single BEC is obtained slightly misalignment the plug beam from the center of the trap. This created a situation in which the atoms are transfer to the deeper potential well. The temperature of the BEC is 435 nK, the total number of atoms is 6.84×10^5, and the condensate fraction is just around of 30. Here, $TOF = 15\,\mathrm{ms}$ 126

Figura 6.4.1 – Schematic diagram for the temporal sequence including the current modulation to measure the OPT frequencies using the parametric heating method. 127

Figura 6.4.2 – Trap frequencies of the OPT. We found four peaks when using the method of parametric heating. 127

Figura 7.2.1 – Theoretical curves using Equation (7.2.1) of the transition probability as a function of the detuning of the excitation light. The peaks shown in the top correspond to the single photon absorption, while the curve in the bottom corresponds to the two-photon absorption. This last peak has two contributions: a Lorentzian and a dispersive part. 133

Figura 7.2.2 – Atomic level scheme for a pair of interacting two-level atoms (left), and when the compound system is treated as a four-level system. . 134

Figura 7.3.1 – Energy levels of the individual atoms and potential energy curve of the interaction. The two photons can excite the pair of atoms if they are interacting. 137

Figura 7.3.2 – Ionization process of the excited atoms after the absorption of photons of the probe beam. 138

Figura 7.3.3 – Experimental sequence for the excitation and detection of the cooperative absorption of two photons in the MOT of sodium atoms. 138

Figura 7.3.4 – Experimental results for the cooperative absorption of two-photon in a MOT of sodium atoms. (a) Frequency scan of the D1 and the D2 line produces the side and big peaks, and the frequency scan around the two-photon frequency produce a peak of 1000 times smaller than the previous ones. (b) The cooperative absorption peak is evident, and we fit the theoretical (black line) curve together with the experimental data and our correction to the theoretical model (red line). In this way we demonstrated the cooperative absorption effect in cold sodium atoms. 140

Figura 7.4.1 – Each point represent the averaged of 6 images when the excitation pulse is present or not. For instance, the first point is made without the excitation beam, the second with the excitation and so on. . . 141

Figura 7.4.2 – Frequency scan around the D2 line transition. (a) We observe the losses of atoms when the beam is in resonant with the D2 transition. We vary the pulse time to avoid the cloud deformation. (b) Temperature as a function of the detuning of the excitation beam. 142
Figura 7.4.3 – The cloud is deformed when the excitation beam is applied to the trap. It seems that intensity should be reduce collimating the beam to a size much greater than the cloud size in order to avoid mechanical effects of the light, as for example, dipole force which would mask the two-photon signal. 143
Figura 7.4.4 – Frequency scan around the D2 line transition. (a) We observe the losses of atoms when the beam is in resonant with the D2 transition. We vary the pulse time to avoid the cloud deformation. (b) Temperature as a function of the detuning of the excitation beam. 144
Figura 7.4.5 – The pulse time was varied for the D2 line. This is a good form of calibrating of our excitation and detection system in order to better understand the process happening the system. 144
Figura 7.4.6 – The pulse time was varied for the D2 line. This is a good form of calibrating our excitation and detection system in order to better understanding the process happening in the system. 145

Contents

1 Introduction **23**

2 Designing, testing and optimizing our atomic source: 2D-MOT vs Zeeman slower **27**

2.1 Choosing the configuration of our source of cold atoms: 2D-MOT vs Zeeman Slower . . . 27

2.2 Important characteristics of 2D-MOT and Zeeman slower . . . 29

2.2.1 Fundamental principles of the Zeeman slower . . . 29

2.2.2 2D-MOT . . . 31

2.3 Experimental setup: 2D-MOT and Zeeman slower . . . 32

2.3.1 Science chamber . . . 32

2.3.2 Features of the Zeeman slower as a source of atoms . . . 33

2.3.3 Features of the 2D-MOT as a source of cold atoms . . . 37

2.4 Comparison between the two atomic sources . . . 41

3 Experimental apparatus for ^{23}Na BEC **43**

3.1 Vacuum system . . . 43

3.1.1 Ultracold sodium atoms machine . . . 43

3.1.2 Achieving high and ultrahigh vacuum . . . 49

3.2 Optical system . . . 52

3.2.1 Lasers . . . 52

3.2.2 Optical setup . . . 55

3.2.3 Laser locking . . . 58

3.3 Control system . . . 60

4 Magneto-Optical Trap: Bright-MOT vs Dark-SPOT MOT Na atoms **65**

4.1 Magneto-optical trap . . . 65

4.2 Bright-MOT . . . 65

4.2.1 Loading atoms in the MOT . . . 66

4.2.2 Our Bright-MOT . . . 69

4.2.3 Experimental tips for obtaining a good MOT 71
4.3 Dark-SPOT MOT (Dark spontaneous-Force optical trap) 73
4.3.1 Our Dark-SPOT MOT 75
4.3.2 Experimental tips to align the Dark-SPOT 81

5 Route to quantum degeneracy of sodium atoms 83

5.1 Optical molasses and transfer to the magnetic trap 84
5.2 Optically plugged magnetic quadrupole trap 86
5.2.1 Principles of magnetic traps 86
5.2.2 Our coils design 89
5.2.3 Principles of an OPT 97
5.2.4 Experimental configuration of our OPT 100
5.3 Evaporative cooling in our OPT 105
5.3.1 Our RF antenna and evaporation process 108
5.4 Imaging system 109
5.4.1 Information from Time-of-Flight for thermal clouds 110
5.4.2 Information from Time-of-Flight for atoms in the BEC 111
5.4.3 Configuration of our imaging system 111

6 Bose-Einstein condensation of sodium atoms 117

6.1 Bose-Einstein condensation of sodium atoms 117
6.2 Evaporation process 117
6.3 Bose-Einstein condensation of sodium atoms 125
6.4 Frequencies of the OPT 126

7 Two-photon two-atom processes 129

7.1 Introduction 129
7.2 Cooperative absorption of two-photons by two two-level interacting atoms 132
7.3 Cooperative absorption of two-photons by two sodium atoms in the magneto-optical trap 136
7.4 2P2A cooperative absorption in a magnetic trap 140
7.5 Light forces on atoms 145
7.5.1 Spontaneous force 146
7.5.2 Dipole force 147

8 Conclusions 151

REFERENCES 153

A Annex - Published papers related to this PhD thesis 161

Chapter 1

Introduction

Since the first demonstration of Bose-Einstein condensation (BEC) in dilute alkali atoms in 1995 (1–3), these systems have become a cornerstone, not just for atomic physics, but in general. Successfully integrating many areas, as for instance, Many-body Condensed Matter Physics, Optics, Atomic Physics, Quantum Optics, cavity Quantum Electrodynamics (cQED), and quantum information, led to many advances in many fields. In all these areas, significant advances have been realized using BECs, in situations like optical lattices, cavities, quantum devices, etc. (4–7)

Cold atom systems use light-matter interaction as the main tool to extract information. From the identification of the occurrence of BEC until the detection of quantum turbulence emerging from a BEC, the interaction of light with the atoms is fundamental. In many cases the interaction is essentially linear and one can correlate light absorption with local atomic density. The atomic interaction, the possibility to have strong correlated system in BECs, as well as the many body aspects of those quantum samples make necessary to go beyond linear light-matter interaction.

The idea of having two or more photons coherently interacting with two or more atoms is the beginning of a new possible class of phenomena that we could call many photons-many body interaction. In this new possibility, photons and atoms will be fully correlated, introducing new aspects to the interaction.

The first step to this new regime of light-atom interaction is the cooperative two-photon absorption in which two interacting atoms absorb two photons generating a pair of correlated atoms and correlated emitted photons. From this first step, we can imagine its extrapolation to many photons-many atoms. This is certainly an open topic to both classical and quantum gases.

Another important topic is quantum turbulence. The possibility to generate tangle quantized vortices in superfluids can be a starting point for the understanding of turbulence in general. In this case, the possibility of mixture of atoms in the quantum regimes creates an extra control. Having a mixture of quantum fluids, allows to transfer vorticity between the fluids, eventually controlling the turbulence process.

On an equivalent way, the mixture of atoms allows to investigate multi-photon interaction by controlling scattering within species or inter-species.

With the aim to start a sequence of studies in this direction, we start to construct a new experimental system with ability to condensate sodium (^{23}Na) and potassium (^{41}K) atoms, allowing studies of light scattering and quantum turbulence in each of the individual species as well as the combination.

Recently, the number of systems able to produce multiple species BEC has raised rapidly. These systems can be boson-boson (8) or boson-fermion (9, 10) mixtures. Our group is interested in the study of superfluidity properties of boson-boson system and has as one of the main goals the generation and transfer collective excitations from one species to the other. Another important goal of the group to be pursued with this system is the control of the inter-species interaction through the Feshbach resonances. Also, the group is interested in the production of vortices in this system and reach quantum turbulence (11), in an alternative way of that obtained by the first time in 2009 (12) by our group.

The main goal of this PhD was to construct the apparatus to produce a double species BEC for future works, and to obtain the BEC of one the species, namely, the sodium atoms. With this system, we wanted to explore some aspects of non-linear light-matter interaction in the sodium BEC.

Nowadays, there are a relatively large number of groups that produce Bose-Einstein condensates in their laboratories, studying many different aspects and applications. Our group is particularly interested in the construction of a system able to produce a double species BEC of sodium and potassium atoms.

The non-linear phenomenon we are interested is the cooperative absorption of two photons by two trapped atoms (2P2A), either in the classical or quantum regime. With the built machine we wanted to explore this effect, revisiting the work realized in my first year of PhD. (13) In this work, we demonstrated by the first time the 2P2A cooperative absorption in colliding cold sodium atoms in a magneto-optical trap. The 2P2A effect is strongly dependent on the density of the sample, in this way we wanted to explore it in denser atomic clouds, as are atoms in the BEC or even in the magnetic trap (MT).

Thus, after performing the work about 2P2A cooperative absorption in a MOT, we started the construction and characterization of the new apparatus, and finally, with the production of the BEC, we started to revisit the 2P2A effect. This is of particular importance, since we are interested in new forms of studying the collective effects, or cooperation, in sample of many atoms, i.e., we could explore many-body states of the BEC, starting with the study of the non-linear light-matter interactions.

The thesis is divided as follows: in chapter 2 is presented the characterization performed to compare the two possible atomic sources that could be used in the apparatus to load the MOT, which is the starting point of the whole process to reach the BEC, then this is of crucial importance. In chapter 3 it is described the constructed machine to obtained the BEC. Also, it is discussed the process to reach ultrahigh vacuum (UHV) conditions, the optical and control system.

In chapter 4 a comparison between the performance of the Bright-MOT and Dark-SPOT MOT is presented. With this, we show why Dark-SPOT MOT is widely used for sodium atoms.

In chapter 5 the complete description of the different stages required for achieving the BEC is shown. Each stage is described individually, point out the important elements and conditions needed for its realization. Chapter 6 shows some results of the BEC characterization which are crucial for knowing the parameters of our system, as are critical temperature, trap frequencies, MT lifetime, and BEC lifetime.

Chapter 7 is devoted to the study of the 2P2A cooperative absorption. Specifically, in this chapter a brief review of the basic concepts behind the phenomenon are presented, and then the results concerning to the 2P2A experiment in the MOT, and the attempts to realized the measurements in a MT of sodium atoms. Following this chapter, the conclusions about the thesis are drawn.

Chapter 2

Designing, testing and optimizing our atomic source: 2D-MOT vs Zeeman slower

In this chapter, I discuss the experimental system projected and implemented to be used as the atomic source for our BEC of sodium atoms' machine. It was necessary to choose the system to be used for producing an atomic flux in order to load a magneto-optical trap (3D-MOT), which is the initial stage of the condensation process. In this way, we had two options: to use a Zeeman slower (ZS) or a two-dimensional magneto-optical trap (2D-MOT) to produce the atomic flux which loads the 3D-MOT. Then, the first effort was to characterize the two different atomic sources and choose the most suitable for our case. After this task was finished, I continued with the next steps (chapters 3, 5, and 6) for the BEC production, i.e., laser cooling, optically plugged quadrupole magnetic trap (OPT), and evaporative cooling. Thus, in this chapter, I show the experimental configuration of the ZS and 2D-MOT as sources of atoms and present a characterization that allows us to directly compare the performance of both, and choose the best one for our system. It is worth to mention that this chapter is based in our published paper (14), where the comparison of the Zeeman slower and 2D-MOT is presented in detail.

2.1 Choosing the configuration of our source of cold atoms: 2D-MOT vs Zeeman Slower

The atom source is a crucial component in Bose-Einstein condensation (BEC) experiments since commonly the first step for realizing AMO (atomic, molecular and optics) experiments is to load a trap with a source of atoms. The trap depth ($E_T = k_B T$), determines the maximum energy an atom can have in order to be captured by the system. This shows the necessity for creating atomic sources able to produce cold atomic beams such that the atoms can be captured by the trap.

Several configurations are commonly used in AMO experiments to efficiently load the traps, and since the initial experiments of atomic cooling and trapping (15, 16), these techniques have evolved looking for more efficient ways to produce a cold atomic beam able to load a trap in shorter times with higher numbers of atoms.

Zeeman-slower (ZS) is one of the first techniques used to decelerate an atomic beam. This technique, designed and implemented by Phillips and Metcalf (15) in 1982, uses the Zeeman shift to compensate the Doppler shift felt by the atoms when they decelerate, keeping them constantly in resonance with the light field. This first deceleration of an atomic beam (15), done with sodium atoms, opened up the possibility to capture these atoms in a magneto-optical trap (MOT) (16), which was one of the most important accomplishment in AMO physics.

Another technique, known as double- MOT configuration (17), uses two vacuum chambers to guarantee an ultra-high vacuum (UHV) region at the final trap chamber. A 3D-MOT is performed in a first chamber using a hot vapor as source of atoms, and then the atoms in this first 3D-MOT are transferred to a second chamber, with higher vacuum, using a laser beam that pushes them from one chamber to the other. Then, only colder atoms in the first chamber are transferred to the second chamber, making the vacuum of the final chamber orders of magnitude better. Because the low axial velocity of the atoms being transferred, the loading time of the 3D-MOT in the UHV chamber (second chamber) is relatively large in comparison with a Zeeman slower source, then this is a drawback of this configuration.

The above statements, about the disadvantage of the double-MOT configuration, tells us that if the axial velocity of the first MOT is increased, the flux of atoms can also be increased, leading to shorter loading times of the second MOT in the UHV chamber. Then, one can overcome this difficulty using a 2D-MOT as a source, instead of the 3D-MOT. This configuration was firstly developed by Dieckmann et al. (18) for ^{87}Rb, and expanded to other species like ^{39}K and ^{41}K (19), and ^{7}Li (20), and is one of the most recent ways to produce a flux of cold atoms comparable with the Zeeman slower.

In our case, of ^{23}Na atoms, the most typical source of slow atoms is the ZS and only recently, a 2D-MOT source for sodium atoms was implemented by Lamporesi et al. (21) We have constructed a 2D-MOT system inspired in this setup. We performed a characterization of both sources of sodium atoms, ZS and 2D-MOT, to know the performance of each configuration.

As will be presented in the next sections, we directly compare both sources in the same experimental system. In the setup, both sources are connected to the same science chamber (SC), allowing us to perform a direct comparison of several important parameters, as for example, loading rates and efficiency, and studied other important parameters of each technique in similar conditions. We used a ZS previously designed using the spin-flip configuration (22–24) to perform the comparison.

The experimental characterization and comparison of both cold atomic sources allows us choosing the most suitable for our experiment. The optimum parameters for each case were obtained by observing the loading rate and the final number of atoms in the 3D-MOT. We concluded that the 2D-MOT provides an atomic flux comparable with that produced by the ZS, but with an enormous advantage with respect to the size of the apparatus.

2.2 Important characteristics of 2D-MOT and Zeeman slower

The working principle of both cold atomic sources, Zeeman-slower (ZS) and 2D-MOT are given in this section, which are necessary to better understand the characteristics of each source.

2.2.1 Fundamental principles of the Zeeman slower

Zeeman slowers are used to decelerate atoms in an atomic beam to velocities smaller than a certain trap's capture velocity (25), which is the velocity that set an upper limit for the trap (MOT), meaning that atoms above this velocity cannot be captured. A ZS uses an atomic cycling transition to slow down an atomic beam via radiation pressure force. This is accomplished when a light field counter-propagating to the atomic beam is combined with a spatially dependent magnetic field that compensates the Doppler shift of the light with the change in energy due to the Zeeman effect.

When a laser beam with wave vector $\vec{k}$ and frequency ω near-resonant to the atomic transition ω_0, is counter-propagating to an atomic beam, one ground state atom absorbs a photon and goes to the excited state, leading to an interchange of momentum. In this process the atom will loss a quantity $\hbar k$ of momentum in the $-\vec{k}$ direction. After a time equal to the excited state lifetime (on average), the atom spontaneously emit a photon with momentum $\vec{k}$ in a random direction. If this process happens many times (in a cyclic transition), the atom will loss a velocity equal to k/m in each cycle in the direction of $\vec{k}$. A semiclassical treatment of the atom-light interaction the force exerted by the light on the atoms is given by

$$F = \hbar k \frac{\Gamma}{2} \frac{s}{1 + s + \frac{4\delta}{\Gamma^2}}, \tag{2.2.1}$$

where Γ is the excited state lifetime, $\delta = \omega - \omega_0$ is the slowing light detuning from resonance, and s is the ratio of the laser intensity (I) to the transition saturation intensity (Is) ($s = I/Is$). Atoms with different velocities see a different laser frequency ω due to the Doppler shift. Taking into account this shift, the detuning in the rest frame of the atoms can be written as $\delta = \omega + \vec{k} \cdot \vec{v} - \omega_0$. In the presence of a static magnetic field (B) the hyperfine splitting of the Zeeman sub-levels is given by: $\Delta E = \mu' B$, where μ' is the magnetic moment of the cycling transition. Therefore, in the presence of a B field the atomic resonance is equal to $\omega_0 + \frac{\mu' B}{\hbar}$. Therefore, to compensate the Doppler shift, a magnetic field is applied, and the final detuning is given by

$$\delta = \omega - \omega_0 + \vec{k} \cdot \vec{v} - \frac{\mu' B}{\hbar}, \tag{2.2.2}$$

Using a spatially inhomogeneous magnetic field, the light field detuning will be spatially dependent, then in principle the light can be maintained in resonance ($\delta = 0$) with the atomic transition at each point of space, causing a maximum deceleration. The maximum deceleration is obtained when $s \gg 1$ and $\delta = 0$ (from Equation 2.2.1), given by $a_{max} = \hbar k \frac{\Gamma}{2m}$, where m is the mass of the atoms. Furthermore, the deceleration of the atoms as being constant, we can use the kinematic equation $(v_{atom}(z))^2 = v_0^2 - 2az$, to obtain the relation between velocity and acceleration, that are combined to finally find the magnetic profile required as a function of the position,

$$B(z) = B_0 - \left(\frac{\hbar k v_0}{\mu'}\right) \sqrt{1 - \left(\frac{z}{z_0}\right)^2}, \tag{2.2.3}$$

where z_0 is the length of the ZS given by $z_0 = \left(v_0^2 - v_{final}^2\right)/2a$ and B_0 is the magnetic field at the point where the atoms have the initial velocity (v_0).

The Maxwell-Boltzmann distribution of the atom source (usually an oven) set the value of the initial velocity (v_0), and also defines the class of velocities, $v_{initial} < v_0$, that will be slowed down up to, or smaller than $v_{capture}$ (capture velocity). The size of the ZS is set depending on the initial velocity of the source. The longer the slower is, the higher the value of v_0, but because v_0 also sets the magnitude of the magnetic field, meaning that high values of v_0 require high values of $|B(z)|$. The bias field B_0 sets the light field detuning from the cycling transition, usually chosen to be red-detuned around 100 MHz,which guarantee that Zeeman slower light beam does not create a large unbalancing force at the trap region. Normally one adds at the end a second coil, inverting the field to match the MOT field. Summarizing, the whole process can be seen in the following simple way: the photons satisfying the relation

$$0 = \Delta + \left|\vec{k} \cdot \vec{v}\right| + \frac{\mu' B(z)}{\hbar}, \tag{2.2.4}$$

(where $\Delta = \omega - \omega_0$) will be absorbed by the atoms and in this way the interchange of momentum between light and atoms works to decelerate the atomic beam. Once one atom absorbs a photon it recoils, losing velocity, and after a spontaneous re-emission of the photon, it gains a random momentum, which on average after many absorption–emission processes is zero, thus having a net momentum exchange in the direction contrary to the motion. (26)

2.2.2 2D-MOT

The confining of neutral atoms is realized using the combination of an inhomogeneous magnetic field and circular polarized light near-resonant to a cycling transition. (16) A position dependence of the hyperfine energy level, whose slope depends on the linear product $-\vec{\mu} \cdot \vec{B} = g_F m_F \mu_B B$, is created by the presence of the inhomogeneous magnetic field (Zeeman effect). Depending on the hyperfine state, the slope can be positive or negative, $m_F > 0$ or $m_F < 0$, respectively.

To produce the opposing dissipative forces, two counter-propagating laser, with frequencies tuned to the red of the transition and with $\sigma^{\pm}$ polarization, with respect the quantization axis created by magnetic field, coming from the $\pm\hat{x}$-direction, are aligned. The force of the beams are

$$F_{\sigma\pm} = \hbar k \frac{\Gamma}{2} \frac{s}{1 + s + \frac{4\delta_{\pm}}{\Gamma^2}} \left(\pm\hat{x}\right). \tag{2.2.5}$$

If the atom position (x) is $x > 0$ we have $\delta_+ < \delta_-$ and for $x < 0$ we have $\delta_+ > \delta_-$. This means that if the atoms move away from the center of trap in the $\hat{x}$-direction, the atom absorbs the light with σ^+ polarization with more probabilty thant the σ^- light, pushing the atom to the center of the trap. The same happens if the atom escapes in $-\hat{x}$-direction, being pushed to the center by the σ^- light. This creates a net force that bring the atoms to the zero point of the magnetic field. The 2D-MOT uses this same principle to trap the atoms in the $\hat{x}$ and $\hat{y}$ direction.

Once the atoms are cooled down in the 2D-MOT, they are transferred to a 3D-MOT chamber, where a three-dimensional magneto-optical trap is performed. The atoms are transferred using a laser beam that pushes the atoms from the 2D-MOT to the 3D-MOT chamber. This laser beam is called the push beam. This is the scheme of a double-MOT configuration (17) mentioned before, but with a 2D-MOT as the source of atoms for the 3D-MOT.

It is worth to recall important points discussed in reference. (27) About the geometry of the 2D-MOT, they pointed out that the longer is the length of the 2D-MOT (longitudinal size) the higher is the obtained flux of atoms. Also, faster atoms can be captured because the confining region is bigger and then the atoms can travel more distance until they are captured. As a consequence of this, faster atoms are added, increasing the mean velocity of the 2D-MOT. This means that exist a certain optimum length of the 2D-MOT, and above this length a saturation in the efficiency of the flux of atoms is reached.

Then, increasing the length of the 2D-MOT, increase the number of captured atoms, but also the mean velocity of the atoms. This is a drawback because, we want to produce a cold atomic beam able to load the 3D-MOT in the SC, and not a fast atomic beam with average velocitiy greater than the capture velocity of the 3D-MOT.

Another important point is the density: for higher densities, there is an increase in the flux of atoms at low pressures of the vacuum chamber. When the atomic density is higher than a certain optimum value, the pressure in the SC start to increase, leading to bad collisions (see chapter 4) to dominate the process, decreasing the flux of atoms.

2.3 Experimental setup: 2D-MOT and Zeeman slower

Figure 2.3.1 shows the whole experimental apparatus constructed to performed the characterization and comparison of the atomic sources. Science chamber, 2D-MOT and ZS are described independently.

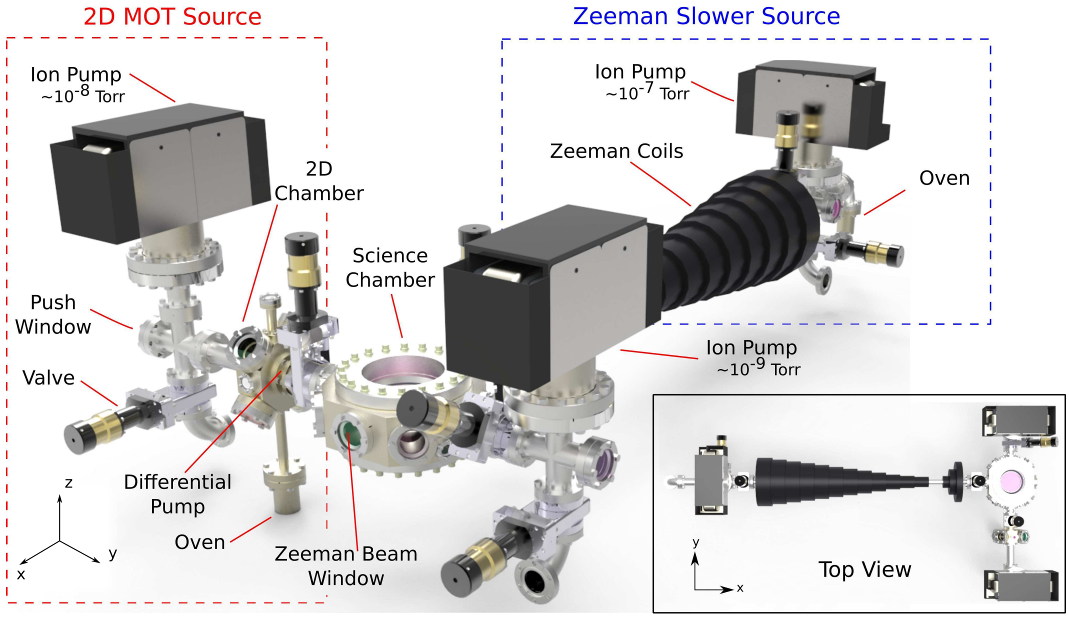
2D MOT Source
Zeeman Slower Source
Ion Pump ~10^{-8} Torr
Ion Pump ~10^{-7} Torr
Zeeman Coils
Oven
2D Chamber
Science Chamber
Push Window
Valve
Ion Pump ~10^{-9} Torr
Differential Pump
z
y
x
Oven
Zeeman Beam Window
Top View
y
x

Figure 2.3.1 – Apparatus constructed to characterize and compare the atomic sources. Left: 2D-MOT. Center: science chamber. Right: Zeeman slower. Source: PEDROZO-PEÑAFIEL (14)

2.3.1 Science chamber

Figure 2.3.1 shows the SC in the center of the setup. The chamber is made of stainless steel 316L, and has six windows in the lateral face and two deep windows in the bottom and top faces. An ion pump of 75 L/s maintains a pressure of 8×10^{-10} Torr. The magnetic field is generated by a pair of coils in anti-Helmholtz configuration. These coils are mounted along the vertical direction (see chapter 5, section 5.2.2 in chapter). A current of 5 A produces a field gradient of approximately 15 G/cm. The three cooling beams used in retro-reflected configuration are obtained from a dye laser (Coherent 899), that we will call Dye laser 1 from now on. Each beam has a diameter of 2.0 cm and intensities of

$15.9\,\mathrm{mW/cm} \simeq 22.5 I_s$, were I_s is the saturation intensity for the D2 line of sodium. From the same dye laser, we obtain the cooling $3^2S_{1/2}(F=2) \rightarrow 3^2P_{3/2}(F'=3)$ and repumper $3^2S_{1/2}(F=1) \rightarrow 3^2P_{3/2}(F'=2)$ frequencies required to produce the 3D-MOT. The laser is locked to the cooling transition observed in the saturation absorption spectroscopy, and the MOT frequency is then red-detuned by 23 MHz. The repumper frequency is obtained by using an Electro-optic modulator (EOM) (Newport) of 1.7 GHz. The diameter of this beam is 2.0 cm and its intensity of $7.8\,\mathrm{mW}/cm^2$ ($I = 1.2 I_s$). We used a Fabry-Perot interferometer to set the ratio between the cooling and repumper intensity.

The number of loaded atoms in the 3D-MOT was obtained through the measurement of the fluorescence emitted by the atoms with a calibrated photodetector. To calculate the number of atoms in the 3D-MOT it is used the relation between the total power emitted by the cloud and the number of atoms (28): $P_{total} = N_{MOT}\hbar\omega_0\Gamma\rho_{ee}$, where P_{total} is the total power emitted by the atoms, N_{MOT} is the total number of atoms, $\hbar\omega_0$ is the energy of the cooling transition, $\Gamma\rho_{ee}$ is the total decay rate the from the excited state, $\Gamma = 2\pi \times 9.795\,\mathrm{MHz}$ is the linewidth of the D2 sodium line, and $\rho_{ee} = \frac{1}{2}\frac{s}{1+s+\left(\frac{2\delta}{\Gamma}\right)^2}$ is the density matrix element for the excited state population, and s is the saturation parameter. (29) The ratio $\frac{P_{PD}}{P_{total}} = \frac{d\Omega}{4\pi} = \frac{\pi r^2}{4\pi f^2}$, takes into account the geometrical factor due to the fact that the optical system only captures a portion of the emitted fluorescence. Here, r and f are radius and focus respectively, of the lens used to focus the fluorescence of the MOT onto the photodetector. Also, the relation between the power of the light emitted by the atomic cloud and the voltage measured by the photodetector is given by the proportionality factor α ($P_{PD} = \alpha V_{PD}$), which is obtained from the calibration of the photodetector, and has units of Watts/Volts. Combining all these relations, the number of atoms is given by,

$$N_{MOT} = \frac{4\alpha f^2}{\hbar\omega_0\Gamma\rho_{ee}r^2}V_{PD}, \tag{2.3.1}$$

and with all the known factor in a proportionality constant we can finally write $N_{MOT} = \kappa V_{PD}$, where $\kappa = \frac{4\alpha f^2}{\hbar\omega_0\Gamma\rho_{ee}r^2}$.

2.3.2 Features of the Zeeman slower as a source of atoms

The ZS is a cylindrical stainless steel tube of 2.39 cm of internal diameter, 2.55 cm of external diameter and 100 cm length covered with a set of coils which generate the ZS magnetic field. The ZS is maintained at a pressure of about 10^{-8} Torr using an ion pump of 75 L/s. An oven (called here oven$_{ZS}$) is attached at the beginning of the ZS using a six way connector. A gate valve is placed between the ZS and the oven$_{ZS}$to separate the two regions when required. To keep the pressure in the ZS and SC in HV (high vacuum) conditions is used a using a differential pumping tube, which avoids the excessive increasing in pressure in the ZS due to the heating of the oven while running the experiment. Figure 2.3.1 shows the configuration of the ZS, showing the position of the vacuum pumps and oven$_{ZS}$.

As mentioned above, the oven$_{ZS}$ is connected to an elbow shape tube with a cooper gasket at the end, which has a nozzle of 4 mm diameter and is attached to the output of the elbow tube in order to produce an effusive collimated atomic beam when the oven$_{ZS}$ is heated.

In this setup, we use the ZS in spin-flip configuration (22, 24) in which the magnetic field at the beginning of the ZS is very high and decrease smoothly until reach a region of zero field and afterward increase again (small magnetic field), but with inverted direction, as shown in Figure 2.3.2. The design and construction of the ZS is well described in (22, 24), thus, I only concentrate in the use of the ZS as a source of atoms, instead of its design and construction details. Figure 2.3.2 also shows the magnetic field profile together with the ZS for comparison.

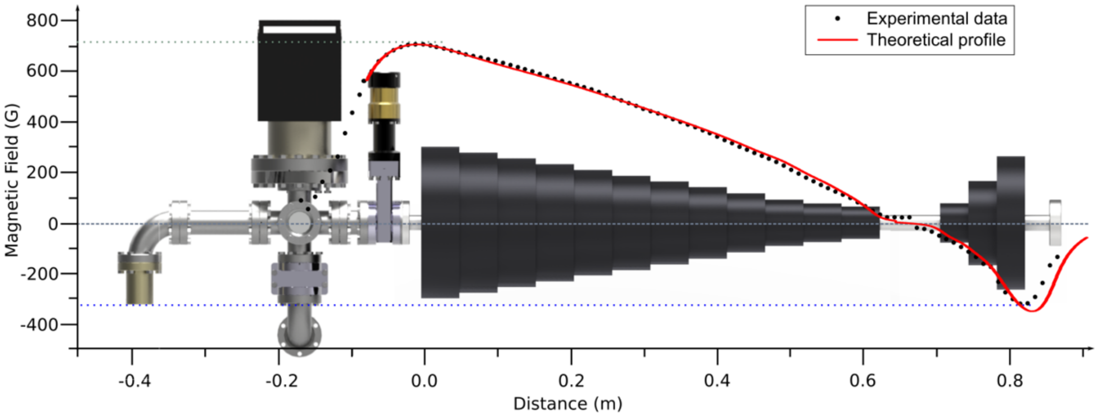

Figure 2.3.2 – Magnetic field profile of the ZS. Red curve is theoretical curve produced by Equation (2.2.3). Dots: Experimental data.
Source: PEDROZO-PEÑAFIEL (14)

The counter-propagating laser beam, used to decelerate the atomic beam, has a diameter of 3 cm and is focused at the nozzle where it had a diameter of $\sim$ 0.6 cm. This light beam has two frequencies, the cooling and repumper, which is obtained using a acoustic-optical modulator, AOM (Brimrose), with an input radio-frequency (RF) around 1.712 GHz. The cooling beam is red-detuned about 180 MHz. The intensity of the cooling and repumper beams are $4.5I_s$ and $1.1I_s$, respectively. The optical setup for producing the frequencies for decelerating the atomic flux and the frequencies for trapping the atoms in the 3D-MOT chamber are depicted in Figure 2.3.3.

All the parameters of the ZS, as temperature of the oven$_{ZS}$, current of the ZS coils, frequency and intensity of the cooling and repumper light, were scanned looking at the number of loaded atoms of the 3D-MOT in the SC. The results of these characterization are shown below.

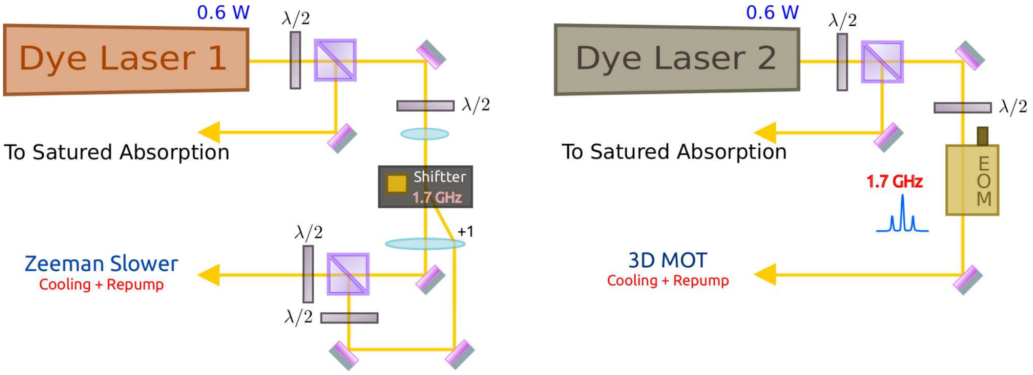
0.6 W
Dye Laser 1
$\lambda/2$
$\lambda/2$
To Satured Absorption
Shiftter
1.7 GHz
$\lambda/2$
+1
Zeeman Slower
Cooling + Repump
$\lambda/2$
0.6 W
Dye Laser 2
$\lambda/2$
$\lambda/2$
To Satured Absorption
1.7 GHz
EOM
3D MOT
Cooling + Repump

Figure 2.3.3 – Optical setup for the production of the 3D-MOT using the ZS as source of atoms.
Source: PEDROZO-PEÑAFIEL (14)

The first scanned parameters were the temperature and current of the ZS coils. Figure 2.3.4 shows the result for this scan. We observed a maximum at a temperature of 300°C for the oven$_{ZS}$. Above this value the pressure in the SC starts to increase producing losses due to collisions with the background atoms. Moreover, it is possible to see the saturation situation for higher values of the current of the coils of the ZS. For this temperature, the best current in the coils was of 12 A.

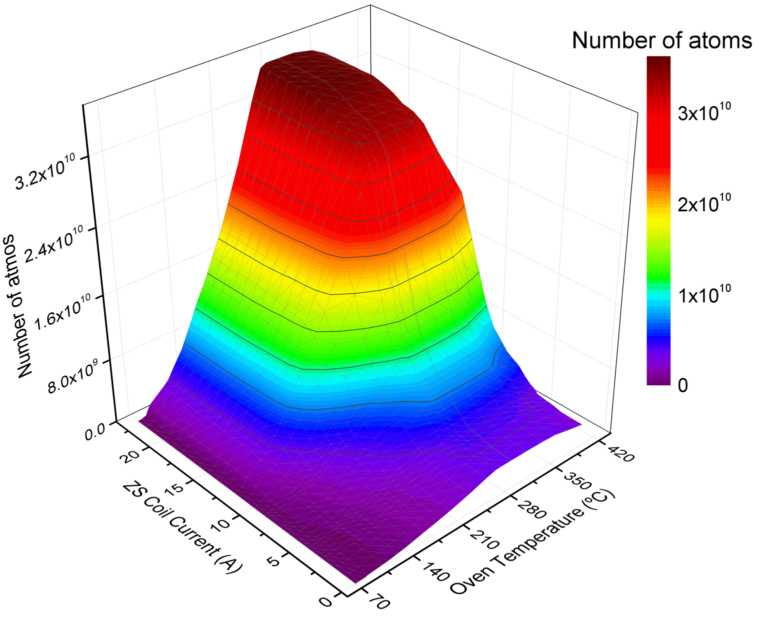

Figure 2.3.4 – Number of trapped atoms vs the oven$_{ZS}$ temperature and current of the ZS coils. The frequency of the cooling transition was fixed at -160 MHz with respect to the cooling transition frequency with an intensity of $\sim 8I_s$, which was the maximum value of the intensity achievable in our system. The linewidth for the D2 line transition of sodium is $\Gamma = 2\pi \times 9.795$ MHz.
Source: PEDROZO-PEÑAFIEL (14)

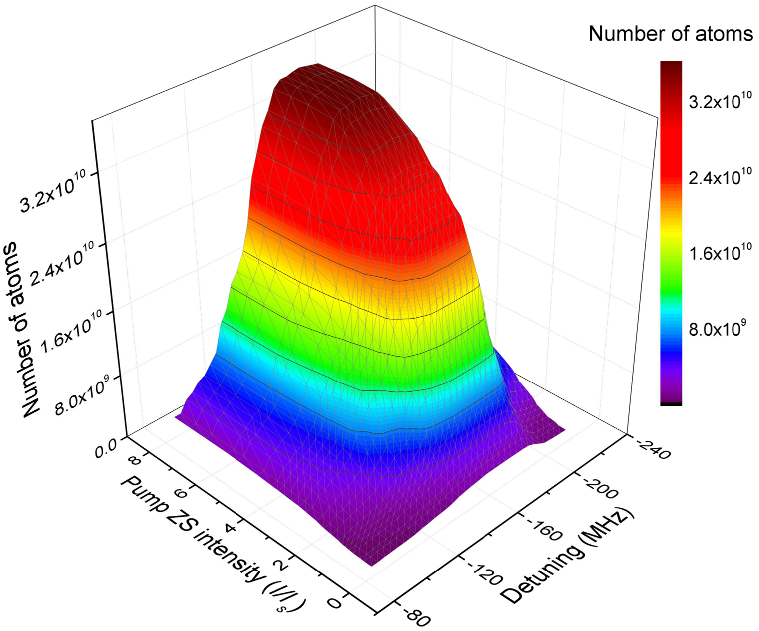

Figure 2.3.5 – Number of atoms vs the Intensity and detuning of the cooling beam of the ZS.
Source: PEDROZO-PEÑAFIEL (14)

The experimental data for the detuning and intensity of the of the cooling beam of the deceleration light is shown in Figure 2.3.5. From this we found that the best detuning for the ZS laser beam is about -180 MHz with respect to the cooling frequency. Also, from Figure 2.3.5 we observed that the detuning can be scan around several tens of MHz and still have a good number of trapped atoms in the 3D-MOT. With relatively low intensity ($\sim 1.7 I_s$), the number of atoms is of the order of 10^{10}. We measured the intensity in the entrance windows, because there is the place we can measure the power and size of the spot. While scanning the cooling (pump) beam parameters, the oven$_{ZS}$ temperature and the current of the ZS coils were kept constant at 300°C and 12 A, respectively, which were the optimal values found before.

The same scan was made for the repumper light of the ZS deceleration beam. From Figure 2.3.6 we found the best frequency about -150 MHz with respect to the repumper frequency transition. The repumper light needed just $\sim I = 1.12 I_s$ of intensity to produce a good atom number.

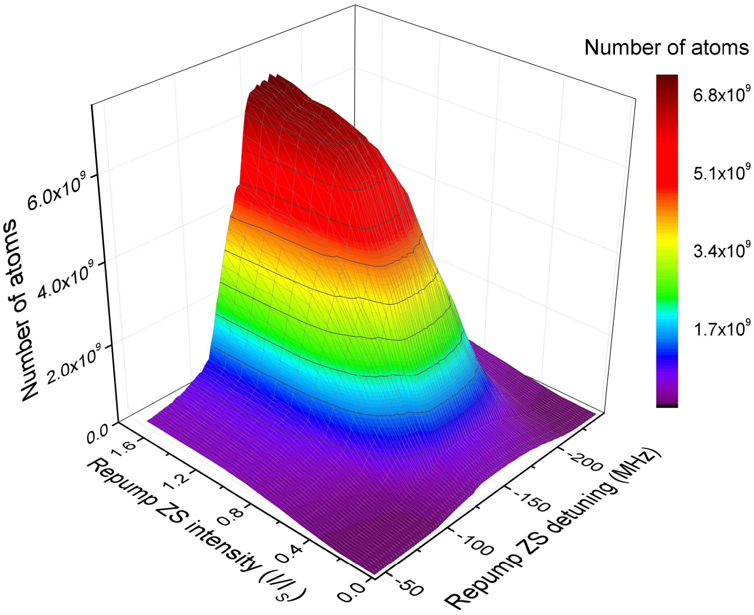

Figure 2.3.6 – Number of atoms as a function of the intensity and detuning of the repumper light beam of the ZS. The defuning is measured with respect to the repumper transition. In this case the intensity of the cooling beam of the ZS were maintained fixed at $4.5 I_s$ and $-180\,\mathrm{MHz}$.
Source: PEDROZO-PEÑAFIEL (14)

2.3.3 Features of the 2D-MOT as a source of cold atoms

The 2D-MOT system is composed by a stainless steel 316L chamber with four windows (2.75" CF flanges) aligned in a crossed geometry 45° rotated from the gravitational axis (z-axis). These windows are used for the trapping light, while the gravitational axis defines the ZS (ZS_{2D}) and oven (oven_{2D}). In the top of the 2D chamber the small window is used as the entrance of the laser that decelerates the atomic beam coming out from the oven placed in the bottom and attached to the 2D chamber through a tube of diameter 1.71 cm and a length of 10 cm (see Figure 2.3.7). This tube also helps to collimate the atomic beam coming out from the oven_{2D}. Then, the 2D-MOT also has a ZS-like magnetic profile produced by the remaining magnetic field of the 2D-MOT, as will be explained briefly.

Four sets of nine magnets are placed around the 2D-MOT chamber to produced the magnetic field for the 2D-MOT. The position of the sets of magnets is shown in Figure 2.3.7. The separation between the centers of the stacks are of 9.0 cm in the horizontal and 10.0 cm in the vertical. The magnets are N42 grade Nb (K&J Magnetics.) with dimensions of 1" ×3/8" ×1/8", and magnetization of 1.0×10^6 A/m and a dipole unit vector perpendicular to both the push and gravitational axis.

This magnet arrangement produced a magnetic field gradient of 49 G/cm in the z-direction. The magnetic field and its gradient are zero along the y-axis. The field profile along the gravitational axis was measured and is used as an effective Zeeman decelerator (ZS_{2D}). Figure 2.3.7 shows the profile of the magnetic field and the respective gradient.

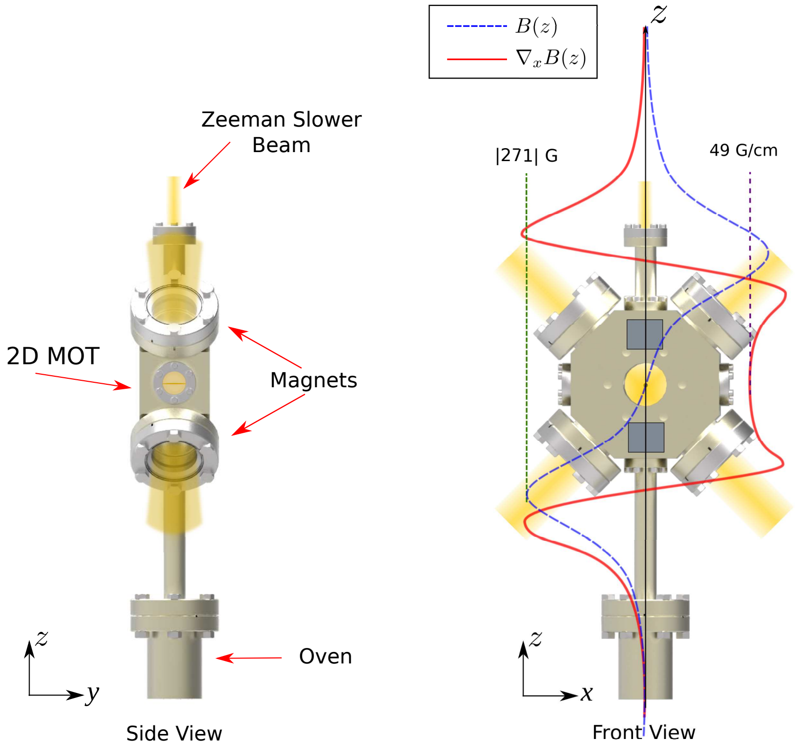
Zeeman Slower Beam
2D MOT
Magnets
Oven
z
y
Side View
$B(z)$
$\nabla_x B(z)$
z
|271| G
49 G/cm
z
x
Front View

Figure 2.3.7 – 2D-MOT chamber and magnet arrangement to produce the magnetic field gradient to realized the 2D-MOT of sodium atoms. The blue curve represents the measured magnetic field and the red curve the calculated gradient from the blue one.
Source: PEDROZO-PEÑAFIEL (14)

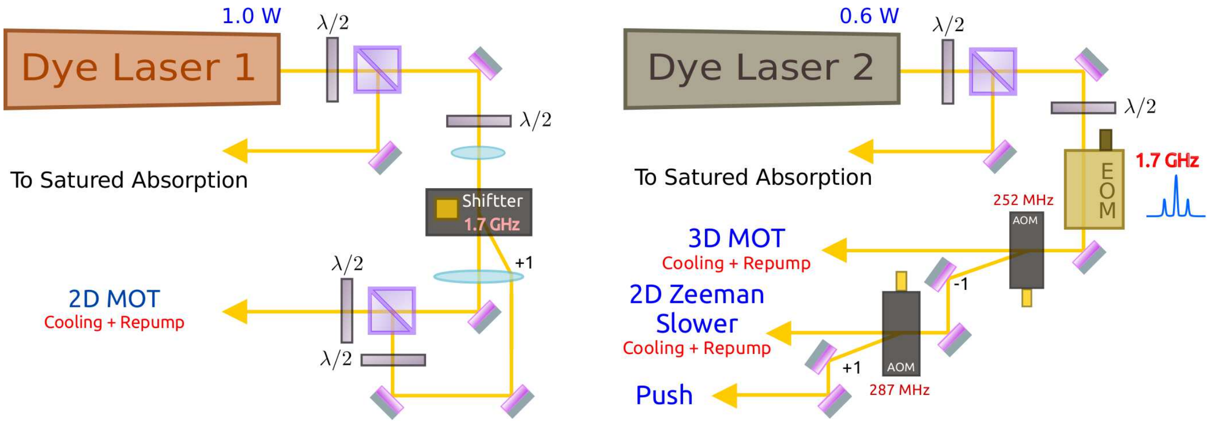
1.0 W
$\lambda/2$
Dye Laser 1
$\lambda/2$
To Satured Absorption
Shifter
1.7 GHz
+1
$\lambda/2$
2D MOT
Cooling + Repump
$\lambda/2$
0.6 W
$\lambda/2$
Dye Laser 2
$\lambda/2$
To Satured Absorption
1.7 GHz
EOM
252 MHz
AOM
3D MOT
Cooling + Repump
-1
2D Zeeman Slower
Cooling + Repump
+1
AOM
287 MHz
Push

Figure 2.3.8 – Optical setup for the 3D-MOT and 2D-MOT.
Source: PEDROZO-PEÑAFIEL (14)

In this setup, the dye laser 2 still is used for the 3D-MOT frequencies, and a fraction of this light is used for the ZS_{2D}. The cooling beam is passed through an EOM (Electro-optic Modulator) to generate the repumper frequency, and finally for a AOM (Acousto-optic Modulator) to produced the correct detuning. A second dye laser (Coherent 699), called Dye laser 2 from now on, is used for generating the cooling and repumper frequencies required for the 2D-MOT. The optical setup for the 2D-MOT is depicted in figure 2.3.8.

The pressure in the SC is three orders of magnitude smaller ($P_{sc} = 10^{-3} P_{2D}$) thanks to a differential pumping tube (see chapter 3), which has 0.2 cm diameter and 2.3 cm length. The atoms in the 2D-MOT are transferred to the SC using a push beam. The frequency of this beam was scanned around the cooling transition frequency, as well as its intensity. The results of these measurements are shown in Figure 2.3.9. From this measurement, we found the best intensity as being $\sim 12.2 I_s$ with a detuning of +12 MHz. The push beam is collimated with a diameter of $\sim$ 1 mm. From Figure 2.3.9, it is also possible to observed that for detuning 0, there is a good number of transferred atoms to the 3D-MOT, but smaller than for the case of +12 MHz. This is because at resonance (detuning 0), the push beam not only pushes the atoms from the 2D-MOT to the 3D-MOT, but also pushes away the atoms trapped in the 3D-MOT. This effect is diminished when the detuning of the beam is increased. The frequency of the push beam is exactly the same reported in (21) for ^{23}Na.

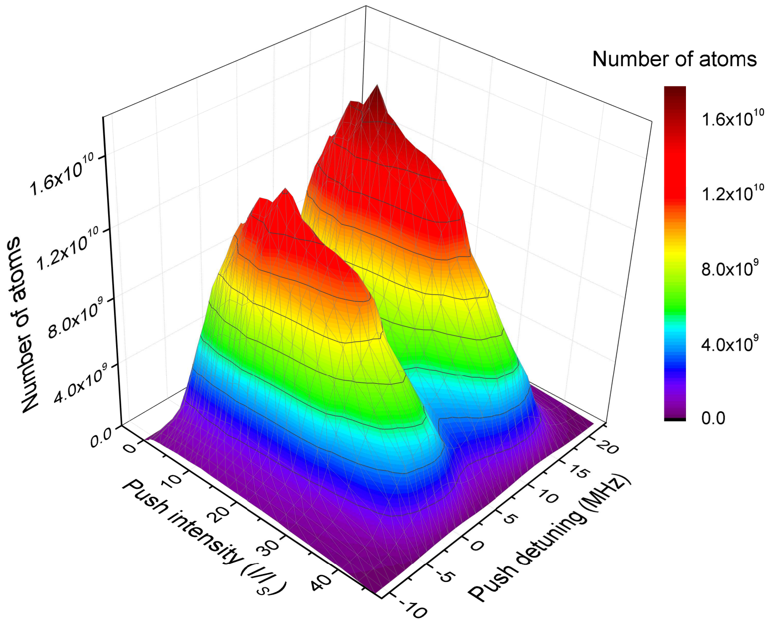

Figure 2.3.9 – Number of trapped atoms vs the push beam intensity and detuning. Source: PEDROZO-PEÑAFIEL (14)

The measurement varying the frequency and intensity of the repumper light is shown in Figure 2.3.10. From this, we can observed that for an intensity of $\sim 4.3 I_s$ we start to have a number of trapped atoms of the order of 10^{10}.

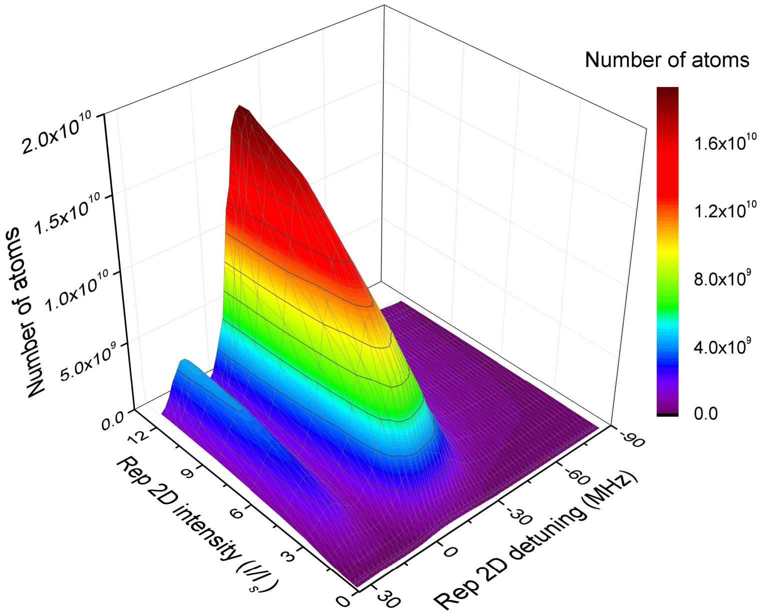

Figure 2.3.10 – Number of trapped atoms vs the repumper intensity and detuning measured with respect to the repumper transition.
Source: PEDROZO-PEÑAFIEL (14)

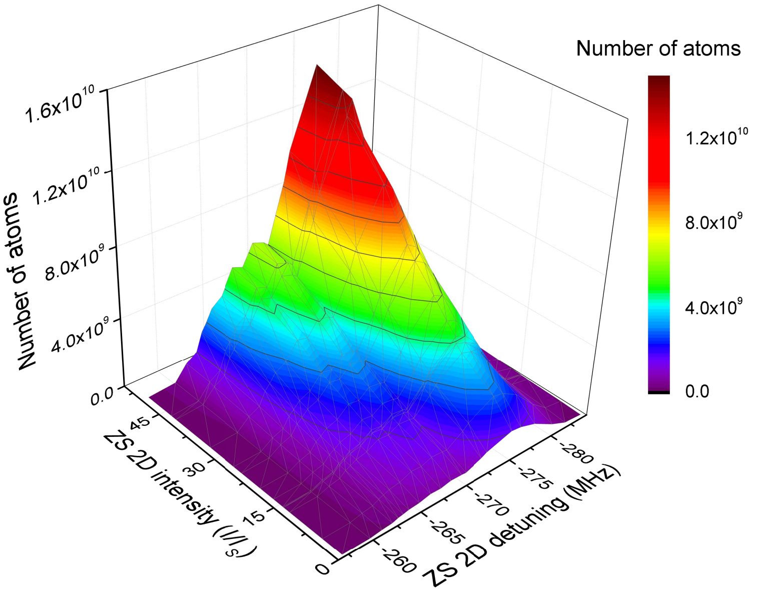

Figure 2.3.11 – Number of trapped atoms vs the intensity of the ZS light beam for the 2D-MOT.
Source: PEDROZO-PEÑAFIEL (14)

The last Figure 2.3.11 shows the scan in intensity and frequency of the ZS light of the 2D-MOT. The ZS light beam is a collimated beam and has a diameter of $\sim 1\,\mathrm{mm}$. With a detuning of $-275\,\mathrm{MHz}$ and an intensity of $I = 31.8 I_s$ the number of atoms is found to be of the order of 10^{10}.

With all these parameters fixed we varied the oven$_{2D}$ temperature oven and was found to be optimum at 210°C. For smaller values of the temperature, there are not enough atoms coming out from the oven and then the atomic flux is low. While increasing the temperature, there are more atoms available to be captured with the right frequency of the trapping beam and the ZS beam. This is important because the detuning of the beams are adjusted for a determined velocity class of atoms. When the temperature reach $210°C$ we observed the maximum value of the number of atoms trapped in the 3D-MOT, and when temperature is increased further this number start to decrease due to collisions between background atoms and trapped atoms. This happens because the pressure increase in the chamber and the number of collisions increases, limiting the number of atoms the system can trap.

For the 2D trapping frequency the best detuning is $-13\,\mathrm{MHz}$ and was used in all the process made above. Taking into account that the linewidth for this transition is $\Gamma = 9.795\,\mathrm{MHz}$ we obtained that the frequency is red-detuned approximately 1.3Γ. The intensity of each retro-reflected arm of the 2D-MOT trapping trapping beam is $\sim 5.1 I_s$.

Summarizing the description of the 2D-MOT principle of operation and looking at the experimental apparatus we can resume the overall operation as follows: The atoms are heated in the oven at approximately 210°C. This produces an effusive vapor of atoms that travel through the tube connecting the oven$_{2D}$ and the 2D-MOT chamber. The tube works as a collimator, creating an atomic beam which will reach the 2D-MOT chamber. In the way to the chamber we use a counter-propagating laser beam which decelerates a fraction of atoms with the help of the remaining magnetic field produced by the permanent magnets used for the magnetic field of the 2D-MOT. When the atoms reach the center of the chamber they feel the dissipative force of the light beams and the magnetic field, being cooled and partially confined in the center of the chamber. Due to the absence of magnetic field and laser light in the longitudinal direction (y-axis) the 2D-MOT exhibits an elongated geometry in this direction, similar to that of a cigarette. Once the atoms are trapped in the 2D-MOT a push beam propagating the in $+y$-direction is turned on, pushing the trapped atoms in the 2D-MOT to the capture volume of the 3D-MOT, where they are finally captured. We again measure the fluorescence of the 3D-MOT, as for the ZS characterization, in order to determine the number of trapped atoms in the 3D-MOT.

2.4 Comparison between the two atomic sources

Table 2.1 shows the optimal values of the different parameters of ZS and 2D-MOT. The characterization of each source involve mostly the determination of the efficiency in the loading of the number of atoms in the 3D-MOT. When all the optimized parameters the loading curves were obtained, and the values of the loading rate for each source are presented in Table 2.1. To compute the loading rate of the 3D-MOT from the ZS and 2D-

MOT, we fit the linear part of the loading curve and take its slope. This is valid because in this initial loading we can neglect the losses due to collisions with other trapped atoms. This collisions, and then the losses, increases with the density.

The parameters presented in Table 2.1 are similar to those reported by Lamporesi et al. (21), with the exception of the ZS beam for the 2D-MOT, for which we use around 6 times higher intensity in order to decelerate the atoms in the atomic beam. Also, the values for the ZS are typical values in this kind of system for ^{23}Na. (22–24)

With the knowledge of the performance of each atomic source, we chose the 2D-MOT as our source of cold sodium atoms. This decision was based in the values presented in Table 2.1, in which we see that the 2D-MOT has a similar performance to the ZS but we can take advantage in the compactness of the setup. This is a very important feature, because the final experimental machine constructed for producing a Bose-Einstein condensation of sodium atoms required a lot of space and Zeeman slowers represents a complication in this sense due to its big size. As mention in the introduction of the thesis, the complete apparatus aims to condense two atomic species, sodium and potassium, and for this reason space is valuable. It is worth to recall that this thesis describes the apparatus in function of sodium atoms only.

In the next chapter, I will describe the complete experimental apparatus designed and constructed to achieve the Bose-Einstein condensation of sodium atoms.

Table 2.1 – Optimal parameters for the ZS and 2D-MOT. Here N represents the number of atoms and L the loading rate of the 3D-MOT. The detuning of the repumper beams (*) are calculated with respect to the repumper transition frequency.

2D-MOT	Zeeman slower
$T_{oven_{2D}} = 210^{\circ}\mathrm{C}$	$T_{oven_{ZS}} = 210^{\circ}\mathrm{C}$
—	ZS Coils Current = 12 A
$\Delta Cool_{2D} = -13\,\mathrm{MHz}$	$\Delta Cool_{ZS} = -180\,\mathrm{MHz}$
$I_{cool_{2D}} = 5.1 I_s$	$I_{cool_{ZS}} = 1.7 I_s$
$\Delta Rep_{2D} = -8\,\mathrm{MHz}^*$	$\Delta Rep_{ZS} = -150\,\mathrm{MHz}^*$
$I_{rep_{2D}} = 4.3 I_s$	$I_{rep_{ZS}} = 1.12 I_s$
$\Delta Cool_{2D}^{ZS} = -275\,\mathrm{MHz}$	—
$I_{cool_{2D}^{ZS}} = 31.8 I_s$	—
$\Delta Rep_{2D}^{ZS} = -250\,\mathrm{MHz}^*$	—
$I_{Rep_{2D}^{ZS}} = 10.3 I_s$	—
$\Delta Push = +12\,\mathrm{MHz}$	$N = 3.0 \times 10^{10}$
$I_{Push} = 12.2 I_s$	—
$N = 2.0 \times 10^{10}$	$N = 3.0 \times 10^{10}$
$L = 1.8 \times 10^{10}$ atoms/s	$L = 4.1 \times 10^{10}$ atoms/s

Source: PEDROZO-PEÑAFIEL (14)

Chapter 3

Experimental apparatus for ^{23}Na BEC

This chapter presents a description of the experimental apparatus used to achieve the quantum degeneracy of sodium atoms. The chapter is divided into three sections: section (3.1) is devoted to showing the vacuum system, where all the process for obtaining the BEC is realized, section (3.2) the optical system used to prepare the light states necessary to laser cooled, trap, and probe the atoms, and finally, section (3.3) the electronic to control the experimental sequence.

3.1 Vacuum system

The vacuum system must be realized in a robust way, as simple as possible to realize the bake-out at high temperatures, and leak tight in order to maintain the UHV condition along the time. Special care must be taken to warrant a good conduction (mass flow) between the vacuum pumps and the chambers. Also, it is desirable to have a bad conduction between zones of UHV and zones of poorer vacuum conditions. To satisfy condition, a differential pumping tubes has to be used, as discussed below.

3.1.1 Ultracold sodium atoms machine

Our machine for producing the BEC can be divided into three sections, two of them consisting of two chambers devoted to produce 2D-MOTs which will provide the atoms for a principal chamber, called science chamber (SC), where the BEC takes place. The working principle of 2D-MOT and the loading process of the 3D-MOT of the SC chamber is described and studied in details in chapters 2 and 4, then, I only describe the technicalities about the machine.

Figure 3.1.1 shows the complete machine from two different views, frontal and in perspective, to better appreciate the components on the backside. The three principal sections are the two 2D-MOT chamber (C1 and C2) and the SC. One 2D-MOT chamber (C1) is used to trap potassium atoms, which are transferred to the SC to realize a 3D-

MOT (^{39}K and/or ^{41}K), transfer into a magnetic trap (MT) and evaporative cooling them, in order to achieve the BEC transition of ^{41}K. Thus, our experimental machine will be used to trap and Bose condensed two atomic species, namely, ^{41}K and ^{23}Na. Also, the team is being able to trap the potassium atoms in the MT, which is a big goal and a great advance in the experiment, and surely soon the ^{41}K BEC will be achieved.

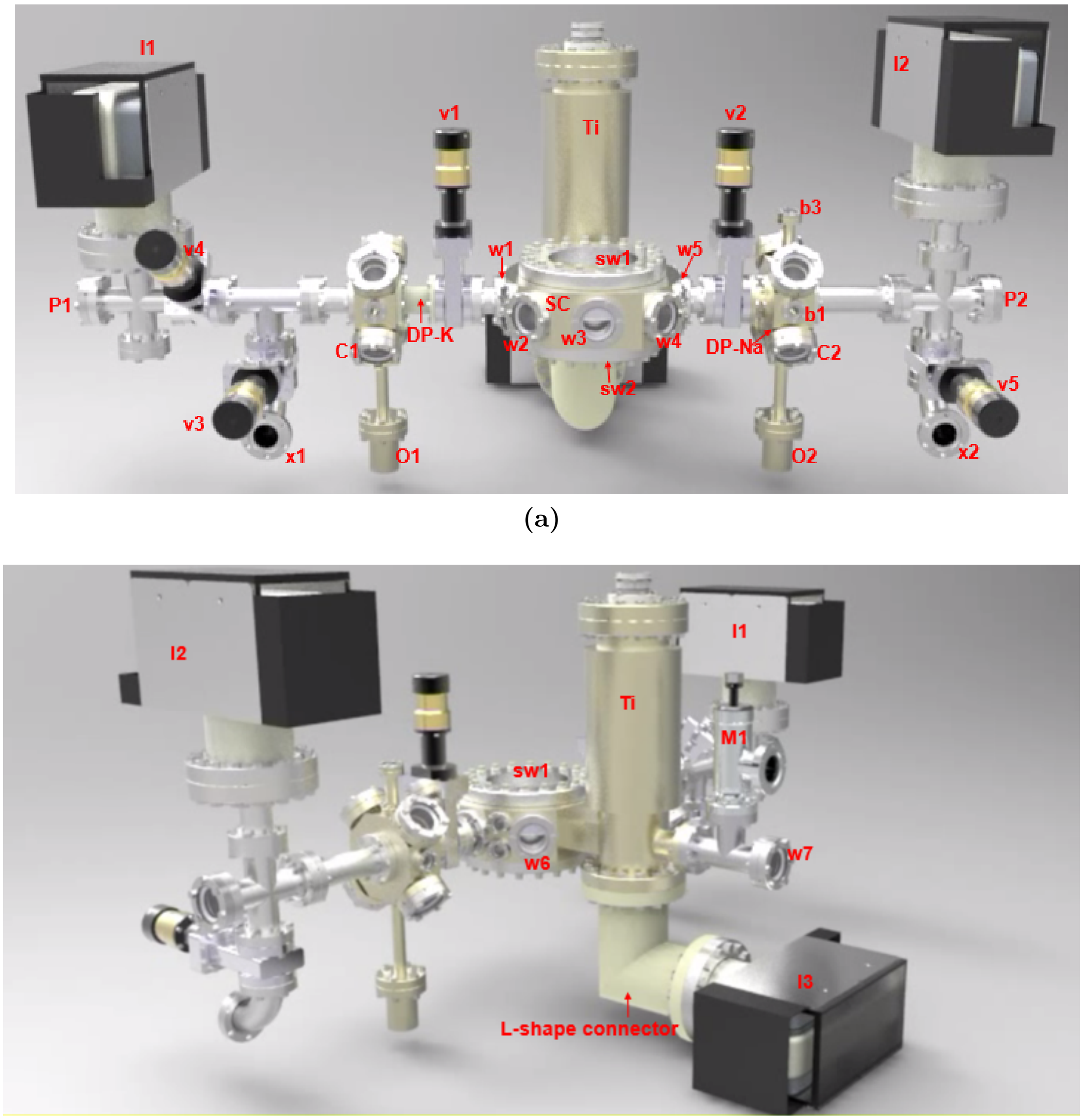
I1
I2
v1
Ti
v2
b3
v4
w1
sw1
w5
P1
SC
P2
b1
DP-K
C1
w2
w3
w4
DP-Na
C2
sw2
v5
v3
x1
O1
O2
x2
I2
I1
Ti
M1
sw1
w6
w7
I3
L-shape connector

(a)

(b)

Figure 3.1.1 – Frontal (a) and perspective (b) views of the machine for producing the BEC of sodium atoms. The components for potassium atoms are present in the picture.

Source: By the author.

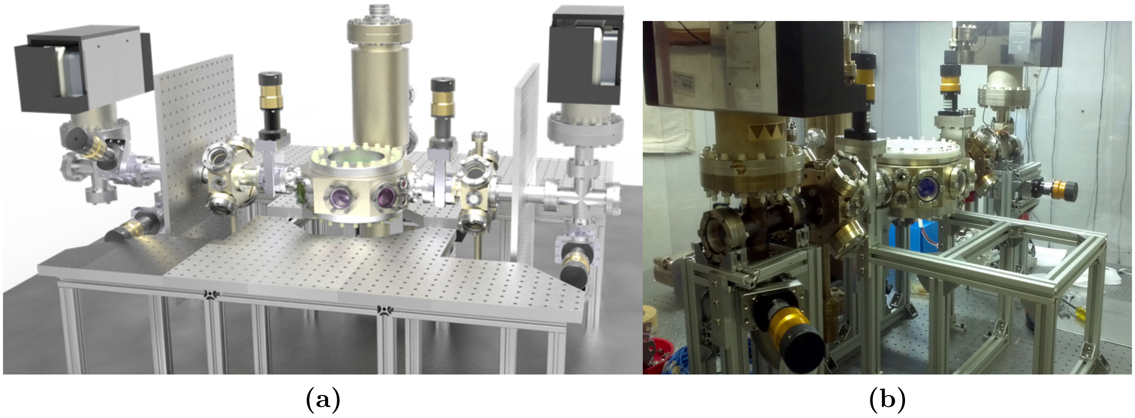
(a) (b)

Figure 3.1.2 – (a) and (b) show the experimental system with the optical table where the optical components are be placed to produce the 3D-MOT, MT and BEC.
Source: By the author.

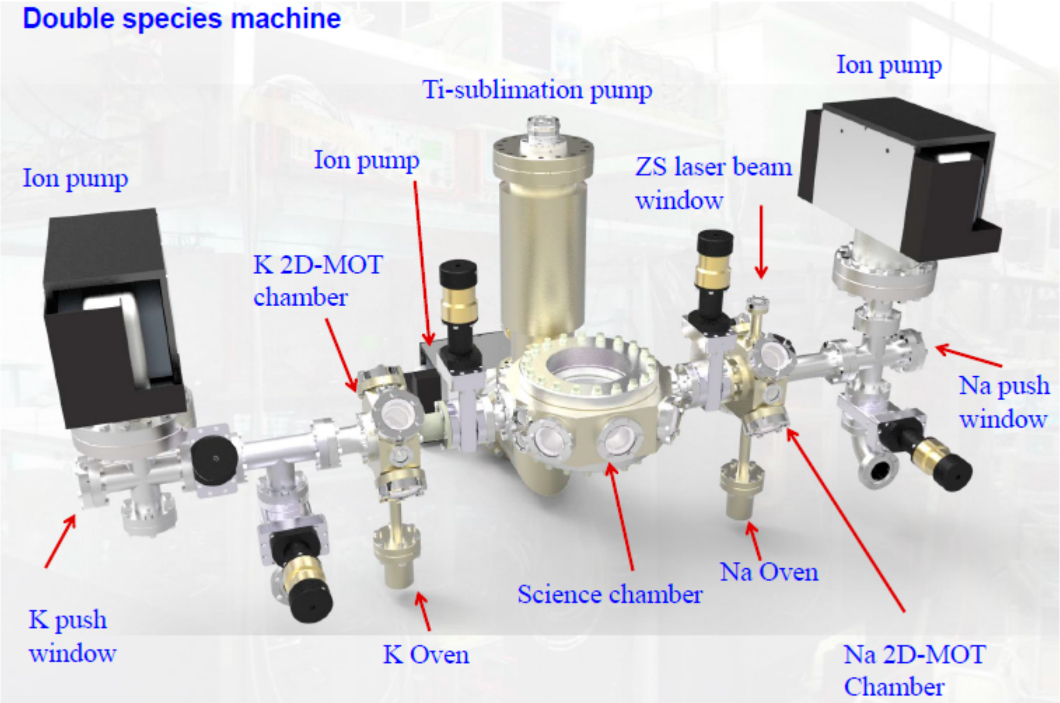
Double species machine
Ti-sublimation pump
Ion pump
Ion pump
Ion pump
ZS laser beam window
K 2D-MOT chamber
Na push window
Na Oven
Science chamber
K push window
K Oven
Na 2D-MOT Chamber

Figure 3.1.3 – Complete experimental system is shown from another perspective.
Source: By the author.

2D-MOT chambers: The 2D-MOT chambers were manufactured in the shop machine of our institute, and are made of stainless steel 316L which presents a low outgassing rate and low magnetization, this being an important point in order to avoid the influence of stray magnetic field produced by the chambers on the atoms position. The 2D-MOT chambers have four principal windows tilted 45°with respect to the gravity-axis (z-axis). These windows are closed with CF-2-3/4 flanges from MDC Vacuum products, LLC, and are used for the cooling beam of the 2D-MOT (see chapter 2). Three windows of 1-1/3 flanges are used for observation (b1 and b2) and for injecting the counter-propagating deceleration laser beam (b3) in the case of sodium (see chapter 2). The geometry of the 2D-MOT chambers is shown in Figure 3.1.4.

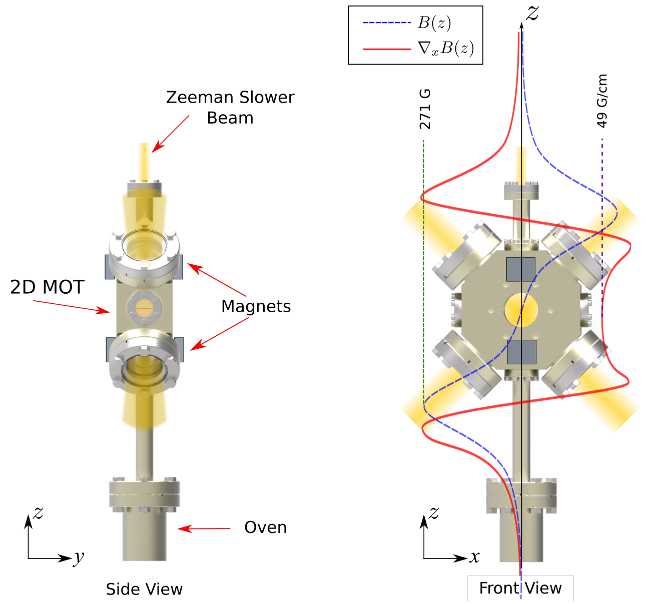

(a)

Figure 3.1.4 – 2D-MOT chamber. In the picture it is shown the 45° tilted windows with respect to gravity axis. The MOT beams and the magnetic field is also shown.

Source: By the author.

Sodium and potassium atoms are supplied to the system in metallic solid form through ampoules of 5 g with a purity of 99.95% from Aldrich Chemical Company, Inc. These ampoules are placed at the bottom ovens of the 2D-MOT chambers (O1 and O2). In the case of sodium atoms the oven is heated using a ceramic heating tape (Heatcon OP24764) at 210°C to produce an effusive atomic beam that reach the center of the 2D-MOT chamber, where the atoms are finally cooled in a 2D geometry. The ovens are identical, and are similar to a “cup” having internal diameters of $d_{oven} = 35\,\mathrm{mm}$ and heigth $h_{oven} = 50\,\mathrm{mm}$. The ovens are connected to the 2D-chambers through tubes of internal diameters of $d_{ube} = 17\,\mathrm{mm}$ and lengths $l_{tube} = 100\,\mathrm{mm}$. This tube also works as a kind of differential pumping tube (DP), as will be explained below.

The 2D-MOT chambers are pumped using ion pumps (I1 and I2) of 75 L/s (Varian Vaclon Plus). With these pumps the vacuum in the 2D-chambers are of the order of 8×10^{-9} Torr for sodium and 5×10^{-8} Torr for potassium, at the time of operation.

There are circular gates valves (MDC) to closed the system and also allow the connection of a turbo molecular pump to realize the first stage of pumping, as will be described later.

Science chamber: The SC is also made of stainless steel 316L, regarding that any possible magnetization of this chamber is more critical because in this chamber the atoms are finally condensed. It consists of eight windows with CF-2-3/4 flanges at the lateral surface. Four of these windows (w2, w4, w6, w8) are used for injecting the cooling, trapping and repumper beam of the 3D-MOT (see chapter 4). The two lateral windows (w1 and w5) connect the SC to the 2D-MOT chambers as can be seen in Figure 3.1.1. These chambers are joined by a differential pumping tubes in for of I connectors. The differential pumping tubes allow to maintain a difference in pressure of 10^{-3} Torr in the SC with respect to the 2D-MOT sodium chamber and 10^{-4} Torr with respect to the 2D-MOT potassium chamber. Figure 3.1.5 shows the differential pumping tube characteristics. Also, there are valves (v1 and v2) that allows to isolate the SC from the 2D-MOT chambers, as this is commonly important as for example, to fix problems in the 2D chambers, or at the time of changing the ampoules of sodium (potassium) atoms without loosing the quality of the vacuum of the SC.

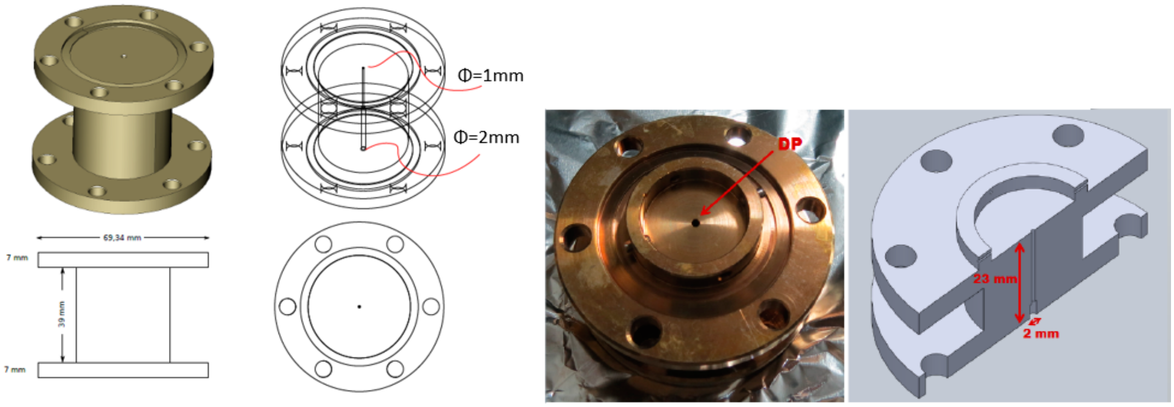

(a) **(b)**

Figure 3.1.5 – Differential pumping tubes placed between the 2D-MOT chambers and the SC. In (a) the length of the canals with diameters $\phi = 1\,\mathrm{mm}$ and $\phi = 2\,\mathrm{mm}$ are the same, $l = 12.7\,\mathrm{mm}$.
Source: By the author.

The SC also has four small windows (CF 1-1/3) used for collecting the fluorescence signal of the MOTs and determine the number of atoms.

The front and rear windows (w3 and w7) are used for the plug laser beam and imaging beam. The rear window is placed at a distance of 55 cm from the center of the chamber, this is because before the window the Ti-sublimation pump (Ti) is placed, as shown in Figure 3.1.1.

The top (sw1) and bottom (sw2) windows are special and customized. We use bonded fused silica non-magnetic re-entrant viewport 316LN CF150 (OD 8”) windows from Torr Scientific LTD. These windows allow a good optical access in the z-direction. These windows support a maximum temperature of 120°C, for this reason, special care must be taken at the time of the bake out process.

We connect to the SC an ion pump of 75 L/s (Varian Vaclon Plus) to reach ultrahigh vacuum. Together with the ion pump the Ti-sublimation pump is connected to the SC through a L-shaped tube (Figure 3.1.1) with ∼ 15 cm diameter (also manufactured in the machine shop of our institute). This tube is made of a double internal surface. The most internal part is where the Ti filaments are placed and the external part is used for circulating water at ∼ 14°C to cool down the surface of the cylinder and allow the titanium to adhere easily and fast to the internal surface.

The ti-sublimation pump (Agilent - Titanium Sublimation Cartridge 916-0050), works releasing Titanium particles when a current circulated through the cartridge. These particles adhere to the surface of the system, trapping any particle colliding with the surface. Normally, the particles colliding with the surface are those almost impossible to be removed with the ion pump, because are very small.

The SC is closed using an all-metal valve (M1) (from MDC). Through this valve is connected a turbo pump system, for realizing the first stage of the vacuum process.

Differential pumping (DP) stages: The objective of setting up the differential pumping tubes is warranty that the SC is maintained at ultrahigh vacuum (UHV) conditions, even if the 2D-MOT chambers can not be at such values of the pressures. It is worth recalling that the 2D-MOT chambers are maintained just in high vacuum conditions (HV), it is because at this chambers arrives an atomic beam with a wide velocity distribution coming from the oven, producing a big atomic background. In the SC the UHV condition is reached with the help of the Ti-sublimation pump as mentioned above. Bose-Einstein condensation is achieved at pressures of the order or less that 10^{-11} Torr, otherwise, the loss-induced collisions will be dominant in the system, avoiding to reach the quantum degeneracy.

To calculate the effect of the differential pumping tubes in the system it is used the typical formula for the conductance (of the flux of particles in the system) for a cilindycal tube given by (24, 30)

$$C_{tube}(m^3/\mathrm{s}) = 121\frac{d^3}{l} \tag{3.1.1}$$

where the approximation $d \ll l$ has been used. For the sodium part of the system, the differential pumping tube has $l = 23\,\mathrm{mm}$ and $d = 2\,\mathrm{mm}$, we have $C_{DP}^{Na} = 4.2\times10^{-5}\, m^3/\mathrm{s} = 4.2 \times 10^{-2}\,\mathrm{L/s}$.

Using the nominal value of the pumping velocity of the ion pump in the UHV chamber (SC), which is $S_{pump} = 75\,\mathrm{L/s}$, and relations for the mass flux conservation, as described in detail in (24, 30), we can compute the effect of the DP tubes on the ratio between the pressures in the HV chamber (2D-MOT chamber) and the UHV chamber (SC), as

$$\frac{P_{UHV}^{SC}}{P_{HV}^{Na}} \simeq \frac{C_{DP}}{S_{pump}} = \frac{4.2\times10^{-2}\,\mathrm{L/s}}{75\,L/s} = 0.56\times10^{-3} \tag{3.1.2}$$

then, $P^{SC}_{UHV} = 0.56 \times 10^{-3} P^{Na}_{HV}$, the pressure in the SC will be three order of magnitude smaller, warranty the SC be always at UHV conditions.

For the potassium DP we have two canals, one with $l_1 = 12.7\,\mathrm{mm}$ and $d_1 = 1\,\mathrm{mm}$, and for the other $l_2 = 12.7\,\mathrm{mm}$ and $d_2 = 2\,\mathrm{mm}$. Then, using Equation (3.1.1) we have for each canal, $C^K_{DP1} = 9.6 \times 10^{-3}\,\mathrm{L/s}$ and $C^K_{DP2} = 7.6 \times 10^{-2}\,\mathrm{L/s}$. The total conductance is given by (24, 30)

$$C^{K-total}_{DP} = \frac{C^K_{DP1} \times C^K_{DP2}}{C^K_{DP1} + C^K_{DP2}} = 8.5 \times 10^{-3}\,\mathrm{L/s} \qquad (3.1.3)$$

then, $P^{SC}_{UHV} = 1.14 \times 10^{-4} P^K_{HV}$.

3.1.2 Achieving high and ultrahigh vacuum

To achieve the HV and UHV conditions, a bake-out of the complete system has to be carefully perform.

Pre-baking: At the time of construction of the vacuum components, atmospheric gasses are normally trapped inside the metal. The outgassing of this components limits the maximum pressure attainable in the vacuum system. This problem can be mitigate realizing a stage of pre-baking of the metal components before assembly the final setup. (24) We performed the pre-baking process during four days at a temperature of 400°C. The pre-baking process helps in improving the vacuum conditions because at high temperatures hydrogen atoms trapped inside the metal are extracted, avoiding outgassing along the time of running the experiment.

The pre-baking stage was performed in a metal box, using high power resistances for heating the vacuum components. To isolate the parts from the metal box were used bricks to avoid burning anything around those components. The temperature was measured using several thermocouples at several points of the box.

Bake-out: The bake-out of the vacuum system must be done in a very carefully way. The experimental system is constituted of different kind of materials, for example, windows (flanges of metal and glass) that can be heated just until $\sim$ 200°C, and pieces of metal that can be heated to $\sim$ 550°C or more. In our system, the two re-entrant viewport windows (top and bottom windows) of the SC can be heated just to a maximum temperature of 120°C, because the glass and the metal are glued with bonded fused silica. For this reason, many components have to be baked to different temperatures. To do this, each component was wrapped with a heating tape, each one fed with an independent Variac, allowing to control the temperature independently.

Before starting the baking process a leak test was realized using a residual gas analyzer (RGA), this was performed with the help of the Cryogenic workshop of our institute. This was performed in order to be sure the system had no leaks, otherwise it would be a lost of time to start the process without fixing the problem. Actually, for other reasons, like problems in the ion pump, we had to performe the baking process several times.

To start the pumping process we have used one turbo pumping station (Pfeiffer Vacuum, HiCube700) with a speed capacity of 680 L/s for the two 2D-chambers and one turbo pumping station for the SC. The system was completely wrapped with different heating tapes and isolated using fiberglass tapes to avoid excessive heat conduction around the table, and finally, all the system was cover with aluminum paper to avoid the spreading in the environment of the fiberglass particles.

The temperature was increased at a rate of approximately 5°C/h, which is safe enough in order to avoid problems with the dilatation of the components, and as they have different dilation coefficient they can easily break (windows are very sensitives) and produce leaks.

The 2D-MOT chambers and metallic components were maintained at $\sim$ 180°C. Ion pumps at $\sim$ 200°C, and the regions near the valves at a maximum temperature of $\sim$ 80°C. The SC were maintained at $\sim$ 110°C. The complete bake-out process took three weeks at a constant temperature. The temperature of different regions of the system was monitored using thermocouples connected to a thermocouple monitor (from Rodhe &Schwarz) able to read until 25 different temperatures and interface with a PC, which facilitates the process of reading the temperature, given the possibility of monitored the temperature in “real time”. Figure 3.1.6 shows the different stages of the baking process, temperatures and pressures at the different chambers.

In the middle of the process (fifth day of constant temperature), the cartridge of the Ti-sublimation pump were baked-out. This was made circulating a current of 30 A through each filament at a time during 7 min. Three cycles were realized waiting 3 min between successive cycles, as shown in Figure 3.1.6d. The cycles were programmed directly in the Sublimation Controller (Varian Vacuum Technologies - Model: 929-0022).

In Figure 3.1.6a we can observe the behavior of the temperature and pressure of the SC when the system is being baked. At the beginning the system starts to heat up with a high pressure ($P > 10^{-5}$ Torr). When the system reaches the steady state the temperature is maintained constant and the pressure starts to fall thanks to the pumping of the turbo-molecular pump. The minimum pressure achievable with the ion pump is of the order of $10^{-6} - 10^{-7}$ Torr, then at this time ($t \sim 380$ h) the system is saturated and no more improve in the pressure can be obtained. At this point we started to decrease the temperature at approximately at the same rate of that we increase the temperature (5°C/h), to avoid any damage in the windows or connections glass-metal cause by abruptly change the temperature. The temperature of the ion pump was decreased before all the rest of the components in order to turn on and start to pump the system. After four days decreasing the temperature and pumping with the turbo pump only, the valve isolating the

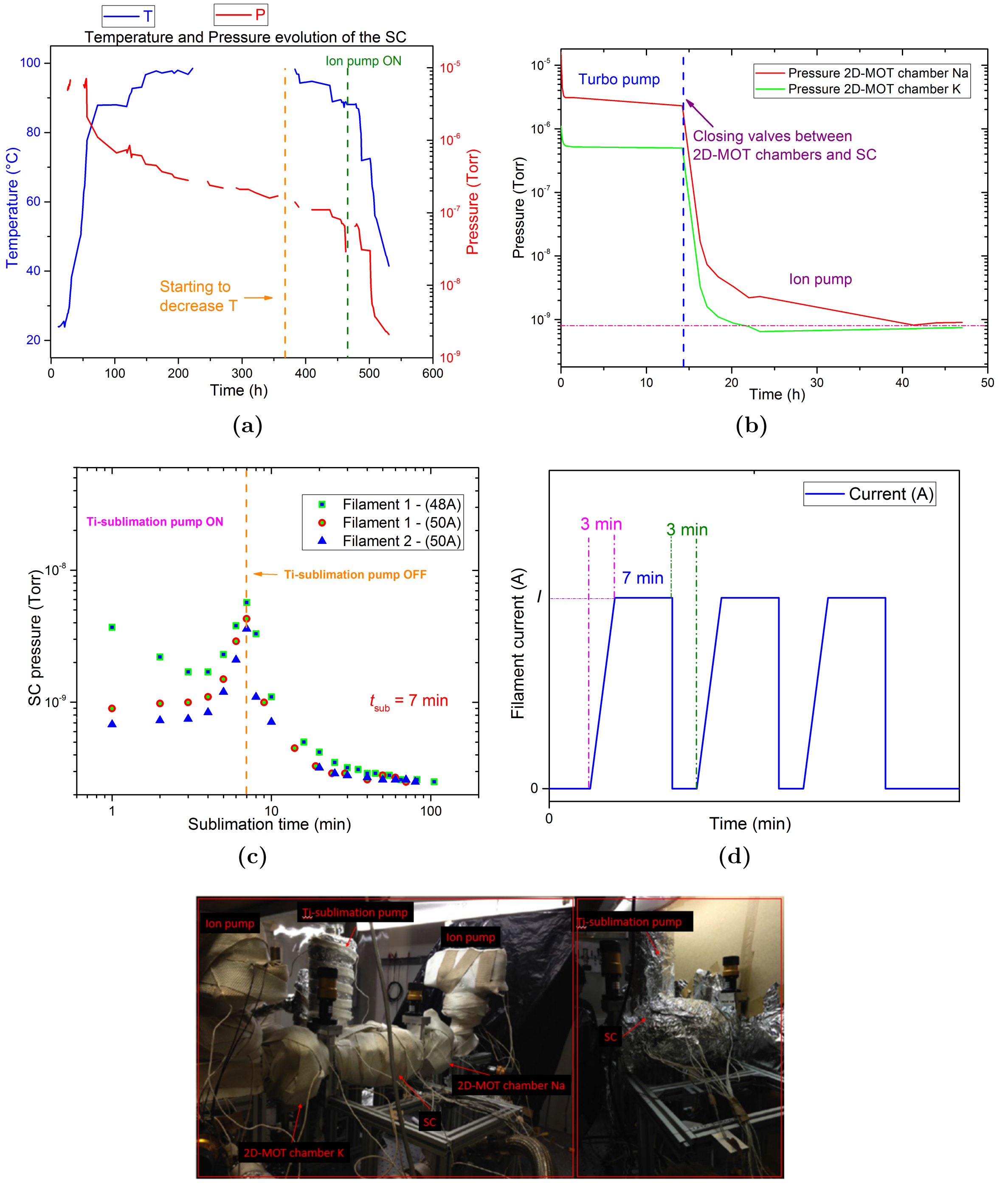

(a) **(b)**

(c) **(d)**

(e)

Figure 3.1.6 – (a) Pressure and temperature of the SC. When the turbo pump is turned on and the ion pump switched on, the pressure fall abruptly to HV conditions. The same effect is observed for the 2D-MOT chambers in (b). (c) shows the decay in pressure, reachin UHV condition when the Ti-sublimation pump is activated with cycles shown in (d).

Source: By the author.

system from the turbo pump (pumping stage) was closed. At this moment the ion pump was turned on and the pressure started to fall abruptly. This is because the limitation in the pumping of the turbo pump was removed and the ion pump is able to pump until UHV conditions. When the system was totally cooled down at room temperature and the all-metal valve was closed, the pressure reaches the pressure of $\sim 1 \times 10^{-9}$ Torr, and at this time the Ti-sublimation was used to reach a pressure of 10^{-11} Torr or less in the SC, necessary to achieved the Bose-Einstein Condensate.

The designed and constructed system after the baking process, satisfy all the requires reaching the quantum degeneracy of alkali atoms. The pressure in the 2D-MOT chamber of sodium atoms is maintained at a pressure of $\sim 1 \times 10^{-9}$ Torr when the oven is off, and $\sim 8 \times 10^{-9}$ Torr when the experiment is running (sodium oven at $T = 210$°C). For the 2D-MOT chamber of potassium atoms $P \sim 3 \times 10^{-9}$ Torr. The SC is maintain at a pressure of $\sim 10^{-11}$ Torr, which is below the the sensibility of the ion pump sensor.

3.2 Optical system

To performe the stages (cool down, trap and probe the atoms) along the experimental sequence for achieving the Bose-Einstein condensation, several light frequencies are required. The light used in experiments of this kind are normally tuned near a closed transition from the ground state. For sodium atoms, the the nuclear spin is $I = 3/2$, leading to a splitting of the ground state into two hyperfine states, ($F = 1$ and $F = 2$), and the second excited state ($3^2P_{3/2}$) into $F' = 0, 1, 2, 3$, then the only closed transition is the $F = 2 \rightarrow F'3$. This transition belong to the $D2$ line of sodium atom with wavelength 589 nm. The frequencies used in the experiment are shown in Figure 3.2.1.

3.2.1 Lasers

The optical system rely in two lasers, which are used to produce all the frequencies required along the realization of the BEC of sodium atoms.

Solid state laser: All the frequencies in the experiment, except the cooling and repumper Zeeman slower (ZS) light beam, are generated for a solid state laser (Toptica DL-RFA-TA-SHG Pro). This laser is an assembly of several individual parts, that set together is able to deliver yellow light at high power, in our case, we obtain 2.9 W of yellow light ($D2$ line). Figure 3.2.2 shows the components of the whole laser and the diagram of the pars of the cavity.

In this laser a grating stabilized diode laser (TOPTICA DL Pro) at 1178 nm is connected to a polarization maintaining optical amplifier for amplification of a narrowband

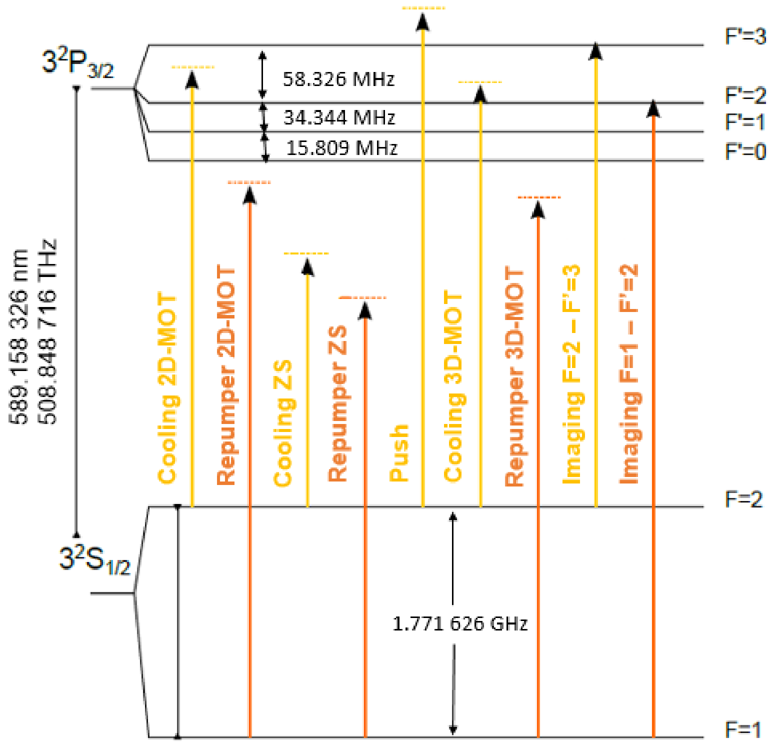
$3^2P_{3/2}$
58.326 MHz
34.344 MHz
15.809 MHz
F'=3
F'=2
F'=1
F'=0
589.158 326 nm
508.848 716 THz
Cooling 2D-MOT
Repumper 2D-MOT
Cooling ZS
Repumper ZS
Push
Cooling 3D-MOT
Repumper 3D-MOT
Imaging F=2 – F'=3
Imaging F=1 – F'=2
F=2
$3^2S_{1/2}$
1.771 626 GHz
F=1

Figure 3.2.1 – Hyperfine level structure of sodium atoms for the $D2$ line. All the frequencies used in the experiment are presented in the diagram. Detunings are lsited in Table 3.1.
Source: By the author.

CW signal. The amplified signal is send to a Second Harmonic Generation (SHG) module. The process of generating high power yellow light can be summarized as follows: a tunable grating stabilized DL Probe provides roughly 20 mW of infrared light (1178 nm), which is injected to the Raman Amplifier module through a polarization maintaining optical fiber. In this module, Stimulated Raman Scattering takes place, leading to amplification to $\sim$ 10 W of the 1178 nm light. The amplified infrared light is finally sent to a resonant doubling cavity (Second Harmonic Generator - SHG), consisting of a Lithium Triborate (LBO) crystal, producing in this way 589 nm yellow light at a power of $\sim$ 2.9 W in our case. References (31, 32) give more specific details about this laser.

Dye laser: To generate the ZS laser beam frequency, we use a dye laser (Coherent 899), which is pumped by a 10 W verdi (from Coheret Inc) (532 nm). This laser uses as nonlinear (medium) dye rhodamine 6G and produce 950 mW of yellow light. The dye is made to circulate using a recirculation pump at a pressure of 40 psi.

The light produce by the dye laser is used exclusively for decelerating the atomic beam going out from the oven. Figure 3.2.3b shows this optical setup.

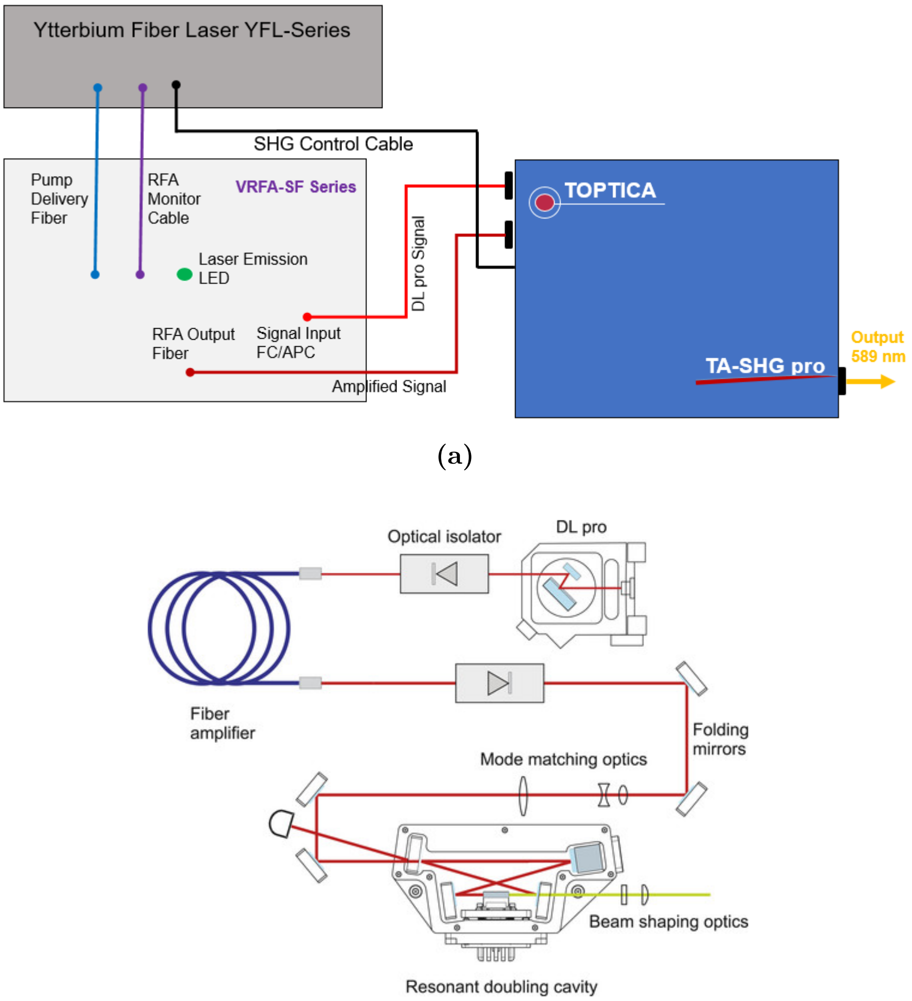
Ytterbium Fiber Laser YFL-Series
SHG Control Cable
Pump
Delivery
Fiber
RFA
Monitor
Cable
VRFA-SF Series
Laser Emission
LED
RFA Output
Fiber
Signal Input
FC/APC
DL pro Signal
Amplified Signal
TOPTICA
TA-SHG pro
Output
589 nm
Optical isolator
DL pro
Fiber
amplifier
Folding
mirrors
Mode matching optics
Beam shaping optics
Resonant doubling cavity

(a)

(b)

Figure 3.2.2 – (a) Schematic diagram of the whole laser system. (b) Components of the SHG box, taken from Toptica website.
Source: By the author.

3.2.2 Optical setup

The scheme showing the optical setup for the frequencies produced by the solid state laser is presented in Figure 3.2.3a. The output of the laser is $\sim$ 2.9 W and is divided into several beams, used for different purposes as cooling and trapping, diagnostic, and frequency stabilization, as shown in Figure 3.2.3a.

To prepare the light state of each beam, we use acousto-optic modulators (AOM - ATM-200C) mainly of 200 MHz of central frequency. Since the light we need in the experiment have to be tuned not exactly at resonance, but with small detuning, the laser frequency is set at a different frequency than that of the resonance, then it is necessary to introduce this AOMs in order to adjust the light beam to the exact frequency.

The experimental system is divided into two optical tables, one of them is exclusively used for the optical system (lasers, etc) and the other one is used for the science chamber. The light is delivered from the optical table of the laser system (OTLS) to the optical table of the science chamber (OTSC) using polarization maintaining optical fibers (from OZ optics). There are several advantages in separating isolating the SC from the optical system. One of them is the reduction of the probability of finding stray light in the SC due to undesired scattered light in any element of the optical system. Vibrations produced by shutters, dye laser recirculating pump, among others, are minimized. Also, the fact of using polarization maintaining optical fibers helps in delivering a very clean Gaussian TEM_{00} spatial mode. It facilitates the alignment, because any time some adjustments have to be done in the optical system (OTLS), no adjustment is needed in the OTSC. The fiber coupling efficiency in our setup is of 65% in average, being enough to obtain the required powers at the OTSC. The output of the optical fibers are collimated using commercial collimators HPUCO-83A-589P62AS from Thorlabs. Table 3.1 presents the values of the power in the output of each fiber in the OTSC.

AOM: This element consists of a crystal that diffracts and shifts the frequency of the light beam passing through it. (28) Vibrations on the crystal are induced by applying an external radio frequency (RF), when the light interacts with this acoustic wave (crystal vibrations) it is diffracted and frequency shifted. The relation between the diffracted angle and the frequency is given by (28, 33) $sin\theta = n\nu/(2\nu_{RF})$, where ν is the frequency of the incident light, ν_{RF} the frequency of the induced acoustic wave, i.e, the external RF applied to the crystal, and n is the diffraction order of the outcoming beam ($n = ... -2, -1, 0, 1, 2, ...$). The frequency is then shifted an amount $\nu_{out} = \nu_{incident} + n\nu_{RF}$.

In our experiment we used AOMs of two different central frequencies, 200 MHz and 80 MHz. These AOMs can be scanned around 20% from the central frequency maintaining almost the same efficiency ($\sim$ 80% in our case) for the first order diffracted light.

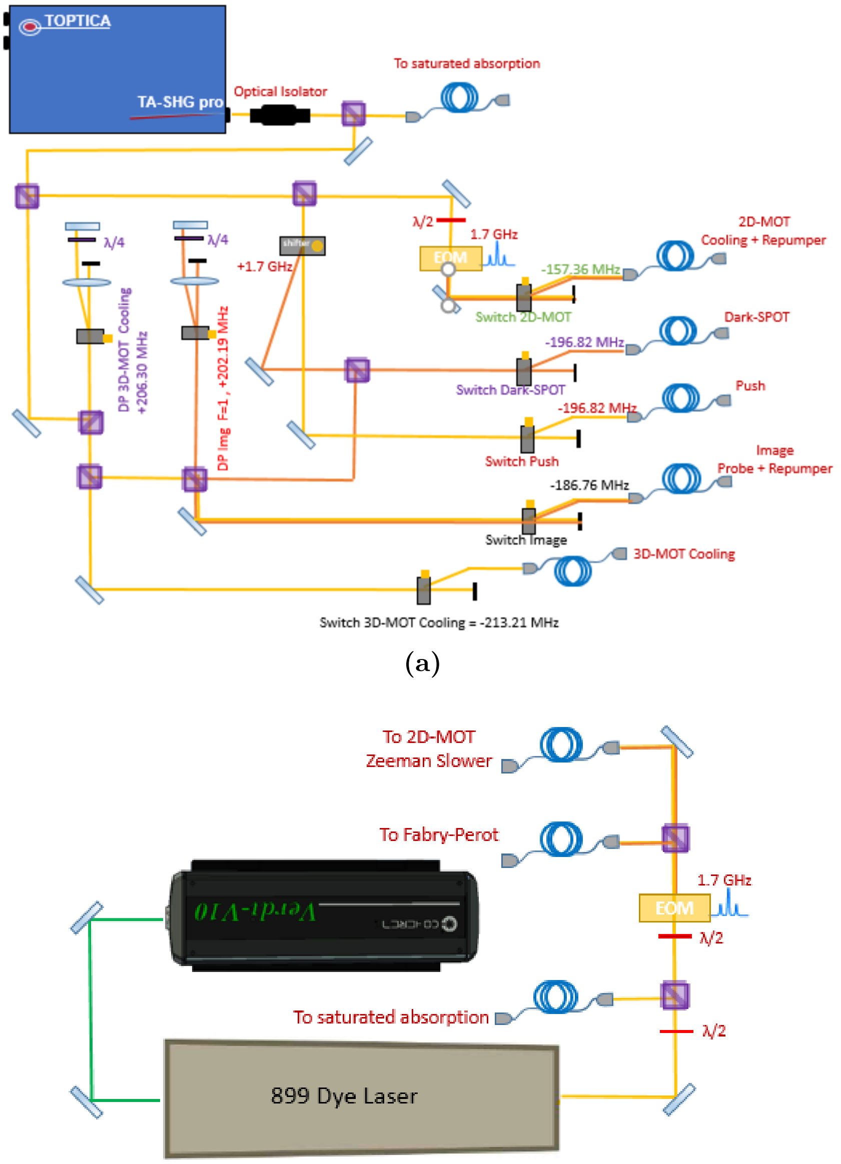
TOPTICA
TA-SHG pro
Optical Isolator
To saturated absorption
λ/4
λ/4
shifter
+1.7 GHz
λ/2
1.7 GHz
EOM
2D-MOT
Cooling + Repumper
-157.36 MHz
Switch 2D-MOT
Dark-SPOT
-196.82 MHz
Switch Dark-SPOT
Push
-196.82 MHz
Switch Push
Image
Probe + Repumper
-186.76 MHz
Switch Image
3D-MOT Cooling
Switch 3D-MOT Cooling = -213.21 MHz
DP 3D-MOT Cooling
+206.30 MHz
DP Img F=1 , +202.19 MHz
To 2D-MOT
Zeeman Slower
To Fabry-Perot
1.7 GHz
EOM
λ/2
Verdi-V10
COHERENT
To saturated absorption
λ/2
899 Dye Laser

(a)

(b)

Figure 3.2.3 – (a) Optical setup for generating the frequencies from the solid state laser. (b) Optical setup for the Zeeman slower light, generated fro the dye laser. Before each optical fiber (not shown in the schemes) in order to switch of the light in a fast way.

Source: By the author.

Table 3.1 – Powers of each beam after the optical fiber, which are the powers being finally delivered to the optical table where the science chamber is placed. Detuning with respect to the cooling transition ($F = 1 \rightarrow F' = 2$), except *, which are taken with respect to the repumper transition ($F = 1 \rightarrow F' = 2$), and given in units of the linewidth of the $D2$ line of sodium, $\Gamma = 2\pi \times 9.795\,\text{MHz}$

Beam	Detuning	Power
2D-MOT Cooling	-5.7Γ	135 mW
2D-MOT Repumper*	-5.6Γ	67.5 mW
Zeeman slower Cooling	-28.1Γ	108 mW
Zeeman Slower Repumper*	-25.5Γ	36 mW
3D-MOT Cooling	-1.5Γ	110 mW
3D-MOT Repumper (Dark-SPOT)*	-1.6Γ	18 mW
Push	$+1.2\Gamma$	0.6 mW

Source: By the author.

We use only the first order because the power drops abruptly for higher order of diffraction. In the experimental sequence several frequencies have to be changed along the running, and from the equation this mean that the direction of the light beams will suffer undesired misalignment. This disadvantage is overcome using the double pass configuration.

In the double pass configuration (as can be seen in Figure 3.2.3 or 3.2.4) the laser is send to the AOM using a polarizing cube, and after optimizing the first order beam in the first passage, the beam is left to propagate some distance and then using a lens of focus f is placed at a distance f from the the AOM. This make all the different orders produced in the AOM to propagate parallel to each other. A mirror sent the desired beam back to the AOM along the same path, causing the double shift in frequency of the light ($\nu_{out} = \nu_{incident} + 2\nu_{RF}$). Setting a quarter wave plate before the mirror, the polarization of the retro-reflected beam is changed by $\pi/2$, allowing to separate the resultant beam from the incident beam in the cube. In our setup we obtained efficiencies of the double pass configuration around 60%.

The RF frequency sent to the AOMs are produced with homemade VCOs (Voltage Controlled Oscillators). The VCOs creates a RF signal with a power around 0 dBm and this signal is sent to an amplifier of 30 dBm or 33 dBm, which finally provides the RF signal to the AOM. The VCOs are equipped with a TTL control and amplitude control, which allow fast switch off the light and manipulate its intensity, respectively.

AOM Shifter: To obtain the repumper frequency of the 3D-MOT and imaging beam, an special AOM, called shifter, is used. From Figure 3.2.1, we can see that the repumper frequency is separated from the cooling frequency by $\sim 1.772\,\text{GHz}$. Thus, the cooling frequency is single passed by a shifter Brimrose of 1.77 GHz, which normally has a low efficiency around $30-40\%$. This beam is particularly critical due to the great spatial deformation of the light beam after passing the shifter crystal. However, this is corrected using a couple of lenses and the optical fiber, as mentioned above.

EOM: To obtain the repumper frequency of the 2D-MOT and the ZS laser beam, we use two independent commercial EOM (Elctro-Optic Modulator) of high power. The RF frequency is sent to the EOM using a commercial RF generator (Stanford) and an amplifier of 5 W, being able to obtaine until 80% of efficiency in the first order sidebands. EOMs use the linear electro-optic modulator (33), producing two sidebands at ν_{RF} relative to the central frequency (frequency of the incident light beam). An EOM generates new frequency components in the light, but instead of spatially separated (as an AOM), it adds frequency components temporally. (33)

In the experimental sequence the light is turned on and off in a fast way using mechanical shutters of two kinds: Uniblitz (series LS3 from Vincent Associates) with 3 mm clear aperture, rise time of $\sim$ 1.5 ms and falling time of $\sim$ 1.2 ms, and Shutters SHT934 (from Sunex Digital Imaging Optics) with open and closing time of 1.6 ms and 0.8 ms, respectively. Both kind of shutters are controlled using a TTL signals.

3.2.3 Laser locking

One special requirement in the laser system is the frequency stability in time. Instabilities in the light frequency can be cause by mechanical noise in the optical table, temperature oscillations, etc.

To stabilize the frequency of our lasers, saturated absorption spectroscopy (SAS) is realized. (26, 34) With this technique, the Doppler broadening is eliminated, allowing to obtain a narrow absorption signal of the resonance transition, in our case the $D2$ line. For the two lasers, we use vapor cell at 150°C, heated with a heating tape wrapped around the cell. The signal obtained with the SAS is an intensity peak at the frequency of each hyperfine levels of the atoms, and also a transition midway of any two transitions, known as crossovers. The SAS setup is shown in Figure 3.2.4.

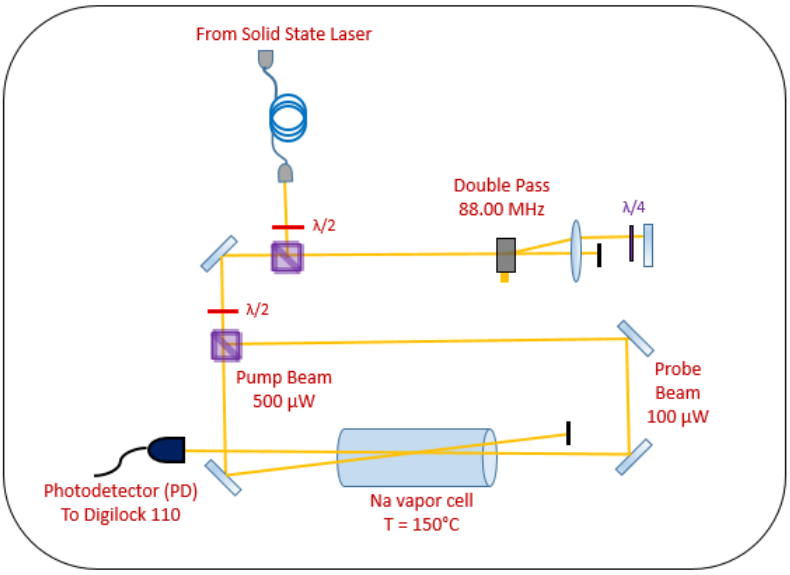

Figure 3.2.4 – Saturated Absorption setup for Lock-In of the solid state laser.
Source: By the author.

In the setup is shown the double pass AOM configuration for the pump and probe beams, using a RF driven frequency of +88.01 MHz. The Doppler free saturated absorption spectrum is sent to a Digilock control software (Digilock 110 from Toptica). With the Digilock software and the Digilock control module of the laser, the laser frequency is scanned at a rate of 2 Hz over a selected frequency range.

Table 3.2 – Parameters of the two internal controllers of the Digilock software.

	PID-1	PID-2
Gain	30	10
P	140	2000
I	50	3
D	0	0

Source: By the author.

Using the feed forward of the Scan Control, we can control the piezo actuator of the Litrow grating by applying a triangular current to the laser diode. Also, it is possible to control the current of the diode with the same module control. Scanning the piezo in this way, we obtain the SAS signal. The pump and probe beams are modulated using a frequency modulation of 17.76 KHz with an amplitude of 0.48 V_{pp} using the internal oscillator of the Digilock. The SAS signal is sent back to the Digilock where the signal is demodulated generating and error signal. Using the fact that the position of the peak in the SAS signal corresponds to a zero point of the error signal, the frequency can be fix at this zero point using a PID regulator. The Digilock software has two internal PID controller. One of the PID controller (PID-1) control the laser current by sending a signal to the Mod DC connector of the DL pro (diode laser) using the Main OUT channel. The other controller (PID-2) regulates the laser frequency through the connector of the Scan Control module. To Lock-IN module of the Digilock software is used to generated the error signal, and the parameters for PID-1 and PID-2, are shown in Table 3.2. Figure 3.3.1 shows the SAS signal and the error signal generated by the Digilock software. The dye laser is locked using the sodium vapor cell at 150°C,but using polarization spectroscopy (PE) (34–36), instead of SAS. The setup for the PE together with the signals are shown in Figure 3.3.2.

3.3 Control system

The experiment is totally controlled with a system that interfaces a computer with all the electronic components in the experimental system. The temporal sequence control requires a system that allow the real-time management of actions. Process ranging from 500 μs to tens of seconds have to be realized, demanding a fast and versatile control. The control system is based in a program developed in professor Randall Hulet's group, at Rice University, and adapted to our experiment by Dr. Rodrigo Shiozaki. This system used two different languages, Python and LabView. The experimental sequence to be realized is written in Python, and this code is called by LabView in order to performed the communication with the National Instrument boards (NI). From the NI boards the signals (voltages) going to the components of the experimental system are delivered, allowing the control of any instrument with TTL (digital signal) or continuous signals (analogue signal).

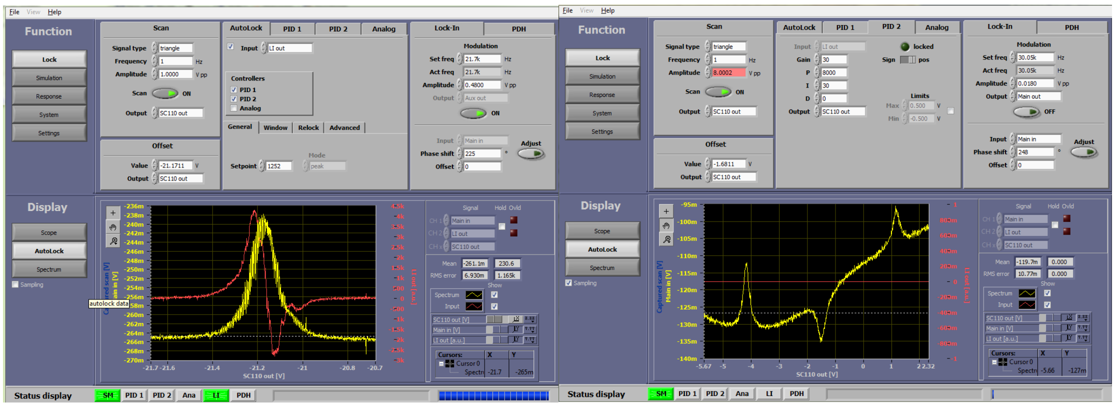

(a) (b)

Figure 3.3.1 – (a) It is shown the SAS signal and the corresponding error signal used to lock the frequency to the zero point. (b) The three peaks of the signal correspond to the transitions $F = 2 \rightarrow F' = 3$ (left peak), $F = 1 \rightarrow F' = 2$ (right peak), and the crossover (central inverted peak) between these two transitions.

Source: By the author.

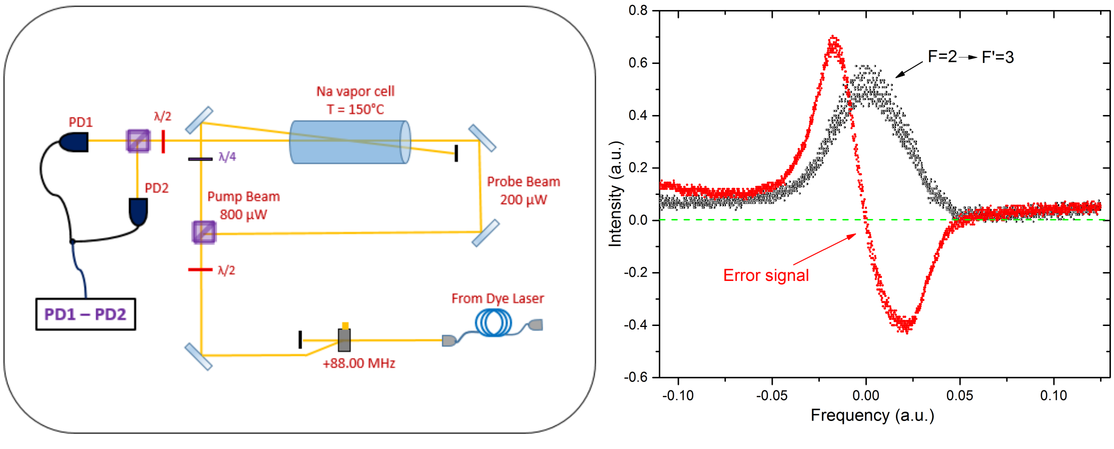
PD1
λ/2
Na vapor cell
T = 150°C
λ/4
PD2
Pump Beam
800 μW
Probe Beam
200 μW
λ/2
PD1 – PD2
From Dye Laser
+88.00 MHz
0.8
0.6
0.4
0.2
0.0
-0.2
-0.4
-0.6
Intensity (a.u.)
F=2 → F'=3
Error signal
-0.10
-0.05
0.00
0.05
0.10
Frequency (a.u.)

(a) **(b)**

Figure 3.3.2 – (a) Setup for the polarization spectroscopy (PE) to lock the dye laser. (b) The red curve is the dispersion signal, obtained directly form the PE scheme. The black curve corresponds to the cooling transition peak.

Source: By the author.

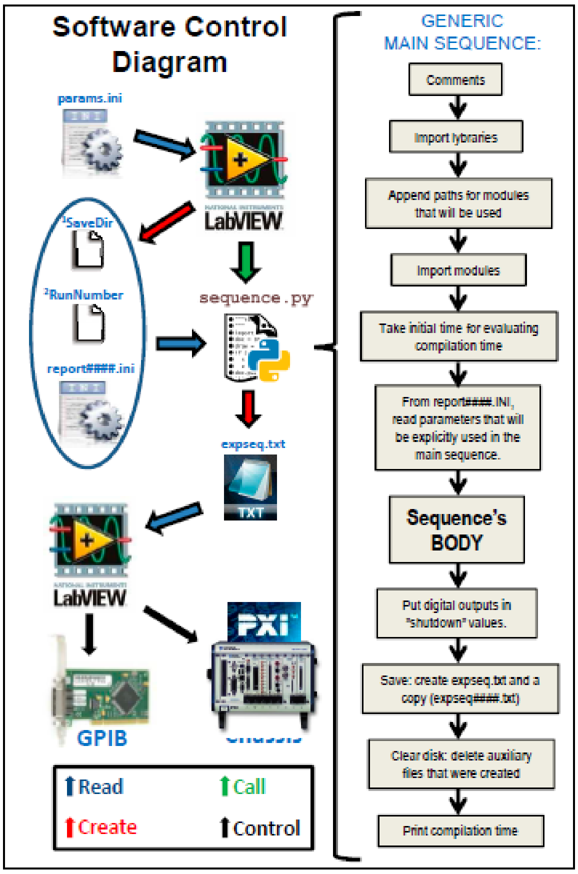
Software Control Diagram
params.ini
LabVIEW
¹SaveDir
²RunNumber
report####.ini
sequence.py
expseq.txt
TXT
LabVIEW
PXI
GPIB
Chassis
Read
Call
Create
Control
GENERIC MAIN SEQUENCE:
Comments
Import lybraries
Append paths for modules that will be used
Import modules
Take initial time for evaluating compilation time
From report####.INI, read parameters that will be explicitly used in the main sequence.
Sequence's BODY
Put digital outputs in "shutdown" values.
Save: create expseq.txt and a copy (expseq####.txt)
Clear disk: delete auxiliary files that were created
Print compilation time

Figure 3.3.3 – Control system logic. It is shown the order in which the communication process between the different programs and components of the control system happen.

Source: By the author.

This form of coding allows to choose from LabView (main program), any sequence written in Python. Thus, different sequences can be tested just choosing or calling the desired Python code. The program can have different ways of indicating the starting point of the experimental sequence. In many case it is used the value of the MOT fluorescence in volts, i.e, in the moment the MOT is complete loaded the temporal sequence begins. For our system we have several boards from National Instruments, NI PCI-6259, NI PCI-6723, and NI PCI-6733. With these board we have enough digital and analog channels to realized the control of all the elements in the BEC of sodium atoms. It is of fundamental importance to synchronize the boards, otherwise the events will occur at different times than that of the desired. The 6733 biard is used as main clock, and has as function to trigger the channels of the other boards. At the same time, two digital channels of the 6723 and 6259 are use to trigger themselves their own analog channels. Another advantage of this kind of code is that it does not require to write a vector for channel when it is not being using in the experimental sequence, i.e., the vector is only wrote when a change is made on that specific channel. This avoid over-saturation of information, leaving the memory of the PC full and slow at the time of running. Figure 3.3.4 shows the interface of the control system, and Figure 3.3.3 show how it works, i.e., how LabView call, read, and apply the actions to the electronic components of the experiment.

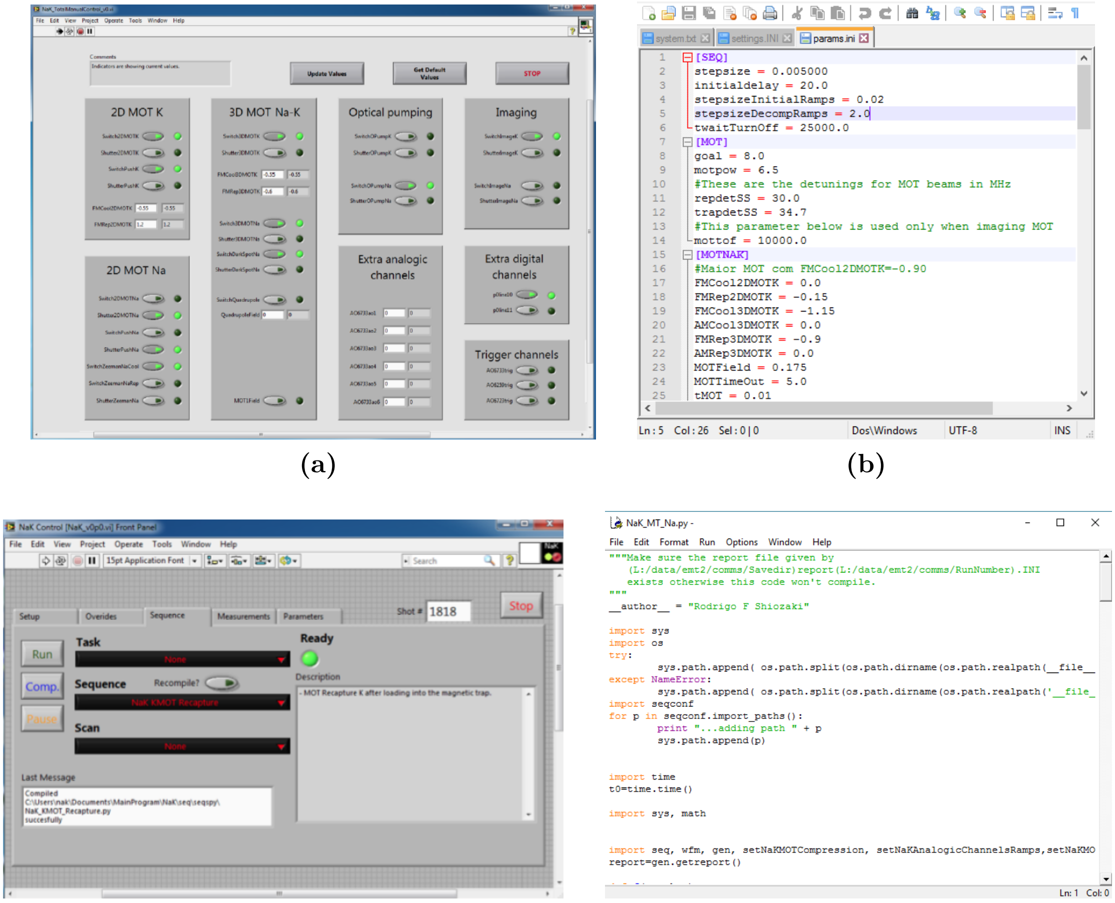
Update Values
Get Default Values
STOP
2D MOT K
3D MOT Na-K
Optical pumping
Imaging
2D MOT Na
Extra analogic channels
Extra digital channels
Trigger channels
system.txt
settings.INI
params.ini
Ln : 5 Col : 26 Sel : 0 | 0
Dos\Windows
UTF-8
INS
NaK Control [NaK_v0p0.vi] Front Panel
File
Edit
View
Project
Operate
Tools
Window
Help
15pt Application Font
Search
Setup
Overides
Sequence
Measurements
Parameters
Stop
Run
Comp.
Pause
Ready
Recompile?
NaK_MT_Na.py -
File
Edit
Format
Run
Options
Window
Help
Ln: 1 Col: 0

(a)

(b)

```
[SEQ]
stepsize = 0.005000
initialdelay = 20.0
stepsizeInitialRamps = 0.02
stepsizeDecompRamps = 2.0
twaitTurnOff = 25000.0
[MOT]
goal = 8.0
motpow = 6.5
#These are the detunings for MOT beams in MHz
repdetSS = 30.0
trapdetSS = 34.7
#This parameter below is used only when imaging MOT
mottof = 10000.0
[MOTNAK]
#Maior MOT com FMCool2DMOTK=-0.90
FMCool2DMOTK = 0.0
FMRep2DMOTK = -0.15
FMCool3DMOTK = -1.15
AMCool3DMOTK = 0.0
FMRep3DMOTK = -0.9
AMRep3DMOTK = 0.0
MOTField = 0.175
MOTTimeOut = 5.0
tMOT = 0.01
```

(c)

Shot # 1818

Task: None

Sequence: NaK KMOT Recapture

Scan: None

Description

- MOT Recapture K after loading into the magnetic trap.

Last Message

Compiled
C:\Users\nak\Documents\MainProgram\NaK\seq\seqspy\
NaK_KMOT_Recapture.py
succesfully

(d)

```
"""Make sure the report file given by
   (L:/data/emt2/comms/Savedir)report(L:/data/emt2/comms/RunNumber).INI
   exists otherwise this code won't compile.
"""
__author__ = "Rodrigo F Shiozaki"

import sys
import os
try:
        sys.path.append( os.path.split(os.path.dirname(os.path.realpath(__file__
except NameError:
        sys.path.append( os.path.split(os.path.dirname(os.path.realpath('__file_
import seqconf
for p in seqconf.import_paths():
        print "...adding path " + p
        sys.path.append(p)


import time
t0=time.time()

import sys, math


import seq, wfm, gen, setNaKMOTCompression, setNaKAnalogicChannelsRamps,setNaKMO
report=gen.getreport()
```

Figure 3.3.4 – (a) and (c) show the interface of the static and dynamic (sequence) control, respectively. (b) shows the notepad file where the experimental parameters are written, and (d) the Python interface program, where the experimental sequence is coded.
Source: By the author.

In the next chapter, I will describe individually all the stages necessary to achieve the BEC of sodium atoms. Those stages are based in the experimental system described in this chapter.

Chapter 4

Magneto-Optical Trap: Bright-MOT vs Dark-SPOT MOT Na atoms

This chapter contains the description of our magneto-optical trap (MOT) in two different configurations: Bright-MOT and Dark-SPOT MOT. A discussion about these kind of setups is presented, giving the arguments why Dark-SPOT MOT (37) is widely used for sodium atoms, and how this configuration helps to overcome some limitations inherent to Bright-MOTs. These limitations are normally in density and collision losses. An experimental comparison between bright and Dark-SPOT MOT give us the foundation to choose this configuration for our experiment.

4.1 Magneto-optical trap

The whole process of condensation starts by loading the atoms in a 3D-MOT. The atoms are cooled and trapped in the MOT using the combination of a linear magnetic field gradient and radiation field coming from a red-detuned laser. In a MOT we can capture a number of atoms of the order of 10^{10} with temperatures around hundreds of μK, the densities of this clouds are of the order of 10^{10} atoms/cm^3 in the case of a Bright-MOT of sodium atoms and of the order 10^{12} atoms/cm^3 for a Dark-SPOT MOT (37), as will be shown later. In our case, we use and take advantage of the higher densities obtained in the Dark-SPOT MOT. The bright and Dark-SPOT MOT are described in the following sections.

4.2 Bright-MOT

The 3D-MOT is loaded from the atomic source of ^{23}Na which consists of a bi-dimensional magneto-optical trap (2D-MOT), as detailed in chapter 2. Three beams are used to produce the dissipative force that causes the dissipation of energy of the atoms in the 3D-MOT. (16) The spatial dependence of this force is introduced by a quadrupole magnetic field which spread the hyperfine levels of the atoms inside the tarp. In other words, the

MOT combines the cooling effect of a three-dimensional optical molasses with confinement using the spatial dependence of the radiative pressure force due to Zeeman shifts. In this way, the MOT is constituted of three pairs of circularly polarized laser beams for the three dimensions and two coils with anti-parallel currents, which produce a quadrupole magnetic field. Thus, using radiation pressure forces from red detuning laser light (16), cooling and trapping are achieved at the same time.

4.2.1 Loading atoms in the MOT

The 3D-MOT can confine atoms whose velocity are smaller than certain capture velocity (v_c) (38, 39), thus it is important to have a source of cold atoms to load the 3D-MOT. In chapter 2, we have shown that 2D-MOT sources are a very good and efficient alternative in comparison with big Zeeman slowers. (22–24)

The capture velocity (38) in a first approximation can be written as

$$v_{\mathrm{C}} = \sqrt{2 R_{scatt} v_{recoil} d} \tag{4.2.1}$$

where d is the diameter of the MOT beams, $v_{recoils} = \hbar k / m_{Na}$, with $k = 2\pi/\lambda_{Na}$ is the wavenumber of the trapping light, and R_{scatt} is the scattering rate of photons given by

$$R_{scatt} = \frac{\Gamma}{2} \frac{I/I_s}{1 + I/I_s + 4\delta^2/\Gamma^2} \tag{4.2.2}$$

here, Γ is the natural linewidth of the transition ($D2$ line for sodium), δ is the detuning of the light with respect to the atomic transition, I_s is the saturation intensity of the $D2$ transition, and I is the intensity of the MOT beams. For our case, the $\Gamma \simeq 2\pi \times 10\,\mathrm{MHz}$, $\delta = -12.5\,\mathrm{MHz}$, $I_s = 6.26\,\mathrm{mW/cm^2}$, $d = 2.0\,\mathrm{cm}$, $v_{recoil} = 2.94\,\mathrm{cm/s}$, and $I \simeq 19\,\mathrm{mW/cm^2}$, then from Equation (4.2.1) we have $v_c \simeq 66.7\,\mathrm{m/s}$ for our 3D-MOT. Normally, the 2D-MOT provides atoms with smaller velocities, which make it an efficient source of cold atoms as mentioned above.

Now, the 3D-MOT loading rate can be described by the rate equation (24, 40)

$$\frac{dN}{dt} = L - \gamma N - \beta \int n_{MOT}^2 (r, t)\, d^3 r \tag{4.2.3}$$

where L is the loading rate (or capture rate) of the 3D-MOT, N is the number of atoms in the MOT, $\gamma = 1/\tau$ is the collision rate between trapped atoms and background atoms, where τ can be seen as the time an atom remains in the trap, β is the loss rate of atoms in the trap (40), normally this constant depends on light intensity and detuning, and finally $n_{MOT}^2 (r, t)$ is the MOT density.

In the loading process, represented by Equation (4.2.3), the density can be considered constant along the whole process, since the volume of the MOT increases at the same rate as the number of atoms that are loaded into the MOT (40). With this consideration, Equation (4.2.3) can be written as

$$\frac{dN}{dt} = L - (\gamma + \beta n_{const})\, N, \tag{4.2.4}$$

where n_{const} is the constant atomic density reached in the trap. The solution to Equation (4.2.4) is given by

$$N = N_0 \left[1 - e^{-(\gamma+\beta n_{const})t}\right]. \tag{4.2.5}$$

The rate constants, γ and β, have been extensively studied in many theoretical and experimental works (40, 41) and are still and important topic in cold and ultracold atoms where denser clouds are desired, and a better understanding is required in order to manipulate BECs, for instance, avoiding loss processes and controlling or minimizing undesired effects. Normally, at the beginning of the loading process, the behavior is linear and the collision rate β can be neglected due to the low density, then Equation (4.2.5) can be further simplified as

$$N = N_0 \left[1 - e^{-t/\tau}\right] \tag{4.2.6}$$

where $N_0 = L\tau$ in this case. The decay rate, when the atomic source is turned off, is then given by $N = R\tau e^{-t\tau}$. Therefore, from all these points it is notable that increasing the number of trapped atoms we can increase the loading rate L, or increase the lifetime, τ, of the atoms in the trap. We can increase L using an atomic source able to provide high flux of atoms with velocities below v_c, this is the case of our 2D-MOT atomic source. For increasing the lifetime, τ, the vacuum in the chamber need to be maintained at levels of high vacuum (HV) or ultrahigh vacuum (UHV).

The atomic density in a MOT is basically limited due to collisions (40, 41) and self-trapping radiation (42, 43) (also known as photon-induced repulsion). The collisions in the MOT may be of different types, collisions between trapped atoms and collisions between trapped atoms and hotter background atom, as expressed above. In the case of collisions between trapped atoms, different effects can give enough energy to the colliding pair to escape from the trap, these can be Radiative Escape (RE) and fine structure changing collisions (FSCC). (40, 44, 45) In the case of the presence of the MOT light beams, a pair of atoms in the ground state interaction potential $3^2S_{1/2}+3^2S_{1/2}$, where the potential goes as $-C_6/R^6$, can absorb a photon ($\omega_{P_{3/2}}$) and be excited to the state $3^2S_{1/2}+3^2P_{3/2}$ where they feel an attractive potential of the form $-C_3/R^3$ which accelerates the atoms together. In the case where the collision takes a time greater than the lifetime of the excited state, two effects may happen: the atoms may decay to the ground state potential emitting a red-detuned photon at some point R_{RE} and the excess of energy is equally distributed to the pair of atoms in the form of kinetic energy. If this energy is greater than the trap depth the atoms can escape from it, this is the so called RE. In the case that the atoms do

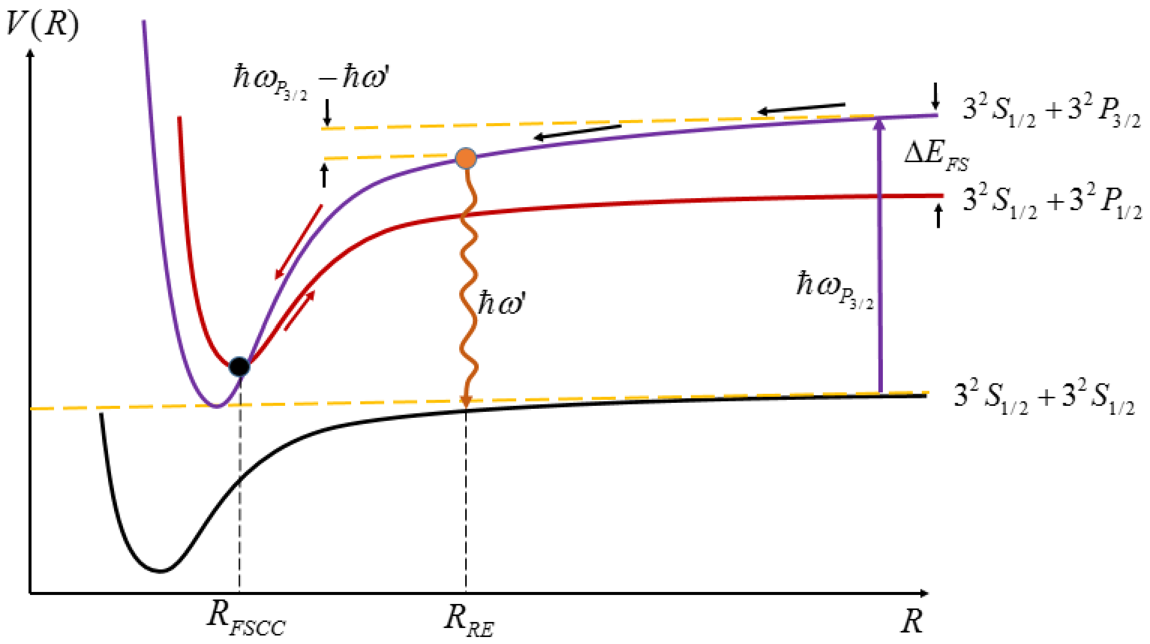
$V(R)$
$\hbar\omega_{P_{3/2}} - \hbar\omega'$
$3^2S_{1/2} + 3^2P_{3/2}$
ΔE_{FS}
$3^2S_{1/2} + 3^2P_{1/2}$
$\hbar\omega'$
$\hbar\omega_{P_{3/2}}$
$3^2S_{1/2} + 3^2S_{1/2}$
R_{FSCC}
R_{RE}
R

Figure 4.2.1 – Schematic diagram showing the Radiative Escape (RE) and FSCC mechanisms. $V(R)$ represents the interaction potential and R the internuclear separation between the atoms.
Source: By the author.

not radiate, they can continue approximating each other until reaching a point (R_{FFSC}) where they can do a transition to the other potential represented by $3^2S_{1/2} + 3^2P_{1/2}$, for this reason, the process is named FSCC. Figure 4.2.1 shows the possible two processes described above.

In a MOT, the most dominant collision losses-induced are those collisions experienced by trapped atoms with untrapped atoms of the background. (40) For this reason, the realization of MOTs required HV or even UHV chambers. Our optimized sodium MOT operates at pressures of about 10^{-11} Torr in our UHV science chamber.

The other important effect is the self-radiation trapping, which strongly limits the atomic density in a MOT. This process arises when trapped atoms in the center of the MOT emits a photon that is absorbed by another trapped atom avoiding the photon to escape from the trap. (40, 42, 43) This absorption leads to an increase in relative linear momentum of the pairs of atoms involved in the process by an amount of $2\hbar k$, and producing in this form a repulsive force which depends on the absorption cross-section of the incident light beams (MOT cooling beams) and the absorption cross-section of the scattered photons produced by the atoms in the center of the MOT. In the stationary situation, where the confining force is equal to the repulsive force, the MOT increases in atom number leading to an increase in volume, then being impossible to increase the density. (40) This effect is circumvented using the technique called Dark-Spot MOT (Dark Spontaneous-Force Optical Trap) proposed and implemented by W. Ketterle in 1993. (37)

This technique and its implementation in our system will be discussed in subsection 4.3.

4.2.2 Our Bright-MOT

In our Bright-MOT, the repumper light ($3^2S_{1/2}(F=1) \rightarrow 3^2P_{3/2}(F'=2)$) co-propagates with all the three cooling beams ($3^2S_{1/2}(F=2) \rightarrow 3^2P_{3/2}(F'=3)$). We use retro-reflected cooling beams configuration for our MOT. One of the advantages of this configuration is that it needs less laser power, but may present a disadvantage with respect to power balance. This drawback can be circumvented using coated-windows in the vacuum chamber to avoid power losses in the trajectory of the beams. Figure 4.2.2 shows the optical setup for the Bright-MOT and for the Dark-SPOT MOT discussed in subsection 4.3.1.

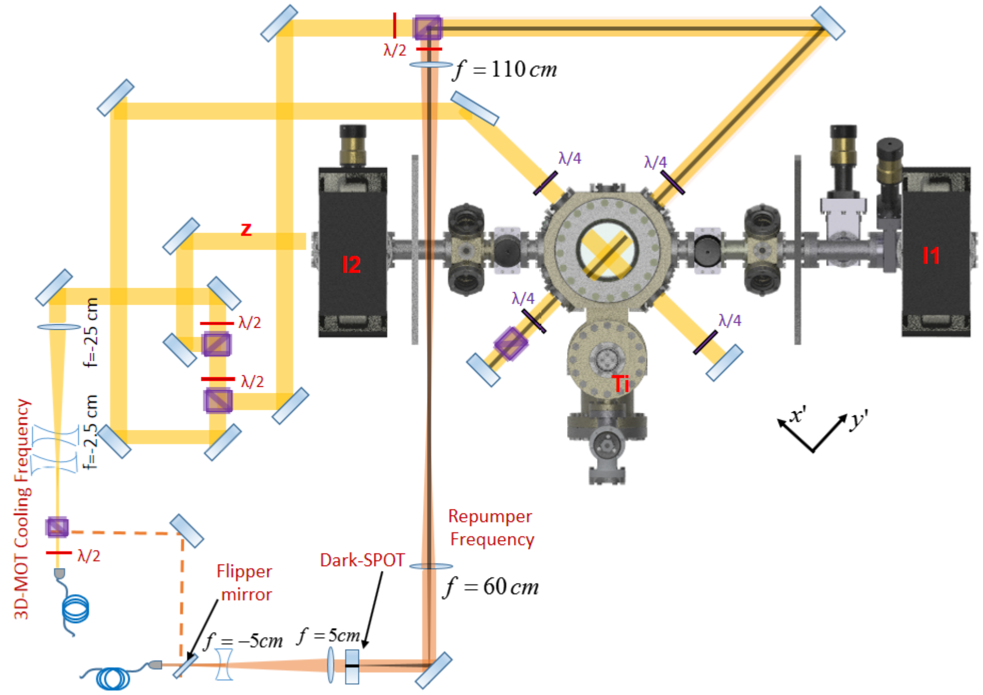

Figure 4.2.2 – Optical setup used for the 3D-MOT. Both configurations are shown, the Bright-MOT and Dark-SPOT MOT configuration.
Source: By the author.

The cooling and repumper light come from different polarization maintaining optical fibers (OZ Optics). There is one optical table exclusively for the lasers and optical system, and the required light is sent to the optical table where the science chamber is placed using polarization maintaining optical fibers (Chapter 3, section 3.2). The size of the trapping beam coming out from the fiber is $\sim 1\,\mathrm{mm}$ diameter, and is expanded to a size of $2\,\mathrm{cm}$ diameter after the expansion telescope as shown in Figure 4.2.2. It is used a combination of divergent and convergent lenses in order to expand the beam in a short distance. After the expansion, a set of $\lambda/2$-waveplates and polarizing cubes are used to divide the beam into three beams, corresponding to each direction of the MOT. This allows optimizing independently the intensity balance of the trapping beams of the MOT. Because each beam is retro-reflected for each axis, it is not possible to adjust separately the intensity of the incoming and retro-reflected beam. In some cases, it can be corrected placing a lens in the reflected path in order to focus a little bit the retro-reflected beam and maintaining the same intensity as the incoming beam. In our case, we did not need to do this, but could be important for newcomer people constructing a system like this. As mentioned above, the advantage of using retro-reflected beams is that it is needed less laser power than in the case of the six independent beams.

The optical fiber allows to have a very clean spatial mode of the MOT beams, at least much cleaner than when not using optical fiber, this is important because the force in the MOT is isotropic and it is then possible to obtain a symmetric and round MOT, which is very good at the time of transferring to the magnetic trap as will be described latter, then Gaussian mode beams are required.

The intensity of each MOT beam is $I_{trap} \sim 6.36\,\mathrm{mW/cm^2}$ and taking into account that the saturation intensity for the $D2$ line is $I_s = 6.26\,\mathrm{mW/cm^2}$, we have that $I_{trap} = 1.05 I_s$. It is important to remember that as a starting point for creating a MOT the beam intensity has to be preferable equal or greater that the saturated intensity in order to have an efficient dissipative force.

The repumper light is also sent to the science chamber table using a polarization maintaining optical fiber. For doing the bright-MOT the same polarizing beam splitter cube that cleans the polarization of the trapping beam once it emerges from the optical fiber is used to combine both beams. Even though both beams have mutually orthogonal polarization, it is corrected by the set of $\lambda/2$-waveplates and polarizing beam splitter cubes that divide the beam into the three MOT beams.

When the beams arrive at the windows of the science chamber, there are $\lambda/4$-waveplates to circularly polarize the beams, required in the trapping process. These $\lambda/4$-waveplates are as near as possible to the windows to avoid distortion of the circular polarization, this commonly happens if the beams encounter optical elements like mirrors where the circular polarization can be distorted into elliptical polarization, and this is undesired. As we send the trapping and repumper beams for the same path and through the same cubes they have the same state of polarization at the atomic cloud. The intensity of the repumper beam is $I_{rep} = 0.34 I_s$. The way these frequencies are generated was shown in chapter 3.

The quadrupole magnetic field is generated by a pair of coils in anti-Helmholtz configuration, which produce a magnetic field gradient of $23.70\,\mathrm{G/cm}$ with $I = 3.68\,\mathrm{A}$. The description of the coils construction and details about the magnetic field calibration will be given in section 5.2.2 of chapter 5. These coils are the same used to produce the magnetic field for the magnetic trap (MT) (section 5.2.1).

4.2.3 Experimental tips for obtaining a good MOT

I think the discussion made in D. Naik PhD thesis (24) is very interesting in relation with tips for realizing a good MOT with respect to the alignment, etc. For people reading this thesis and working for the first time in this kind of systems, it could be interesting to read these recommendations.

Basically, the parameters for creating a good MOT are the intensity, detuning, alignment of the trapping and repumper beams, and B-field gradient. In the case of the Dark-SPOT MOT the position of this Dark-SPOT into the MOT volume is crucial.

A good starting point is to set the intensity equal or greater than the saturation intensity of the transition being used for cooling and trapping. The frequency is normally red-detuned by Γ (linewidth of the transition), and then scanned to optimize the value of this detuning (normally looking at the number of atoms). At the beginning, the repumper light may be set at zero detuning and then scanned to be optimized. The intensity is normally smaller than the saturation intensity and thus, the force this beam do on the atoms is very weak, of course because the objective of this beam is just to bring to the cycle transition those atoms that went to the dark state $3^2S_{1/2}(F = 1)$ and no longer participate of the cooling process. But, the intensity has to be enough for the beam be able to bring back the atoms to the state $3^2S_{1/2}(F = 2)$ where the cycling transition for cooling and trapping the atoms in the MOT occurs. The B-field gradient for alkali atoms are around 10 G/cm. This value has to be scanned for obtaining the best value for each system. The "spring constant" κ of the restoring force that bring the atoms back to the trap center depends not only on the light intensity but also on the B-field gradient, doing both parameters very linked between each other.

For aligning the MOT beams, it is recommendable to place an iris after the expansion optics, then it can be chosen to close the iris and align the remaining small three beams exactly in the center of each window of the science chamber, and then the retro-reflection has to coincide with the incoming beam. When the iris is open and the MOT is ready, misalignment can be detected in the following way: if one retro-reflected beam is moved away from the center, the force on this direction decreases, allowing the MOT to move in that direction due to the excess of force. If the beam is gradually moved back to the correct the misalignment the MOT will recover slowly. If the beams are correctly aligned the MOT will be very round. In the case of sodium atoms, it is relatively simple to see the shape of the MOT due to the bright yellow fluorescence. Another nice way to align the MOT is to increase the B-field gradient, then compressing the MOT to a smaller ball. Now, if the iris is slowly closed until observing an even smaller cloud, the MOT beams may be adjusted in order to bring the biggest density, number of atoms or fluorescence to the center of the small beams. With this procedure, we can warranty that the optical force match with the zero of the magnetic field. This is really important because at the time of doing optical molasses (sub-Doppler cooling) and transferring the atoms to the MT the atoms in the MOT have to be in the center of the B-field, otherwise the atoms will feel a force when the B-field for doing the optical molasses process is switched off, expelling the atoms from the center of the trap.

As sodium atoms emit a bright yellow fluorescence, it is possible to see the molasses stage when the MOT is cold enough and allows to see the atoms moving while expanding. If the expansion, seen by eye, is isotropic, then this is an indicative of a good alignment of the MOT beams and the match of the optical force with the center of the trap (zero B-field position). Compensation coils have to be placed in addition to the principal coils with the objective of adjusting the zero B-field with the optical force. These coils are adjusted independently in the three directions. Figure 4.2.4b shows the position of this coils around the science chamber.

Another effect is related to interference between the incoming and retro-reflected beam (in every direction). This interference is produced when the two beams create a standing wave due to the reflection of each beam in the internal faces of the science chamber windows. This effect causes spatial irregularities in the MOT which are undesired. Figure 4.2.3 shows the cases when the MOT beams create the interference pattern, clearly visible in the spatial distribution of atoms in the MOT and a MOT when the pattern has been removed after some fine adjustments in the alignment.

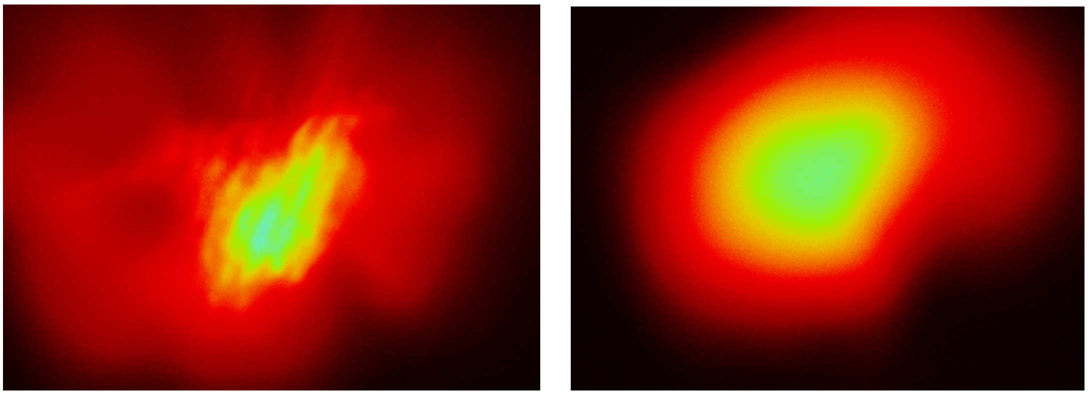

(a) (b)

Figure 4.2.3 – (a) Irregular MOT due to interference of the trapping beams. (b) After some fine adjustment the interference pattern is eliminated.
Source: By the author.

Figure 4.2.4a shows the 3D-MOT fluorescence. The strong yellow fluorescence is clearly visible, even when observed far from the science chamber, this is one of the nice and beautiful characteristics of a sodium MOT. Figure 4.2.4b shows our MOT configuration.

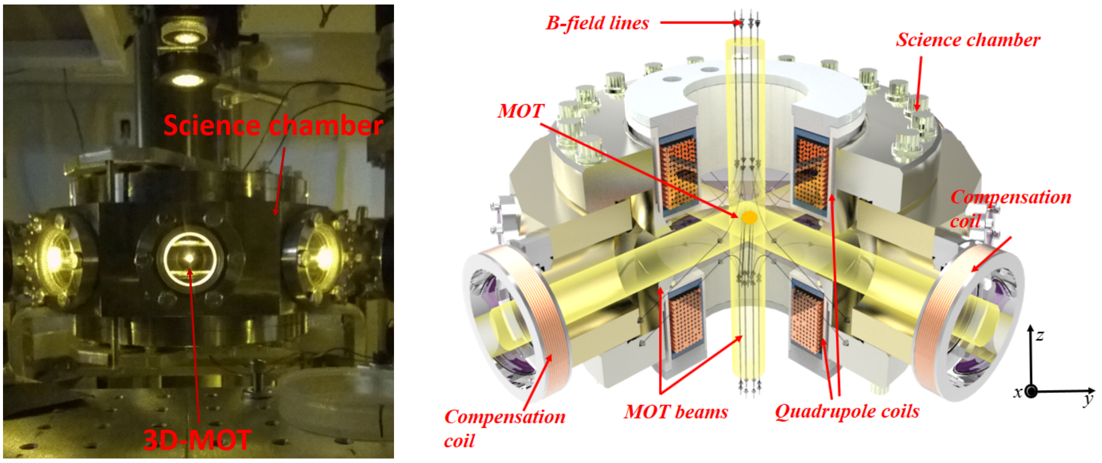

(a) (b)

Figure 4.2.4 – (a) Yellow fluorescence from the sodium MOT with around 4×10^9 atoms. (b) Configuration of the MOT.
Source: By the author.

In this experiment, we initially performed all these steps when the MOT is loaded continuously. But also, we performed the steps optimizing all the parameters, one-by-one, looking at the MT, i.e. observing the number of atoms that are finally transfer to the MT, due to that we are interesting in transferring the greatest number of atoms as possible and starts the evaporative cooling process to reach the Bose-Einstein condensation.

To characterize our 3D-MOT we realize several measurements of the atom number loaded as a function of light intensity and detuning, some of these results were shown in chapter 2. The loading rate for the Bright-MOT is presented together with the loading rate for the Dark-SPOT MOT in order to compare both.

4.3 Dark-SPOT MOT (Dark spontaneous-Force optical trap)

As mention above, the Bright-MOT has some limitations in the atomic density mainly due to loss-induced collisions and re-absorption of light by atoms in the trap, also leading to the heating of the atomic cloud. This heating is evident when we measure the temperature of the MOT and found $T \simeq 600\,\mu\text{K}$, which is $2.5 T_D$ where $T_D = 240\,\mu\text{K}$ is the Doppler temperature for sodium atoms in a MOT.

To circumvent the limitations in density, a Dark-SPOT MOT, first realized by Ketterle(37) and widely used for sodium atoms, is used. This technique consists of a physical Dark-SPOT in the repumper beam as shown in Figure. 4.3.1.

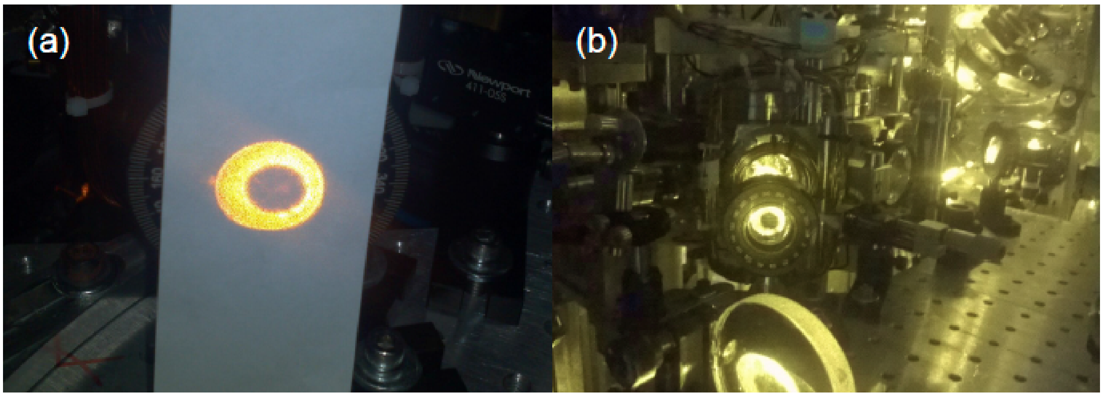

Figure 4.3.1 – (a) The repumper beam with a dark hole in the center. (b) The repumper beam propagating along the optical system for producing the MOT.

Source: By the author.

As explained before, to trap the atoms in a MOT it is necessary the presence of two frequencies, cooling and repumper. This is because the cooling transition is not totally closed and the atoms in the excited state ($|F' = 2\rangle$) can decay to the state ($|F = 1\rangle$) where they are not resonant anymore with the cooling light. Then, repumper light is necessary to keep the atoms in the cooling cycle.

When the repumper beam has a Dark-SPOT in the center (see Figure 4.2.2) it creates a region in the MOT center where, approximately, all the atoms decay to the state $|F = 1\rangle$ and then these atoms do not absorb cooling light. In this dark state the atoms neither absorb nor emit photons from the cooling light, avoiding in this way the self-trapping radiation. (40, 42, 43) Atoms in the center of the trap are the colder ones, and they remain $\sim 99\%$ of the time in the $|F = 1\rangle$ state. As the Dark-SPOT creates a cylinder-like tube of repumper light (Figure 4.3.1), atoms escaping from the MOT, interact again with the repumper light and are cooled down, being sent again to the center of the trap. Thus, it is created a kind of reservoir of atoms being cooled down outside the "core" of the MOT and brought to the center because on the surface of the MOT they feel the light force of the cooling beam once they have been pumped to the $|F = 2\rangle$ hyperfine state. In this way, the heating and density limitations due to self-trapping radiation are avoided. Also, losses due to excited state collisions or radiative escape are minimized because the atoms are the most of the time in the state $3^2S_{1/2}\,(F = 1)$. Therefore, the Dark-SPOT MOT will be colder and denser than the bright-MOT.

It is worth to mention that for other alkali atoms, this method is not so efficient, for example for rubidium (^{85}Rb and ^{87}Rb) the hyperfine separation of the ground state is very large, making the probability the atoms fall into $|F = 1\rangle$ state very low, then it is needed to use additional pumping to this ground state. (46) Instead, other techniques are used, for example, the MOT compression technique. (47) For potassium atoms, the Dark-SPOT technique is neither suitable due to the saturation intensity of the transition be very low, thus, any low intensity strayed light can pump the atoms into the $|F = 2\rangle$ state. For lithium the Dark-SPOT technique does not work since the hyperfine splitting of the ground state is very small, preventing to create a really dark state. (46)

4.3.1 Our Dark-SPOT MOT

To create the Dark-SPOT it is used a transparent glass window with a black dot in the center of 5.39 mm diameter. The black dot is just a thin circular piece of metal painted of black (nail polish works very well).

At the first time, we tried to send just the collimated beam to the science chamber, but along the path the diffraction of the light in the borders of the black dot expanded not allowing to have a really Dark-SPOT, instead we have a gray spot with a lot of straight lines going radially to the center. To create a very nice and really dark spot it is necessary to do the image of the black dot onto the atomic cloud position. The scheme of this configuration is shown in Figure 4.2.2. We expanded the beam to obtain a Dark-SPOT image on the atoms of ~ 10.3 mm diameter.

To optimize the size of our Dark-SPOT, we had several black dots. When testing every Dark-SPOT, we measure the number of atoms transferred the MT 5.3. We use a RF frequency (“Knife”) of 30 MHz, which removed all the atoms with higher energy than certain value (defined by the RF), always keeping the atoms in the MT with the same energy as is explained in section 5.3. We could have measured a quantity that gives direct information about the phase-space density, this is the quantity $N/T^{3/2}$. It is worth remember that the phase space density is given by $\rho_{PSD} = \left(\frac{h^3}{V(3mk_B)^{3/2}}\right)\frac{N}{T^{3/2}}$ (29), but we preferred to measure the number of atoms transferred to the MT, since this is the ultimate goal and we do this directly. Taken some measurements of N and T in the Dark-SPOT MOT we obtained a ρ_{PSD} around 10^{-6}. It is important to recall that in our (and typically) Bright-MOTs of sodium atoms the densities are of the order of $10^{10}\,\mathrm{cm}^{-3}$ with atoms numbers between $10^9 - 10^{10}$, then the phase-space density is around $10^{-7} - 10^{-8}$. In the case of the Dark-SPOT, the density is increased typically in two order of magnitude ($10^{12}\,\mathrm{cm}^{-3}$), then $\rho_{PSD} \sim 10^{-6}$, which helps in the process of obtaining the BEC of sodium atoms. In the case of the Dark-SPOT MOT the number of atoms is of the order of 4×10^9 and the MOT temperature around $340\,\mu$K. The number of atoms and the temperature of the MOT was estimated using absorption images with the time-of-flight technique (TOF) describes in section 5.4.

This characterization is shown in Figure 4.3.2, and we can see that for a diameter of 5.39 mm of the Dark-SPOT, which corresponds to a Dark-SPOT image of ~ 10.3 mm diameter at the atomic cloud position it is obtained the best atom transfer to the MT. We preferred to perform the measurement of number of atoms in the MT because the image and parameters are more precisely determined by the Gaussian Fit on the image, because the smaller size of the cloud, thus we can realize larger TOF expansion, which improves the accuracy of the measurement. For this characterization we use a $TOF = 19\,\text{ms}$ and a Radio Frequency (RF) “knife” in the MT of 30 MHz (see section 5.4).

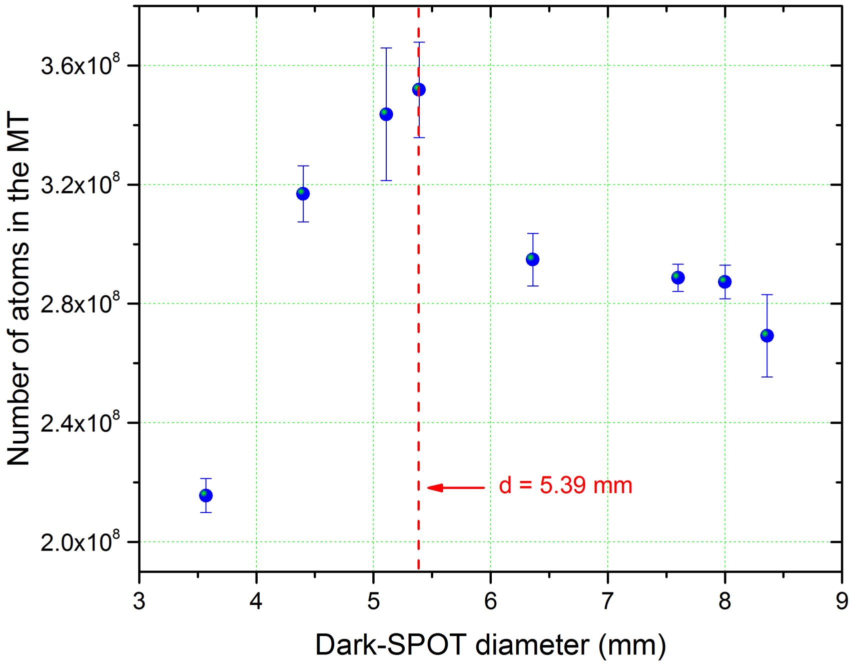

Figure 4.3.2 – Optimization of the size of the Dark-SPOT. We look at the number of atoms transferred to the MT for each the Dark-SPOT size. In the MT we put a RF “knife” of 30 MHz and $TOF = 10\,\text{ms}$.
Source: By the author.

Finally, to compare the performance of the Dark-SPOT and compare with that of the Bright-MOT we measured the loading rate for both. Initially, we measure the number of atoms in the Bright-MOT as a function of the intensity of the 3D-MOT cooling beams, the intensity of the 2D-MOT, and the intensity of the Zeeman slower beam (see chapter 2) as shown in Figures 4.3.3, 4.3.4, and 4.3.5.

Figure 4.3.3 shows the evaluation of the loading rate of the Bright-MOT . First, in (a) is shown the loading curves for several intensities of the 2D-MOT cooling beams and from here we obtain the loading rate from the linear part of the loading curves. These loading rates give information about the flux of capturable atoms going into the science chamber. With the loading rates, we can observe what are the conditions necessary to obtain a higher number of atoms in the trap. We see that for poor 2D-MOTs the loading rate is very small because the flux of atoms going to the science chamber is small. From (c) we see that the maximum loading rate we reach in our system for the Bright-MOT is 1×10^{10} atoms/s.

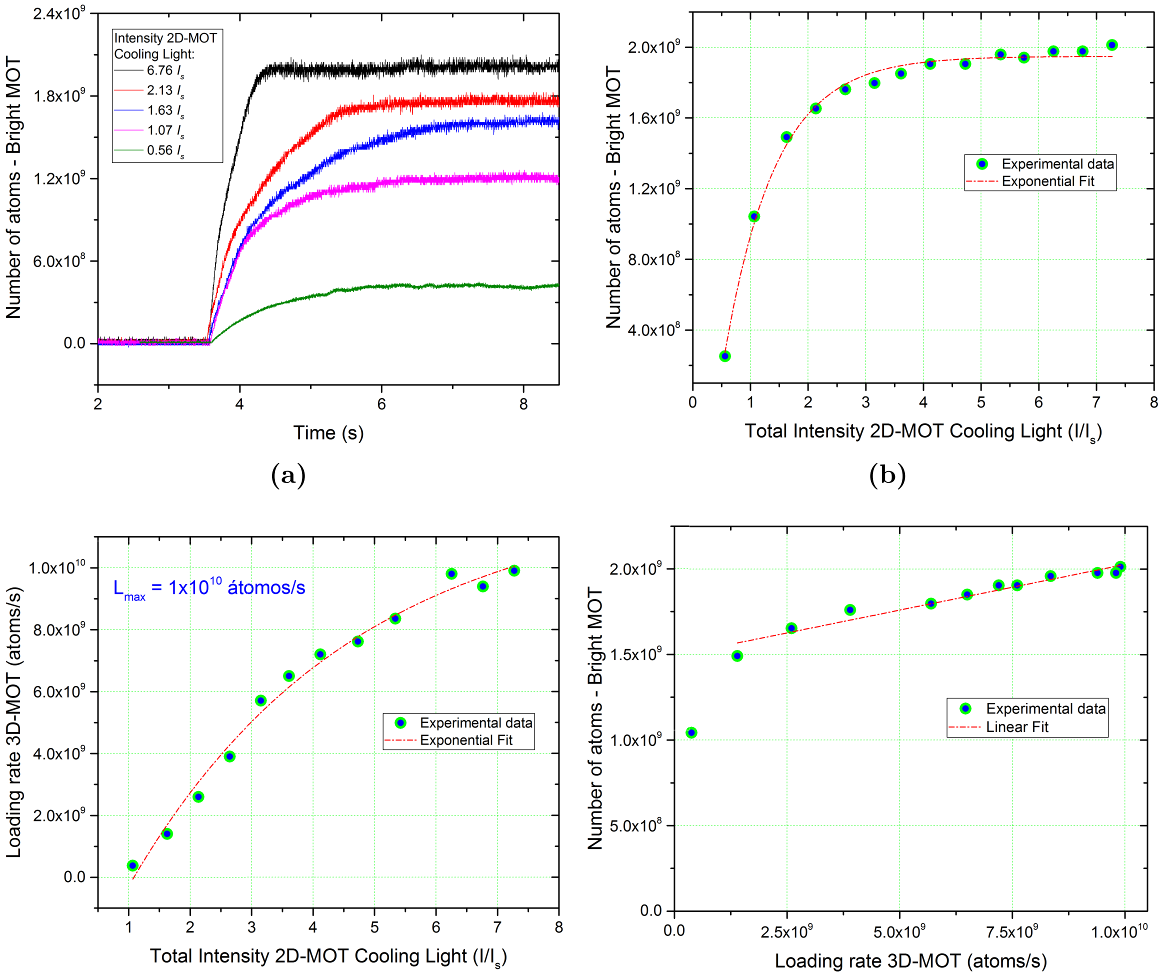

(a) (b)

(c) (d)

Figure 4.3.3 – Evaluating the performance of the Bright-MOT. We measure the loading rate as a function of the 2D-MOT intensity cooling light. The intensities of the other beams were: $I_{3D}^{cooling} = 1.67 I_s$ per beam, $I_{3D}^{repumper} = 0.81 I_s$, $I_{push} = 7.32 I_s$, and $I_{ZS} = 25.73 I_s$.
Source: By the author.

From (d) we can see clearly the saturation of the number of atoms as a function of the loading rate, i.e. increasing the loading rate at the initial parts does not mean a higher final (stationary) number of atoms, because when the number of atoms is high losses-induced collisions predominate, as explained in subsection 4.2.

Figure 4.3.4 shows the performance of the Bright-MOT as a function of the 3D-MOT cooling beams. In (b) we see that we can approximately reach the stationary number of atoms which is of the order of 2×10^9. From (c) we see that from $2.80\, I_s$ the loading rate again saturates and as it is shown in (d) more intensity does not increase the number of atoms anymore. Then, we can know the limit of our system.

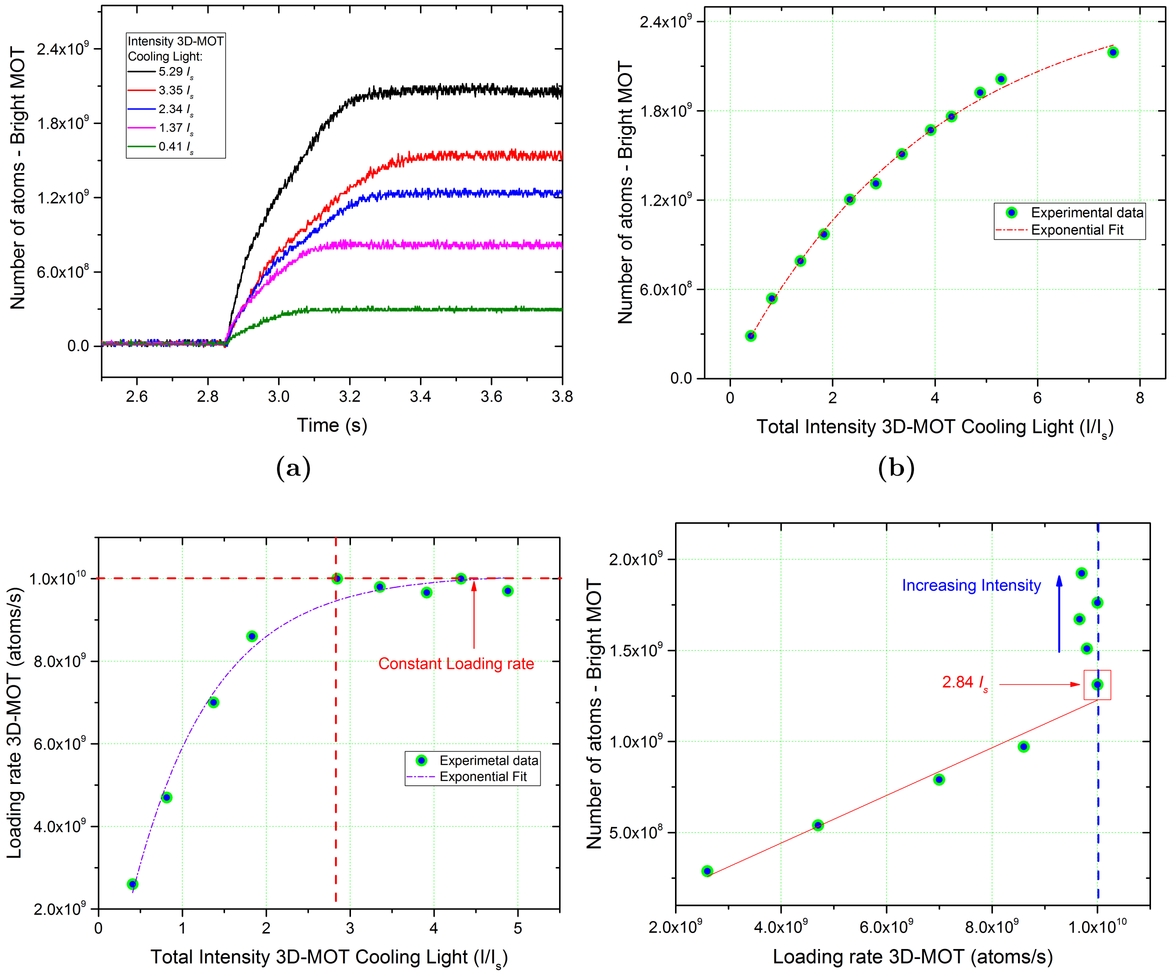

(a) **(b)**

(c) **(d)**

Figure 4.3.4 – Evaluating the performance of the Bright-MOT. We measure the loading rate as a function of the 3D-MOT intensity cooling light. The intensities of the other beams were: $I_{2D}^{cooling} = 3.74I_s$ per beam, $I_{3D}^{repumper} = 0.81I_s$, $I_{push} = 7.32I_s$, and $I_{ZS} = 25.73I_s$.

Source: By the author.

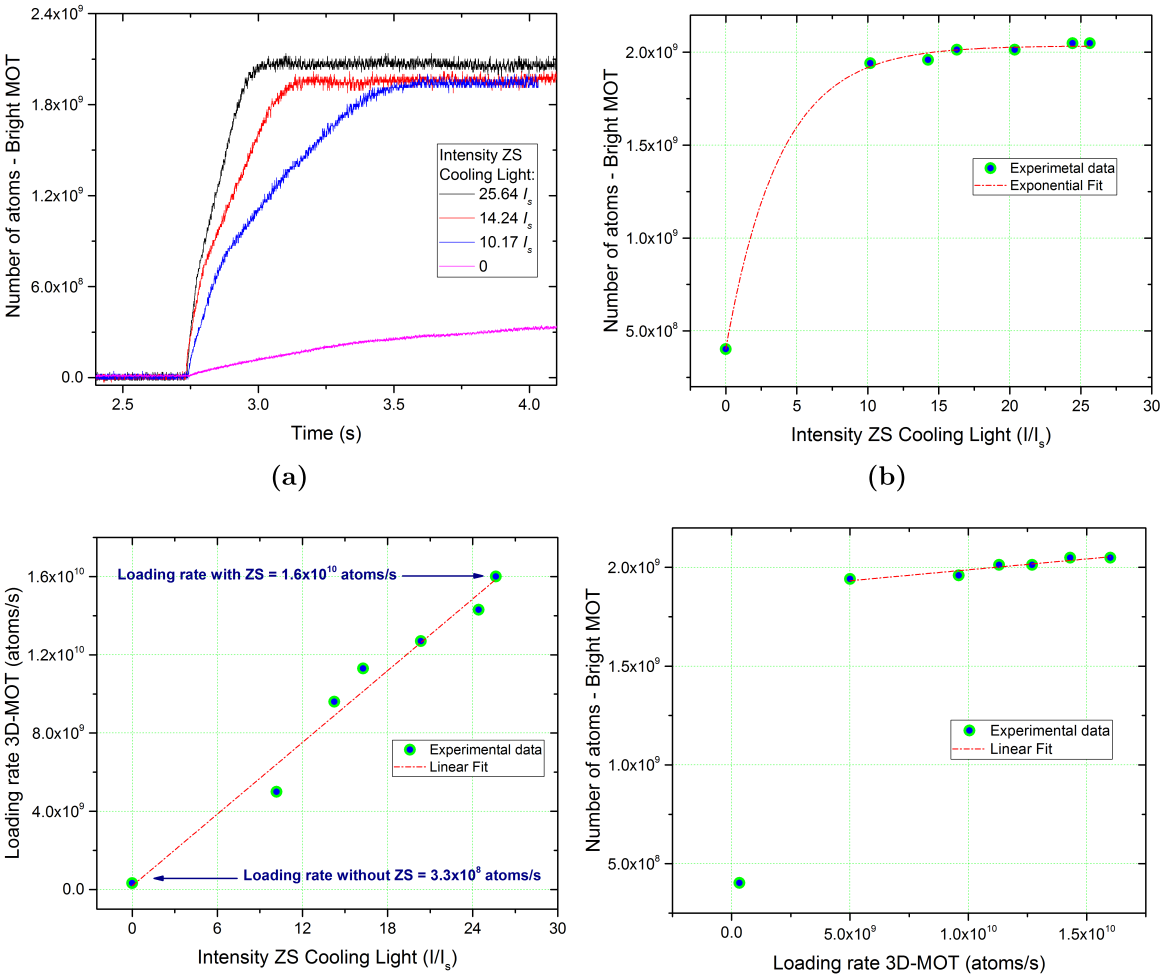

(a) (b)

(c) (d)

Figure 4.3.5 – Evaluating the performance of the Bright-MOT. We measure the loading rate as a function of the ZS intensity cooling light. The intensities of the other beams were: $I_{3D}^{cooling} = 1.67 I_s$ per beam, $I_{2D}^{cooling} = 3.74 I_s$ per beam, $I_{3D}^{repumper} = 0.81 I_s$, and $I_{push} = 7.32 I_s$.

Source: By the author.

Figure 4.3.5 shows an extremely important parameter, the intensity of the ZS, we see from (c) that when the ZS beam is in maximum intensity we can reach from our laser system, the loading rate is about 1×10^{10} atoms/s, and when the ZS is switched off the loading rate is approximately 3.3×10^{8} atoms/s, and we can see from (a) that for this loading rate, the final number of trapped atoms in the Bright-MOT is very low, pink curve with atom numbers around 2×10^{8}.

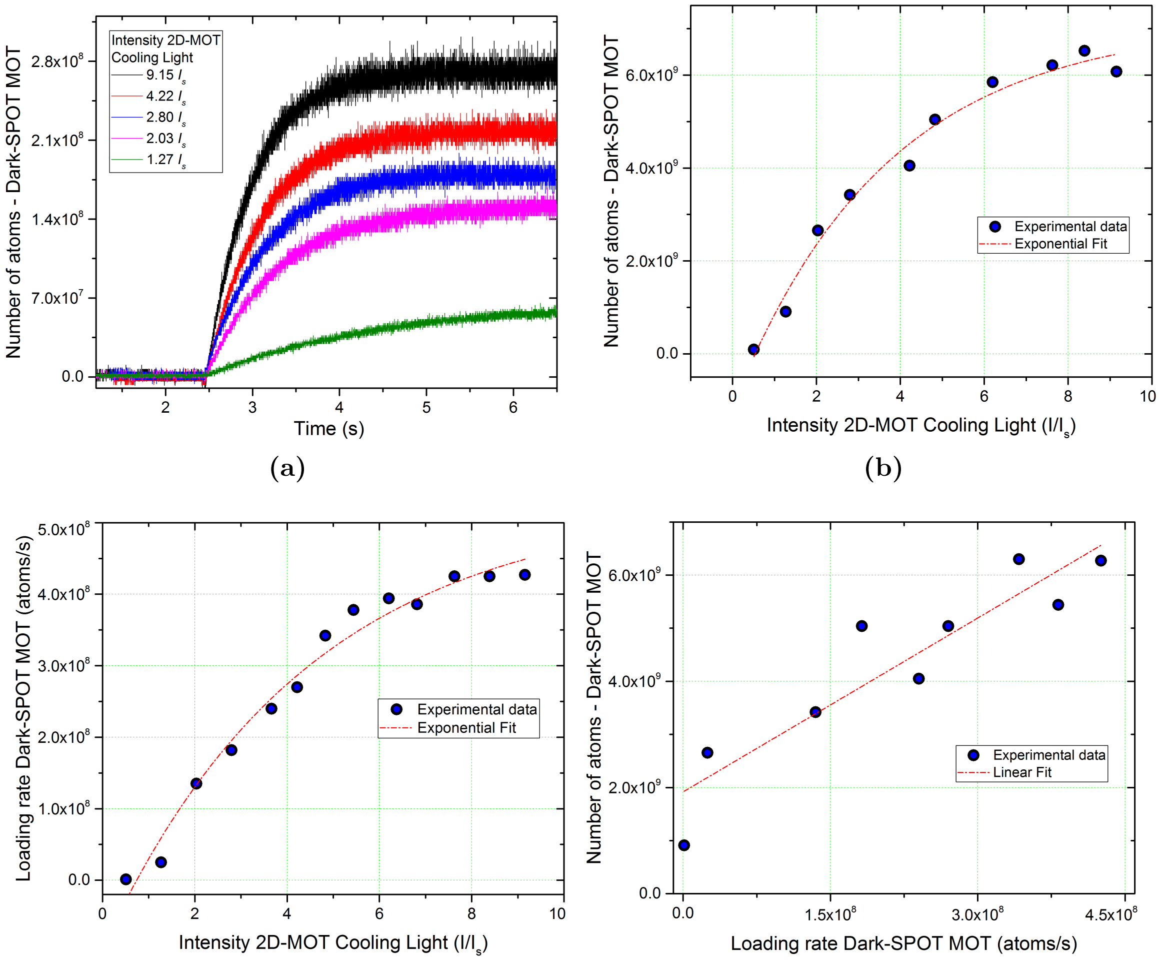

(a) (b)

(c) (d)

Figure 4.3.6 – Evaluating the performance of the Dark-SPOT MOT. We measure the loading rate as a function of the 2D-MOT intensity cooling light. The intensities of the other beams were: $I_{3D}^{cooling} = 1.67 I_s$ per beam, $I_{3D}^{repumper} = 0.81 I_s$, $I_{push} = 7.32 I_s$, and $I_{ZS} = 25.73 I_s$.
Source: By the author.

It is important to mention that the expected behavior of the number of atoms as a function of the loading rate is a linear dependence as expressed by Equation (4.2.4), that can be further simplified for low densities at the initial loading process (linear part of the curve). In the case of the Bright-MOT, we see a linear behavior for some range of the loading rate values (intensities). For these curves, when the light intensity is low, then the loading rate is also low we see an "abrupt jump" from a value of low number of atoms to a high value. Since we have a loading rate of the order of 1×10^{10} atoms/s the stationary number of atoms is of the order of 10^9 and we expected it to increase further, but this is nor the case, then it seems like there are some limitations in the system with respect to the limiting number of atoms that can be captured in the Bright-MOT.

In the case of the Dark-SPOT, we see that this is improved and the behavior of the number of atoms in the Dark-SPOT MOT as a function of the loading rate is linear, which is the most expected situation. The loading rate curves for the Dark-SPOT MOT (Figure 4.3.6) has to be thought as a curve proportional to the real loading rate. This is because in the Dark-SPOT MOT the fluorescence comes only from atoms on the surface of the MOT where the repumper light is present. Thus, to measure the "real" number of atoms in the Dark-SPOT MOT it was used absorption images.

4.3.2 Experimental tips to align the Dark-SPOT

It is possible to send the Dark-SPOT beam co-propagating with the three trapping beams, but this may cause some experimental complications because it is hard to superimpose the three beams and coincide the Dark-SPOT of each beam in the center of the trap. Furthermore, the retro-reflected beams can send stray repumper light to the center. The same problem is present if the Dark-SPOT beam is sent just in the plane, for instance, the xy-plane. Even though this is less complicated, we wanted to simplify the setup. For this reason, we choose to send the Dark-SPOT beam only in one direction, that we chose to be y' (Figure 4.2.2). Figure 4.2.2 shows the dark-SPOT beam path and how this is combined with the trapping beam in the y'-direction using a polarizing cube.

In the first attempt to observe the Dark-SPOT, we realized that it is hard to align the retro-reflected Dark-SPOT beam exactly in the same position than the incident one, leading to stray repumper light into the MOT causing low efficiency. To avoid the stray light effect of the retro-reflected Dark-SPOT beam it was placed a polarizing cube between the last window and the retro-reflecting mirror in order to minimize the intensity of the Dark-SPOT beam coming back to the chamber (see Figure 4.2.2), then eliminating the retro-reflected Dark-SPOT beam, then we use the Dark-SPOT propagating just in one direction.

We use a CCD (charge-couple device) Stingray F-145 camera to better align the Dark-SPOT beam. We also use a probe beam in resonance with the repumper transition in order to see the absorption on the CCD. We align the beam onto the atoms and look at the shadow created in the beam due to the absorption. We try to get in the image as dark as possible, and at that point, we know that the Dark-SPOT is good enough to move forward in the next steps of the experiment. Also, it is possible to look at the fluorescence signal and try to decrease the signal when aligning, but it is recommended to look at the absorption in the CCD.

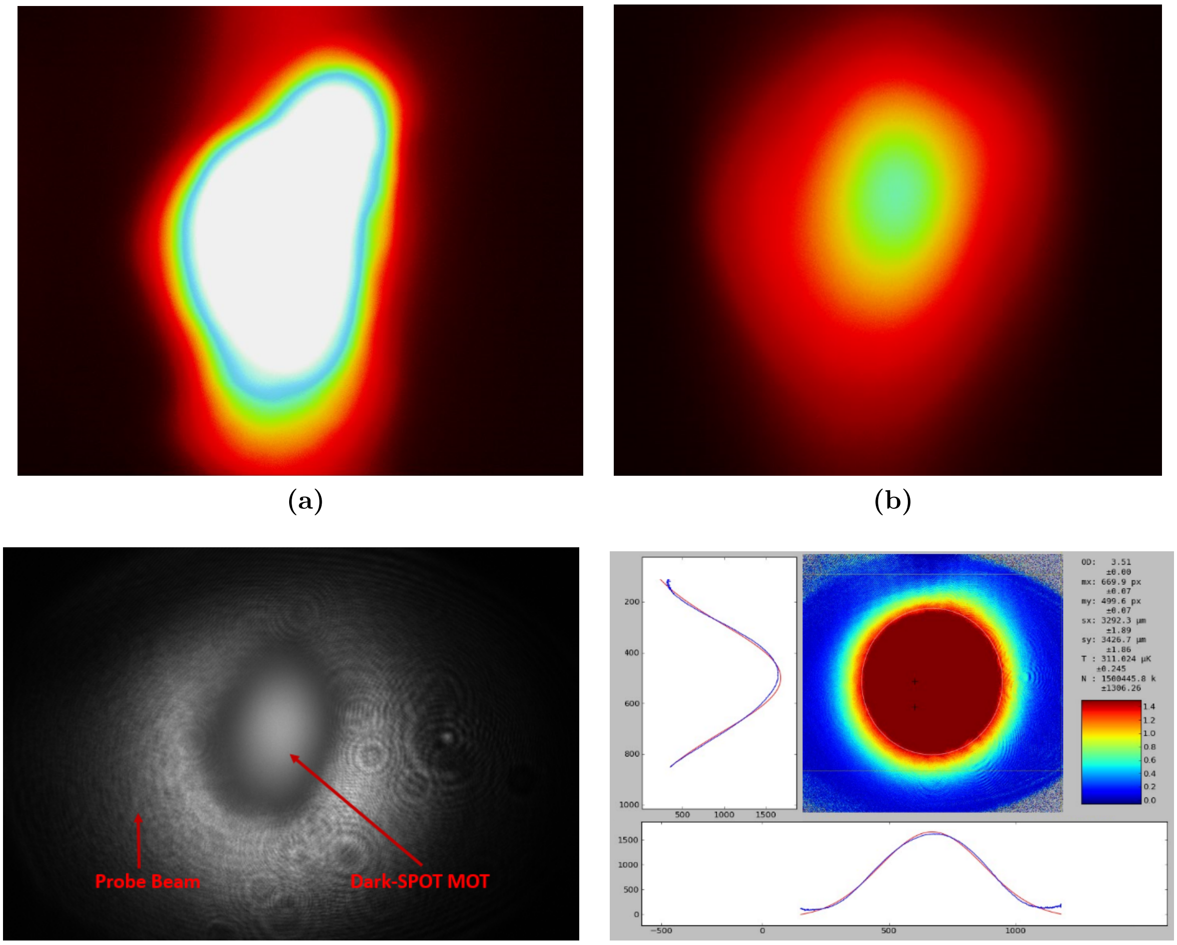
Probe Beam
Dark-SPOT MOT
OD: 3.51
±0.00
mx: 669.9 px
±0.07
my: 499.6 px
±0.07
sx: 3292.3 µm
±1.89
sy: 3426.7 µm
±1.86
T : 311.024 µK
±0.245
N : 1500445.8 k
±1306.26
1.4
1.2
1.0
0.8
0.6
0.4
0.2
0.0
200
400
600
800
1000
500
1000
1500
1500
1000
500
0
−500
0
500
1000

(a) **(b)**

(c) **(d)**

Figure 4.3.7 – (a) Bright-MOT. The MOT camera is left to saturate just to show the strong fluorescence of the atomic cloud. (b) The Dark-SPOT MOT enormously diminished the fluorescence of the atomic cloud because 99% of the atoms are in the dark state $|F = 1\rangle$. The fluorescence seen in the picture is mainly emitted by the atoms in the surface of the MOT, where the atoms interact with the cooling beam. (c) Absorption of the probe beam $(3^2S_{1/2}\,(|F = 1\rangle) \rightarrow 3^2P_{3/2}\,(|F' = 2\rangle))$. It is very helpful to align the Dark-SPOT looking at this picture, i.e. diminishing the fluorescence while aligning. And (d) shows the normalized absorption image (section 5.4) , clearly shown the high optical density of the Dark-SPOT MOT.

Source: By the author.

In the next chapter, I will present the subsequent stages required to obtain the BEC of sodium atoms. These stages will be described separately in order to discuss the working principle and experimental details for their realization.

Chapter 5

Route to quantum degeneracy of sodium atoms

In this chapter, I describe separately all the stages in the experimental sequence required for obtaining the Bose-Einstein condensation (BEC) of sodium atoms. All these stages are put together in the experimental sequence to pursuit the main goal, which is the following: *decrease the temperature and increase the phase-space density.* When the condition for the phase-space density is reached, the BEC transition is achieved.

In order to obtain a sample dense enough with a lower temperature than μK it is required the implementation of several processes of cooling and compression. The stages used in this thesis are: the magneto-optical trap (MOT), molasses (also called sub-Doppler cooling), and evaporative cooling in an optically plugged magnetic quadrupole trap (OPT). After this stages, the Bose-Einstein condensation can be observed with absorption image technique, which is the tool we use to performe the diagnosis of the cloud, i.e. to evaluate if the atomic cloud realized the transition to BEC or is just a thermal cloud. Clear signatures can be seen with the absorption images to determine if the cloud is in the classical or quantum regime.

Figure 5.0.1 shows the stages along the time in the experimental sequence to achieve the Bose-Einstein condensation.

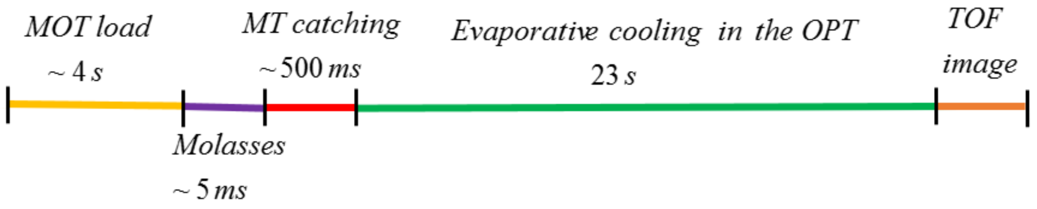

Figure 5.0.1 – Schematic diagram of the stages in the Bose-Einstein condensation process. Figure is not to scale.
Source: By the author.

5.1 Optical molasses and transfer to the magnetic trap

After the Dark-SPOT MOT has been loaded, the experimental sequence starts. When the atoms are in the Dark-SPOT MOT, that I will call just MOT from now on, the temperature is around $350\,\mu$K. These atoms need to be transferred to the MT to start the evaporative cooling process (section 5.3). Before transferring the atoms to the MT, a stage of optical molasses (sub-Doppler cooling) is realized in order to improve the efficiency of the transfer, otherwise, most of the atoms will be lost.

The molasses stage realized immediately after loading the MOT, decrease the temperature of the atomic cloud below the Doppler limit. It is important to recall particularly for sodium atoms, that many experiments in different groups do not realize the sub-Doppler cooling and transfer the atoms directly to the MT. (2, 48–50) This is done because in principle the Dark-SPOT MOT reach a sufficiently high density and low temperature and then the molasses stage does not improve further the system. On the other hand, other groups perform the molasses stage if the temperature of the atomic cloud in the MOT is not so low, and the sub-Doppler cooling can decrease the temperature in a considerable factor. In our case, the molasses stage is of fundamental importance and we obtain temperatures of approximately $100\,\mu$K, which is low enough to do a good transfer to the MT.

After loading the MOT, which takes around 4 s, the B-field is switched off and the cooling beams are further red-detuned to 60 MHz from the resonance. The intensity of the beams are reduced to $0.58 I_s$ (around 50% the value of the MOT intensity per beam) and this sub-Doppler cooling stage is realized during 5 ms.

Here, I summarize the working principle: when the detuning of the cooling beams is increased, these beams interact with faster atoms, cooling them further. Furthermore, an important effect that takes place is the Sisyphus cooling (or polarization gradient cooling). Because the three beam pairs are circularly polarized with opposite circulation, a spatial dependence potential is created by the polarized beams interfering and creating a standing wave. When an atom move to the maximum (“hill”) of the potential it losses kinetic energy, and if at this point the atom is optically pumped to the ground state (or the minimum, “bottom” of the potential) without gaining kinetic energy this leads to a reduction of its velocity.

Transfer to the MT

When the atoms are transferred to the MT some important aspects have to be considered in order to performe an efficient transfer or minimize losses and excessive heating of the atomic cloud. One important point is the position of the MOT with respect to the minimum of the MT. Due to unbalance of the MOT beam intensities, alignment, and polarization, the MOT can be in a different position that the minimum of the MT. This can harm the whole process of transfer and/or unnecessarily produce heating of the cloud. The difference between the MOT and the MT geometries is an important issue, the atom cloud in a MOT has some millimeters in diameter while the cloud in the MT is confined to around $500\,\mu$m and this also normally contribute to losses and heating of the cloud.

To ensure an efficient transfer to the MT a statistic process is realized. We observe the image of the atomic cloud in MT (section 5.4) and do some marks for referencing the position of the center of the cloud. After that, an *in-situ* image of the MOT is observed while adjusting the balance of the trapping beam intensities, light polarization, and compensation B-field. In this stage is worth to increase the MOT B-field gradient to see a smaller cloud and better identify the center of the MOT (see 4.2.3). After it is reached the best mode-matching of the MOT center with respect to the center of the MT, a dynamical optimization may be done. In this case, the experimental sequence is running and the transfer into the MT is evaluated observing the number of atoms and temperature of the cloud in the MT with evaporation to some RF frequency or just without any evaporation as will be explained in section 5.3. When the mode-matching condition is satisfied the transfer to the MT will be the first step to cool the atoms further to the condensation using evaporative cooling (section 5.3).

In conclusion, good mode-matching led to an efficient transfer from the MOT to the MT, and bad mode-matching will lead to atom losses in the transfer and excessive heating of the cloud. This is important because for realizing an efficient evaporative cooling we need to transfer the maximum number of atoms to the MT with less heating possible in the transfer. Then, in this way the runaway condition (section 5.3) is easier and faster to obtain.

Many experiments with atoms other than sodium need to realize a stage of MOT compression (C-MOT) (47) in order to increase the density of the cloud, then the molasses stage, and finally the optical pumping process. In our system, the C-MOT is not necessary due to the high densities reached with the Dark-SPOT MOT meaning that a C-MOT process does not help anymore to increase the density and could instead lead to heating (49). With respect to the optical pumping, the atoms in the MOT are equally distributed in the magnetic hyperfine states of the ground state $3^2S_{1/2}(F=1)$, namely $|m_F=1\rangle, |m_F=0\rangle, |m_F=-1\rangle$. Using optical pumping, most of the atoms populate a particular state, increasing the number of atoms in the MT. In the MT only low-field-seeking atoms can be trapped and in this case this correspond to the state $|F=1, m_F=-1\rangle$. In our case, we do not perform optical pumping stage and then the MT can capture only 1/3 (33.33%) of the total population, i.e., the atoms in $|F=1, m_F=-1\rangle$. Instead of this, we realized a pre-pumping stages. This consists just in turning off the repumper light, then only the cooling light is turned ON during 1 ms leading to a net transfer of all the atoms that were in the ground state $3^2S_{1/2}(F = 2)$ to the state $3^2S_{1/2}(F = 1)$. In our system, this pre-pumping stage improve a lot the number of atoms captured in the MT.

5.2 Optically plugged magnetic quadrupole trap

There are several schemes or configurations to magnetically trap the atoms for the realization of evaporative cooling in order to obtain the BEC (29). Also there is the possibility to transfer the atoms to a pure optical dipole trap to do the evaporation. In this PhD work, we choose the route of an optically plug magnetic trap (2, 48, 50, 51), which consists in a gradient magnetic field generated by a pair of coils in anti-Helmholtz configuration and a blue-tuned laser focused at the center of the trap to avoid Majorana losses as described in subsections 5.2.1 and 5.2.3. The goal of this section is to explain the basic elements of an optically plugged magnetic quadrupole trap in simple terms.

5.2.1 Principles of magnetic traps

When the atoms are cooled down to very low temperatures and the de Broglie wavelength is comparable with the dimensions of the particles, it is required a quantum mechanical description of the motion, but we can still go further with the predictions of the semiclassical considerations and still have a reasonable good description of the "behavior of the particles" immersed in the magnetic field (29) and know the efficiency of these traps. This means that although magnetic traps act on particles that are totally quantum objects, this kind of systems are well described using classical electromagnetic theory. (52)

The quadrupole magnetic trap is the simplest way to trap neutral atoms. It consists of a pair of coils in anti-Helmholtz configuration, as those used in the MOT, but using higher current and producing an order of magnitude higher magnetic field (B-field). This magnetic trap (MT) presents a zero at the center and increase linearly in all directions, as can be seen from

$$B = b'\sqrt{\rho^2 + 4z^2}, \tag{5.2.1}$$

where $\rho = x^2 + y^2$, and b' is the constant B-field gradient generated by the coils. As described in (29), this MT is neither harmonic nor central, thus the angular momentum is not conserved. (29)

A magnetic dipole moment $\vec{\mu}$ immerses in the B-field has energy (26)

$$V = -\vec{\mu} \cdot \vec{B}, \tag{5.2.2}$$

and for an atom in the state $|IJFM_F\rangle$, this corresponds to a Zeeman energy

$$V = g_F \mu_B M_F B, \tag{5.2.3}$$

Then the potential energy is given by

$$U_{quadrupole} = g_F \mu_B M_F b' \sqrt{\rho^2 + 4z^2}, \tag{5.2.4}$$

then, the force that the magnetic dipole experiences is given by

$$\vec{F} = -\nabla V = -g_F \mu_B M_F \nabla B. \tag{5.2.5}$$

For the trap be able to confine the atoms, the orientation of the magnetic moment $\vec{\mu}$ with respect to the B-field must be preserved as the atoms move inside the trap. If this is not the case the atoms may be expelled rather than confined. (29) This adiabatic interaction between the atomic moment $\vec{\mu}$ and the B-field requires that the atom move with low velocities. In regions where the B-field is small, the energy separation between the trapping and non-trapping states is small, increasing the probability of these states to mix, and then doing transitions to non-trapping states. Obviously, at low temperatures of the BEC experiments, this is particularly critical. Therefore, to determine the stability of a neutral atom trap is not sufficient to treat just the energy considerations that focus only on the trap depth, instead of these quantum state calculations and their consequences must also be considered. (29)

For the trap, we can find the stable circular orbits, of radius ρ, in the $z = 0$ plane using the classical relation for the radial (centripetal) force $\mu \nabla B = Mv^2/\rho$, where M is the mass of the atom, ρ the radius of the orbit where the atoms move,$v = \sqrt{\rho a}$ its velocity, and $a \equiv \mu \nabla B / M$ is the centripetal acceleration supplied by the field gradient (cylindrical coordinates are appropriate). As it is well known, the angular frequency of these orbits is given by $\omega_T = \sqrt{a/\rho}$, and for traps of few cm size and a few hundred Gauss depth, $a \sim 250\,\mathrm{m}/s^2$, and the fastest trappable atoms in circular orbits have $v \sim 1\,\mathrm{m/s}$ so $\omega_T/2\pi \sim 20\,\mathrm{Hz}$. The potential is anharmonic, having as a consequence that the orbital frequencies depend on the orbit size, but in general, atoms in lower energy orbits have higher frequencies. For the MT to work, the atomic magnetic moments must be oriented so that they are repelled from regions of strong field. For this reason, only certain magnetic hyperfine states can be trapped. The expression $\omega_Z = \omega_L \gg |dB/dt|/B$, give the condition for adiabatic motion, here $\omega_L = \mu B/\hbar = \mu_B g_F m_F B/\hbar$ is the Larmor precession rate in the field. For circular motion, $\omega_T = v/\rho$ is the orbital frequency, and since $v/\rho = |dB/dt|/B$ for a uniform field gradient, the adiabaticity condition is

$$\omega_L \gg \omega_T. \tag{5.2.6}$$

The adiabaticity condition can be easily calculated for the two-coil quadrupole trap: for circular orbits in the $z = 0$ plane we have $v = \sqrt{\rho a}$, the adiabatic condition for a practical trap ($A \sim 1\,\mathrm{T/m}$) requires $\rho \gg (\hbar^2/M^2 a)^{1/3} \sim 1\,\mu\mathrm{m}$ as well as $v \gg (\hbar a/M)^{1/3} \sim 1\,\mathrm{cm/s}$. (29) Note that violation of these conditions (i.e., $v \sim 1\,\mathrm{cm/s}$ in a trap with $A \sim 1\,\mathrm{T/m}$) results in the onset of quantum dynamics for the motion (de Broglie wavelength $\approx$ orbit size). Using the arguments given so far, we can fin the radius of the Majorana hole approximating the region around this hole as being spherical as

$$\rho_{Maj} = \sqrt{\frac{2v\hbar}{\mu_B m_F g_F B'}}. \tag{5.2.7}$$

Because the non-adiabatic region of the trap is small (less than $10^{-18}\,m^3$ compared with typical sizes of $\sim 2\,\mathrm{cm}$ corresponding to $10^{-5}\,m^3$), nearly all the orbits of most of the atoms are restricted to regions where they are adiabatic. At laboratory vacuum chamber pressures of typically 10^{-11} Torr, the mean free time between collisions that can eject trapped atoms is $\sim 2\,\mathrm{min}$, so the transitions caused by non-adiabatic motion are not likely to be observable in atoms that are optically cooled. However, evaporative cooling reduces the average total energy of a trapped sample sufficiently that the orbits are confined to regions near the origin so such losses dominate, and several schemes have been developed to prevent such losses from non-adiabatic transitions. The consequence of not satisfying the adiabatic condition (5.2.6) is the presence of Majorana losses. (53–56) To circumvent this, different schemes have been implemented from the beginning of condensation experiments. To mention the one of the most common ones is the Time-Orbiting Potential (TOP) trap (1, 57), used in the production of the first reported BEC, which uses two additional orthogonal sets of coils driven with out-of-phase ac currents to add a slowly rotating uniform field that moves the point of zero field continuously.

The Ioffe-Pritchard trap (26, 29, 58) offers another solution to the loss problem. In this trap the minimum value of B never vanishes. This trap has the flexibility of being able to adjust the straight and end-coil currents, in order to adjust the position of the zero of the B-field, but is a shallower trap with an elongated trapping volume. (29, 59)

One of these variations is the replacement of wires and currents by permanent magnets. (60) This trap has the advantage of being compact and reliable in the sense that you avoid problems like heating and then avoid adding experimental complications as cooling systems for the coils, but suffers from the inability to change or turn off the fields. The second variation is the replacement of each of the four straight currents by two parallel, separated loops, making eight additional coils along with the end coils, for a total of ten. (61) This "butterfly" or "cloverleaf" trap offers more complete optical access to its interior.

Another configuration is the Optically Plug Quadrupole Magnetic Trap (OPT), firstly used by Ketterle et al. (2) for producing the first Bose-Einstein condensate of ^{23}Na atoms in 1995. This is the configuration we use in our work and is explained in more details in section. 5.2.3

5.2.2 Our coils design

The coils constructed and described in this subsection, are used to produce the MOT quadrupole B-field and the OPT. These coils are set in anti-Helmholtz configuration. We used a copper wire of 2.18 mmdiameter wound in a reel of 88 mmouter diameter and 50 mm high which is remove after the process of winding. To improve the thermal conduction we use a glue Epoxy "Duralco 132" between each layer, this helps to dissipate the heat in the coils. In total, the coils have 10 layers of 16 winds each, then the final coils have internal and external diameter of 40.4 mm and 62.2 mm. The coils are immersed in a cylinder-like structure made of Nylon in which is possible to circulate water at a pressure of $\sim$ 25 psi at a temperature of 12 °C to cool down the coils. This is very important in order to avoid the excessive change in the resistance of the coils due to heating and hence diminishing the B-field generated. As source of current we use a Delta Elektronika SM3300-SERIES, which is able to supply a current up to 110 A. The measured resistances of the coils were of 0.265 Ω and 0.254 Ω,which represent a variation less than 8% of the expected one.

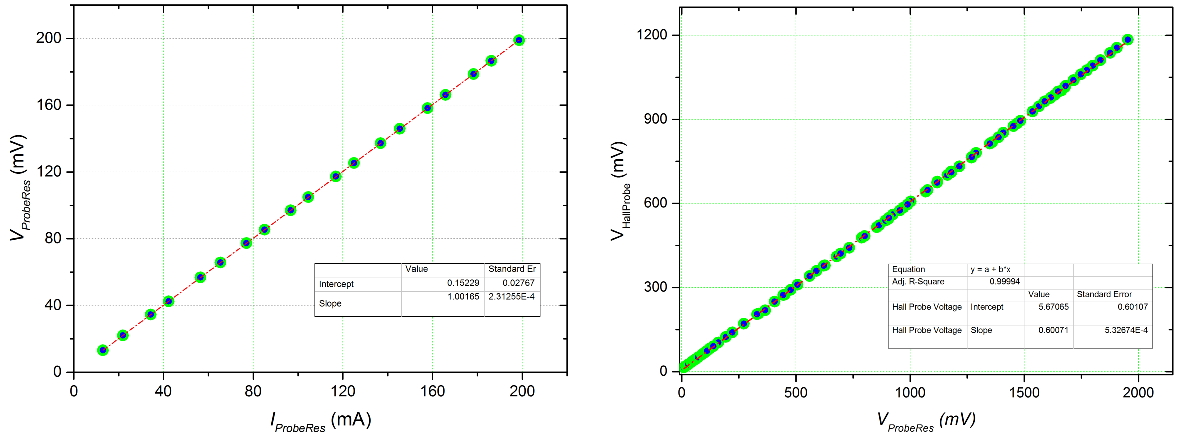

(a) (b)

Figure 5.2.1 – Calibration of the Hall probe used to measured the quadrupole magnetic field.

Source: By the author.

To measure the resistance of the quadrupole coils it was used a calibrated precision resistance (probe resistance, WH5 1RO 5%) and a high precision power supply. Before measuring the resistance of the quadrupole coils it was calibrated the probe resistance. To do this, the probe resistance was place on a heat sink and the current and voltage through it was measured using a high precision multimeter. The voltage ε of the power supply was varied, and thus with the value of the current and voltage through the probe resistance we can calculate the value of this resistance in a very precise way using the

Ohm law ($V_{ProbeRes} = R_{probe}I_{ProbeRes}$), as shown in Figure 5.2.1a and given a value of $(1.0017 \pm 0.0002)\,\Omega$.

Thus, with the probe resistance in series with each coil separately we measured the resistance of the coils. Varying the current of a source of current, measuring the voltage through the resistance (to calculate the current that circulate through the coils using the Ohm law), and measuring the voltage through the coil, we can determine the resistance of each coil. Figure 5.2.2 shows the curves of voltage vs current for each coil to compute the resistances.

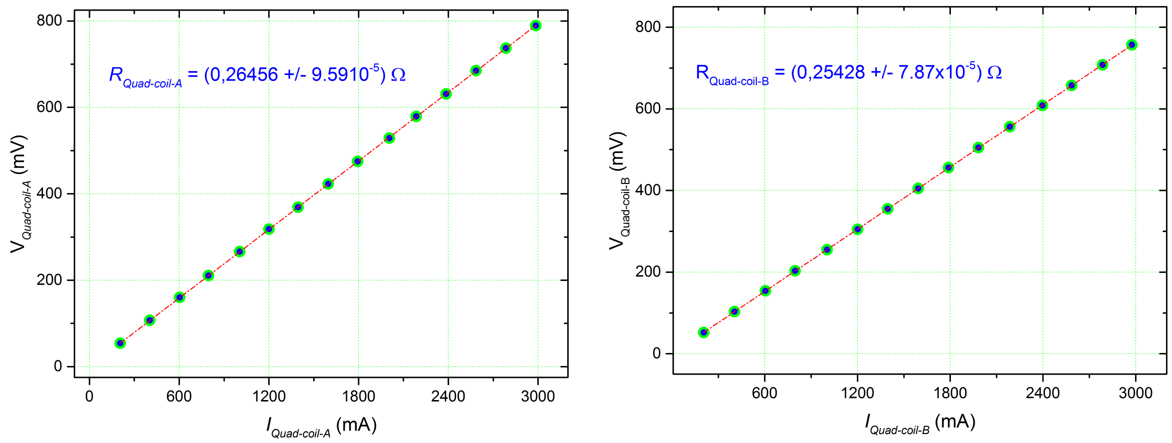

(a) **(b)**

Figure 5.2.2 – Voltage vs current circulating through the quadrupole coils for obtaining the resistance of both coils separately, A and B. A source of precision and a high stable source was used.

Source: By the author.

To calibrate the Hall probe (sensor CSA-1V Sentron), used to measure the magnetic field, it was used a solenoid of 451 turns with a length of (26.00 ± 0.05) cm. The solenoid and the probe resistance were set in series and fed by the high precision power supply. To measure the current circulating through the solenoid it was applied the Ohm law to the probe resistance. Thus, varying the voltage ε of the power supply and measuring the current through the solenoid, and having the voltage measured by the Hall probe, it is easy to find the relation between the magnetic field generated by the solenoid and the voltage measured by the Hall probe. The linear relation between the voltage in the probe resistance and the voltage measured by the Hall probe can be given as $V_{HallProbe} = \alpha V_{ProbeRes} + \kappa$, and from the Ampère law the magnetic field inside a solenoid is given by

$$B = \frac{\mu_0 N}{L} I = \frac{\mu_0 N}{L}\frac{V_{ProbeRes}}{R_{Probe}} = \beta\left(V_{HallProbe} - \kappa\right), \tag{5.2.8}$$

where $\beta = \frac{\mu_0 N}{R_{Probe} L \alpha}$. With $\mu_0 = 4\pi \times 10^{-7}\,\mathrm{N}A^2$, $N = (451 \pm 2)$ turns, $L = (0.2600 \pm 0.0005)$ m, $R_{Probe} = (1.0017 \pm 0.0002)\,\Omega$, and from Figure 5.2.1b $\alpha = 0.6007 \pm 0.0005$, and $\kappa = (5.7 \pm 0.6)$ mV, it is obtained $\beta = (0.0362 \pm 0.0003)$ G/mV. Thus, the magnetic field is given by

$$B = [(0.0362 \pm 0.0003)\,\mathrm{G/mV}]\, V_{HallProbe} - (0.20 \pm 0.02)\,\mathrm{Gaus}.$$

It is worth recall that for each measurement of $V_{HallProbe}$ it was subtracted the local offset $V_{offset}(local)$ (background magnetic field).

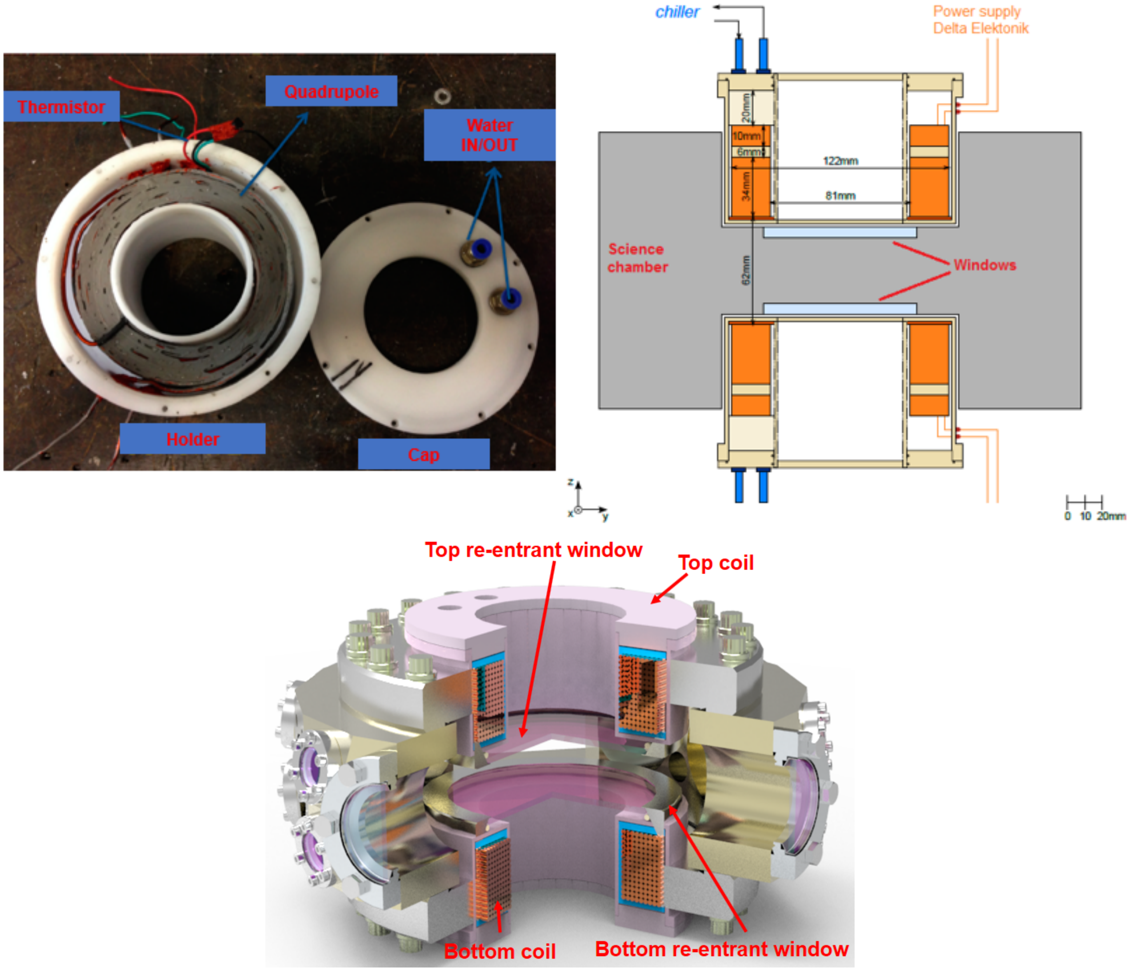
Thermistor
Quadrupole
Water IN/OUT
Holder
Cap
chiller
Power supply
Delta Elektonik
20mm
10mm
6mm
34mm
122mm
81mm
Science chamber
Windows
62mm
z
x
y
0 10 20mm
Top re-entrant window
Top coil
Bottom coil
Bottom re-entrant window

Figure 5.2.3 – Coils in the holder support and installed on the science chamber. The vertical windows are deeper than the other ones in order to be nearer to the atoms, in this way the needed current to create high the magnetic field gradient is smaller. Also, this setup allows good optical access in the $z-$axis.

Source: By the author.

As it is shown in Figure 5.2.3 (also described in chapter 3) the vertical windows of the science chamber has a geometry that allows to go inside the science chamber and place the coils very near to the atoms. The distance between the glass and the center of the chamber (where the atoms will be confined) is 3 cm, this is advantageous in order to minimize the current we need to supply for obtaining a high B-field in the desired region. The separation between the coils is 62 mm, then the current needed for producing the B-field for the MT is 46.90 A and the B-field gradient is of 302 G/cm. With this value of current the dissipated power is ~ 480 W.

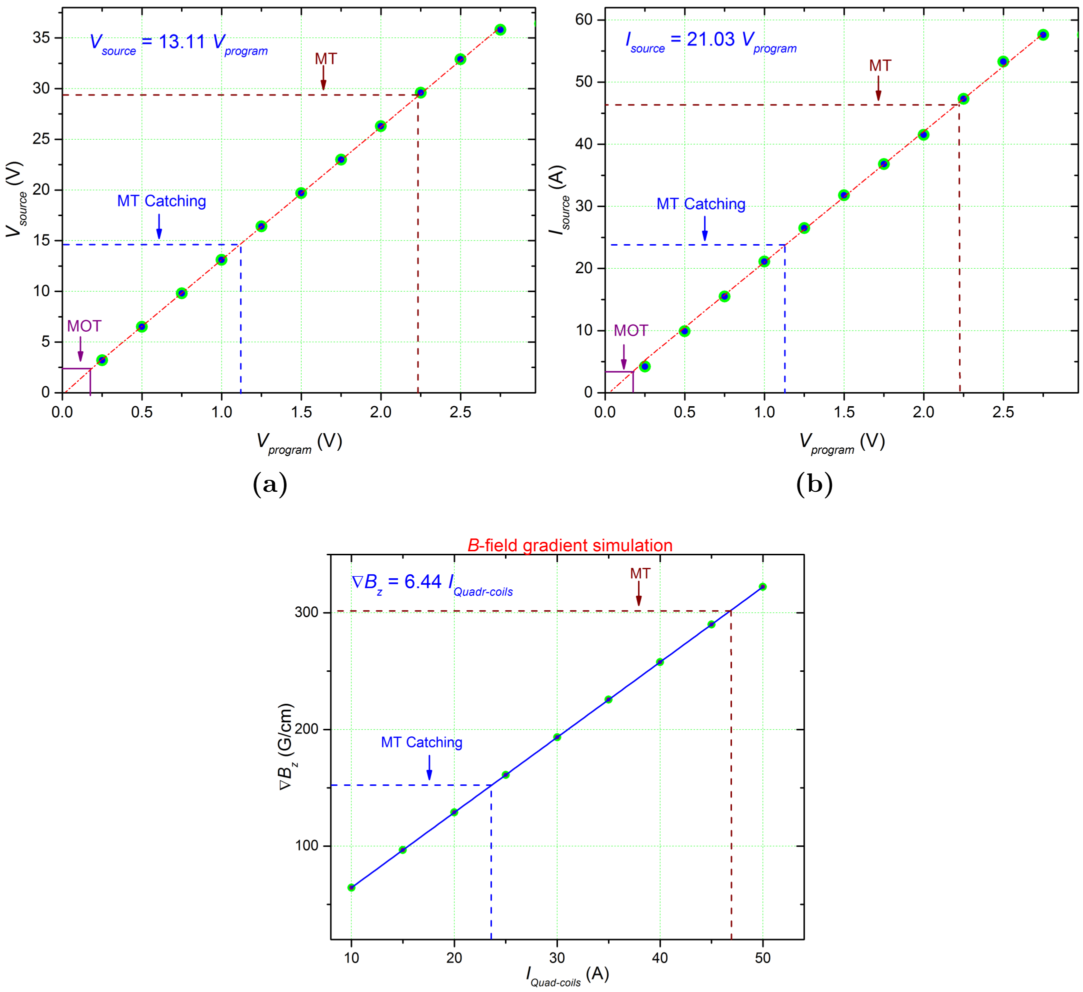

(a) **(b)**

(c)

Figure 5.2.4 – Curves showing the convertion between the values used in the program of the control system the real values of voltage and current provided to the power supply, then to the quadrupole coils. In (c) it is shown the simulated B-field gradient in the z-direction as a function of the current. For the magnetic trap it is used 46.90 A which represents a B-field gradient of 302 G/cm.

Source: By the author.

The magnetic field was calibrated in order to know the relation between the voltage given by the control system, through the National Instruments Boards (using an analogical channel), and the voltage and current the of the source of current. Figure 5.2.4 shows this calibration, giving the relation between the voltage set in the control system and the voltage and current of the source, which are the ultimate values provided to the quadrupole coils. In Figure 5.2.4c, it is shown the simulation of the B-field gradient in the z-axis as a function of the current in the quadrupole coils. For the magnetic trap, it is used 46.90 A which represents a B-field gradient of 302 G/cm.

Figure 5.2.5 shows the estimated B-field and that generated experimentally by the coils along its axis (z-axis) using 1.2 A.

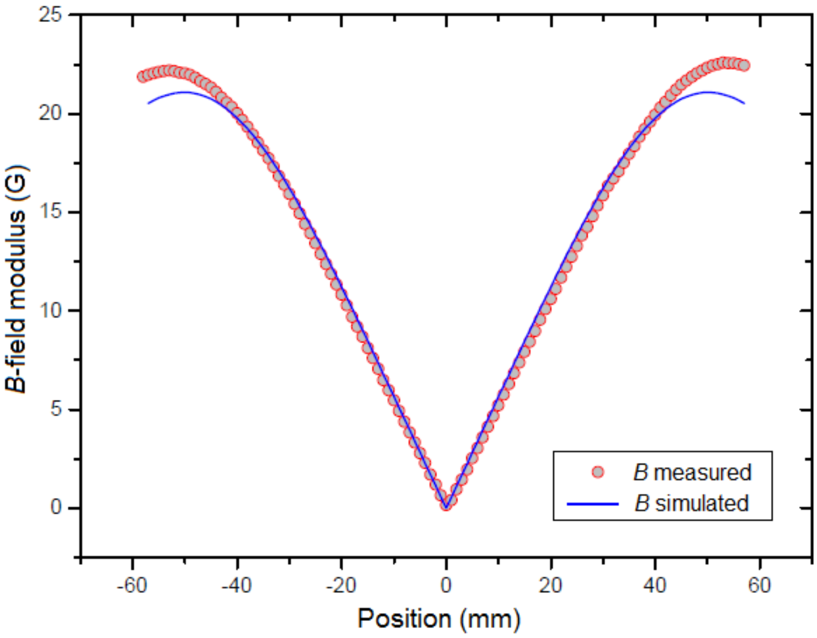

Figure 5.2.5 – Modulus of the magnetic field generated for the quadrupole coils. Around the center of the trap the $B-$field gradient is constant.
Source: By the author.

An important point about the magnetic field is the time it can be switch on and off. This is crucial because if, for instance, the process of turning off the coils is large, there will be a residual magnetic field which certainly will introduce an external perturbation on the atoms at the time they are suppose to be free. To do the fast switching on/off of the B-field, it is used an IGBT (Semikron SKM150GAR12T4) circuit connected in series with the quadrupole coils. The control of the current for switching on/off is made directly to the gate channel of the IGBT, instead of the power supply. The current in the coils was monitored using a current transducer IT 200-S Ultrastab (LEM) and the B-field by the calibrated Hall probe. Figure 5.2.6 presents the curves for the process of switching on/off of the current in the coils.

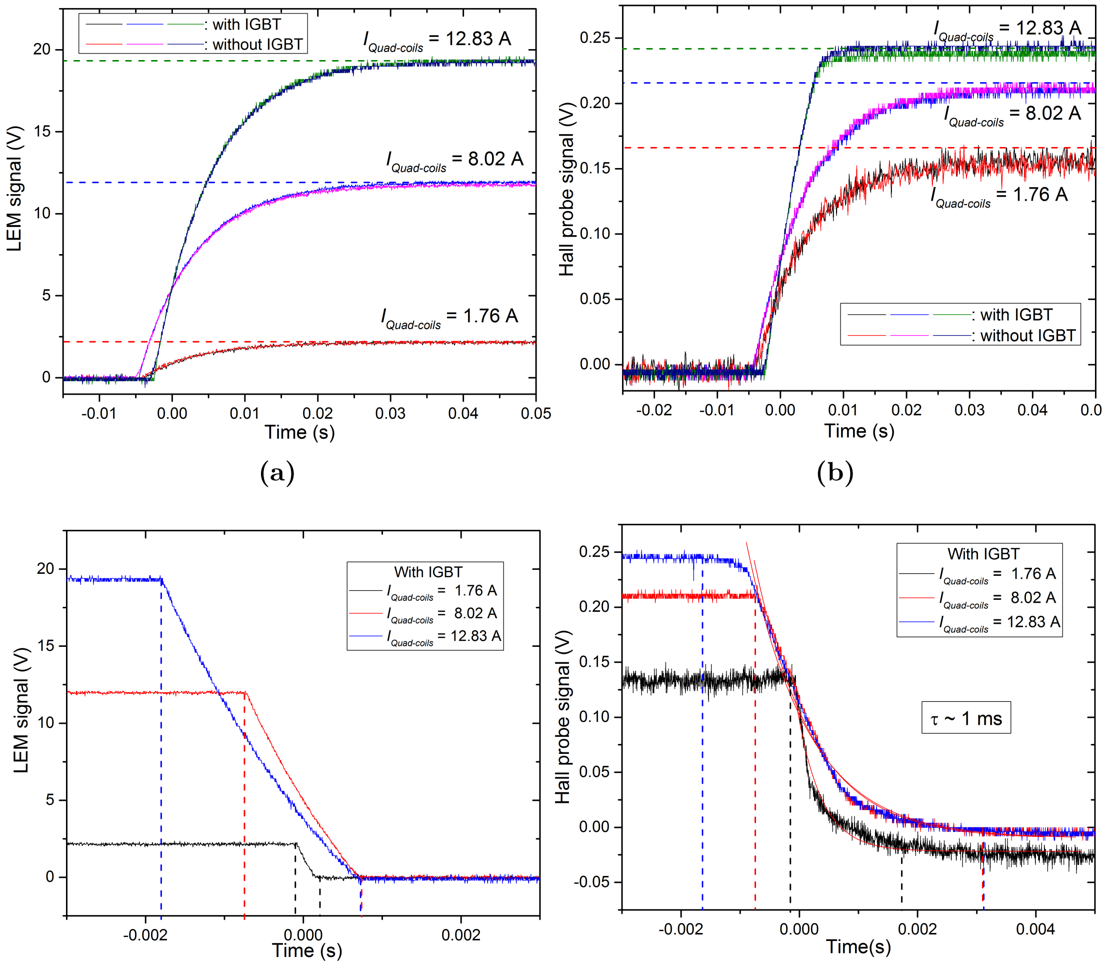

(a) (b)

(c) (d)

Figure 5.2.6 – (a) and (b) show the process of switching on the current from the power supply. For different currents it was monitored the time it takes to turn off comparing both situations: when the control is made using IGBT and when it is not. It is possible to see that there is no significative difference when using or not the IGBT when switching on the magnetic current and B-field. In (c) and (d) it is shown the big difference in turning off the current in the coils (consequently the B-field) when the IGBT is used. The corresponding time for the B-field to fall to the value $1/e$ is $\tau \sim 1\,\mathrm{ms}$, which is fast enough for this setup.

Source: By the author.

To test the cooling system of the quadrupole coils, water circulating through the Nylon case at a temperature of 14°C and a pressure of 78 psi, two kind of measurements were made.

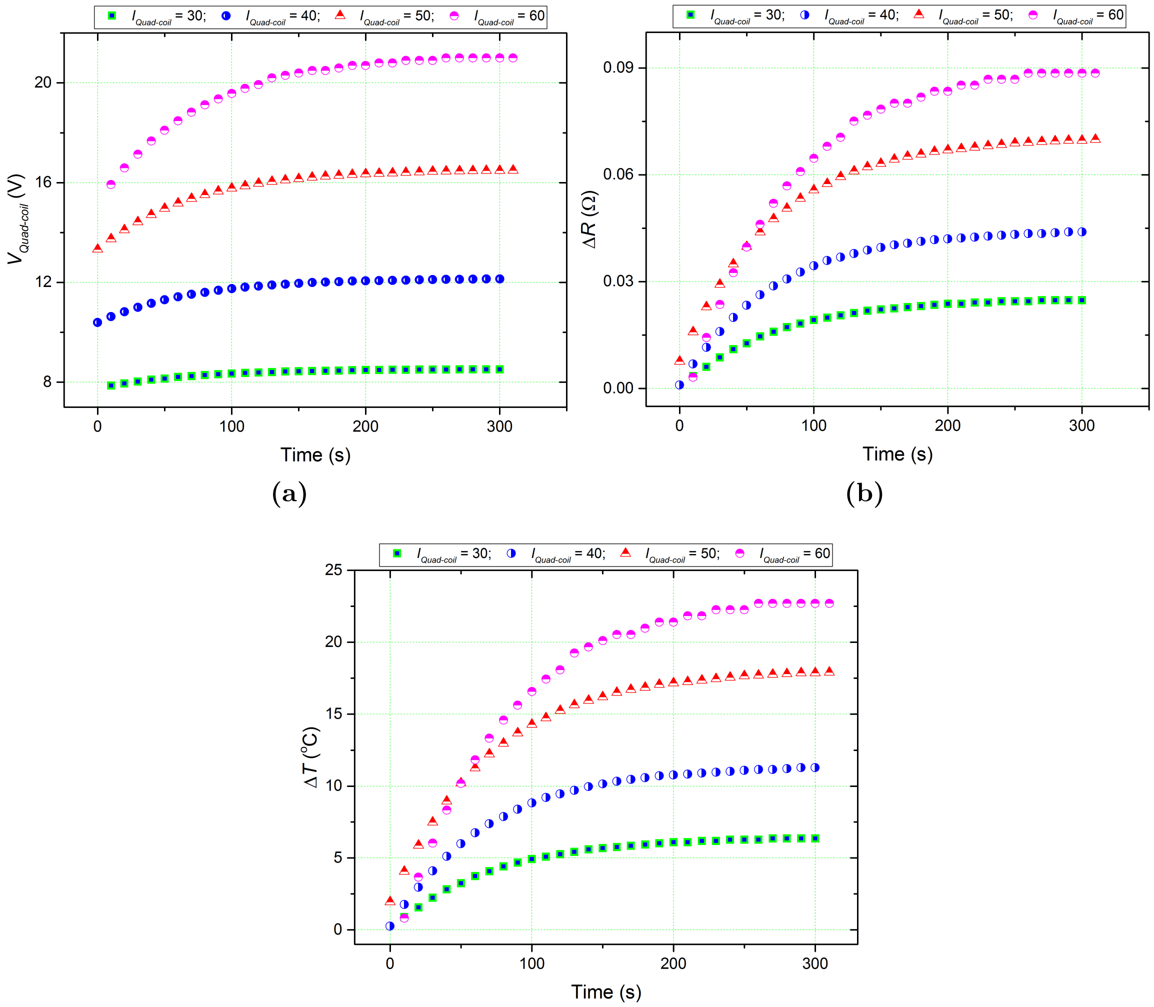

(a) (b)

(c)

Figure 5.2.7 – Test of the cooling system of the coils. In (a) we can see the variation of the voltage through the coils as a function of time for different currents. The variation of the voltage is due to the variation of the resistance as a consequence of the heating. In (b) the variation in the resistance is calculated from (a) using the Ohm law. Then in (c), it is plotted the variation in temperature of the Nylon case.

Source: By the author.

1) *Continuous situation*: For a fixed value of the current, the voltage through the coil was monitored during 6 min approximately. Measuring the voltage variation through the coil (Figure 5.2.7a) it was obtained the variation of the resistance as a function of time as shown in Figure 5.2.7b. The resistance as a function of the temperature is given by

$$R = R_{20°\mathrm{C}}\left[1 + \alpha_{20°\mathrm{C}}\left(T - 20\right)\right], \tag{5.2.9}$$

where $R_{20°\mathrm{C}} = \frac{L}{A}\rho_{20°\mathrm{C}}$ is the resistance at $T = 20°\mathrm{C}$, L is the wire length, A is the area cross-section of the wire, $\rho_{20°\mathrm{C}} = 1.72 \times 10^{-8}\,\Omega\mathrm{m}$ is the electrical resistivity, and $\alpha_{20°\mathrm{C}} = 3.9 \times 10^{-3}$ is the thermal coefficient of the copper. The variation of the resistance is then given by

$$\Delta R(T) = R(T) - R(T_0) = R_{20°\mathrm{C}}\alpha_{20°\mathrm{C}}\left(T - T_0\right). \tag{5.2.10}$$

For 60 A it is possible to see a considerable heating, representing a change in the resistance of approximately 0.08 %, which is still low and enough to realize the experimental sequence. The temperature was measured using two temperature sensors LM35 (calibration= 10 mV/°C) placed in the external surface of the Nylon case.

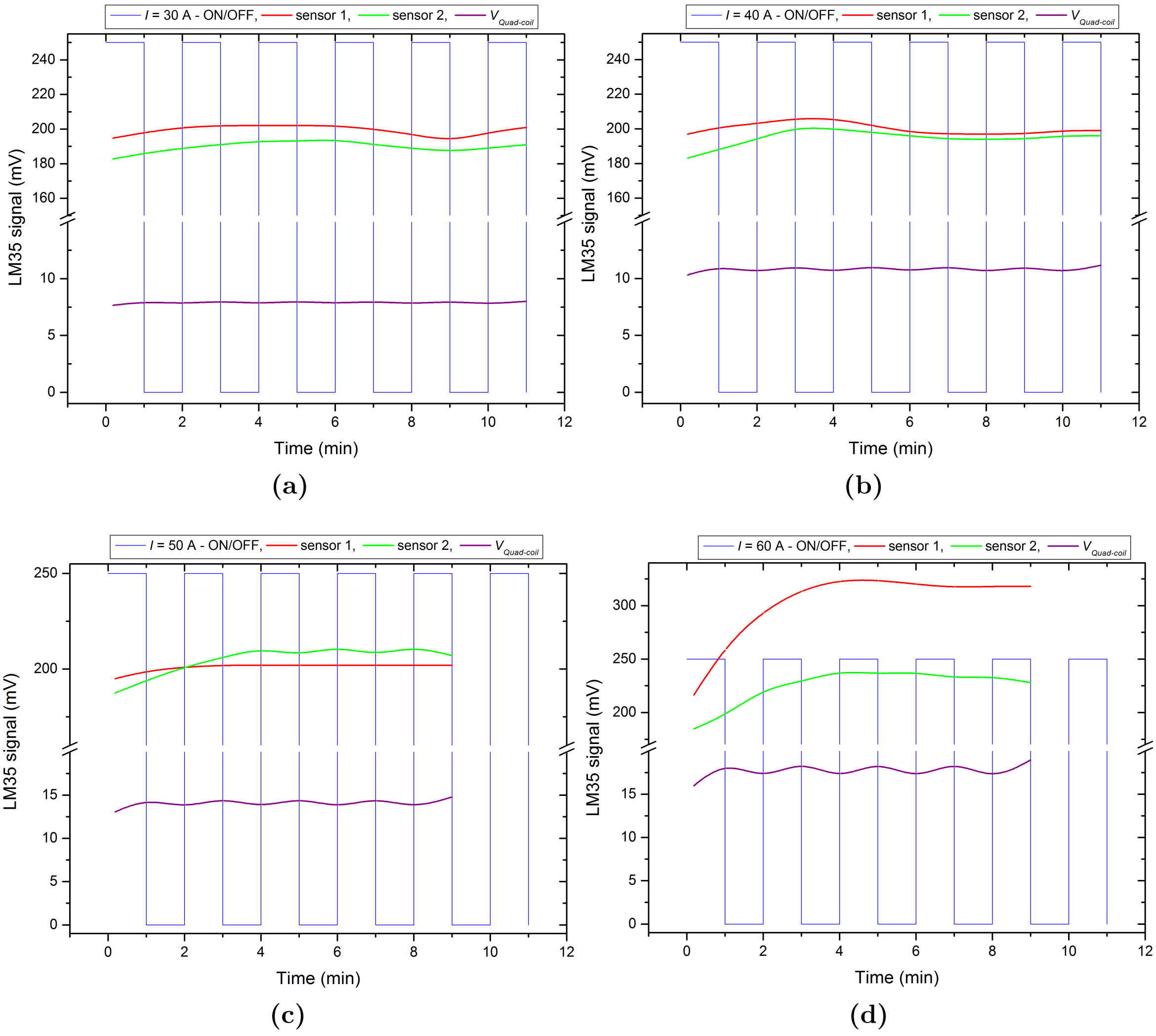

(a) (b)

(c) (d)

Figure 5.2.8 – Test of the cooling system of the coils simulating an experimental sequence. The current is made to circulate during 1 min and then switched off for other 1 min. This this very similar o the real experimental sequence, and give information about the capacity to maintain the temperature at a constant value, which is very important to hold the resistance of the coils the same, then the B-field is always the same.

Source: By the author.

1) *Cyclical*: For each current, the voltage variation was measured by cycles of 1 min ON and 1 min OFF. This is more similar to the real experimental sequence, were the coils are switched ON for approximately 1 min and then switched OFF for approximately 1 min from the production of one BEC and the subsequent production of the next BEC. From Figure 5.2.8 it is possible to observe that for all the currents a stable situation is reached. In our experimental sequence it is used a current of 46.90 A which is smaller than the triangle point curve that reach a stable situation very fast, then we can conclude that the cooling system for the coils is efficient enough in order to realize the MT with a reproducible value of current, and then B-field, in each run.

This system has another pair of coils for producing a magnetic field that will supply a B-field able to compensate the gravity to levitate the atoms along some times in the experiment. They have 10 layers of 6 turns each one and are installed above the quadrupole coils. In this work we don´t use this coils for this purpose but as compensation coils in the z-axis. In addition to this z-axis compensation coils we use also compensation coils for each direction (x and y) in order to produce a compensation B-field that allows to adjust and optimize the zero B-field position. This is important because magnetic force and the radiation force have to match, which is critical for realizing the molasses stage and transfer to the MT (see section 5.1).

5.2.3 Principles of an OPT

Atoms in presence of a laser field experience a modification in their potential, this phenomenon is known as AC Stark Shift. (26) This effect takes place because the electric field of the light ($\vec{E}$) induces an atomic oscillating dipole moment ($\vec{p}$) with frequency equal to that of the driving field. Thus, this induced dipole moment can interact itself with the electric field of the light producing a potential energy that vary in space (26) given by

$$U_{dip} = -\frac{3\pi c^2}{2\omega_0^3}\left(\frac{\Gamma}{\omega_0 - \omega} + \frac{\Gamma}{\omega_0 + \omega}\right) I\left(r\right), \tag{5.2.11}$$

where ω_0 is the resonant atomic transition, $I\left(r\right)$ is the intensity of the laser, and Γ is the linewidth of the excited state. In the case of a Gaussian beam propagating along the $\hat{x}$-direction, the intensity profile is given by

$$I\left(\vec{r}\right) = I\left(r, x\right) = \frac{2P}{w_0^2}\frac{1}{1 + \left(x/x_R\right)^2} exp\left[-\frac{2r^2}{w_0^2}\frac{1}{1 + \left(x/x_R\right)^2}\right], \tag{5.2.12}$$

where P is the laser power, $x_R = \pi w_0^2/\lambda$ is the Rayleigh length, and $r = \sqrt{y^2 + z^2}$.

When $\omega > \omega_0$ (blue detuned laser), the atoms will be repelled from high intensities of the laser beam. If $\omega < \omega_0$ the atoms will be attracted to to the high intensity area of the laser beam (red detuned laser). Therefore, a blue detuned laser beam shining in the

Majorana region can effectively push the atoms away from this hole and then Majorana transitions losses.

Commonly, the laser beam is tightly focused in the center of the MT where the magnetic field is zero (Majorana hole), to produce barriers of the order of $100\,\mu$K, which are greater than the average energy of the atoms in the trap at temperatures ($T \approx 20\,\mu$K) when the Majorana losses are significant. In this way the OPT takes the advantages of a tight confinement of the quadrupole trap and remove the drawback of this traps with respect to Majorana losses with the presence of the plug laser.

Then, the total potential of the OPT is given by the combination of the magnetic potential generated by the quadrupole ($U_B\left(\vec{r}\right)$), the dipole potential generated by the plug laser $U_D\left(\vec{r}\right)$, and the gravity, thus we express this total potential as (51)

$$U_{OPT}\left(\vec{r}\right) = U_B\left(\vec{r}\right) + U_D\left(\vec{r}\right) + mgz. \tag{5.2.13}$$

In our configuration we define the symmetry axis of the coils as being the z-axis, and the propagation of the plug beam in the $\hat{x}$-direction, as shown in Figure 5.2.11. Several cases have been discussed in the literature, as for instance, for the case of the plug beam propagating in the same direction as the symmetry axis (z-axis) of the coils (48, 51), and in the case we consider here (51) where the plug beam propagates in the $\hat{x}$-direction. In both cases, the plug beam creates a ring shape potential (48) when the beam profile plug is perfectly Gaussian. When the plug beam is slightly deviated from the perfect Gaussian profile in the wings, like an elliptical profile, a double well potential is predominantly generated (48). It is also possible, as demonstrated by M. Heo et al. (50), that a slightly misalignment of the plug beam can lead to the production of a single well potential, leading to a single BEC. In our case of a OPT, a blue detuned laser ($\Delta = \omega - \omega_0 > 0$), is focused and aligned passing through the center of the quadrupolar magnetic trap (MT), being the resultant potential given by sum or contribution of the magnetic and optical potential, which can be written as

$$U_{OPT} = \frac{\mu B'}{2}\sqrt{x^2 + y^2 + 4z^2} + \frac{U_0}{1 + \left(x/x_R\right)^2} exp\left[-\frac{2r^2}{w_0^2}\frac{1}{1 + \left(x/x_R\right)^2}\right] - mgz, \tag{5.2.14}$$

where $U_0 = \frac{3c^2\Gamma P}{\omega_0^3 w_0^2 \Delta}$ is the deep of the optical potential, and $r = \sqrt{y^2 + z^2}$. Figure 5.2.9 shows the potential generated using equation (5.2.14) along x-, y- and z-axis for $B' = 200\,\mathrm{G/cm}$, $P = 7\,\mathrm{W}$, $\lambda_{plug} = 532\,\mathrm{nm}$, and $w_0 = 30\,\mu\mathrm{m}$.

Around the minimum $y = y_{\text{min}}$, shown in Figure 5.2.9, the potential can be approximated by a harmonic potential with frequencies given by

$$\begin{aligned}\omega_x &= \sqrt{\frac{g_F m_F \mu_B B'}{2 m y_{\text{min}}}}, \\ \omega_y &= \omega_x \sqrt{\frac{4 y_{\text{min}}^2}{w_0^2} - 1} \\ \omega_z &= \omega_x \sqrt{3}\end{aligned} \tag{5.2.15}$$

Using the parameters of Figure 5.2.9 we found the frequencies to be

$$f_x = 255\,\text{Hz},\; f_y = 761\,\text{Hz},\; f_z = 442\,\text{Hz}. \tag{5.2.16}$$

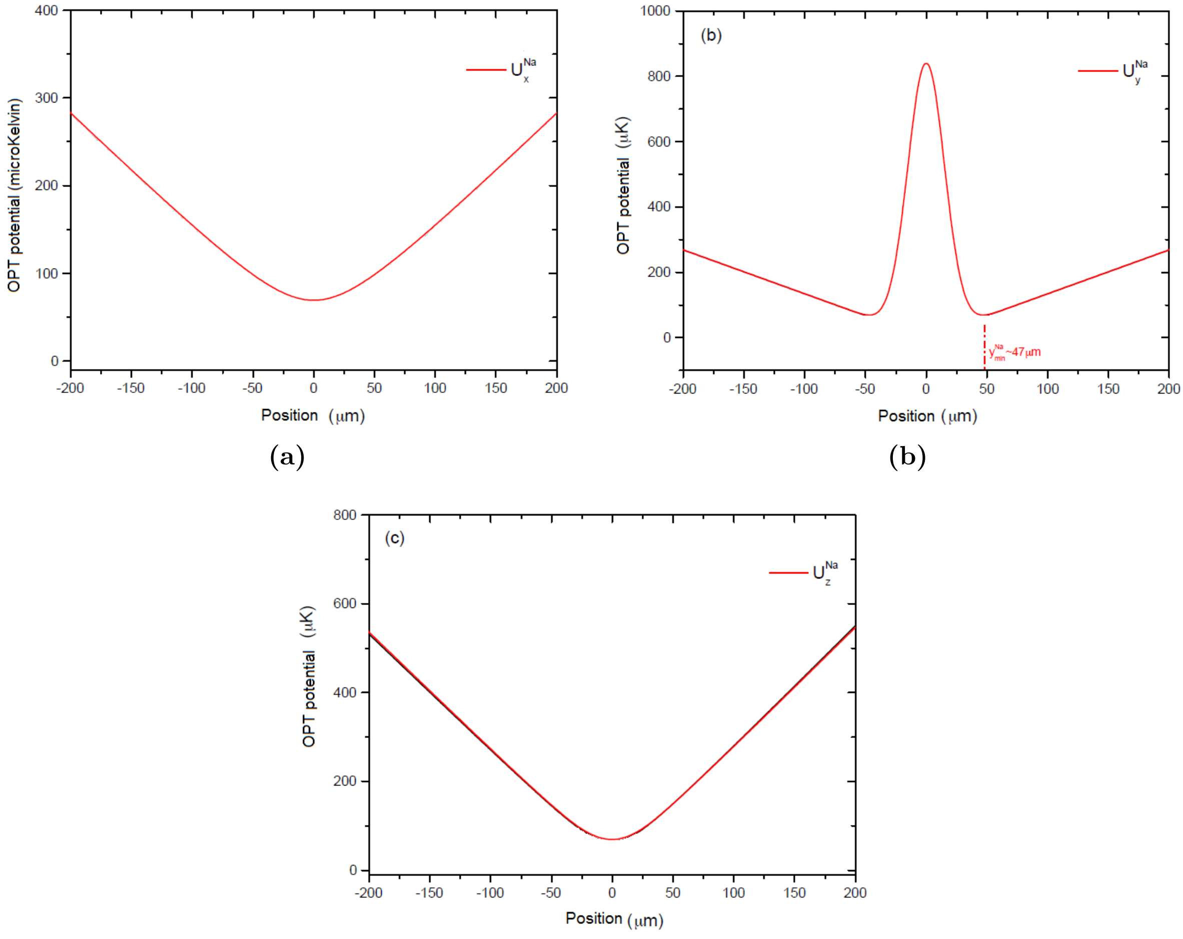

(a) (b)

(c)

Figure 5.2.9 – OPT potential along the three axis.
Source: By the author.

It is important to take into account that the plug laser beam waist has to be bigger than the Majorana radius ($w_0 > \rho_{Maj}$) to satisfy that the optical barrier in the position ρ_{Maj} be at least 70% its peak value. In this way, only the most energetic atoms can overcome the optical barrier and eventually go inside the region of losses, where this atoms are not strongly susceptible. A second important point is that the difference between the optical potential (U_0) and the minimum potential of the OPT, $U_{\text{plug}}\,(0,\, y_{\text{min}},\, 0)$, has to be enough to expel the atoms while Majorana losses are still not relevant. For instance, for sodium atoms at $40\,\mu$K the lifetime in the quadrupole MT is about 60 s,then, optical potentials around $400\,\mu$K would be enough to push away from the Majorana region all the atoms of the cloud, even the most energetic. As third point, it is important to recall the difficulty in aligning the plug laser beam in the center of the MT as the waist of the beam is reduced.

5.2.4 Experimental configuration of our OPT

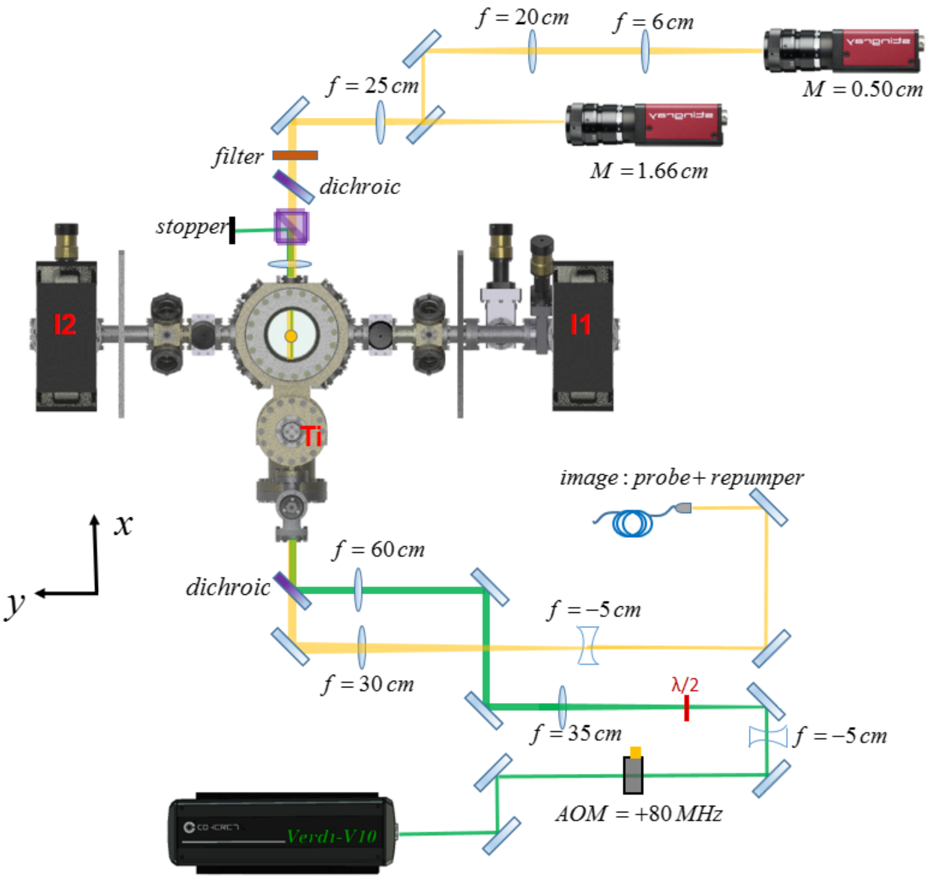
f = 20 cm
f = 6 cm
M = 0.50 cm
f = 25 cm
M = 1.66 cm
filter
dichroic
stopper
I2
I1
Ti
image : probe + repumper
x
y
f = 60 cm
dichroic
f = −5 cm
f = 30 cm
λ/2
f = 35 cm
f = −5 cm
AOM = +80 MHz
Verdi-V10

Figure 5.2.10 – The plug beam is focused in the center of the chamber and the center of the MT. The plug beam propagates along the same path the image beam, being possible to obtain the image of the plug in the CCD camera. This helps in the alignment of the plug.
Source: By the author.

The final configuration of our OPT is shown in Figure 5.2.10, and the superposition of the plug beam with the magnetic field in the science chamber is shown in Figure 5.2.11.

As explained before, the OPT consists of quadrupole magnetic field with a blue-detuned laser focused near the center of the quadrupole, where the magnetic field is zero. The production of the quadrupole magnetic field is explained in section 5.2.2. For the production of the plug beam, we use a Coherent Verdi V10 able to produce 10 W at 532 nm.

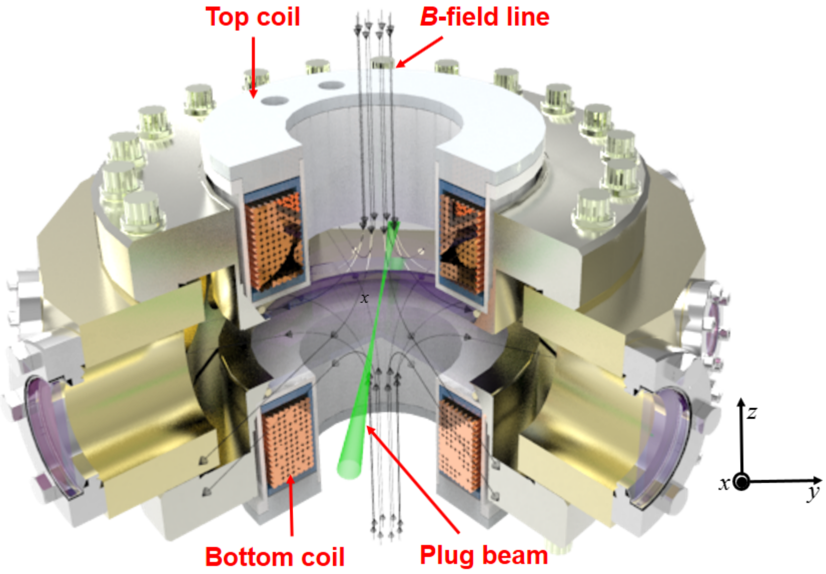

Figure 5.2.11 – Principle of the optically plugged quadrupole trap. The plug beam propagates along the x-direction.
Source: By the author.

The plug beam passes through a 80 MHz acousto-optic modulator (AOM) (Westerntek Model 3080-125) necessary to switch off the plug beam in a very short time. Before focusing the plug beam to approximately 40 μm waist at the atomic cloud position in the center of the science chamber, we first expand it to a size of approximately 5.9 mm diameter, and then a doublet lens of focus 60 cm focus the beam to 40 μm waist as mentioned before. The lens that focus the plug beam is mounted in a stable manual translation stage to finely adjust the position of the lens, and then the position of the focus. The plug beam propagates along the same path of that of the absorption imaging beam, then we take advantage of the imaging system to know the position of the plug beam onto the cloud, .i.e., we image the plug beam focus onto the CCD camera as well as the atomic cloud. The imaging system will be described in section 5.4. Figure 5.2.10 also shows the path of the imaging beam. As the plug beam travel in the same direction of the imaging beam, it will strike in the CCD camera that we use to do the image of the atoms, we nee to block the plug beam before reaching the CCD, then we avoid to damage the CCD and do a clean image. To do this, we place a polarizing cube for 532 nm who reflect almost all the green light. As there is some leak, that is still strong for the CCD, we place a dichroic that reflect the green light and transmit the imaging beam. Furthermore, for completely block the plug, we use a filter after the dichroic. Also, in front the CCD is it used a very narrow filter that helps in obtaining a cleaner pictures. To start the alignment of the plug beam, we first look at the center of the magnetic field on the CCD Stingray camera. To do this, we realize an image of the atomic cloud in the magnetic trap, using a very short time of flight ($\sim 5\,\mathrm{ms}$), evaporating to 4.5 MHz (this process will be explained in the next section) in order to have a small cloud, and then a more precise knowledge of the center of the MT. If we leave a very weak leak of the plug to reach the camera (being very careful about the power reaching the CCD) we can see the image of the plug and its position with respect to the already marked MT center. With the dichroic that combined the plug and imaging beams (Figure 5.2.10), we can place the beam in the marked position of the MT center. This coarse alignment is made commonly the first time the system is being setting up. Once the plug have being aligned, normally it will be onto the atomic cloud and the image will be seen easily on the image of the atoms. Anyway, to do the fine adjustment, we look at the atomic cloud doing absorption images in time-of-flight. If the plug beam is ON while the atoms are expanding, and is just switched off when taken the absorption image sequence, we can observe a hole in the center of the atomic cloud. Therefore, we can steer the plug beam until reach the center of the MT, where the Majorana losses take place. We easily know when the plug beam is properly or not aligned, looking at the density or number of atoms measured by the imaging system. When the plug is out the center, the Majorana losses predominate and the cloud is very dilute, with a low number of atoms. Where the plug beam reach the center of the Majorana hole, the cloud become very dense with a high number of atoms, in this situation it is said that the Majorana hole has been plugged. Figure 5.2.12 shows a picture of the plug beam in the cloud and the effect it has on it.

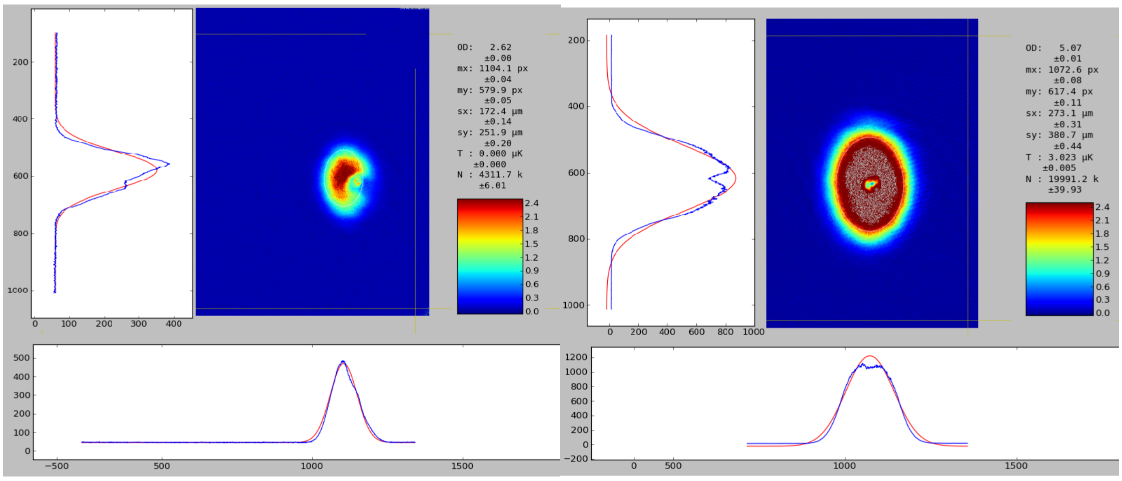

(a) **(b)**

Figure 5.2.12 – Image of the plug beam in the CCD camera. It is clearly visible the hole produced by the plug beam. (a) When the plug beam is misaligned (out of the Majorana hole) the cloud is very dilute due to the great loss of atoms by Majorana losses. (b) When the plug beam is correctly aligned the atoms are kept in the trap and the cloud become very dense.

Source: By the author.

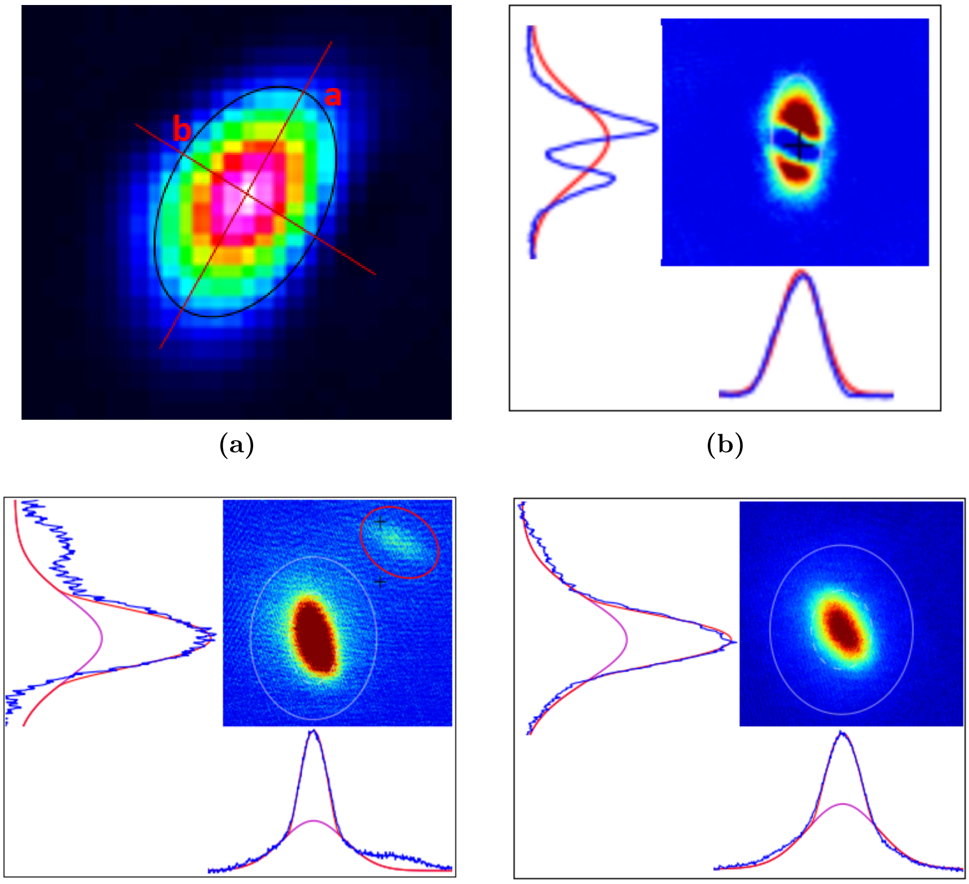

(a) **(b)**

(c) **(d)**

Figure 5.2.13 – (a) plug beam profile showing the slightly elliptical mode with radius $a = 43.47\,\mu\text{m}$ and $b = 36.09\,\mu\text{m}$. (b) Because of the symmetry broken due to the slightly elliptical shape of the plug, the atomic cloud separate in two (double well potential), instead of a ring shape. This image correspond a evaporation until 1.3 MHz with a $t_{TOF} = 10\,\text{ms}$. (c) It is shown that the most of the atoms can be transferred to a single well potential when the plug beam is slightly misaligned. Here, BEC of sodium atoms showing the bimodal fit. Inside the red circle in the top right of the picture it is possible to see the remaining atoms at one of the potential wells. (e) BEC of sodium atoms with all the atoms transferred to a single potential well.
Source: By the author.

The optimization of the plug position is repeated at lower RF frequencies, i.e., with smaller atomic clouds to warranty that the beam is really plugging the Majorana hole. This is because at lower rf frequencies, the atoms will be more sensitive to Majorana transitions, thus the position of the plug beam is more critical.

The generation of the single well potential is realized slightly misaligning the plug beam, braking the symmetry of the potential well with respect to the x-direction. The beam waist was determined using a CCD camera beam profiler (BC106N-VIS / Thorlabs). Figure 5.2.13 shows the beam profile of the plug beam and the double well potential created by it. Because of the symmetry broken due to the slightly elliptical shape of the plug, the atomic cloud separate in two (double well potential), instead of a ring shape. Moreover, with a slight misalignment it is possible to transfer all the atoms to a single well potential.

5.3 Evaporative cooling in our OPT

Evaporative cooling for ultracold gases has become the best method for increasing phase space densities to levels beyond what a standard MOT can achieve. So far, evaporative cooling is the only method that allows to achieve phase space densities of the order necessary for the production of BECs. This method was originally proposed by H. Hess (62) in 1986 and implemented for N. Masuhara et al. (63) in 1988. This method for cooling ultracold gases has become the best method for increasing phase space densities to levels beyond what a standard MOT can achieve.

Evaporative cooling of a gaseous sample in a MT can be summarized in a very simple way as follows: considering that the gas obeys the Maxwell-Boltzmann distribution, then removing the highest energy atoms from the system lead to a rethermalization producing a new Maxwell-Boltzmann distribution with smaller average energy per particle, and therefore smaller temperature. If this process is continually repeated (called Forced Evaporative Cooling), it can lead to an increasing density as the temperature decreases, even though atoms are being lost. The main drawback of this cooling scheme compared to others is that it requires rather high initial densities. (64, 65)

For evaporative cooling works, it is necessary to satisfy two important requirements: fast elastic collisions and selectively remove the highest energy atoms.

1) *Fast elastic collision rates*: When the most energetic atoms of the thermal distribution are removed, the new distribution at smaller energies is achieved due to redistribution of energy through elastic collisions. The elastic collision rate have to be greater than the loss rate, otherwise the process just will removes atoms from the system without cooling. (29) This means that the cloud needs to have to rethermalize (by elastic collisions) before realizing the subsequent evaporation step.

The linear MT is the best configuration to realize evaporative cooling because its tightly confinement offers the largest elastic collision rates, as pointed out by Davis et. al. (2) This can be seen, recalling that the potential energy with the form $U = \mu B_0 \left(r/R\right)^s$ is able to confine an atomic cloud of radius r and temperature T, i.e, of energy $k_B T$ with the following condition

$$k_B T = \mu B_0 \left(\frac{r}{R}\right)^s, \tag{5.3.1}$$

where s is the power (power law) of the trap, R is the radius of the coils that produce the B-field. The collision rate is given by $\Gamma_{el} = n\sigma_{el}\bar{v}_{thermal}$, where ,$n \propto 1/\left\langle r\right\rangle^3$ is the density, σ_{el} is the elastic scattering cross-section, and $\bar{v}_{thermal} = \left(8k_BT/m\pi\right)^{1/2}$ is the relative velocity between the atoms. Using Equation (5.3.1), we see that the density goes as $n \propto 1/T^{3/2}$. Thus, the elastic collision rates is proportional to

$$\Gamma_{el} \propto \frac{N(T)}{T^{3/s-1/2}}. \tag{5.3.2}$$

From this equation we can see that for a linear trap, $s = 1$, the scattering rate has its maximum value when the temperature is decreased. (2)

The fact that elastic collision rate decreases when the density decreases (when the temperature is lower) is overcame due the atoms occupy a smaller volume each time the system reduce the temperature (then energy), going to the deeper zone of the potential. Thus, a condition to maintain a sustainable evaporative cooling is to maintain constant or increase Γ_{el}. (24)

2) *Selectively remove the highest energy atoms*: To remove the highest energy atoms from the MT it is performed radio-frequency (RF) evaporation. In the MT the different hyperfine states of the atoms are subject to the Zeeman effect, and since the B-field varies linearly, the potential energy also will vary linearly as a function of position from the origin. In our case we trap atoms in the hyperfine state $F = 1$, which splits in three different magnetic components, $m_F = -1, 0, 1$. Atoms in the state $F = 1$, $m_F = -1$ are a low-field seekers, and this is the state we use in our trap. Atoms in $m_F = 0$ are untrappable and in $m_F = 1$ said to be in an anti-trap state, i.e, these atoms will expelled from the trap.

Because the energy of the atoms depend on the position, increasing linearly with respect to the center, atoms with smaller energies will be in the deeper part of the potential experienced a smaller Zeeman splitting. Atoms with higher energies will reside far from from the center, suffering a greater Zeeman splitting between the hyperfine levels.

Applying resonant radiation which that drives the most energetic the atoms to change their hyperfine state, flipping into the $F = 1$, $m_F = 1$ state, will selectively take out the high energy atoms. When the atoms realized the transition to the $F = 1$, $m_F = 1$ state, they will be expelled from the trap. To selectively remove atoms with an energy E (temperature T), the RF has to drive the transition between the trapped state ($F = 1$, $m_F = -1$) to the the anti-trapped state ($F = 1$, $m_F = -1$), this means, $hf_{RF} = 2k_BT$, and then

$$f_{RF} = \frac{2k_BT}{h}, \tag{5.3.3}$$

where the factor of 2 is due to the fact that the atoms are first transfer to untrappable state ($F = 1$, $m_F = 0$) and then to the anti-trapped state (66, 67), as can bee seen in Figure 5.3.1

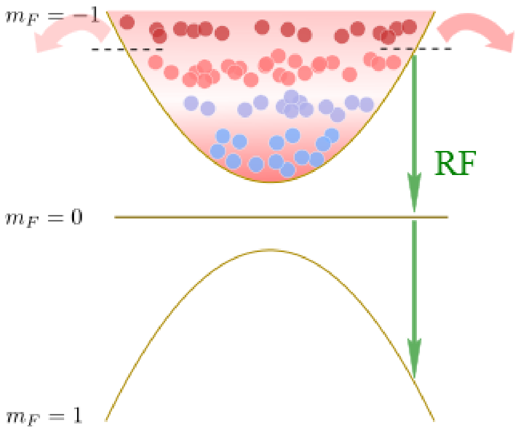

Figure 5.3.1 – Working principle of evaporation by Radio frequency (RF). Atoms are transferred from the trappable state $m_F = -1$ to the untrappable $m_F = 1$, where they see a repulsive potential and then are expelled from the trap.

Source: By the author.

In general, the initial RF frequency in the evaporation process is chosen according to the temperature of the cloud transferred to the MT. This means that, if the RF is set such that $hf_{RF} < k_B T$ we will remove atoms that we could cooled down in the evaporative cooling process. Then, it is recommended to start the process removing a small fraction of the high energy tail of the Maxwell-Boltzmann distribution. (24)

The efficiency of the evaporation (γ) process, can be measured in several forms, one of them being evaluating the quantity

$$\gamma = -\frac{d\ln(\rho_{PSD})}{d\ln(N)}, \tag{5.3.4}$$

where $\rho_{PSD} = n\lambda_{DB}^3$, is the phase space density with $\lambda_{DB} = \sqrt{2\pi\hbar^2/(mk_BT)}$ being the de Broglie wavelength. The objective of evaporative cooling is to increase the phase space density of the sample, then it is necessary satisfy the condition $\gamma > 0$.

Information about the efficiency of the evaporation can be obtained from

$$\alpha = \frac{d\ln T}{d\ln N}, \tag{5.3.5}$$

which is a quantity that describes the temperature decrease per lost particle. (29)

Both methods of evaluating the efficiency of the evaporation can be realized in the same way, measuring the temperature and number of atoms at certain points of the evaporation process. (24) From Equation (5.3.5) the parameter α has to satisfy the condition $\alpha > 2/3$, as it is shown in (24) in general.

5.3.1 Our RF antenna and evaporation process

In our experiment we use an antenna made of 1 mm diameter copper wire. It consists of two turn of 38 mm diameter. A RF signal generator Standford Research Systems model SG384, able to produce frequencies until 4 GHz and peak-to-peak amplitudes of 10 V is used to feed the antenna. We use a 50 Ω resistor in series with the antenna, in order to improve the RF coupling between the RF synthesizer and to minimize RF reflections. To know the capacity of coupling of our antenna, it was measured the RF coupling as function of the frequency sent to the antenna, for this we use an one-dimensional (directional) coupler from Mini Circuits, model ZFDC-20-5+. With this coupler, it is possible to measure the power of the reflected radiation, i.e. the non-coupled RF by the antenna using an spectrum analyzer, then, the smaller the measured power the better the coupling by the antenna. Figure 5.3.2 shows the power reflected by the antenna. To compare, we did three different measurements: 1) when no antenna was connected (minimum coupling, of course), this was done to know the reference point; 2) connecting only the 50 Ω resistor (maximum coupling), and finally 3) when the antenna + resistor is connected to the coupler.

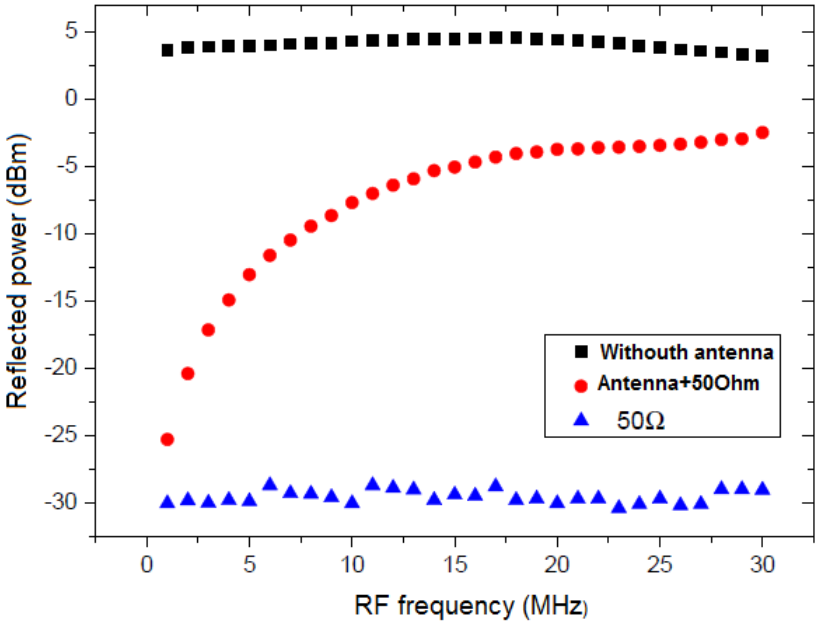

Figure 5.3.2 – Measurement of the reflected power by the antenna in series with a resistor of 50 Ω(red circles). In black squares and blue triangles are the measurements of power without antenna and only the resistor, respectively.

Source: By the author.

From Figure 5.3.2 we observe a good coupling of RF by the antenna which is fundamental for the evaporative cooling process. It is worth to note that for smaller RF

Table 5.1 – Values of the RF and time for our evaporation ramp.

Time (s)	RF (MHz)
0	45
6.5	14
15	4.5
18	2.5
20	1.3
23	0.65

Source: By the author.

frequencies, in the final part of the evaporation process where we need a better RF control, the coupling becomes better, approximating to the limit of the $50\,\Omega$ resistor. The signal generated and sent to the antenna by the synthesizer is injected to a homemade amplifier of +33 dBm, in order to obtain enough power in the RF wave. Thus, the final power sent to the antenna was +26 dBm.

The antenna is placed outside of the vertical top window at approximately 3 cm from the atoms.

Our evaporation process start with a radio frequency (known as knife) of 60 MHz, immediately after the transferred of the atoms from the Dark-SPOT MOT + molasses has been done. This frequency was experimentally found to be a good starting point in number and temperature of the cloud. Instantaneously the RF goes to 45 MHz, and from this point the evaporation process starts. Thus, the RF frequency is ramp down from 45 MHz to 0.65 MHz in 23 sin five steps, as shown in Table 5.1. At this last frequency the BEC is obtained. A curve of the evaporation process will be given in the next chapter where several processes to reach the BEC of ^{23}Na atoms and some parameters of the BEC itself were characterized and optimized.

5.4 Imaging system

One of the most useful method to study our system is the absorption imaging technique. It consists of shining the atomic cloud with a collimated laser beam resonant with one of the electronic transition of the atoms. In our system we use the $3^2S_{1/2}(F=2) \rightarrow 3^2P_{3/2}(F'=3)$ transition. The cloud absorb part the light of the beam doing a dark shadow in the beam. Imaging the shadow using an appropriate optical system we can obtain the density profile of the cloud. In our experiment the atoms are initially in the $3^2S_{1/2}(F=1)$ state, being necessary to pump the atoms to the state $3^2S_{1/2}(F=2)$, for this we use a repumper pulse of light with frequency tuned to the transition $3^2S_{1/2}(F=1) \rightarrow 3^2P_{3/2}(F'=2)$, for a time in which all the atoms are totally transfer to $3^2S_{1/2}(F=2)$.

We use a camera Stingray F-145. We use a magnification of 1.66. The chip size of the camera is 10.2 mm × 8.3 mm, with each pixel being 6.45 μm × 6.45 μm, and a resolution of 1388 × 1038 pixels.

The absorption image system produces a normalized picture that give us the information require to obtain the different relevant parameters of the atomic cloud or BEC. This normalized image is obtained after a sequence of pictures. First it is made an image of the of the probe beam when the atoms are present in the trap, i.e image of the shadow onto the CCD camera, following this, it is made an image of the beam without atoms and finally a dark picture is taken. The resultant picture is the subtraction of the background to the atom picture with its respective normalization. We can express this operation as

$$\frac{(Beam\,with\,atoms) - (Dark\,field)}{(Beam\,without\,atoms) - (Dark\,field)} = Absoption\,image. \tag{5.4.1}$$

5.4.1 Information from Time-of-Flight for thermal clouds

An absorption image of atoms expanding in time-of-flight (TOF) represents the density distribution of the cloud in two dimensions; since the beam passes through the cloud along one of the axis (the z-axis), this axis is integrated out. Specifically, the attenuation of a weak probe beam inside the cloud is exponential

$$I = I_0 exp\left[-\int \sigma n(r) dz\right] \tag{5.4.2}$$

The density of the thermal gas is given by (68)

$$n(r) = n_0 g_{3/2} exp\left[-\frac{1}{R^2}\left(x^2+y^2+z^2\right)\right]. \tag{5.4.3}$$

Then, the real density is obtained as

$$\begin{aligned} \int ndz &= n_0 \int_{-\infty}^{+\infty} dz g_{3/2} exp\left[-\frac{1}{R^2}\left(x^2+y^2+z^2\right)\right], \\ \int ndz &= n_0 R\sqrt{\pi} g_2 exp\left[-\frac{1}{R^2}\left(x^2+y^2\right)\right]. \end{aligned} \tag{5.4.4}$$

We can then fit our absorption images with Equation (5.4.4) and extract the widths; this can be done either through a full two-dimensional fit, which is quite an intensive process, or through a one dimensional slice from our image (in both the horizontal and vertical direction) and two one-dimensional fits. Extracting the widths of the cloud, we can estimate the thermal velocity of the atoms by taking pictures of the cloud at two different time-of-flights and using $v_{thermal} = (x_{width2} - x_{width1})/\Delta TOF$. If we don't have two pictures at different TOF, we can still get an accurate measurement by taking just one picture, extract one width and use $v_{thermal} = x_0/TOF$. This method is still accurate because for large TOF, the dependence on the initial size becomes negligible (69) and we can assume the atoms start off with zero width.

The number of atoms and density can be extracted from our fit by taking the amplitude of the fit and extracting n_0 and using

$$N = \int dV n_0 g_{3/2} exp\left[-\frac{1}{R^2}\left(x^2+y^2+z^2\right)\right]. \tag{5.4.5}$$

The temperature can be found using

$$k_B T = \frac{1}{2} m v_{thermal}^2. \tag{5.4.6}$$

5.4.2 Information from Time-of-Flight for atoms in the BEC

For condensates, the time-of-flight dynamics are quite different. Since the atoms behave as a quantum wave, while the atoms are in the trap, their ground state density distribution will be dictated by the ground state wavefunction of the trap. But once the trapping potential is off and they are expanding, Mean Field repulsion will change the wavefunction of the freely expanding condensed atoms. (70) For the case of harmonic traps, this is not the case, as the condensate expansion will just be a simple scaling of the shape in the trap by a factor given by their velocity.

The density of a condensate inside a harmonic trap is given by

$$n = n_0\left(1 - \frac{x^2}{x_0^2} - \frac{y^2}{y_0^2} - \frac{z^2}{x_0^2}\right), \tag{5.4.7}$$

where the widths of the condensate in the different directions depends on the shape of the trap. The real density will be given by

$$\int_{-z'}^{+z'} n dz = \frac{4}{3} n_0 z_0 \left[1 - \left(\frac{x}{x_0}\right)^2 - \left(\frac{y}{y_0}\right)^2\right]^{3/2}, \tag{5.4.8}$$

where $z' = z_0\sqrt{1-\left(\frac{x}{x_0}\right)^2-\left(\frac{y}{y_0}\right)^2}$.

Although expansion of a condensate from a linear trap does not follows this simple scaling rule, the two main differences are still there 1) condensate does not expand like a g_2 function but has a more complicated, non-parabolic, expansion and 2) the expansion is anisotropic. Even though expansion from the linear trap is more complicated than expansion from a harmonic trap, we can still fit our linear trap data to harmonic trap.

5.4.3 Configuration of our imaging system

The arrangement of the optical system to produce do the image of the atomic cloud is shown in Figure 5.2.10, together with the plug beam, due to that both light beams propagate along the same path ($\hat{x}$-direction).

Our imaging setup is able to realize two kind of images, one with magnification $M = 0.5$ and other with $M = 1.66$. The first system, has the purpose of imaging the MOT which is very large, then being necessary to reduce its image in order to fit in the CCD camera. The second one, is to image the atomic cloud in the MT and BEC, which are very small and then being needed to do the magnification. We can choose one of the two path using a manual flipper mirror, depending if we want to do the MOT alignment or we want to see the MT or BEC. Figure 5.2.10 shows the position of this mirror in the path.

The most important optical system is the setup for magnifying the cloud, because we want ultimately to observe the BEC. The first lens of this setup is a 2” diameter lens with $f_1 = 15\,\text{cm}$ focus, follow by a lens of $f_2 = 25\,\text{cm}$ (2” diameter), therefore the magnification is $M = 1.66$. The numerical aperture of this system is given by $NA = R/\sqrt{R^2 + f_1^2}$, where R is the radius of the first lens, thus the maximum numerical aperture for this system is $NA = 0.16$. The optical resolution is given by (28) $OR = 0.61\lambda/NA$, where $\lambda = 589.158\,\text{nm}$ is the wavelength of the imaging beam. Thus, for our system the optical resolution is $OR = 2.24\,\mu\text{m}$, which is the minimum separation between two points that the imaging system can resolve. (28)

To take the images of the atomic cloud, we use a Stingray F-145 CCD camera with chip size $10.2\,\text{mm} \times 8.3\,\text{mm}$ of 1388×1038 pixels, where each pixel has dimensions of $6.45\,\mu\text{m} \times 6.45\,\mu\text{m}$. As described in section 5.2.4 (OPT configuration), the plug travels along the same path of the imaging beam, being necessary to stop it before reaching the CCD camera. To do this, we place a polarizing cube for 532 nm who reflect almost all the green light. As there is some leak, that is still strong for the CCD, we place a dichroic that reflect the green light and transmit the imaging beam. Furthermore, for completely block the plug, we use a filter after the dichroic. Also, in front the CCD is it used a very narrow filter that helps in obtaining a cleaner pictures. Figure 5.2.10 shows these elements in the optical system.

Imaging in the $F = 2$ state

As mentioned before, we trap the atoms in the state $F = 1$, $m_F = -1$. The absorption imaging can be realized in two forms: using the transition $3^2S_{1/2}(F = 2) \rightarrow 3^2P_{3/2}(F' = 3)$ or the transition $3^2S_{1/2}(F = 1) \rightarrow 3^2P_{3/2}(F' = 2)$, where in the latter case it is needed to use a repumper beam, transferring the population from $F = 1$ to $F = 2$. We use the latter procedure for taking our images because the absorption cross-section for this transition is twice the absorption cross-section for the transition ($F = 1 \rightarrow F\,'{=}2$) ($\sigma_{1\rightarrow 2'} = 0.0831\,\mu\text{m}$, and $\sigma_{1\rightarrow 2'} = 0.1662\,\mu\text{m}$). (24)

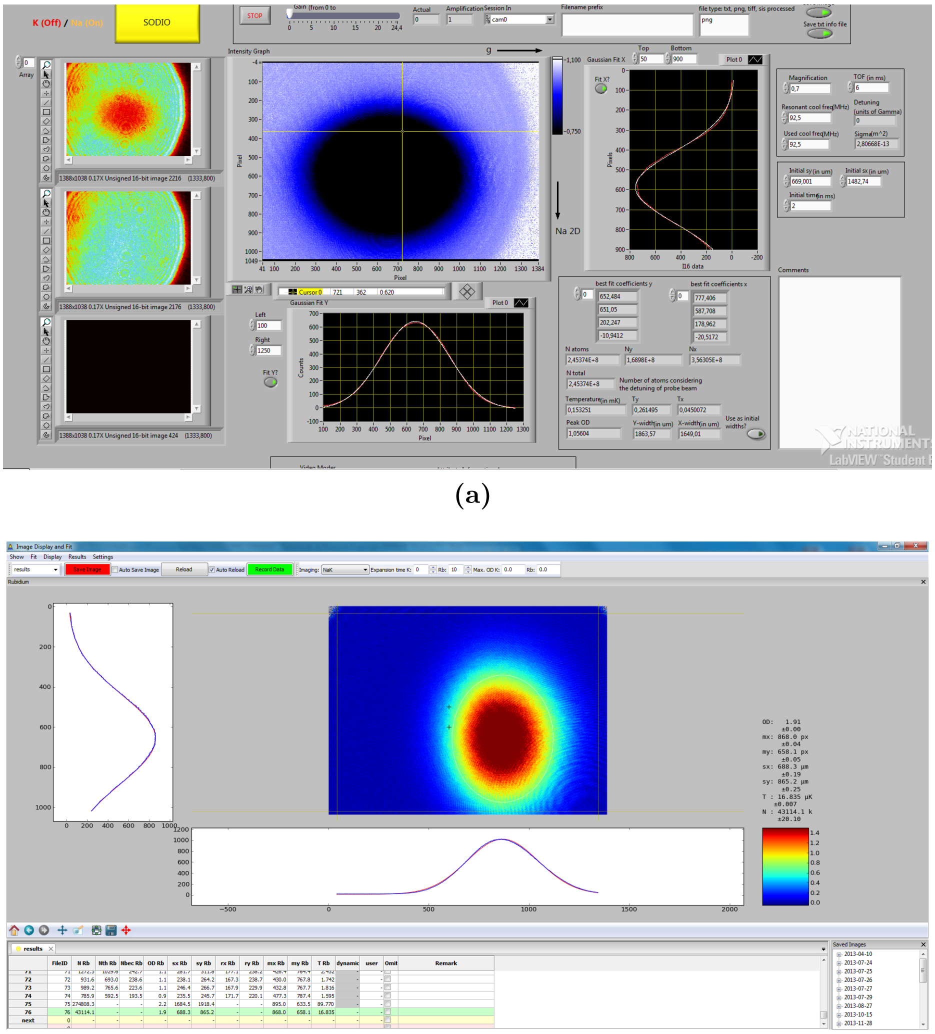

(a)

Magnification: 0,7
TOF (in ms): 6
Resonant cool freq(MHz): 92,5
Detuning (units of Gamma): 0
Used cool freq(MHz): 92,5
Sigma(m^2): 2,80668E-13
Initial sy (in um): 669,001
Initial sx (in um): 1482,74
Initial time (in ms): 2

best fit coefficients y: 0; 652,484; 651,05; 202,247; -10,9412
best fit coefficients x: 0; 777,406; 587,708; 178,962; -20,5172
N atoms: 2,45374E+8
Ny: 1,6898E+8
Nx: 3,56305E+8
N total: 2,45374E+8
Number of atoms considering the detuning of probe beam
Temperature(in mK): 0,153251
Ty: 0,261495
Tx: 0,0450072
Peak OD: 1,05604
Y-width(in um): 1863,57
X-width(in um): 1649,01
Use as initial widths?

OD: 1.91 ±0.00
mx: 868.0 px ±0.04
my: 658.1 px ±0.05
sx: 688.3 µm ±0.19
sy: 865.2 µm ±0.25
T : 16.835 µK ±0.007
N : 43114.1 k ±20.10

results

	FileID	N Rb	Nth Rb	Nbec Rb	OD Rb	sx Rb	sy Rb	rx Rb	ry Rb	mx Rb	my Rb	T Rb	dynamic	user	Omit	Remark
71	71	1272.3	1029.6	242.7	1.1	281.7	311.8	177.1	238.2	426.4	764.4	2.432	-	-	☐	
72	72	931.6	693.0	238.6	1.1	238.1	264.2	167.3	238.7	430.0	767.8	1.742	-	-	☐	
73	73	989.2	765.6	223.6	1.1	246.4	266.7	167.9	229.9	432.8	767.7	1.816	-	-	☐	
74	74	785.9	592.5	193.5	0.9	235.5	245.7	171.7	220.1	477.3	787.4	1.595	-	-	☐	
75	75	274808.3	-	-	2.2	1684.5	1918.4	-	-	895.0	633.5	89.770	-	-	☐	
76	76	43114.1	-	-	1.9	688.3	865.2	-	-	868.0	658.1	16.835	-	-	☐	
next	0	-	-	-	-	-	-	-	-	-	-	-	-	-	☐	

Saved Images
2013-04-10
2013-07-24
2013-07-25
2013-07-26
2013-07-27
2013-07-29
2013-08-27
2013-10-15
2013-11-28

(b)

Figure 5.4.1 – (a) Normalized image in the LabView program used to process the image, which send the normalized image to a program in Python that finally process the absorption image (b), given ll the parameters needed for the analysis. The image in (a) and (b) does not correspond to the same atomic cloud, which were put here just for illustration.
Source: By the author.

To realized the image in the $F = 2$ state, we need to pump the atoms from $F = 1$ using the same repumper frequency used for the MOT. Then, after the atoms have been pumped into the $F = 2$ state, resonant light driving the transition $F = 2,\, m_F = 2 \rightarrow F' = 3,\, m_{F'} = 3$ (probe beam). The repumper light is send to the cloud a little bit before the probe beam, in order to transfer all the atoms to the $F = 2$ state. The two frequencies are combined and sent to the science chamber table through a polarization maintaining optical fiber.

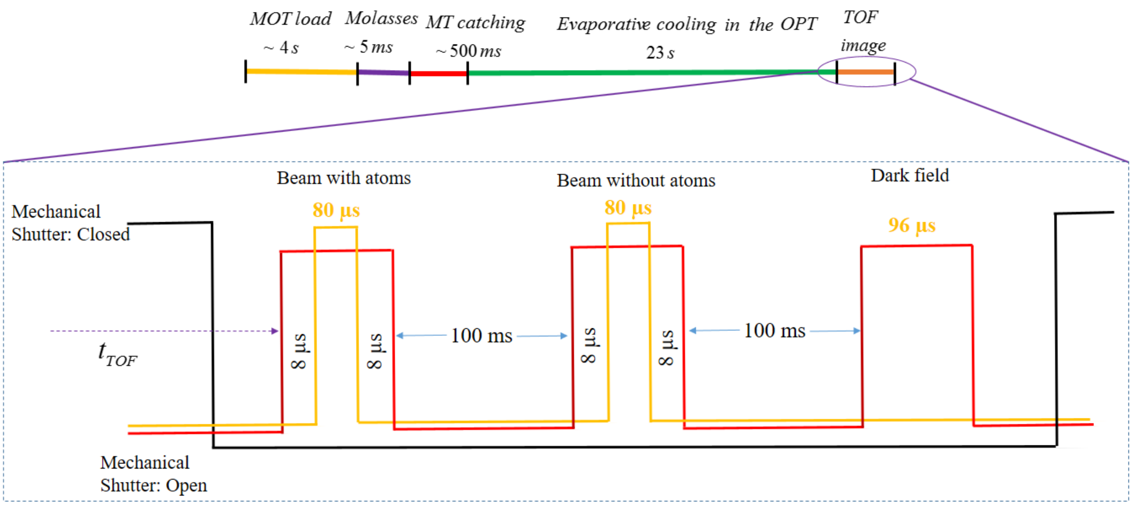
MOT load
~ 4 s
Molasses
~ 5 ms
MT catching
~ 500 ms
Evaporative cooling in the OPT
23 s
TOF
image
Beam with atoms
80 µs
Beam without atoms
80 µs
Dark field
96 µs
Mechanical
Shutter: Closed
t_{TOF}
8 µs
8 µs
100 ms
8 µs
8 µs
100 ms
Mechanical
Shutter: Open

Figure 5.4.2 – Temporal sequence for the TOF imaging beam to produce a normalized image. Not to scale.

Source: By the author.

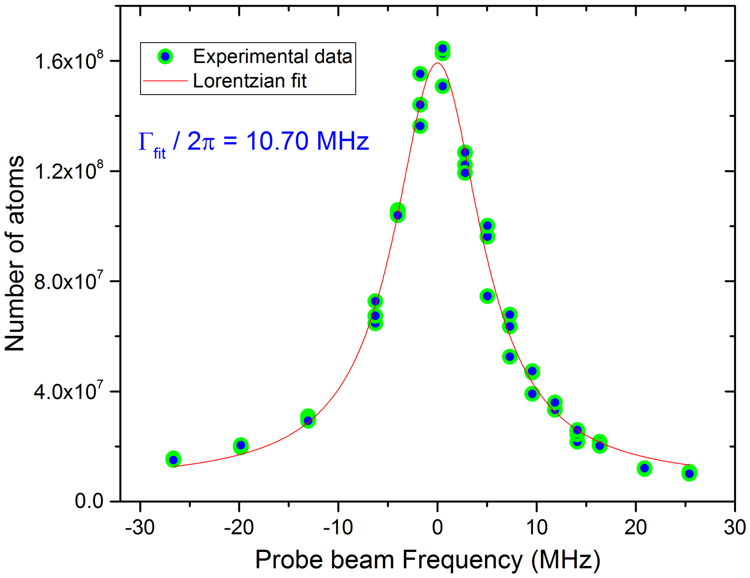

Figure 5.4.3 – Optimization of the probe beam frequency. All frequencies used in the experiment are calculated relative to this. The value of the linewidth obtained from the curve deviate just 9% of the exact value ($\Gamma_{exact}/2\pi = 9.795\,\text{MHz}$). This curve was realized taking images of an atomic cloud evaporated until 8 MHz with $t_{TOF} = 10\,\text{ms}$. $f_{probe} = 0$ in the Curve, corresponds to a value of 1.62 V in the control program system, driving the frequency of the double-pass AOM, and corresponds to a frequency of $-36.80\,\text{MHz}$ with respect to the frequency obtained when $V_{program} = 0$. This is the frequency taken as reference, $\delta_{lock} = -36.80\,\text{MHz}$, because the probe beam has to exactly tuned to the transition $F = 2 \rightarrow F' = 3$.

Source: By the author.

Figure 5.4.2 shows the temporal sequence used to obtain the normalize image, described by Equation (5.4.1). In Figure 5.4.1a and 5.4.1b, it is shown the main window of the acquisition program in LabView, which send the normalized image to a program in Python that finally process the absorption image, given all the parameters needed for the analysis, as temperature, atom number, and optical density. The Python program was written in the European Laboratory for Non-linear Spectroscopy (LENS) from the University of Florence.

To optimize the frequency of the probe beam, it was scanned around the the transition $F = 2 \rightarrow F' = 3$. To obtain a better result , the images were taken evaporating the cloud until 8 MHz and with $t_{TOF} = 10\,\mathrm{ms}$.

Figure 5.4.3, shows the frequency scan of the probe beam. The value of the linewidth obtained from the curve deviate just 9% of the exact value ($\Gamma_{exact}/2\pi = 9.795\,\mathrm{MHz}$). This is the reason why in all the experiments, this frequency is taken as reference for deriving all the other frequencies of the experiment.

In the next chapter, I will present the experimental sequence used to obtained the BEC of sodium atoms, and how the characterization of the most relevant parameters were made using the elements described in this chapter.

Chapter 6

Bose-Einstein condensation of sodium atoms

In this chapter, I describe the experimental sequence used to obtain the BEC of sodium atoms. Also, it is shown the characterization of the BEC, namely, the way we measure the frequencies of the trap, and other important parameters. It is crucial to know all these parameters in order to better understand the system we are dealing with. In this way, we can perform our measurements with the appropriates experimental parameters.

6.1 Bose-Einstein condensation of sodium atoms

Before starting to describe the processes used to measure the parameters of the TOP trap and the optimization of the evaporation ramp for obtaining the BEC of sodium atoms, I explicitly write down what value each parameter takes along the experimental sequence, from the MOT loading process to the final achieving of the BEC. Figures 6.1.1 and 6.1.2 show the values of each parameter as a function of the experimental sequence time.

6.2 Evaporation process

As pointed out in chapter 5, the technique used to achieve the Bose condensation is evaporative cooling. (29) In this process, the most energetic atoms are removed from the atomic cloud in the magnetic trap, in order to reduce the temperature of the cloud.

The evaporation process was realized in a ramp of five steps, i.e, divided in five linear ramps. When the atoms are transferred to the MT, a RF knife of 60 MHz is applied, and instantaneously the RF frequency is set up in a value of 45 MHz. From this value the evaporation ramp is started until reach a final value of 0.65 MHz in a total time of 23 s. The different steps of the evaporation ramp are write down in Table 6.1 and the form of the curve is shown in Figure 6.2.1.

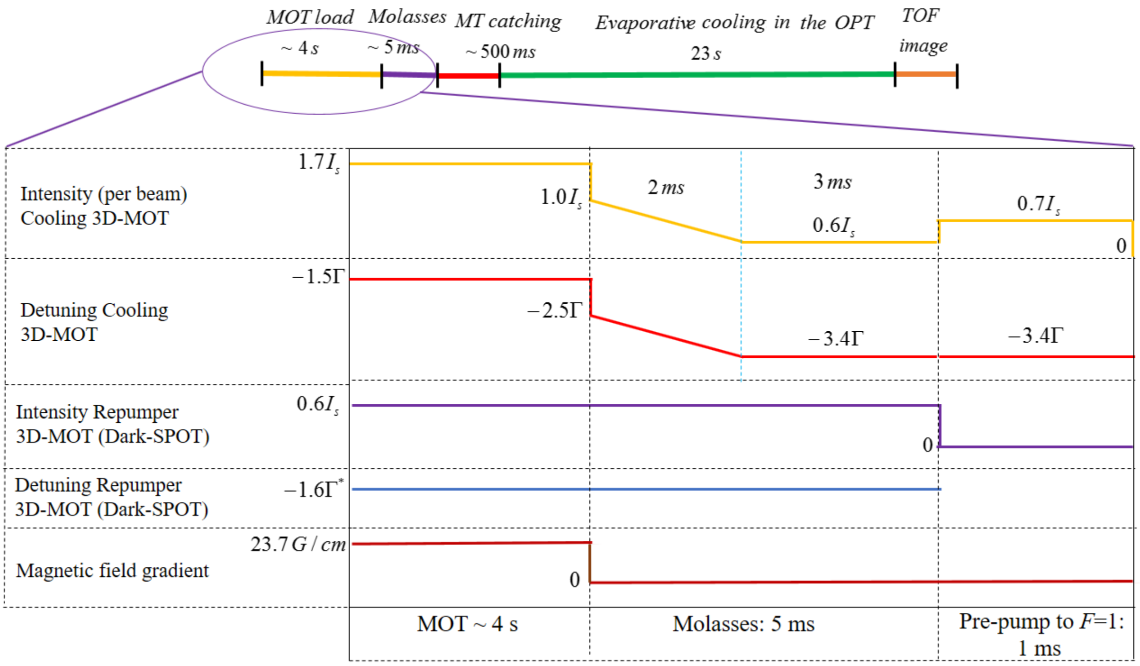
MOT load
~ 4 s
Molasses
~ 5 ms
MT catching
~ 500 ms
Evaporative cooling in the OPT
23 s
TOF
image
Intensity (per beam)
Cooling 3D-MOT
1.7I_s
1.0I_s
2 ms
3 ms
0.6I_s
0.7I_s
0
Detuning Cooling
3D-MOT
−1.5Γ
−2.5Γ
−3.4Γ
−3.4Γ
Intensity Repumper
3D-MOT (Dark-SPOT)
0.6I_s
0
Detuning Repumper
3D-MOT (Dark-SPOT)
−1.6Γ*
Magnetic field gradient
23.7 G / cm
0
MOT ~ 4 s
Molasses: 5 ms
Pre-pump to F=1:
1 ms

Figure 6.1.1 – Schematic diagram (Not to scale) for the temporal sequence taken into account only the parameters involved in the processes between MOT loading and pre-pumping to the $F = 1$ stage. This last stage is realized in order to send most the atoms to the ground state $F = 1$. The detuning of the repumper light (*) is calculated with respect to the repumper transition.

Source: By the author.

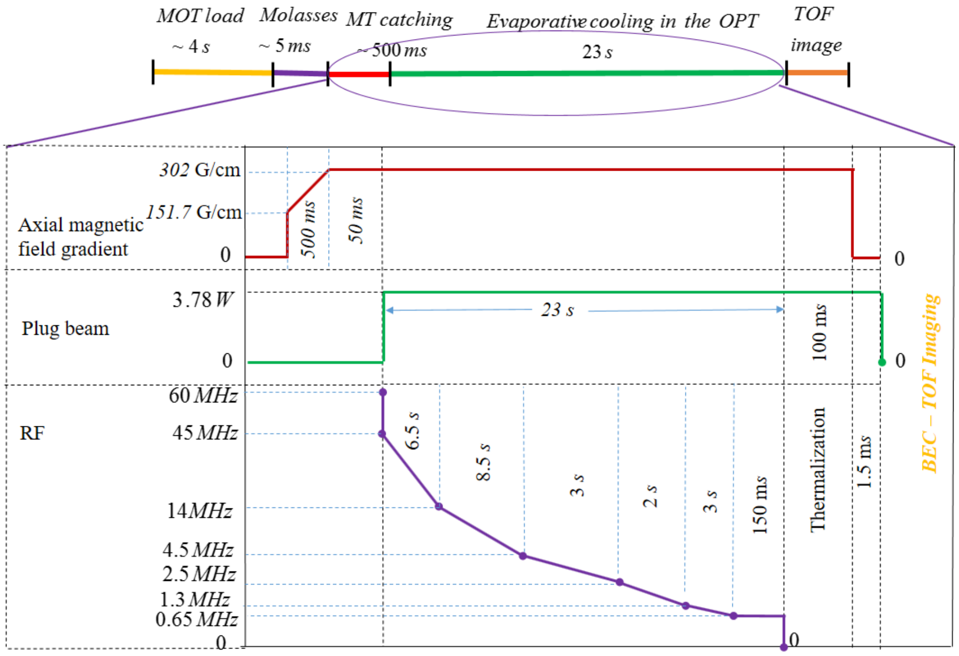
MOT load
~ 4 s
Molasses
~ 5 ms
MT catching
~ 500 ms
Evaporative cooling in the OPT
23 s
TOF
image
Axial magnetic
field gradient
302 G/cm
151.7 G/cm
0
500 ms
50 ms
0
Plug beam
3.78 W
0
23 s
100 ms
0
RF
60 MHz
45 MHz
14 MHz
4.5 MHz
2.5 MHz
1.3 MHz
0.65 MHz
0
6.5 s
8.5 s
3 s
2 s
3 s
150 ms
Thermalization
1.5 ms
0
BEC – TOF Imaging

Figure 6.1.2 – Schematic diagram for the temporal sequence of the magnetic field gradient, plug intensity, and RF frequency. Not to scale.

Source: By the author.

Table 6.1 – Optimal values of the RF and time for our evaporation ramp.

Time (s)	RF (MHz)
0	45
6.5	14
15	4.5
18	2.5
20	1.3
23	0.65

Source: By the author.

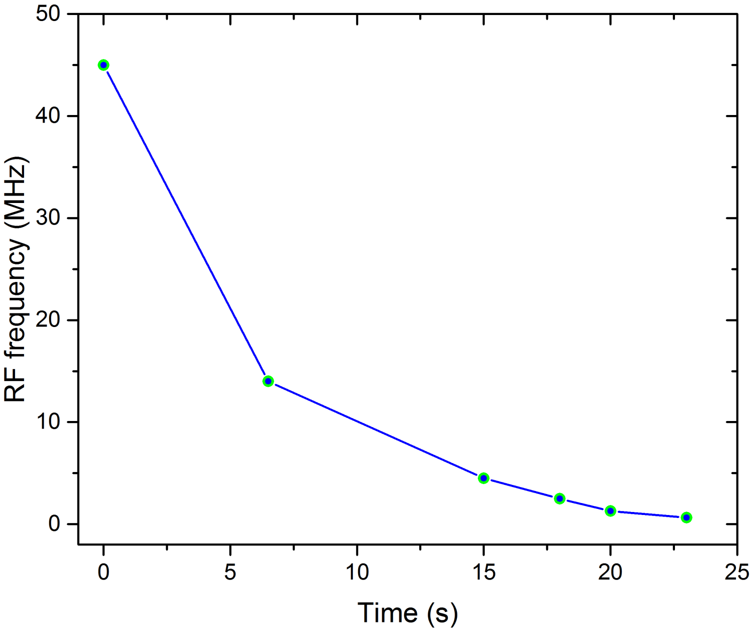

Figure 6.2.1 – (a) Optimized Evaporation ramp for sodium atoms. The evaporation ramp is divided in five steps, each step is a linear ramp. At the final value of the ramp, 0.65 MHz, the BEC of sodium atoms is achieved. (b) Absorption images of the atoms in each step of the evaporation process. Source: By the author.

It is essential to know the lifetime of the atoms in the MT before starting any evaporation process. This is because, we need to guarantee that the atoms can remain in the MT for a longer time than that time needed for realizing the evaporative process, otherwise the atoms will be lost before they reach the BEC transition. The procedure we used to measure the lifetime consists in the following: the atoms are transferred to the MT and a RF knife of 30 MHz is applied during one second. After the transfer, the atoms are leaved in the trap during different hold times. For each hold time, the number of remaining atoms in the MT was measured using the TOF imaging technique, with $t_{TOF} = 6\,\text{ms}$. Figure 6.2.2 shows the curve obtained for the lifetime measurements in the

MT. From this curve, an exponential is fitted to the experimental points, given a lifetime approximately 47 s ($\tau \simeq 47$ s). Recalling that the total evaporative cooling process takes 23 s, we can conclude that the lifetime of our MT is reasonable good, being properly for realize evaporative cooling without worrying a lot with background collisions, i.e., collisions of trapped atoms with atoms in the background, Γ_b being the loss rate for this kind of loss mechanism.

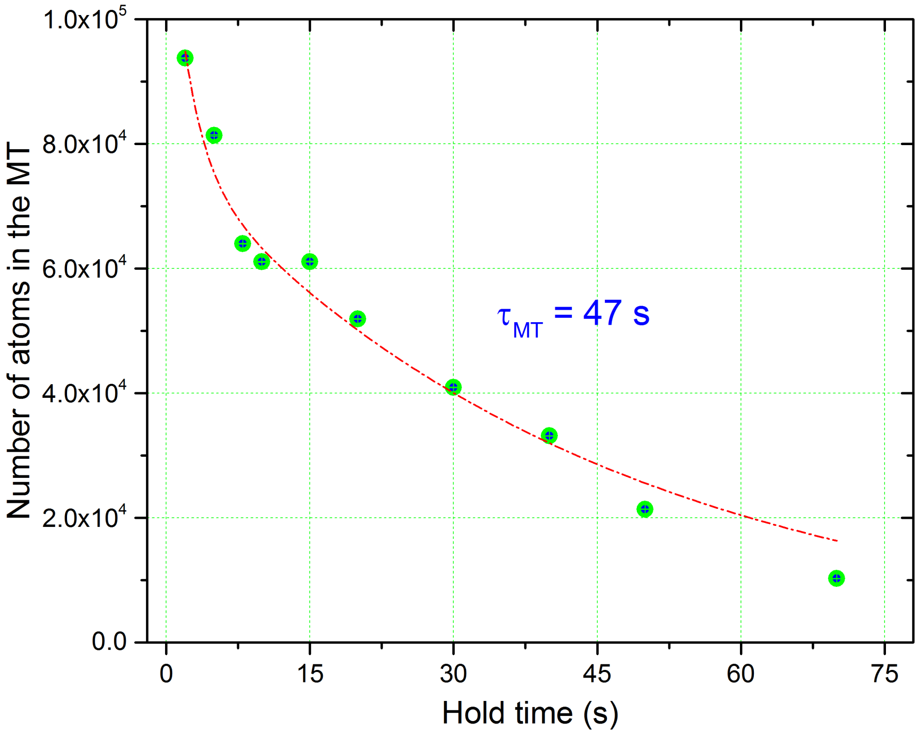

Figure 6.2.2 – Lifetime of the atoms in the MT. The number of atoms was measured in the magnetic trap, using a knife of 30 MHz, and using TOF imaging with $t_{TOF} = 6$ ms

Source: By the author.

Effect of Majorana losses in the evaporation process

As mention in the precedent chapter, the principal drawback of a bare quadrupole trap is the presence of a magnetic field zero at the center of the trap. This region of zero magnetic field, lead to Majorana transitions, which avoid the achievement the condensation transition.

To evaluate the evaporation process in the bare MT, and to compare with that in the presence of the plug, we started optimizing the evaporation for each pair of points in the linear evaporation ramps. In each step, we tried to reduce the loss of atoms while decreasing the temperature of the atomic cloud. For this to be accomplished, the parameter to be observed is in some cases are γ, or α, described in chapter 5, and given by Equations (5.3.4) and (5.3.5), respectively. The parameter α, describes the temperature decrease per lost particle. (29)

Thus, to optimize our evaporation ramp, we looked at the temperature and number of atoms in the OPT trap. Figure 6.2.3 shows the evaporation process in both cases, in the bare MT and in the OPT trap.

The red points are the experimental data taken when evaporation is realized in the bare quadrupole trap. Clearly, we can see that around $27\,\mu$K, the Majorana losses start to be dominant in the evaporation process. Below this point, the Majorana losses are very strong, preventing the achievement of the runaway condition and then, preventing to reach the zone where the Bose-Einstein condensation occurs. The loss rate, Γ_M, due to Majorana transitions in a quadrupole trap scales as $\Gamma_M \propto (\mu B'/k_B T)^2\,\hbar/m$ (50, 57), meaning that the Majorana losses strongly increase when the temperature decreases, as the atoms each time occupy regions where the magnetic field is smaller, increasing the probability of Majorana spin flips.

When the evaporation is performed in the presence of the plug beam, i.e., in the OPT trap, the Majorana hole is plugged, and the loss rate decreases. The green dots in Figure 6.2.3, represents the evaporation process in the OPT. In this curve, the number of atoms is maintained high while decreasing the temperature. This is basically because the presence of the plug beam creates a barrier that suppress the Majorana losses. As described in (50), there is an atomic density suppression in the region of low-field where the spin flips are stronger due to the optical repulsive potential of the plug. The reduction of the Majorana loss rate, is given by (50)

$$\Gamma_M^{plug} = \Gamma_M \times f \exp\left(-U/k_B T\right) \tag{6.2.1}$$

where U is the characteristic potential of the plug, and f is a factor that depends on the shape, position, and power of the plug beam.

From the superposition of the red and green curves in Figure 6.2.3, we can see that the plug has almost no effect above T_{Maj}, this indicate that the potential barrier created by the plug beam need to be above this value.

The slope of the green curve gives a very close value to 1, which is the required for a runaway evaporation condition. Thus, we are very close to this condition, being possible to condensate easily when the evaporation ramp is continued. From this curve, we obtained the critical temperature for our OPT trap, being $T_C = 1\,\mu$K, which correspond to a RF of 1.1 MHz. Below this RF frequency, we can increase the fraction of condensed atoms. The evaporation process finish exactly at 0.65 MHz, with a condensed fraction temperature around 500 nK.

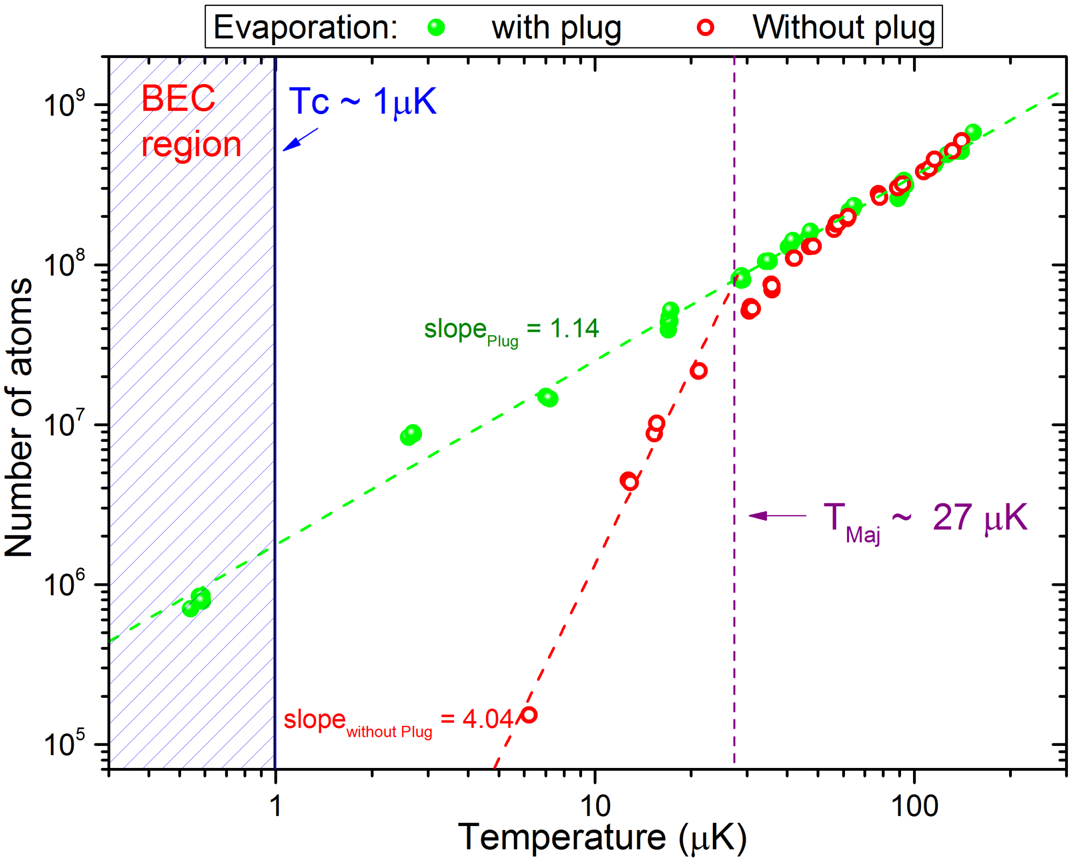

Figure 6.2.3 – Evaporation ramp for sodium atoms. The black dots are the points of in the MT with the plug beam, and the red points represents evaporation without plug beam. From this, we can observe the importance of the plug beam in avoiding the Majorana losses in the MT.
Source: By the author.

The bottom of the potential of the OPT trap was measured lowering the RF frequency until removing all the atoms from the trap. We observed that at a RF frequency of 0.26 MHz, no atoms remained in the trap. This measurement can be important if the radius of the potential well minimum want to be calculated (50). It is worth to mention that the bottom of this potential slightly varies as the position of the plug beam changes, thus it is a little bit difficult to have the same bottom potential in all the experiments. This will be improved with the use of a mirror controlled electronically, getting better precision and control over this and others parameters.

Lifetime of the BEC fraction in the OPT

The lifetime of the fraction of Bose condensed atoms in the OPT trap was measured in the same form than the lifetime of the MT. Figure 6.2.4 shows the lifetime of the condensate, i.e., the time in which the condensate survives in the trap. We measured the lifetime for different final RF frequencies, one when the condensate is obtained evaporating until

0.8 MHz and when obtained evaporating until 0.65 MHz, being this last value the typical used in the subsequent experiments.

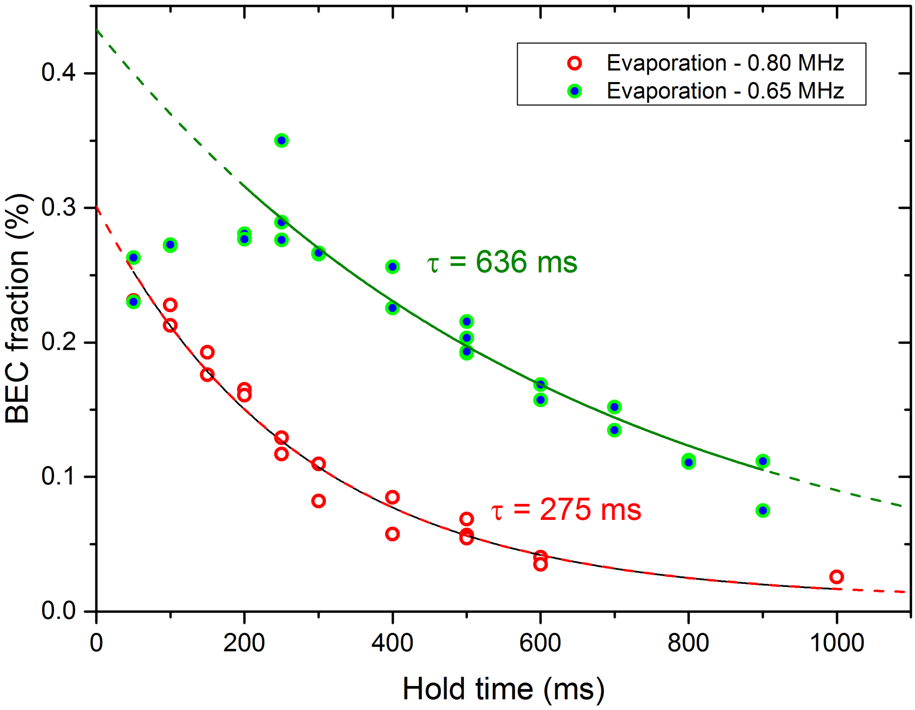

Figure 6.2.4 – The lifetime of the BEC is measured keeping the atoms in the OPT for different times after the BEC is reached. The curve is made for different final evaporation RF. The lifetime for the final RF (0.65 MHz) used in the subsequent experiments is $\tau = 636\,\mathrm{ms}$, enough for the the realization of the experiments of interest.

Source: By the author.

Finally, we tried to measure the aspect ratio of the BEC when freely expanding. This is an important feature of a Bose-Einstein condensate. Figure 6.2.5 shows the tentative to measured the aspect ration of the BEC without totally success at this time. So far, this signature was difficult to measured due to the tight potential of the OPT, which causes the BEC change the aspect ration in the first millisecond seconds of the expansion. At this first moments it is difficult to measured the radius of the cloud due to the high densities. This causes blackouts or saturation in the imaging system, thus preventing for obtaining with with accuracy the parameters of the fit.

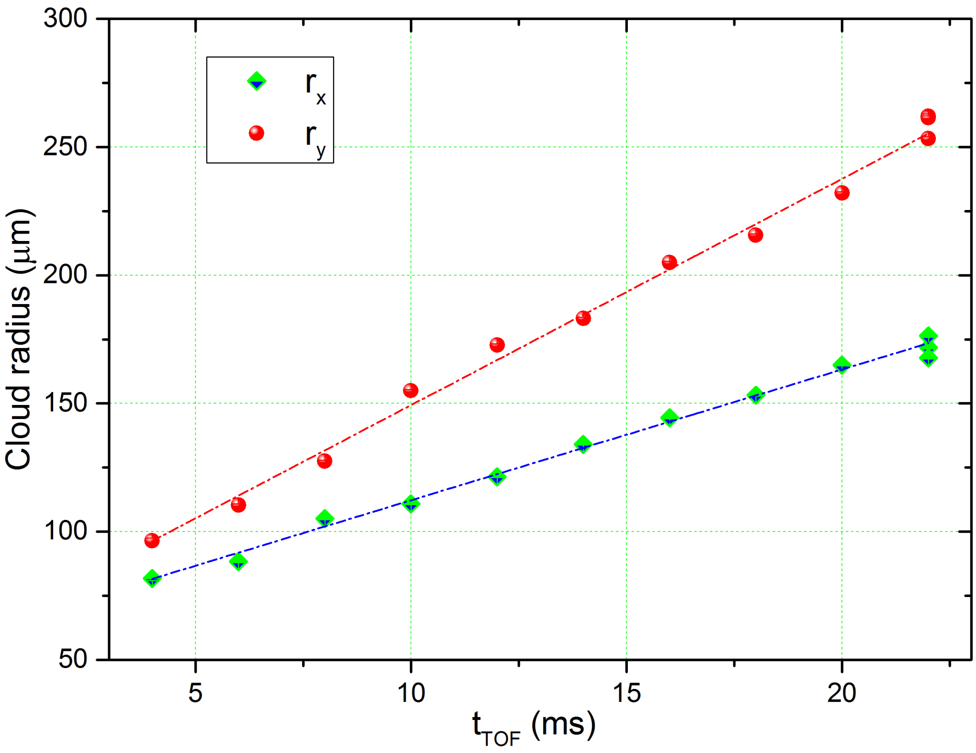

(a)

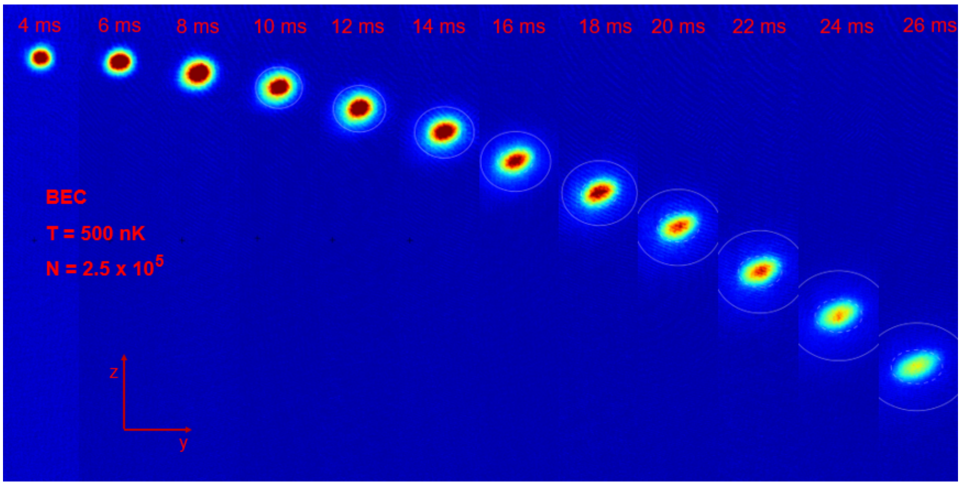
4 ms
6 ms
8 ms
10 ms
12 ms
14 ms
16 ms
18 ms
20 ms
22 ms
24 ms
26 ms
BEC
T = 500 nK
N = 2.5 x 10^5
z
y

(b)

Figure 6.2.5 – Tentative to measure the aspect ration of the condensate. It is hard for this system to measure the aspect ration because the change occurs in the initial milliseconds of the expansion, making the BEC very dense and dense the image inaccurate due to saturation. (b) Images of the BEC for different t_{TOF}. From this picture, it is possible to note that the aspect ration is not completely evident as we would like. Thus, it is concluded, that before $t_{TOF} = 4\,\mathrm{ms}$ the cloud was tightly confined in the y direction because this is the axis with strongest frequency.

Source: By the author.

6.3 Bose-Einstein condensation of sodium atoms

In February 1th of 2016 we obtained the first BEC of sodium atoms using an OPT configuration in our laboratory. As described above, the condensation transition is observed at 1.1 MHz, giving a critical temperature of $T_c = 1\,\mu$K, with a number of condensed atoms around 2.5×10^5 (normally the condensed atom fraction is about 50%). Figures 6.3.1 and 6.3.2 show two of the several possibilities of condensation geometries in the OPT trap. One of these possibilities is the formation of two BEC in each of the two well potentials created when the plug beam deviated from the perfect Gaussian profile in the wings, as described by (48), and shown in Figure 6.3.1. The other possibility is the production of a BEC in a single well potential, as shown in Figure 6.3.2, obtained when the the plug beam is slightly misaligned, breaking the symmetry of the total potential, and then leading to the single BEC.

Figure 6.3.2 shows the bimodal fit of the cloud, the Gaussian fit corresponding to the thermal cloud and the Thomas-Fermi fit tho the distribution of the condensed sodium atoms.

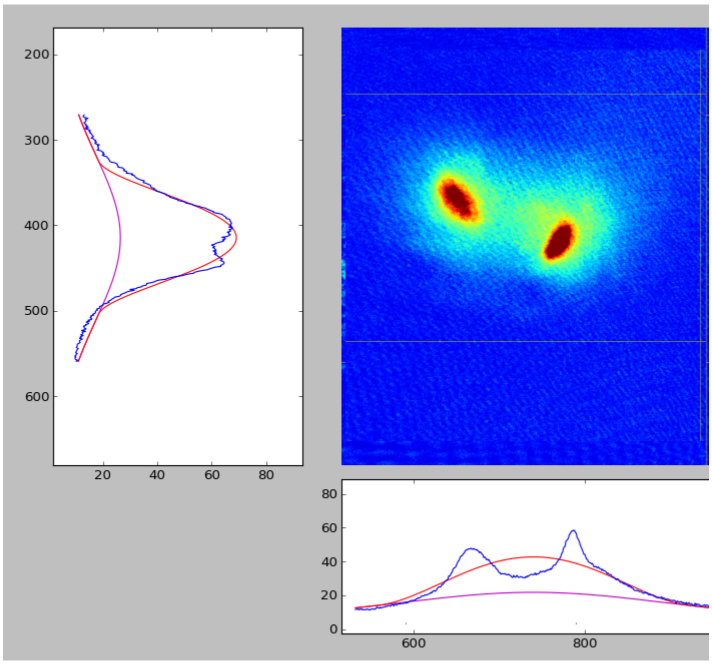

Figure 6.3.1 – BEC of sodium atoms in an OPT configuration. The two BECs corresponds to atoms in the two potential wells created by the plug beam.
Source: By the author.

As mentioned above, for transferring most of the atoms to a single well potential it is necessary to slightly displace the plug beam away from the center of the trap, this small misalignment creates an asymmetric potential, in which one of them is deeper than the other. Then, the atoms are preferentially transfer to the deeper potential well.

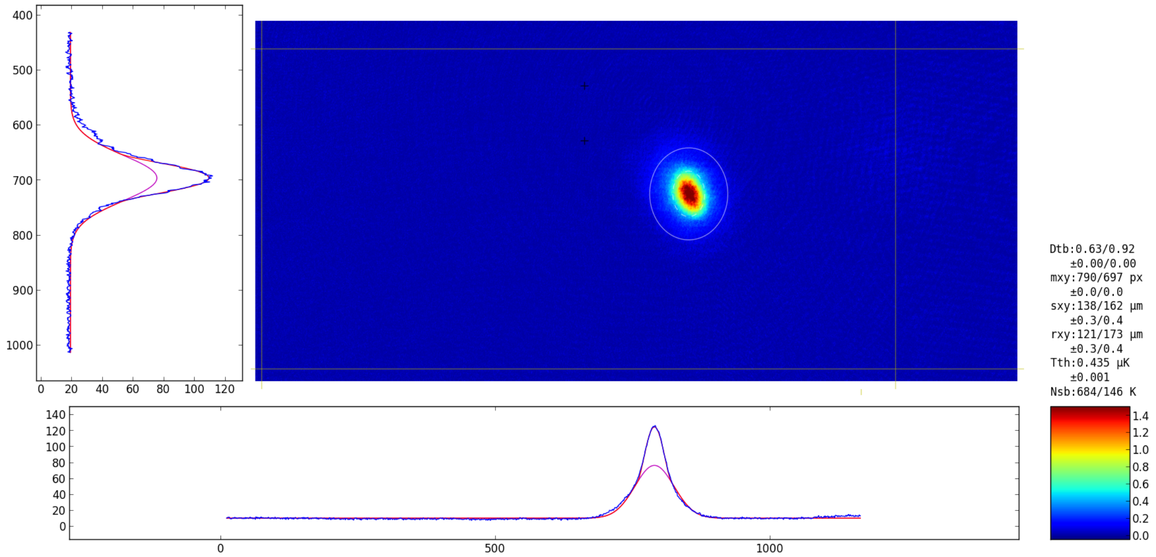

Figure 6.3.2 – Single BEC in a OPT configuration. The single BEC is obtained slightly misalignment the plug beam from the center of the trap. This created a situation in which the atoms are transfer to the deeper potential well. The temperature of the BEC is 435 nK, the total number of atoms is 6.84×10^5, and the condensate fraction is just around of 30. Here, $TOF = 15\,\mathrm{ms}$

Source: By the author.

6.4 Frequencies of the OPT

Another essential parameters are the trap frequencies. The geometry and other dynamical aspects of the BEC are determined by these frequencies, as for example, the critical temperature. (48) To estimate the oscillation frequencies of our OPT trap we used the parametric heating method. This method consists in exciting the parametric oscillation of the trapped cloud modulating the current of the quadrupole coils that produce the magnetic field. In this way, the cloud position and the trap frequencies are modulated.

The current was modulated at the end of the evaporation process. The modulation was applied during 500 ms with and amplitude of 13% the value of the current used for the MT. After this, the current (and then the magnetic field) was maintained constant during 100 ms. In this thermalization time, the excitation is transformed in heating. The schematic diagram including this process in the experimental sequence is shown in Figure 6.4.1.

The modulation of the current is given by (51)

$$I(t) = I_0 \left[1 + \epsilon \sin\left(2\pi\nu_{mod} t\right)\right], \tag{6.4.1}$$

where $\epsilon = 13\%$ is the amplitude of the modulation, ν_{mod} is the modulation frequency, I_0 is the constant current of the quadrupole coils, and t is the time the modulation is applied.

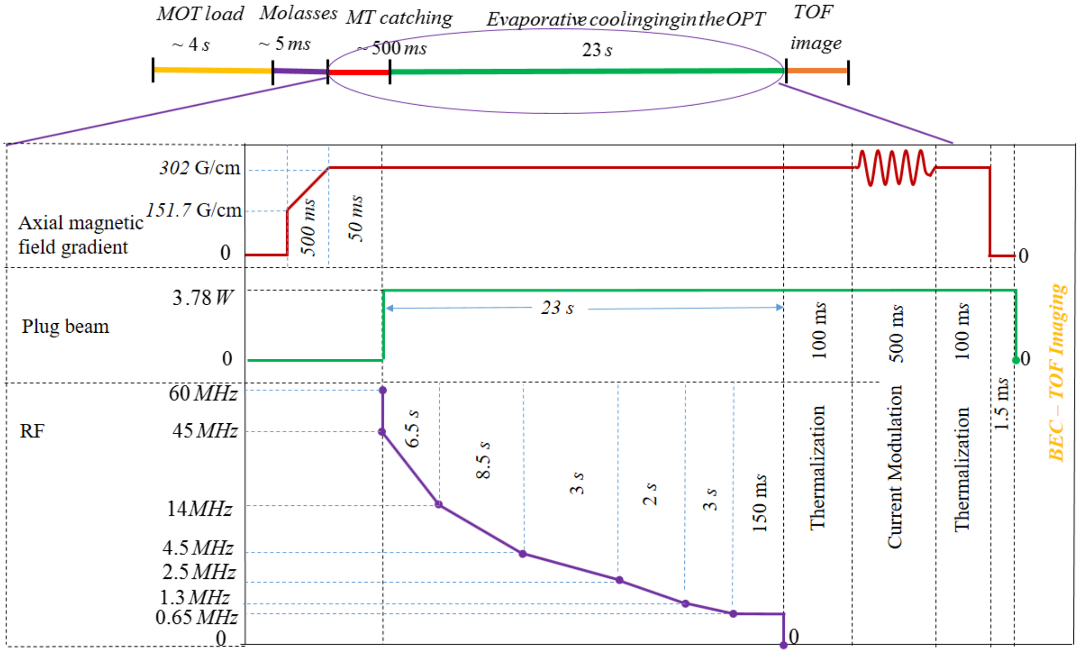
MOT load
~ 4 s
Molasses
~ 5 ms
MT catching
~500 ms
Evaporative coolinginginthe OPT
23 s
TOF
image
Axial magnetic field gradient
302 G/cm
151.7 G/cm
0
500 ms
50 ms
0
Plug beam
3.78 W
0
23 s
0
RF
60 MHz
45 MHz
14MHz
4.5 MHz
2.5 MHz
1.3 MHz
0.65 MHz
0
6.5 s
8.5 s
3 s
2 s
3 s
150 ms
0
100 ms
Thermalization
500 ms
Current Modulation
100 ms
Thermalization
1.5 ms
BEC – TOF Imaging

Figure 6.4.1 – Schematic diagram for the temporal sequence including the current modulation to measure the OPT frequencies using the parametric heating method.

Source: By the author.

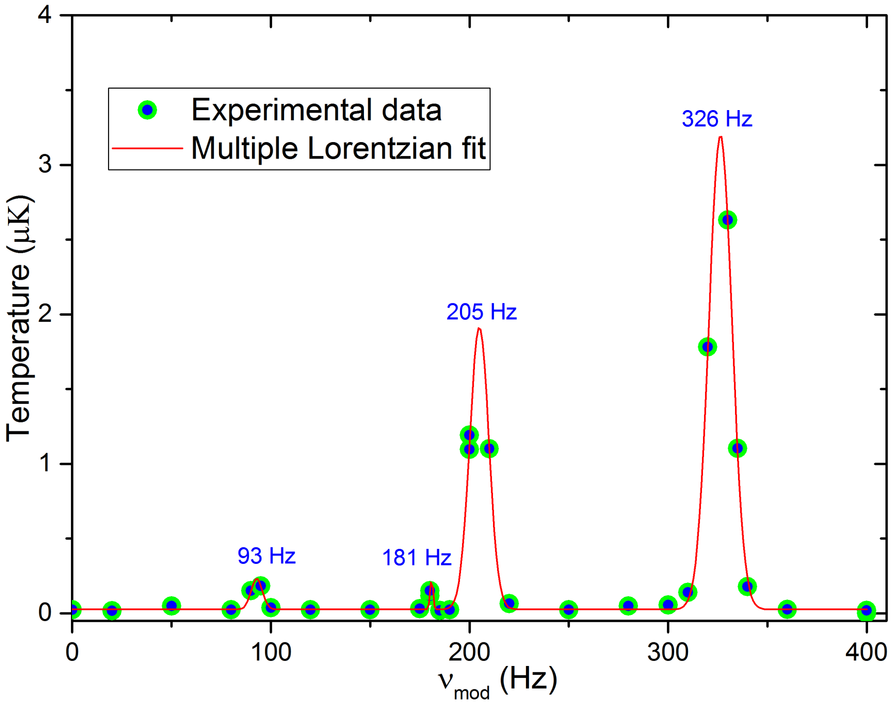

Figure 6.4.2 – Trap frequencies of the OPT. We found four peaks when using the method of parametric heating.

Source: By the author.

Fig. 6.4.2 shows the frequencies found for the OPT trap using the parametric heating method. We see that when the frequency of the current modulation (magnetic field) achieves a value of one of the parametric frequencies of the trap, the atoms will oscillate in resonance with this external perturbation, leading to an increase in temperature. This resonance has as consequence the heating or even the ejection of these atoms from the trap. Therefore, for measuring the resonance frequencies, it is possible to measure either the temperature increase or the atom number. In our case we measured the temperature, as it seems to have a nicer behavior. This measurement was performed using the TOF method with $t_{TOF} = 10\,\text{ms}$. The expected frequencies of the OPT trap are given by Equation (5.2.15) with values given by Equation (5.2.16).

So far, we have achieved the Bose-Einstein condensation of sodium atoms with a number of condensed atoms of 2.05×10^5 and a temperature of $435\,\text{nK}$. In the next chapter we will performed some studies on non-linear light-matter interaction, specifically, cooperative absorption of two photons by two trapped sodium atoms (2P2A).

Chapter 7

Two-photon two-atom processes

In this chapter, I discuss briefly the concepts needed to understand the two-photon cooperative absorption by two interacting atoms (2P2A). I also describe the model proposed by several authors (71–74) to study the system under consideration. Also, I explain the necessary conditions for the occurrence of 2P2A cooperative absorption. Other effects, like light forces, which correspond to single-photon single-atom interactions (1P1A) may be present in our experiment, for this reason, a short review of these effects is given in this chapter. Deeper discussions can be found in the references given in this chapter.

7.1 Introduction

Non-linear light-matter interaction has been an important subject with a growing relevance after the advent of the laser that allowed the exploration of this type of phenomena requiring high light intensities. (75) Two-level systems in the presence of a laser field became the most simple, suitable and interesting arrangement to serve as a model to handle more complicated systems. (76)

Since the development of the laser, non-linear effects, and specially two-photon absorption has been widely studied (75). This allowed the study of energy levels that can not be accessed using one-photon absorption techniques, i.e., states with the same parity are now accessible with this technique. In two-photon absorption process, two-photon with individual energy $\hbar\omega$ can be absorbed by one atom if the resonance condition for the transition energy is fulfilled, $2\hbar\omega = \hbar\omega_0$, where $\hbar\omega_0$ is the resonance atomic transition. (75) This was extended to the case dealing with a system of two atoms and one photon. (77) The energy of the excited state of each atom is $\hbar\omega_a$ and $\hbar\omega_b$, for atoms A and B, respectively. Then, one photon of energy $\hbar\omega$ is absorbed when the condition $\hbar\omega = \hbar\omega_a + \hbar\omega_b$ is satisfied. The first demonstration of this effect was accomplished by Varsanyi and Dieke (78) in a rare earth crystal of Pr^{3+} and was explained using first-order perturbation theory by Dexter (77), evidencing that dipole-dipole (dd) interaction leads to the simultaneous excitation of atoms.

When the two effects described above are considered together, we then are dealing with cooperative absorption of two-photon by pair of atoms (2P2A), i.e., two interacting atoms can absorb two photons when the resonance condition, now given by $2\hbar\omega = \hbar\omega_a + \hbar\omega_b$ is fulfilled. It is worth to mention that also, in this case, both photons are far-off resonance with the atomic transition but the sum of the energy of the two photons are equal to the energy to the couple excited stated.

Cooperative effects have been seen as a possibility to probe pair interactions (71) since the initial studies in crystals. Several theoretical and experimental works have been performed (71, 73) on this topic. The dynamics of dense atomic systems was studied by many authors, modeling the system as pair of atoms interacting with a laser field. (77) The relevance of cooperative effects was based on the fact that it could reveal interesting and beautiful features which are absent in the case of non-interacting atoms, as for instance, the appearance of new resonances in the absorption and fluorescence spectrum (79–81). In (79) the new resonances are explained taking into account the dressed level description of the system consisting of two atoms interacting with a laser field. Many confirmations about the creation of novel induced resonances at the sum frequency of the atomic transitions due to *dd*-interactions have been given in works investigating optical emission (82, 83) and absorption (84) processes in dense media.

Cooperative effects also led to the study and production of special types of light. This kind of light is produced from the spontaneous decay of atom pairs cooperatively excited, then, it is possible to study quantum beats produced in the intensity and intensity correlations. (85) Also, the squeezing properties of the emitted fluorescence (86) have also been shown to yield information about the dynamical correlations between atoms.

The effect of cooperative absorption of two-photon by two interacting atoms was first treated theoretically by Rios Leite and C.B. Araujo in 1980 (71) and D. L. Andrews and M. J. Harlow in 1983 (72), being experimentally demonstrated in a mixture in 1981 in crystal of Ba/Ti. After these initial works, the subject of cooperative effects in crystals and other atomic systems gained more attention, and in 2002 Hettich et al. (87) using cryogenic laser spectroscopy showed several interesting results. First, they succeeded in the identification of two individual molecules looking at the fluorescence produced after cooperative absorption of two-photon by pairs of molecules, in a configuration identical to that described by Rios Leite and C. B. Araujo. (71) With this technique, they were able to detect single terrylene molecules embedded in a para-terphenyl crystal at a temperature of $T \simeq 1.4\,\mathrm{K}$. In the same work, they determined the photon statistics of the fluorescence light emitted after the molecules been excited by two-photon cooperative absorption, showing photon-bunching phenomenon. (87, 88)

Also, after the improvement of new techniques in cooling, trapping and confining neutral atoms and few ions at small interatomic separations in ion and neutral atom traps (89) the phenomena of cooperative effects gained a renewal interest due to the tunability and control these systems offer. For example, in ion traps the distance between a pair of ions could be manipulated modifying directly the strength of the interaction. Also, these experimental systems allow the clearer separation between the effects due to correlations between the atoms, or cooperativity, and those due to just one-atom.

In 2012, which correspond to the beginning of this PhD work, we demonstrated in one these systems, specifically in a magneto-optical trap containing around 10^{10} atoms, the cooperative absorption of two-photon by pairs of colliding cold sodium atoms. (13) In this work, clear evidence about the cooperative absorption is given, and a improvement of the model described above (71) was performed taking into account the spatial dependence of the frequency in the real potential curves generates due to the atomic interaction. This opened a door to study and better understanding of cold collisions and determination of scattering length in cold atom systems. (40)

Theoretical works has been also developed in other very interesting systems, as for instance, pair of atoms in optical cavities (90), where the radiation background enclosing the atoms modifying the physical *dd*-interaction. In several interesting papers was investigated the possibility of two-photon cooperative absorption without the physical *dd*-interaction, and using particular entangled states of the excitation light to induce the cooperative two-photon absorption (91, 92), i.e., the entangled states of the light now carry out the role of the *dd*-interaction or mechanism of correlation or information transfer in the system. This could be of certain relevance in quantum optics and quantum information experiments, where using these systems specific photon states can be put in evidence. (74) In this sense, the group at NIST-Boulder has shown in a relatively recent article (93) that collective resonances can induce double-quantum excitations. Theoretically they considered atomic *dd*-interaction together with molecular dynamic simulations to described the experimental data.

A very nice PhD thesis (74), written by Z. Zheng, review all the topics mentioned above and presented a theoretical description of the 2P2A cooperative absorption in the case where there is physical interaction set out by *dd*-interaction and in the case where this interaction is absence but considering certain correlated and entangled states of the exciting light.

Furthermore, these systems could be explored in order to create new ways of generating pair of correlated photons and entangled atomic states as demonstrated by J. Beugnon et al. (94, 95) with independently trapped neutral atoms and P. Maunz (96) in atomic ions.

The extension of cooperative effects in Bose-Einstein condensates could be an interesting tool to explore aspects still unexplored in relation to non-linear light-matter interaction and non-linear interaction between the atoms in the BEC, study of particles correlations (97) and exploration of the spatial coherent of the BEC, among others.

7.2 Cooperative absorption of two-photons by two two-level interacting atoms

Let us consider a two two-level atom system interacting via dipole-dipole ($d{-}d$) interaction and in the presence of a laser field providing photons of frequency ω (71). Each atom has a ground state represented by $|g_i\rangle$ and the excited stated represented by $|e_i\rangle$, where $i = 1, 2$ are the index referring to atom labeled as 1 or 2 (or A and B), the energy of each state being $\hbar\omega_i$, decay constant Γ_i and electric dipole moment μ_i. When considering the composed system of two-atom interacting the wavefunction is given by $|\alpha_i\beta_j\rangle$, with $\alpha, \beta =$ g and e and $i, j = 1$ and 2. The energy of the composed system is given by $\hbar\omega_{\alpha_i} + \hbar\omega_{\beta_i}$. The energy levels for the individual atoms and composed system are shown in Figure 7.2.2. As mentioned in (71), the atomic interaction is considered so strong to allow cooperative effects between the atom pair but weak enough in order to consider the wavefunction of the composed system as a combination of the wavefunctions of the individual atoms when there is no interaction. If this were not the case, modifications in the wavefunction would have to be taken into account due to the overlapping of those wavefunctions.

Considering the interaction Hamiltonian of the two-photon two-atom system as being (98)

$$H_I = -e\vec{r}_1.\vec{E}cos(\omega t) - e\vec{r}_2.\vec{E}cos(\omega t) + \frac{e^2}{\rho^3}\left[x_1x_2 + y_1y_2 - 2z_1z_2\right], \tag{7.2.1}$$

where ρ is the relative distance between the atoms, x_1, x_2, y_1, ... are the coordinates of each electron with respect to its nucleus, and $\vec{E}$ is the applied electric field, in this case referring to the laser light. The interaction of each single-atom with the laser field is accounted in the first two terms, while the atomic interaction is given by the last term.

With all these ingredients Rios Leite and C. B. Araujo (71) found the expression for the absorption cross-section of the total spectrum of two-photon two-atom system (TPTA) as being

$$\begin{aligned}\sigma_{TPTA} \propto & \left[\frac{(\mu\epsilon/2\hbar)^2}{(\omega-\omega_1)^2+\left(\frac{\Gamma}{2}\right)^2}\right]\left[\frac{(\mu\epsilon/2\hbar)^2}{(\omega-\omega_1)^2+\left(\frac{\Gamma}{2}\right)^2}\right]\times \\ & \left[1+\frac{4\langle H_I\rangle^2/\hbar^2}{(2\omega-\omega_1-\omega_2)^2+\left(\frac{\Gamma}{2}\right)^2}+\frac{4(2\omega-\omega_1-\omega_2)\langle H_I\rangle/\hbar}{(\omega-\omega_1)^2+\left(\frac{\Gamma}{2}\right)^2}\right],\end{aligned} \tag{7.2.2}$$

where ϵ is the electric field amplitude of the external field, which is treated as a classical electromagnetic field of frequency ω. The expression above was found using the assumptions $\Gamma_1 = \Gamma_2 = \Gamma$, $\mu_1 = \mu_2 = \mu$, and $\langle e_1g_2|\, H_I \,|g_1e_2\rangle = \langle g_1e_2|\, H_I \,|e_1g_2\rangle$ and second-order perturbation in the external field. (71) The wave functions for the interacting atoms are described in function of the wavefunction of the non-interacting atoms using first-order correction in the perturbative calculation and are given by

$$|\chi_{ij}\rangle = |\alpha_i\beta_j\rangle + \sum_{(\kappa_j,\varphi_j)\neq(\alpha_i,\beta_j)} \frac{\langle\kappa_i\varphi_j|\, H_I \,|\alpha_i\beta_j\rangle}{\hbar\omega_{\kappa_i\varphi_j} - \hbar\omega_{\alpha_i\beta_j}} |\kappa\varphi\rangle \,. \tag{7.2.3}$$

In this representation the atomic wave function are modified, but the energy levels remained unchanged.

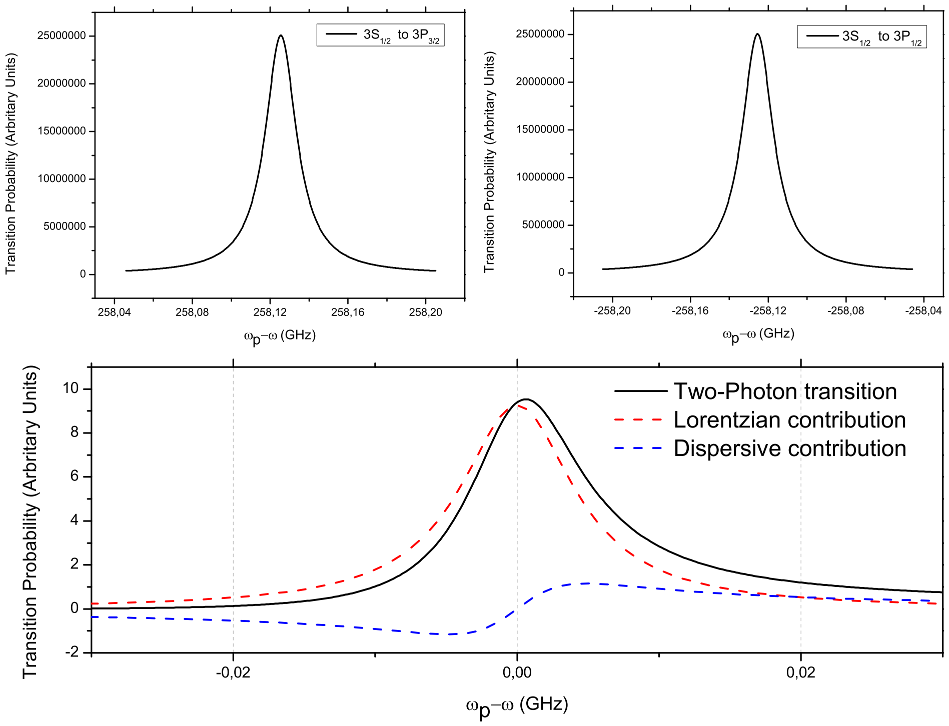

Figure 7.2.1 – Theoretical curves using Equation (7.2.1) of the transition probability as a function of the detuning of the excitation light. The peaks shown in the top correspond to the single photon absorption, while the curve in the bottom corresponds to the two-photon absorption. This last peak has two contributions: a Lorentzian and a dispersive part.
Source: Paiva (99)

As pointed out by the Rios Leite and C. B. Araujo (71), the first two terms in brackets in Equation (7.2.2) refer to the single-photon transition probability for atom 1 or 2, having the typical Lorentzian shape. The last bracket contain the expression responsible for describing the 2P2A cooperative absorption. The number one inside this last brackets warrants the recovering of the Lorentzian profiles when there is no interaction between the atoms, i.e. $\langle H_I\rangle = 0$. The second and third terms in the last bracket represent the 2P2A cooperative absorption having an asymmetric lineshape with center exactly at $\omega = (\omega_1 + \omega_2)/2$. As also discussed in (71), the last term in the last bracket account for the asymmetric in the lineshape, which is related to a Fano profile. (71, 100) The total lineshape given by the last two terms is a consequence of the interference between the two transition amplitudes via $|g_1 e_2\rangle$ and $|e_1 g_2\rangle$ intermediate states, one of them being perturbed by the atom-atom interaction. Figure 7.2.1 shows this situation.

From (71) the resonance condition for the 2P2A effect is from Equation (7.2.2) $2\omega - \omega_1 - \omega_2$, which express that when $\omega = (\omega_1 + \omega_2)/2$ the compose system has an absorption peak. Particularly at this frequency there is an enhancement of the energy transfer due to that the defect of energy for one transition is compensated by the excess of energy in the other transition of the other atom, which can be expressed as $\omega - \omega_1 = -(\omega - \omega_2)$.

Let's turn to the treatment performed by Z. Zheng (74), in which it is described the two two-level atoms interacting with a quantized field, and performing perturbative calculations it is found the transition probability for the 2P2A system. Figure 7.2.2 shows the scheme of energy levels of the two two-level atom system when considering *dd*-interaction.

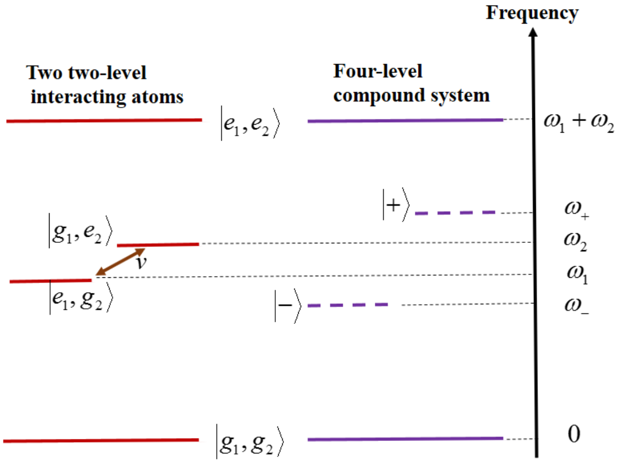

Figure 7.2.2 – Atomic level scheme for a pair of interacting two-level atoms (left), and when the compound system is treated as a four-level system.
Source: Zheng (74)

The atomic Hamiltonian for the atoms when there is no interaction is taken as (74)

$$H_{Ind-At} = \hbar\omega_1 |e_1\rangle\langle e_1| \otimes \hat{1}_2 + \hbar\omega_2 \hat{1}_1 |e_2\rangle\langle e_2|, \tag{7.2.4}$$

where the energy of the ground states were taken to be zero. In this form this Hamiltonian can be represented in matrix form as

$$H_{Ind-At} = \hbar \begin{bmatrix} 0 & 0 & 0 & 0 \\ 0 & \omega_2 & 0 & 0 \\ 0 & 0 & \omega_1 & 0 \\ 0 & 0 & 0 & \omega_1 + \omega_2 \end{bmatrix}. \tag{7.2.5}$$

The eigenstates of this Hamiltonian are for the ground state $|g\rangle = |g_1\rangle \otimes |g_2\rangle$, for the intermediate states $|g_1\rangle \otimes |e_2\rangle$, $|e_1\rangle \otimes |g_2\rangle$, and for the excited state $|e\rangle = |e_1\rangle \otimes |e_2\rangle$. The eigenfrequency for the ground state in this basis is zero, for the intermediate states ω_1 and ω_2, and for the excited state $\omega_1 + \omega_2$.

To take into account the *dd*-interaction, $V_{dd}\left(\vec{r}_1, \vec{r}_2\right)$, this term has to be added to H_{Ind-At} to produced the description of the combined system, then the total atomic Hamiltonian carrying out the interaction reads (74)

$$H_{At} = \hbar\omega_1 \left|e_1\right\rangle \left\langle e_1\right| + \hbar\omega_2 \left|e_2\right\rangle \left\langle e_2\right| + \hbar\vartheta \left(\left|e_1 g_2\right\rangle \left\langle g_1 e_2\right| + \left|g_1 e_2\right\rangle \left\langle e_1 g_2\right|\right), \tag{7.2.6}$$

where the interaction Hamiltonian is written as $V = \hbar\vartheta \left(\left|e_1 g_2\right\rangle \left\langle g_1 e_2\right| + \left|g_1 e_2\right\rangle \left\langle e_1 g_2\right|\right)$ (74) and in matrix form

$$H_{At} = \hbar \begin{bmatrix} 0 & 0 & 0 & 0 \\ 0 & \omega_2 & \vartheta & 0 \\ 0 & \vartheta & \omega_1 & 0 \\ 0 & 0 & 0 & \omega_1 + \omega_2 \end{bmatrix}. \tag{7.2.7}$$

As also, pointed out in that work (74), the states $|g\rangle = |g_1\rangle \otimes |g_2\rangle = |g_1 g_2\rangle$ and $|e\rangle = |e_1\rangle \otimes |e_2\rangle = |e_1 e_2\rangle$ are taken as non-interaction, then, being eigenstates of H_{At}. The atomic *dd*-interaction is related to that situations when one atom is excited and the other is in the ground state and vice-versa. As a consequence of this, it is necessary to diagonalized H_{At}, obtaining the new eigenstates given by (74)

$$|+\rangle = \frac{\vartheta \left|g_1 e_2\right\rangle + \left(\omega_+ - \omega_2\right) \left|e_1 g_2\right\rangle}{\sqrt{\left|\vartheta\right|^2 + \left(\omega_+ - \omega_2\right)^2}}, \tag{7.2.8}$$

$$|-\rangle = \frac{\left(\omega_+ - \omega_2\right) \left|g_1 e_2\right\rangle - \vartheta \left|e_1 g_2\right\rangle}{\sqrt{\left|\vartheta\right|^2 + \left(\omega_+ - \omega_2\right)^2}}, \tag{7.2.9}$$

with eigenfrequencies

$$\omega_\pm = \frac{\omega_1 + \omega_2}{2} \pm \sqrt{\left(\frac{\omega_1 - \omega_2}{2}\right)^2 + \left|\vartheta\right|^2}. \tag{7.2.10}$$

As mentioned in (74) these eigenstates generated due to the interaction are entangled states, as is certainly expected that at least exist correlations between the interacting atoms. The sum of the eigenfrequencies are $\omega_+ + \omega_- = \omega_1 + \omega_2$, and then $\omega_+ - \omega_2 = -\left(\omega_- - \omega_1\right)$, which is exactly the condition for 2P2A resonance. The Hamiltonian in this basis is given by (74)

$$H_{At-dia} = \hbar\omega_- \left|-\right\rangle \left\langle -\right| + \hbar\omega_+ \left|+\right\rangle \left\langle +\right| + \hbar\omega_e \left|e\right\rangle \left\langle e\right|. \tag{7.2.11}$$

The decay rates of the intermediate states generated by the interaction are given by (74, 87)

$$\Gamma_+ = a^2\Gamma_1 + b^2\Gamma_2 + 2ab\Gamma_{12}, \tag{7.2.12}$$

$$\Gamma_- = a^2\Gamma_2 + b^2\Gamma_1 - 2ab\Gamma_{12}, \tag{7.2.13}$$

here Γ_1 is the decay rate of the state $|e_1 g_2\rangle$ and Γ_2 the decay rate of the state $|g_1 e_2\rangle$ in the case of non-interacting atoms. The values a and b comes from Equations (7.2.8) and (7.2.9) (74)

$$|+\rangle = a(\vartheta)|e_1 g_2\rangle + b(\vartheta)|g_1 e_2\rangle, \tag{7.2.14}$$

$$|-\rangle = a(\vartheta)|g_1 e_2\rangle + b(\vartheta)|e_1 g_2\rangle, \tag{7.2.15}$$

with $a^2(\vartheta) + b^2(\vartheta) = 1$.

The transition rate for this system at long time is given by (74)

$$R^{2P2A}_{transition} = \frac{f_1^2 f_2^2}{\left[(\omega-\omega_+)^2 + \Gamma_+^2\right]\left[(\omega-\omega_-)^2 + \Gamma_-^2\right]}\left|1 + \frac{\vartheta}{\omega - (\omega_+ + \omega_-)/2 + i\Gamma}\right|^2, \tag{7.2.16}$$

with $\Gamma = (\Gamma_+ + \Gamma)/2$.

In the next section, I show the realization of the experiment of cooperative absorption in a magneto-optical trap, and the verification of the theory described so far.

7.3 Cooperative absorption of two-photons by two sodium atoms in the magneto-optical trap

The experiment of cooperative absorption of two photons in a magnetic trap and BEC of sodium atoms is the continuation of the work realized in 2012 at the second year of my PhD. In that experiment we used a magneto-optical trap to provide the atoms to be excited. Initially, the atoms in the MOT are kept trap all the time and then we shined the cloud with a laser beam which provides the photons with the frequency $\omega_{2P} = \left(\omega_{P_{1/2}} + \omega_{P_{3/2}}\right)/2$, i.e., with the frequency in the middle of the D1 and D2 line transition. A pair of atoms in the MOT will interact via *dd*-interaction producing a new set of energy levels, as mentioned in section 7.2. Two-photons with the sum of their frequency being equal to the excited state energy of the composed system, can excite the pair of atoms if they are interacting, providing a mechanism to transfer energy or excitation. Figure 7.3.1 shows an scheme of the potential $V(r)$ of the atoms and the energy sum of the two-photons.

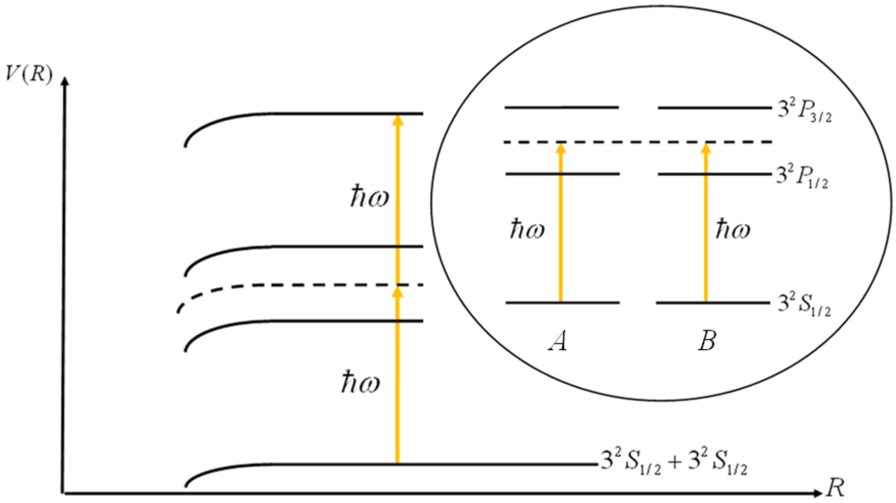

Figure 7.3.1 – Energy levels of the individual atoms and potential energy curve of the interaction. The two photons can excite the pair of atoms if they are interacting.
Source: By the author.

To perform the experiment we used a dye laser, able to scan the probe frequency (ω_{2P}) in a very wide range. When this probe laser is scanned around all this frequency interval a curve similar to that presented in Figure 7.2.1 is expected. Experimentally, to count how many atoms were excited in the MOT by means of the 2P2A cooperative transition, we directly count ions using an ion counter, which is one of the most sensitive ways of measuring low intensity signals. This technique works as follows: when the probe frequency is scanned through a transition, let's suppose the D1 line ($3^2S_{1/2} \rightarrow 3^2P_{1/2}$), the atoms will be excited following a Lorentzian profile for the absorption as a function of the detuning. When an atom is in the excited state ($3^2P_{1/2}$), an ionization laser beam (405 nm) with enough energy to lead the atom to the continuous of states is applied, ionizing the atom. Inside the chamber, there is a metal plate that produces an strong electric field fed with a voltage of $-2500\,\mathrm{V}$. This electric field will accelerate any ion to an ion counter (channeltron), where the ion is registered. Figure 7.3.2 shows the process of ionization of each transition.

Figure 7.3.3 shows the experimental sequence implemented to realized the measurements. In the temporal window A we realized a background counting and in B we performed the excitation and detection of excited atoms. Subtracting this two signals, we obtained the total number of atoms excited by the probe beam.

The signal obtained from this experiment is shown in Figure 7.3.4. The frequency scan was realized around each transition, and the number of excited atoms using ion counting, as explained before. The higher peaks at the left and right of the graphic correspond to the transitions $3^2S_{1/2} \rightarrow 3^2P_{1/2}$ and $3^2S_{1/2} \rightarrow 3^2P_{3/2}$, respectively. The ions

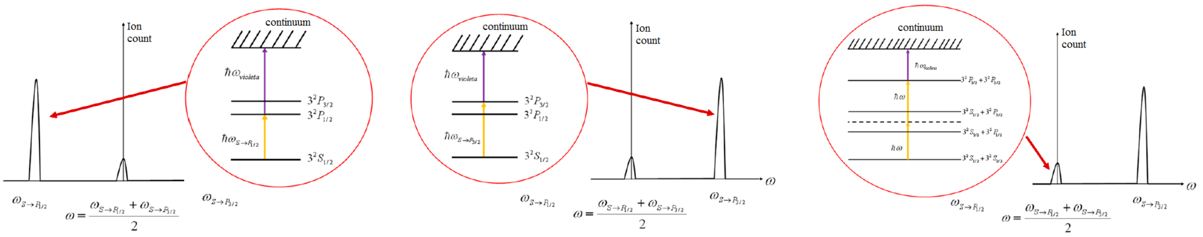
Ion count
continuum
$\hbar\omega_{violeta}$
$3^2P_{3/2}$
$3^2P_{1/2}$
$3^2S_{1/2}$
$\omega_{S\to P_{1/2}}$
$\omega = \frac{\omega_{S\to P_{1/2}} + \omega_{S\to P_{3/2}}}{2}$
$\omega_{S\to P_{3/2}}$
ω
$\hbar\omega$

(a) (b) (c)

Figure 7.3.2 – Ionization process of the excited atoms after the absorption of photons of the probe beam.

Source: By the author.

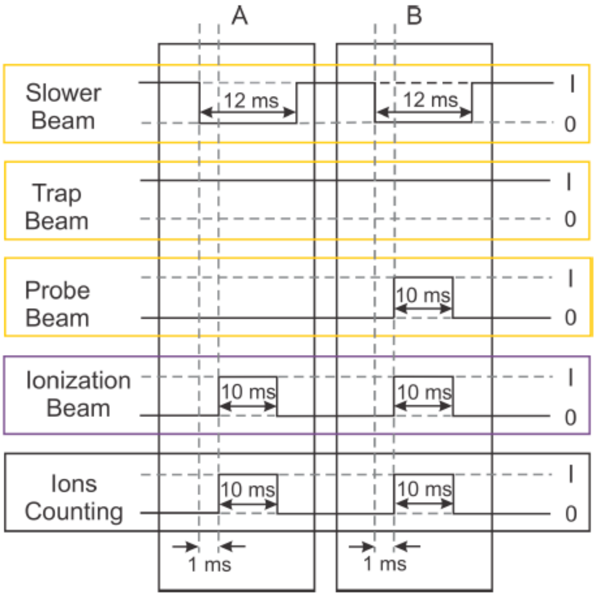
A
B
Slower Beam
12 ms
12 ms
I
0
Trap Beam
I
0
Probe Beam
10 ms
I
0
Ionization Beam
10 ms
10 ms
I
0
Ions Counting
10 ms
10 ms
I
0
1 ms
1 ms

Figure 7.3.3 – Experimental sequence for the excitation and detection of the cooperative absorption of two photons in the MOT of sodium atoms.

Source: PEDROZO-PEÑAFIEL (13)

counted for this peaks are ~ 6000 in an integration time of 10 ms. The peak corresponding to cooperative absorption was expected to be 10^3 times smaller than the single photon transition peaks, and this is clearly observed in the center of Figure 7.3.4a. The high of this peak, which corresponds to the 2P2A effect is in complete agreement with the theoretical description given by Rios Leite et al. (71), for two-level systems.

With this experimental data, we realized a fit of the theoretical curve given in (71) for comparison with our experimental results. The black line-dot curve is the fit following Equation (7.2.2), and we see that there is a displacement in frequency with respect to the experimental curve. We explained this discrepancy saying that in this theoretical model the dependence of the frequency on the atomic separation was not taken into account. To improve the description of this equation, we introduced the dependence of the frequency with the distance (separation between a pair of interacting atoms) in Equation (7.2.2). With this modification, the transition probability reads

$$\begin{aligned}
PA \;\propto\; & \int_0^\infty dR \left[\frac{\left(\mu_{P_{1/2}}E/2\hbar\right)^2}{\left(\omega_{P_{1/2}} - \frac{C^{(3)}_{1/2}}{R^3} - \omega\right)^2 + (\Gamma/2)^2}\right]\left[\frac{\left(\mu_{P_{3/2}}E/2\hbar\right)^2}{\left(\omega_{P_{3/2}} - \frac{C^{(3)}_{3/2}}{R^3} - \omega\right)^2 + (\Gamma/2)^2}\right] \times \\
& \left[1 + \frac{4\left\langle H_I\right\rangle^2/\hbar^2}{\left(2\omega - \omega_{P_{1/2}} - \omega_{P_{3/2}} - \frac{C^{(3)}_{1/2}}{R^3} - \frac{C^{(3)}_{3/2}}{R^3}\right)^2 + \Gamma^2}\right. \\
& \left. + \frac{4\left(2\omega - \omega_{P_{1/2}} - \omega_{P_{3/2}} - \frac{C^{(3)}_{1/2}}{R^3} - \frac{C^{(3)}_{3/2}}{R^3}\right)\left\langle H_I\right\rangle/\hbar}{\left(2\omega - \omega_{P_{1/2}} - \omega_{P_{3/2}} - \frac{C^{(3)}_{1/2}}{R^3} - \frac{C^{(3)}_{3/2}}{R^3}\right)^2 + \Gamma^2}\right]
\end{aligned} \tag{7.3.1}$$

Fitting this equation (Figure 7.3.4b) we can see the agreement in frequency and shape of this theoretical curve with the experimental one. With this we can conclude that our simple model is adequate for the effect when considering real atoms, and not just two-level atoms with constant transition frequency when interacting. Also, we can conclude that we successfully demonstrated the cooperative absorption in a magneto-optical trap, which was the first demonstration of this effect in this kind of systems.

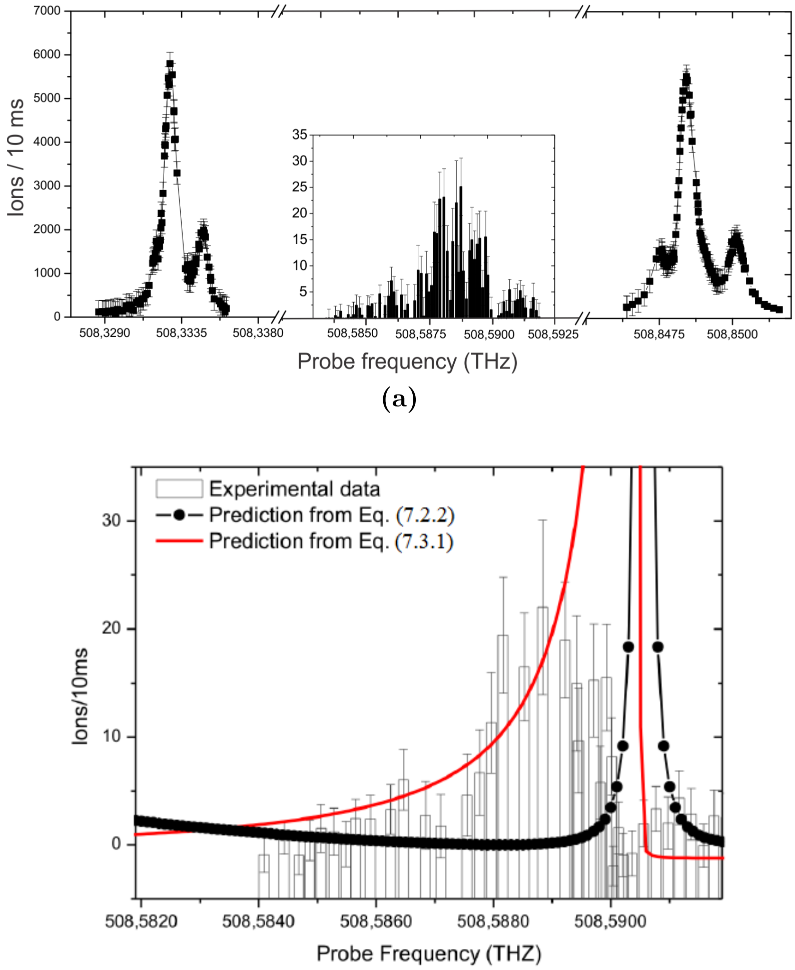

(a)

(b)

Figure 7.3.4 – Experimental results for the cooperative absorption of two-photon in a MOT of sodium atoms. (a) Frequency scan of the D1 and the D2 line produces the side and big peaks, and the frequency scan around the two-photon frequency produce a peak of 1000 times smaller than the previous ones. (b) The cooperative absorption peak is evident, and we fit the theoretical (black line) curve together with the experimental data and our correction to the theoretical model (red line). In this way we demonstrated the cooperative absorption effect in cold sodium atoms.

Source: PEDROZO-PEÑAFIEL (13)

7.4 2P2A cooperative absorption in a magnetic trap

After we finished the construction and characterization of the new experimental system for producing Bose-Einstein condensates of sodium atoms, we started to re-explore the cooperative effect in the magnetic trap (MT). As the phenomenon is strongly dependent on the density of the sample, we expected to improved the signal obtained in the magneto-optical trap and even more if measurements are realized in a BEC.

The first attempt to perform the measurement in the MT is shown below.

For measuring the cooperative absorption of two-photon in this system we cannot use the ion counter anymore. This is mainly due to vacuum requirements and other technical issues. Instead, we decided to measure the cooperative absorption using the trap loss technique. In this technique, we send the excitation beam during a variable pulse time when the atoms are still trapped in the MT. The excitation beam is expected to transfer the atoms to the states $3^2P_{1/2}$ and $3^2P_{3/2}$, and in this way the atoms will be ejected from the trap. Measuring the initial number of trapped atoms, and the number of atoms that remained in the trap we can determined how many atom pairs made the transition to the excited states and ejected from the trap, this is the reason of the name of the technique. The number of atoms is determined using the time-of-flight (TOF) technique explained in chapter 5.

In the first attempt to observe some signal due to 2P2A cooperative effect, we send the probe beam at the two-photon frequency (ω_{2P}) to a evaporated cloud until 4.5 MHz with $\sim 2.0 \times 10^7$ atoms and a temperature of $\sim 16\,\mu$K.

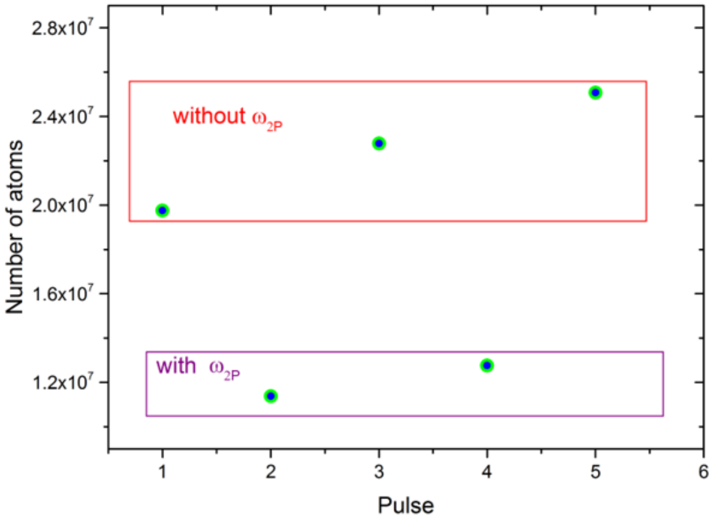

Figure 7.4.1 – Each point represent the averaged of 6 images when the excitation pulse is present or not. For instance, the first point is made without the excitation beam, the second with the excitation and so on.
Source: By the author.

Fig. 7.4.1 shows the attempt to observe some effect of the cooperative effect in a MT. The excitation pulse was shine in the MT for 2 seconds and was focused to $\sim 250\,\mu$m at the position of the atomic cloud. We alternate the measurement, i.e., in the first measurement we kept the excitation beam OFF and in the second one we kept the excitation beam ON. At a first look, it seems that we observed some signal of the two photon absorption, but a carefully look shows that there are other effects that masked our signal. These effects are the dipole force and/or radiation pressure force, which are normally stronger than the

2P2A effect.

Figure 7.4.2 shows the data concerning to number of atoms as a function of the pulse time. With the exponential decay of this curve, we can obtain the rate at which we lost the atoms and compare with the value of the dipole and pressure force scattering rate, as is presented later.

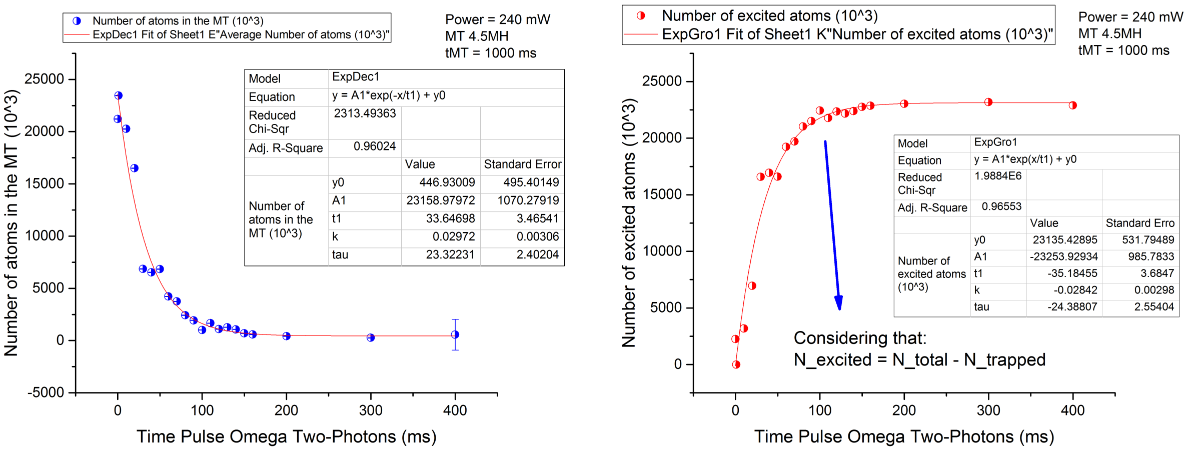

Model	ExpDec1		
Equation	y = A1*exp(-x/t1) + y0		
Reduced Chi-Sqr	2313.49363		
Adj. R-Square	0.96024		
		Value	Standard Error
Number of atoms in the MT (10^3)	y0	446.93009	495.40149
	A1	23158.97972	1070.27919
	t1	33.64698	3.46541
	k	0.02972	0.00306
	tau	23.32231	2.40204

Model	ExpGro1		
Equation	y = A1*exp(x/t1) + y0		
Reduced Chi-Sqr	1.9884E6		
Adj. R-Square	0.96553		
		Value	Standard Erro
Number of excited atoms (10^3)	y0	23135.42895	531.79489
	A1	-23253.92934	985.7833
	t1	-35.18455	3.6847
	k	-0.02842	0.00298
	tau	-24.38807	2.55404

(a) **(b)**

Figure 7.4.2 – Frequency scan around the D2 line transition. (a) We observe the losses of atoms when the beam is in resonant with the D2 transition. We vary the pulse time to avoid the cloud deformation. (b) Temperature as a function of the detuning of the excitation beam.

Source: By the author.

To look carefully at the effects present in our experiment, we started to tune the excitation beam far-off resonance from the value of the $\omega_{2photon}$. We observed that even when the excitation beam has a frequency in which no effect of 2P2A is expected, we observe the same behavior in the data, which is an indication that these other effects are dominant in the system. At this point the excitation beam was focused to a waist of $\sim 250\,\mu$m and power of 250 mW, certainly this can produce a dipole force of the radiation that can eject or trap the atoms in some regions of the trap, depending on the transitions we consider, and then deforming the cloud as we see in Figure 7.4.3. This happens more strongly when the excitation beam is near to the resonance.

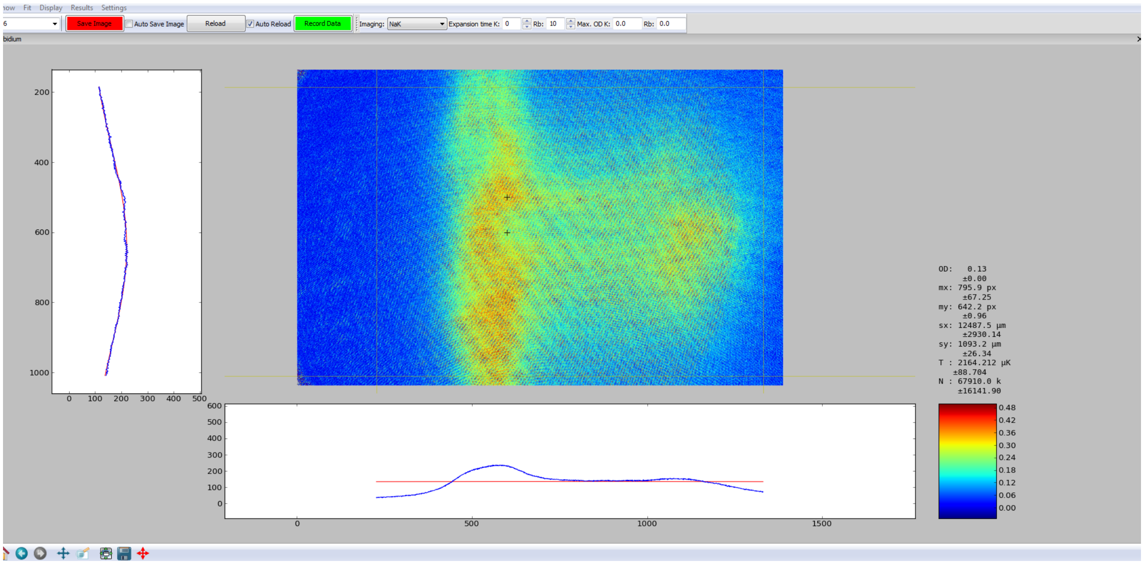

Imaging: NaK Expansion time K: 0 Rb: 10 Max. OD K: 0.0 Rb: 0.0

```
OD:   0.13
     ±0.00
mx: 795.9 px
     ±67.25
my: 642.2 px
     ±0.96
sx: 12487.5 µm
     ±2930.14
sy: 1093.2 µm
     ±26.34
T : 2164.212 µK
    ±88.704
N : 67910.0 k
    ±16141.90
```

Figure 7.4.3 – The cloud is deformed when the excitation beam is applied to the trap. It seems that intensity should be reduce collimating the beam to a size much greater than the cloud size in order to avoid mechanical effects of the light, as for example, dipole force which would mask the two-photon signal.

Source: By the author.

One of the possible effects is the dipole force created by the tightly focused excitation beam. To circumvent this drawback of focusing the excitation beam, we decided to expand and collimate the beam to a diameter of approximately 1 mm, and explore the different parameters as the frequency, power and time of the pulse of the excitation beam, to better understand the mechanical effects of this beam. Another force, the radiation pressure force is also present in the measurements even when the detuning of the beam is of the order of hundreds of GHz.

One possibility to avoid the effect of 2P2A be masked by the dipole force and/or radiation pressure force is to reduce the power when the laser is far-off resonance with respect to ω_{2P} until no effect of the excitation beam is observe. This certainly define a very well established background and we could see and increment in the signal due to the 2P2A effect when the excitation laser is bring back to ω_{2P}. The problem with this approach was that probably the excitation beam intensity was so low that the signal is also very low, and then, undetectable by the trap loss technique.

To perform this approach while observing some signal that could serve as reference, we decided to scan the excitation laser around the D2 line transition. Here, we varied frequency, power and time of pulse. Figures 7.4.4a and 7.4.4b show the frequency scan around the D2 line observing the number of atoms and the temperature of the cloud. In Figure 7.4.4a it is possible to observe the well define D2 transition. The minimum width of this line obtained decreasing the power of the excitation beam was around 40 MHz, which is large compare to the natural linewidth of the transition, which is 9.795 MHz.

This is an indication that the trap loss technique is not sensitive enough to measure the 2P2A cooperative absorption. The behavior of the temperature is a kind of misleading, because when the atoms are lost, the cloud suffer abrupt changes in this parameter, which made of it a not reliable one.

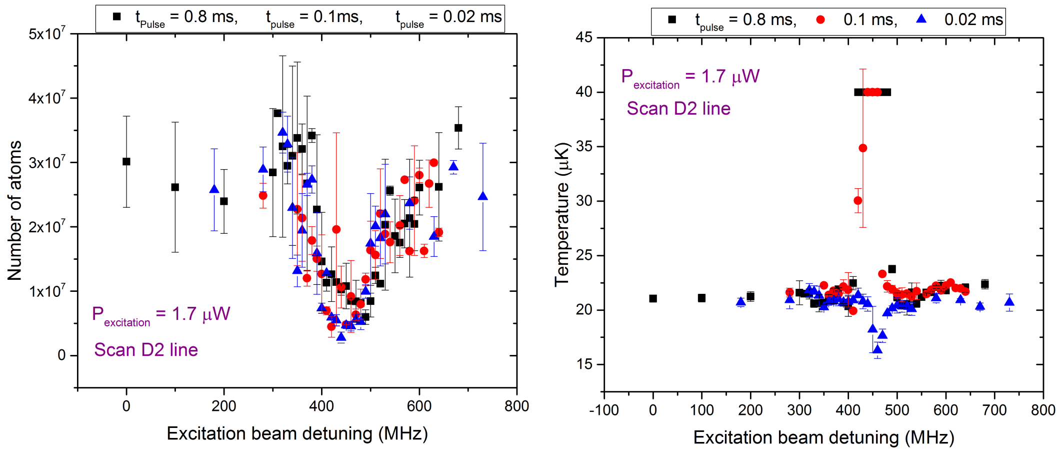

(a) (b)

Figure 7.4.4 – Frequency scan around the D2 line transition. (a) We observe the losses of atoms when the beam is in resonant with the D2 transition. We vary the pulse time to avoid the cloud deformation. (b) Temperature as a function of the detuning of the excitation beam.
Source: By the author.

We varied the pulse time looking for the ideal time, in which we can see excitation without destroying the atomic cloud. Figure 7.4.5 shows the number of atoms as a function of this parameter. Figure 7.4.6 the number of atoms as a function of the power of the excitation laser.

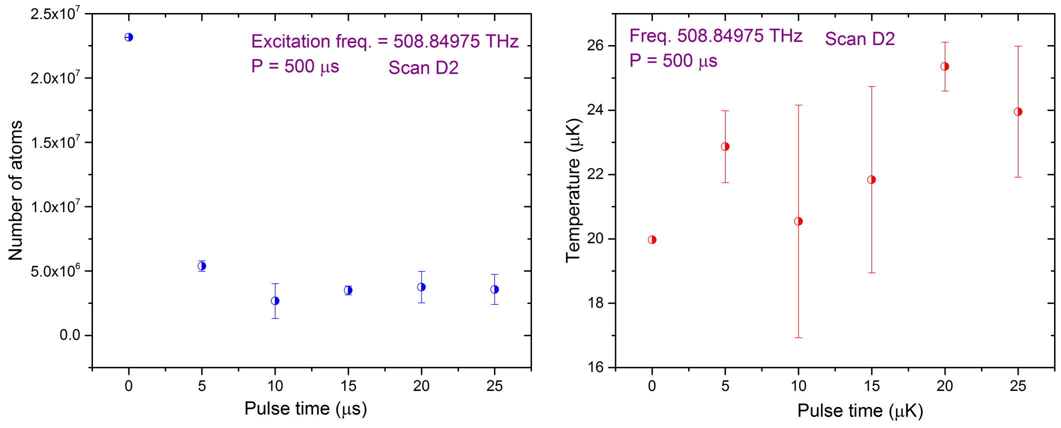

(a) (b)

Figure 7.4.5 – The pulse time was varied for the D2 line. This is a good form of calibrating of our excitation and detection system in order to better understand the process happening the system.
Source: By the author.

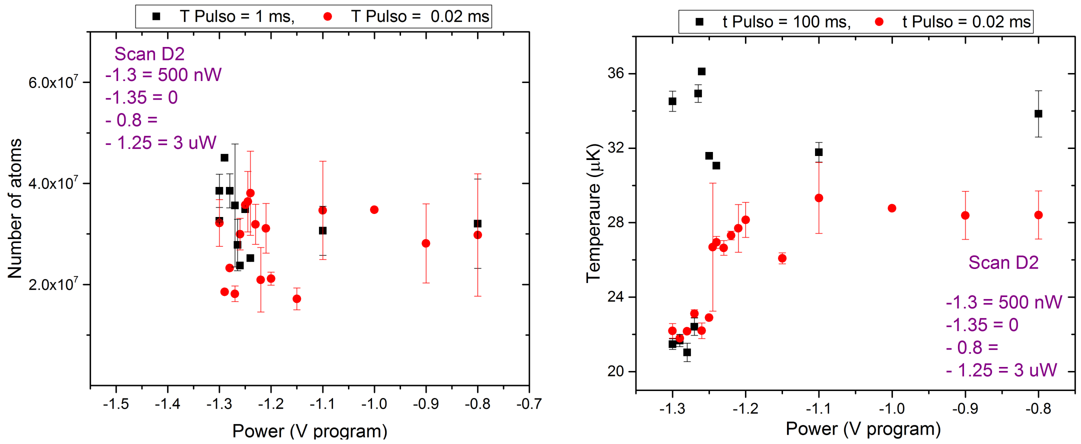

(a) **(b)**

Figure 7.4.6 – The pulse time was varied for the D2 line. This is a good form of calibrating our excitation and detection system in order to better understanding the process happening in the system.
Source: By the author.

To understand the effects that are present in the experiment, it is important to consider the forces the light exerts on the atoms. The two kind of forces, dipole and radiation pressure are discussed in the next section.

7.5 Light forces on atoms

It is worth in this chapter to briefly describe some features of the light-matter interaction in the context of single photon interaction with single-atom systems. The most important part of this topic is the forces the light can exerts on the atoms, namely, the spontaneous force, also called scattering force or radiation pressure force, and the dipole force. Both types of forces can have strong impact in the system because they are due to single-atom single photon interaction and gradient of light intensity. As we are dealing with cold atoms, this forces can have a considerable mechanical effects on the trapped atoms, leading mainly to heating in the case of the spontaneous force and repulsion or attraction to the intensity maxima or minima, depending on the detuning of the light, in the case of the dipole force. In both cases, these are undesired effects that may be present in our experiment, leading to losses of trapped atom, and of course, we certainly want to know the role these effects play in the experiments of interesting here about 2P2A cooperative absorption. I summarize the main features of both forces to better understand the effects may be present in the experiment due to light-matter interaction.

7.5.1 Spontaneous force

Atoms can be submitted to light-induced forces as a result of energy and momentum conservation when interacting with a radiation field. For example, when a two-level atom is shined with a radiation field of frequency ω, the absorption and re-emission of photons produces a net change in the linear momentum of the atom given by $\Delta p = -h/\lambda$, where h is the Planck constant and $\lambda = 2\pi c/\omega$ is the wavelength of the incident light, where we consider just one dimension. Therefore, any time an atom absorb and re-emit a photon it gain a quantity of momentum known as momentum recoil and given by $\hbar k$, i.e., equal to the momentum of the photon, with $k = 2\pi/\lambda$. Th relation between momentum and the random thermal energy is given by (64)

$$\frac{1}{2}k_B T_{recoil} = \frac{\hbar^2 k^2}{2m} = \frac{h^2}{2m\lambda^2} \tag{7.5.1}$$

therefore, the associated temperature to this effect is

$$T_{recoil} = \frac{h^2}{mk_B\lambda^2} \tag{7.5.2}$$

for sodium atoms $T_{recoil} = 2.4\,\mu K$. This is an important value to consider because when the atoms gain more energy than the trap depth they cannot be maintained trapped, and this effect can mask the effect of 2P2A cooperative absorption in the case of the magnetic trap when the signal of cooperative absorption is measured by atom trap losses.

The spontaneous force is found multiplying the photon momentum with the total scattering rate of photon for certain atomic transition (26),

$$F_{spont} = \hbar k R_{scatt}^{spont} \tag{7.5.3}$$

and the scattering rate is given by $R_{scatt}^{spont} = \Gamma\rho_{22}$, here Γ is the linewidth or transition rate of the excited state and ρ_{22} is the density matrix element representing the population in the excited state and given by (88)

$$\rho_{22} = \frac{\Omega^2}{4\delta^2 + \Gamma^2 + 2\Omega^2} \tag{7.5.4}$$

where Ω is the Rabi frequency (88), $\delta = \omega - \omega_0 + kv$ is the detuning of the laser light with respect to the atomic transition frequency ω_0 taking into account the Doppler effect kv. Using the relation $\frac{I}{I_s} = \frac{2\Omega^2}{\Gamma^2}$, where I_s is the saturation intensity, the scattering rate is finally expressed as (26)

$$R_{scatt}^{spont} = \frac{\Gamma}{2}\frac{I/I_s}{1 + I/I_s + 4\delta^2/\Gamma^2} \tag{7.5.5}$$

and finally the spontaneous force as

$$F_{spont} = \hbar k \frac{\Gamma}{2} \frac{I/I_s}{1 + I/I_s + 4\delta^2/\Gamma^2} \tag{7.5.6}$$

For the $D2$ line of sodium atoms $I_s = 6.26\,\mathrm{mW}/cm^2$.

7.5.2 Dipole force

The dipole force emerges from the interaction of the induced electric dipole moment ($\vec{p}$) of the atom with the radiation field. (26) Then interaction potential between the electric dipole and the electric field of the light ($\vec{E}$)

$$U_{dip} = -\frac{1}{2}\left\langle \vec{p}.\vec{E} \right\rangle = -\frac{1}{2\epsilon_0 c}\mathrm{Re}\left(\alpha\right) I \tag{7.5.7}$$

where α is the complex polarizability, giving for the common expression $\vec{p} = \alpha\vec{E}$, that related the atomic polarization with the external electric field (26), $I = 2\epsilon_0 c \left|E\right|^2$ is the intensity of the light field, and the factor 1/2 is a consequence of the electric dipole moment be induced and not a permanent one. From this, the dipole force is derived as the gradient of the dipole potential, since U_{dip} is conservative, then

$$\vec{F}_{dip}\left(\vec{r}\right) = -\nabla U_{dip}\left(\vec{r}\right) = \frac{1}{2\epsilon_0 c}\mathrm{Re}\left(\alpha\right)\nabla I\left(\vec{r}\right) \tag{7.5.8}$$

The atom treated as an oscillator (26) absorbs certain power of the incident field given by

$$P_{abs} = \left\langle \left(\frac{\partial \vec{p}}{\partial t}\right).\vec{E} \right\rangle = \frac{\omega}{\epsilon_0 c}\mathrm{Im}\left(\alpha\right) I \tag{7.5.9}$$

then, the re-emission is made as dipole radiation.

The scattering rate resulting from this process is given by

$$R_{scatt}^{dipole}\left(\vec{r}\right) = \frac{P_{abs}}{\hbar\omega} = \frac{1}{\hbar\epsilon_0 c}\mathrm{Im}\left(\alpha\right) I\left(\vec{r}\right) \tag{7.5.10}$$

With the polarizability in the semiclassical approach is found to be

$$\alpha = 6\pi\epsilon_0 c^3 \frac{\Gamma/\omega_0^2}{\omega_0^2 - \omega - i\left(\omega^3/\omega_0^2\right)\Gamma} \tag{7.5.11}$$

The final expressions for the optical dipole potential, dipole force, and scattering rate are given by (26)

$$\begin{aligned} U_{dipole} &= -\frac{3\pi c^2}{2\omega_0^3}\left(\frac{\Gamma}{\omega_0-\omega}+\frac{\Gamma}{\omega_0+\omega}\right) I\left(\vec{r}\right) && (7.5.12)\\ F_{dipole} &= -\frac{\hbar\delta}{2}\frac{1}{1+I/I_s+4\delta^2/\Gamma^2}\frac{\nabla I\left(\vec{r}\right)}{I_s} && (7.5.13)\\ R_{scatt}^{dipole} &= \frac{3\pi c^2}{2\hbar\omega_0^3}\left(\frac{\omega}{\omega_0}\right)^3\left(\frac{\Gamma}{\omega_0-\omega}+\frac{\Gamma}{\omega_0+\omega}\right)^2 I\left(\vec{r}\right) && (7.5.14) \end{aligned}$$

In the special case when the detuning is much smaller than the driven frequency ($\delta \ll \omega-\omega_0$), then the counter-rotating term $\omega_0+\omega$, can be neglected in the broadly used rotating-wave approximation (RWA), the above expressions for U_{dipole} and R_{scatt}^{dipole} are reduced to

$$\begin{aligned} U_{dipole} &= \frac{3\pi c^2}{2\omega_0^3}\frac{\Gamma}{\delta} I\left(\vec{r}\right) && (7.5.15)\\ R_{scatt}^{dipole} &= \frac{3\pi c^2}{2\hbar\omega_0^3}\left(\frac{\omega}{\omega_0}\right)^3\left(\frac{\Gamma}{\delta}\right)^2 I\left(\vec{r}\right) && (7.5.16) \end{aligned}$$

and this two quantities are related by

$$\hbar R_{scatt}^{dipole} = \frac{\Gamma}{\delta} U_{dipole} \tag{7.5.17}$$

We are dealing with sodium atoms, and to this respect the external light field is tuned between the $D1$ line ($3^2S_{1/2} \longleftrightarrow 3^2P_{1/2}$) and the $D2$ line ($3^2S_{1/2} \longleftrightarrow 3^2P_{3/2}$).

For this situations we can take into consideration the contribution of the two states, $3^2P_{1/2}$ and $3^2P_{3/2}$, to the dipole force

$$U_{dipole}\left(\vec{r}\right) = \frac{\pi c^2}{2\omega_0^3}\left(\frac{2+\chi_{pol} g_F m_F}{\Delta_{2,F}}+\frac{1-\chi_{pol} g_F m_F}{\Delta_{1,F}}\right) I\left(\vec{r}\right) \tag{7.5.18}$$

where $\chi_p = 0, \pm 1$ represents the polarization of the light (linear $=0$, $\sigma^+ = 1$, $\sigma^- = -1$), and $\Delta_{1,F}$ and $\Delta_{2,F}$ are the energy splitting between the ground state in consideration ($3^2S_{1/2}(F)$) and the center of the hyperfine split $3^2P_{1/2}$ and $3^2P_{3/2}$.

The photon scattering rate when considering alkali atoms is also given by

$$R_{scatt}^{dipole}\left(\vec{r}\right) = \frac{\pi c^2}{2\hbar\omega_0^3}\left(\frac{2}{\Delta_{2,F}}+\frac{1}{\Delta_{1,F}}\right) I\left(\vec{r}\right) \tag{7.5.19}$$

With these tools, we can estimated the effect of each kind of force on the system. One parameter that gives useful information is the scattering rate of photons by the atoms. Using the above equations for the scattering rates we found that $R_{scatt}^{spont} \simeq 139\,\text{photons/s}$ and $R_{scatt}^{dipole} \simeq 0.09\,\text{photons/s}$. Comparing with the scattering rate for the 2P2A process, which is $R^{2P2A}_{scatt} \sim 0.1$ photons/s (from (71)), we see that the predominant process is the single photon scattering due to the spontaneous force.

From this values, we see that the spontaneous force has a considerable effect on the atoms. In the case of resonance, just 10 photons in a pulse of $20\,\mu$s are enough to heat the atomic cloud such that the atoms can escape from the trap. About the dipole force, this produce a potential of the order of $60\,\mu$K, which is almost three time the energy of the the trapped atoms ($\sim 16\,\mu$K), then being considerably strong.

From Figure 7.4.3, we see that the atomic cloud separate into two clouds. This can be explained by means of the dipole potential generated by the excitation beam. Because the laser is midway the D1 and D2 line, there are two kind of potentials, repulsive and attractive. The excitation beam frequency is red-detuned with respect to the D2 line transition, creating an attractive potential, while the same laser is blue-detuned with respect to the D1 line, creating a repulsive potential. Due to this, part of the atoms in the cloud feel a repulsive potential and the others an attractive potential, leading to the division of the atomic cloud.

From the graphs characterizing the D2 line transition, where we tried to calibrate our detection system, we can see that the error in the measurements is of the order of 3×10^4 atoms. On the other hand, considering the results obtained in the MOT, where the signal was of the order of 20 ions/ms = 2000 ions/s (Figure 7.3.4) with an atomic density of the order 10^{11} atoms/cm^3, we expected that an increase in the density will produce a quadratic improvement of the signal. In the MT at 4.5 MHz, the density is slightly greater than that of the MOT, then we expect an improvement of about one order of magnitude in the signal, i.e., 20000 ions/s. Comparing this value of the signal with the error of the detection system, we can conclude that this technique is not efficient to measured the 2P2A effect. The ideal case was the ion counter in the MOT.

Unfortunately, we did not have a Channeltron in the new experimental system for technical reasons related to the vacuum of the science chamber. For this reason, we can not conclude anything about the 2P2A effect in the MT.

In a future work, we will look at the fluorescence instead to the number of excited atoms by imaging techniques. We will use single photon detectors to collect the fluorescence of the atoms decaying to the fundamental state after they have been excited by cooperative absorption of light. One possible advantage with the fluorescence scheme measurement is that we can study not only the cooperative absorption of light, but also the production of correlated pair of photons as well entangled atoms. This could have interesting applications in a near future.

Thus, to conclude, in this chapter I presented the results obtained when studying the 2P2A effect in a magneto-optical trap using a very efficient detection system (ion counter), and the attempts to measure this effect in a magnetic trap. Unfortunately, the detection system was inefficient, for this reason a new scheme based of fluorescence measurements is being projected.

In the next chapter, I will present the conclusion of this PhD work.

Chapter 8

Conclusions

In this thesis we have constructed an experimental system able to efficiently produced a Bose-Einstein condensate (BEC) of sodium atoms in a magneto-optical trap (MOT). This was the first proposed goals and we have successfully reached it.

As the construction and characterization of this apparatus is a hard task that spend a lot of time and effort, the project was divided in several stages.

The first stage was the construction and characterization of an atomic source of cold sodium atoms. To choose the most suitable configuration for our experiment and necessities, we realized a comparison between two kind of atomic sources: the Zeeman slower and a 2D-MOT. We constructed and assembly the system to study the performance of both sources, concluding successfully that the 2D-MOT was the best option for our BEC apparatus. This is based in the efficiency and compactness of the 2D-MOT, that even it needs a some more light power, it has the great advantage of a small size when compared with the normally big ZSs.

Once we have chosen the atomic source, the next step was to compared the performance of the trap that capture the atoms coming form the cold atomic source. This basically consisted in study the performance of a Bright-MOT and a Dark-SPOT MOT. We experimentally verified the advantages of the Dark-SPOT MOT, as for example, the increase in density of the MOT which is crucial in AMO experiments. We pointed out that this configuration circumvent some limitations of the Bright-MOT, as losses-induced collisions and self trapping radiation. Thus, with our characterization we were able to choose in a conscious way the Dark-SPOT MOT as the final setup in our experiment.

After we had all the elements to cool and trap the atoms in the MOT, we transferred them to an optically plugged quadrupole trap (OPT). In this OPT we realized efficiently the evaporative cooling process and finally obtained the BEC of sodium atoms of $\sim 5\times 10^5$ atoms with a critical temperature of $\sim 1.1\,\mu$K. It is worth to recall that this is the first time a BEC is achieved in an OPT in our laboratory. Actually the system is ready to follow the next steps, and surely very soon two species will be condensed. Then the contribution of this thesis is significant in the sense that set up the basis for the subsequent experiments to be realized.

With the BEC machine constructed and characterized, and the BEC working regularly in our lab, the next step was to revisit an effect of non-linear light-matter interaction. Specifically, we explore the cooperative absorption of two photons by two trapped atoms (2P2A). In the first year of my PhD we demonstrated by the first time this effect in a cold atoms sample. This was gained some interested in recent years, and we wanted to take advantage of the new experimental system to explore new features of this phenomenon.

Therefore, we started trying to measure the 2P2A cooperative effect in a magnetic trap, expecting the improvement in record signal due to the higher densities of the MT when compared with MOTs. Also the BEC offers new possibilities in the sense of higher densities, knowing that this effect is strongly dependent on this parameter.

Unfortunately, the detection system was not efficient enough to detect any signal. Then, in a near future, new measurements could be tried using another scheme based on the measurement of the fluorescence emitted by the excited atoms when they decay to the fundamental state. Using single photon counters will give the possibility to record very small signals, typical of this effects. In this way, we could explore not just the phenomenon of cooperative absorption, but also the pair of photons emitted. This photons will be correlated, opening the possibility to explore new mechanism of producing correlated pairs of photons as well entangled atoms. This phenomena could have very interesting applications in a near future.

REFERENCES

1 ANDERSON, M. H. et al. Observation of Bose-Einstein condensation in a dilute atomic vapor. *Science*, v. 269, n. 5221, p. 198–201, 1995.

2 DAVIS, K. B. et al. Bose-Einstein condensation in a gas of sodium atoms. *Physical Review Letters*, v. 75, n. 22, p. 3969–3973, 1995.

3 BRADLEY, C. C. et al. Evidence of Bose-Einstein condensation in an atomic gas with attractive interactions. *Physical Review Letters*, v. 75, n. 9, p. 1687–1690, 1995.

4 RAIMOND, J. M.; BRUNE, M.; HAROCHE, S. Manipulating quantum entanglement with atoms and photons in a cavity. *Review of Modern Physics*, v. 73, n. 3, p. 565–582, 2001.

5 BLOCH, I.; DALIBARD, J.; ZWERGER, W. Many-body physics with ultracold gases. *Review of Modern Physics*, v. 80, n. 3, p. 885–964, 2008.

6 BLOCH, I.; DALIBARD, J.; NASCIMBENE, S. Quantum simulations with ultracold quantum gases. *Nature Physics*, v. 8, n. 4, p. 267–276, 2012.

7 HAROCHE, S. Nobel lecture: controlling photons in a box and exploring the quantum to classical boundary. *Review of Modern Physics*, v. 85, n. 3, p. 1083–1102, 2013.

8 MYATT, C. J. et al. Production of two overlapping Bose-Einstein condensates by sympathetic cooling. *Physical Review Letters*, v. 78, n. 4, p. 586–589, 1997.

9 MODUGNO, G. et al. Collapse of a degenerate fermi gas. *Science*, v. 297, n. 5590, p. 2240–2243, 2002.

10 HADZIBABIC, Z. et al. Two-species mixture of quantum degenerate Bose and Fermi gases. *Physical Review Letters*, v. 88, n. 16, p. 160401, 2002.

11 TSATSOS, M. C. et al. Quantum turbulence in trapped atomic Bose-Einstein condensates. *Physics Reports*, v. 622, p. 1 – 52, 2016.

12 HENN, E. A. L. et al. Emergence of turbulence in an oscillating Bose-Einstein condensate. *Physical Review Letters*, v. 103, n. 4, p. 045301, 2009.

13 PEDROZO-PEÑAFIEL, E. et al. Two-photon cooperative absorption in colliding cold Na atoms. *Physical Review Letters*, v. 108, n. 25, p. 253004, 2012.

14 PEDROZO-PEÑAFIEL, E. et al. Direct comparison between a two-dimensional magneto-optical trap and a zeeman slower as sources of cold sodium atoms. *Laser Physics Letters*, v. 13, n. 6, p. 065501, 2016.

15 PHILLIPS, W. D.; METCALF, H. Laser deceleration of an atomic beam. *Physical Review Letters*, v. 48, n. 9, p. 596–599, 1982.

16 RAAB, E. L. et al. Trapping of neutral sodium atoms with radiation pressure. *Physical Review Letters*, v. 59, n. 23, p. 2631–2634, 1987.

17 LU, Z. T. et al. Low-velocity intense source of atoms from a magneto-optical trap. *Physical Review Letters*, v. 77, n. 16, p. 3331–3334, 1996.

18 DIECKMANN, K. et al. Two-dimensional magneto-optical trap as a source of slow atoms. *Physical Review A*, v. 58, n. 5, p. 3891–3895, 1998.

19 CATANI, J. et al. Intense slow beams of bosonic potassium isotopes. *Physical Review A*, v. 73, n. 3, p. 033415, 2006.

20 TIECKE, T. G. et al. High-flux two-dimensional magneto-optical-trap source for cold lithium atoms. *Physical Review A*, v. 80, n. 1, p. 013409, 2009.

21 LAMPORESI, G. et al. Compact high-flux source of cold sodium atoms. *Review of Scientific Instruments*, v. 84, n. 6, p. 063102, 2013.

22 DURFEE, D. S. *Dynamic properties of dilute Bose-Einstein condensates.* 1999. 204 p. Thesis (Ph.D. in Science) — Massachusetts Institute of Technology, Cambridge, 1999.

23 STREED, E. W. et al. Large atom number Bose-Einstein condensate machines. *Review of Scientific Instruments*, v. 77, n. 2, p. 023106–1–023106–13, 2006.

24 NAIK, D. S. *Bose-Einstein condensation: building the testbeds to study superfluidity.* 2004. 193 p. Thesis (Ph.D. in Science) — Georgia Institute of Technology, Atlanta, 2006.

25 MUNIZ, S. R. et al. Measurements of capture velocity in a magneto-optical trap for a broad range of light intensities. *Physical Review A*, v. 65, n. 1, p. 015402, 2001.

26 FOOT, C. J. *Atomic Physics.* New York: Oxford University Press Inc, 2005. 331p.

27 SCHOSER, J. et al. Intense source of cold rb atoms from a pure two-dimensional magneto-optical trap. *Physical Review A*, v. 66, p. 023410, 2002.

28 SEMAN, J. A. *Study of excitations in a Bose-Einstein condensate.* 2011. 189 p. Thesis (Ph.D. in Science) — Institute of Physics of Sao Carlos, University of Sao Paulo, Sao Carlos, 2011.

29 METCALF H. J.; STRATEN, P. *Laser cooling and trapping.* New York: Springer-Verlag Inc., 1999. 323 p.

30 O'HANLON, J. F. *A user's guide to vacuum technology.* New Jersey: John Wiley and Songs, Inc, 2003. 516p.

31 RIET, C. *Spatial non-destructive imaging of spin domains in Bose-Einstein Condensates.* 2014. 66 p. (Masters thesis) — University of Utrecht, Utrecht, 2014.

32 GONZALES, I. S. *LiNaK: Multi-Species apparatus for the study of ultracold quantum degenerate mixtures.* 2012. 113 p. (Masters thesis) — Massachusetts Institute of Technology, Cambridge, 2012.

33 YARIV, A. *Quantum electronics.* New Jersey: John Wiley and Songs, Inc, 1989. 704p.

34 DEMTRODER, W. *Laser Spectroscopy.* Berlin: Springer-Verlag Inc., 2003. 987 p.

35 OOIJEN, E. van; KATGERT, G.; STRATEN, P. van der. Laser frequency stabilization using doppler-free bichromatic spectroscopy. *Applied Physics B*, v. 79, n. 1, p. 57–59, 2004.

36 PEARMAN, C. P. et al. Polarization spectroscopy of a closed atomic transition: applications to laser frequency locking. *Journal of Physics B*, v. 35, n. 24, p. 5141, 2002.

37 KETTERLE, W. et al. High densities of cold atoms in a *dark* spontaneous-force optical trap. *Physical Review Letters*, v. 70, n. 15, p. 2253–2256, 1993.

38 GIBBLE, K. E.; KASAPI, S.; CHU, S. Improved magneto-optic trapping in a vapor cell. *Optics Letters*, v. 17, n. 7, p. 526–528, 1992.

39 MAGALHAES, K. M. F. et al. The escape velocity in a magneto-optical trap and its importance to trap loss investigation. *Laser Physics*, v. 12, n. 1, p. 145 – 151, 2002.

40 WEINER, J. et al. Experiments and theory in cold and ultracold collisions. *Reviews of Modern Physics*, v. 71, n. 1, p. 1–85, 1999.

41 PRENTISS, M. et al. Atomic-density-dependent losses in an optical trap. *Optics Letters*, v. 13, n. 6, p. 452–454, 1988.

42 WALKER, T.; SESKO, D.; WIEMAN, C. Collective behavior of optically trapped neutral atoms. *Physical Review Letters*, v. 64, n. 4, p. 408–411, 1990.

43 SESKO, D. W.; WALKER, T. G.; WIEMAN, C. E. Behavior of neutral atoms in a spontaneous force trap. *Journal of the Optical Society of America B*, v. 8, n. 5, p. 946–958, 1991.

44 MARCASSA, L. et al. Direct measurement of fine structure changing collisional losses in cold trapped 85rb. *European Physical Journal D*, v. 7, n. 3, p. 317–321, 1999.

45 MANCINI, M. et al. Intensity and detuning dependence of fine structure changing collisions in a 85 rb magneto-optical trap. *European Physical Journal D*, v. 13, n. 3, p. 317–322, 2001.

46 TOWNSEND, C. G. et al. High-density trapping of cesium atoms in a dark magneto-optical trap. *Physical Review A*, v. 53, n. 3, p. 1702–1714, 1996.

47 PETRICH, W. et al. Behavior of atoms in a compressed magneto-optical trap. *Journal of the Optical Society of America B*, v. 11, n. 8, p. 1332–1335, 1994.

48 NAIK, D. S.; RAMAN, C. Optically plugged quadrupole trap for Bose-Einstein condensates. *Physical Review A*, v. 71, n. 3, p. 033617, 2005.

49 STAM, K. M. R. van der et al. Large atom number Bose-Einstein condensate of sodium. *Review of Scientific Instruments*, v. 78, n. 1, p. 013102–1 – 013102–10, 2007.

50 HEO, M.-S.; CHOI, J.-y.; SHIN, Y.-i. Fast production of large ^{23}Na Bose-Einstein condensates in an optically plugged magnetic quadrupole trap. *Physical Review A*, v. 83, n. 1, p. 013622, 2011.

51 DUBESSY, R. et al. Rubidium-87 Bose-Einstein condensate in an optically plugged quadrupole trap. *Physical Review A*, v. 85, n. 1, p. 013643, 2012.

52 PERE-RIOS, J.; SANZ, A. S. How does a magnetic trap work? *American Journal of Physics*, v. 81, n. 11, p. 836–843, 2013.

53 MAJORANA, E. Atomi orientati in campo magnetico variabile. *Il Nuovo Cimento (1924-1942)*, v. 9, n. 2, p. 43–50, 1932.

54 MIGDALL, A. L. et al. First observation of magnetically trapped neutral atoms. *Physical Review Letters*, v. 54, n. 24, p. 2596–2599, 1985.

55 BERGEMAN, T. H. et al. Quantized motion of atoms in a quadrupole magnetostatic trap. *Journal of the Optical Society of America B*, v. 6, n. 11, p. 2249–2256, 1989.

56 SUKUMAR, C. V.; BRINK, D. M. Spin-flip transitions in a magnetic trap. *Physical Review A*, v. 56, n. 3, p. 2451–2454, 1997.

57 PETRICH, W. et al. Stable, tightly confining magnetic trap for evaporative cooling of neutral atoms. *Physical Review Letters*, v. 74, n. 17, p. 3352–3355, 1995.

58 PRITCHARD, D. E. Cooling neutral atoms in a magnetic trap for precision spectroscopy. *Physical Review Letters*, v. 51, n. 15, p. 1336–1339, 1983.

59 BERGEMAN, T.; EREZ, G.; METCALF, H. J. Magnetostatic trapping fields for neutral atoms. *Physical Review A*, v. 35, n. 4, p. 1535–1546, 1987.

60 TOLLETT, J. J. et al. Permanent magnet trap for cold atoms. *Physical Review A*, v. 51, n. 1, p. R22–R25, 1995.

61 MEWES, M.-O. et al. Bose-Einstein condensation in a tightly confining dc magnetic trap. *Physical Review Letters*, v. 77, n. 3, p. 416–419, 1996.

62 HESS, H. F. Evaporative cooling of magnetically trapped and compressed spin-polarized hydrogen. *Physical Review B*, v. 34, n. 5, p. 3476–3479, 1986.

63 MASUHARA, N. et al. Evaporative cooling of spin-polarized atomic hydrogen. *Physical Review Letters*, v. 61, n. 8, p. 935–938, 1988.

64 FOX, M. *Quantum optics: an introduction.* New York: Oxford University Press, 2006. 378p.

65 HENN, E. A. L. et al. Evaporation in atomic traps: A simple approach. *American Journal of Physics*, v. 75, n. 10, p. 907–910, 2007.

66 DAVIS, K. B. *Evaporative cooling of sodium atoms.* 1995. p9 p. Thesis (Ph.D. in Science) — Massachusetts Institute of Technology, Cambridge, 1995.

67 DAVIS, K. B. et al. Evaporative cooling of sodium atoms. *Physical Review Letters*, v. 74, n. 26, p. 5202–5205, 1995.

68 NAIK, D. S.; MUNIZ, S. R.; RAMAN, C. Metastable Bose-Einstein condensate in a linear potential. *Physical Review A*, v. 72, n. 5, p. 051606, 2005.

69 KETTERLE, W.; DURFEE, D. S.; KURN, S. D. M. Making, probing and understanding Bose-Einstein condensates. In: INGUSCIO, M.; STRINGARI, S.; WIEMAN, C. E. (Ed.). *Bose-Einstein condensation in ctomic gases*. New York: IOS Press, 1999. (Proceedings of the International School of Physics Enrico Fermi, Course CXL).

70 PETHICK, C. J.; SMITH, H. *Bose-Einstein condensation in dilute gases*. Cambridge: Cambridge University Press, 2008. 569p.

71 LEITE, J. R.; ARAUJO, C. B. D. Lineshape of cooperative two-photon absorption by atom pairs in solids. *Chemical Physics Letters*, v. 73, n. 1, p. 71 – 74, 1980.

72 ANDREWS, D. L.; HARLOW, M. J. Cooperative two-photon absorption. *The Journal of Chemical Physics*, v. 78, n. 3, p. 1088–1094, 1983.

73 VARADA, G. V.; AGARWAL, G. S. Two-photon resonance induced by the dipole-dipole interaction. *Physical Review A*, v. 45, n. 9, p. 6721–6729, 1992.

74 ZHENG, Z. *Two-photon-two-atom excitation with quantum multimode light states*. 2014. 153 p. Thesis (Ph.D. in Science) — Universite Pierre et Marie Curie, Paris, 2014.

75 BOYD, R. W. *Nonlinear Optics*. San Diego: Academic Press, 2003. 578 p.

76 COHEN-TANNOUDJI, C. N. *Atom-photon interactions: basic processes and applications*. New York: John Wiley and Songs, Inc, 1992. 656p.

77 DEXTER, D. L. Cooperative optical absorption in solids. *Physical Review*, v. 126, n. 1, p. 1962–1967, 1962.

78 VARSANYI, F.; DIEKE, G. H. Ion-pair resonance mechanism of energy transfer in rare earth crystal fluorescence. *Physical Review Letters*, v. 7, n. 12, p. 442–443, 1961.

79 FREEDHOFF, H. S. Collective atomic effects in resonance fluorescence: dipole-dipole interaction. *Physical Review A*, v. 19, n. 3, p. 1132–1139, 1979.

80 AGARWAL, G. S. et al. Analytical solution for the spectrum of resonance fluorescence of a cooperative system of two atoms and the existence of additional sidebands. *Physical Review A*, v. 21, n. 1, p. 257–259, 1980.

81 KUS, M.; WODKIEWICZ, K. Two-atom resonance fluorescence. *Physical Review A*, v. 23, n. 2, p. 853–857, 1981.

82 LIDOW, D. B. et al. Inelastic collision induced by intense optical radiation. *Physical Review Letters*, v. 36, n. 9, p. 462–464, 1976.

83 WHITE, J. C. et al. Observation of radiative collisional fluorescence. *Phys. Rev. Lett.*, v. 41, n. 25, p. 1709–1712, 1978.

84 WHIT, J. C. et al. Observation of atomic-pair absorption with an incoherent source. *Optics Letters*, v. 4, n. 5, p. 137–139, 1979.

85 FICEK, Z.; SANDERS, B. C. Quantum beats in two-atom resonance fluorescence. *Physical Review A*, v. 41, n. 1, p. 359–368, 1990.

86 KURIZKI, G. Quantum features of resonance fluorescence as probes of two-atom dynamical correlations. *Physical Review A*, v. 43, n. 5, p. 2599–2602, 1991.

87 HETTICH, C. et al. Nanometer resolution and coherent optical dipole coupling of two individual molecules. *Science*, v. 298, n. 5592, p. 385–389, 2002.

88 SCULLY, M. O.; ZUBAIRY, M. S. *Quantum optics*. Cambridge: Cambridge University Press, 2001. 630p.

89 NAGOURNEY, W.; SANDBERG, J.; DEHMELT, H. Shelved optical electron amplifier: observation of quantum jumps. *Physical Review Letters*, v. 56, n. 26, p. 2797–2799, 1986.

90 KIM, M. S.; AGARWAL, G. S. Cavity-induced two-photon absorption in unidentical atoms. *Physical Review A*, v. 57, n. 4, p. 3059–3064, 1998.

91 MUTHUKRISHNAN, A.; AGARWAL, G. S.; SCULLY, M. O. Inducing disallowed two-atom transitions with temporally entangled photons. *Physical Review Letters*, v. 93, n. 9, p. 093002, 2004.

92 ZHENG, Z. et al. Two-photon-two-atom excitation by correlated light states. *Physical Review A*, v. 88, n. 3, p. 033822, 2013.

93 DAI, X. et al. Two-dimensional double-quantum spectra reveal collective resonances in an atomic vapor. *Physical Review Letters*, v. 108, n. 19, p. 193201, 2012.

94 BEUGNON, J. et al. Quantum interference between two single photons emitted by independently trapped atoms. *Nature*, v. 440, n. 7085, p. 779–782, 2006.

95 GAETAN, A. et al. Observation of collective excitation of two individual atoms in the Rydberg blockade regime. *Nature Physics*, v. 5, n. 2, p. 115–118, 2009.

96 MAUNZ, P. et al. Quantum interference of photon pairs from two remote trapped atomic ions. *Nature Physics*, v. 3, n. 8, p. 538–541, 2007.

97 PERRIN, A. et al. Hanbury Brown and Twiss correlations across the Bose-Einstein condensation threshold. *Nature Physics*, v. 8, n. 3, p. 195–198, 2012.

98 HARRIS, S. E.; LIDOW, D. B. Nonlinear optical processes by van der waals interaction during collision. *Physical Review Letters*, v. 33, n. 12, p. 674–676, 1974.

99 PAIVA. *Two-photon two-atom process*. 2013. 95 p. Thesis (Ph.D. in Science) — Institute of Physics of Sao Carlos, University of Sao Paulo, Sao carlos, 2013.

100 FANO, U. Effects of configuration interaction on intensities and phase shifts. *Physical Review*, v. 124, n. 6, p. 1866–1878, 1961.

Appendix A

Annex - Published papers related to this PhD thesis

- *Two-Photon Cooperative Absorption in Colliding Cold Sodium Atoms*

- *Direct comparison between a two-dimensional magneto-optical trap and a Zeeman slower as sources of cold sodium atoms*

PRL **108,** 253004 (2012) PHYSICAL REVIEW LETTERS week ending 22 JUNE 2012

Two-Photon Cooperative Absorption in Colliding Cold Na Atoms

E. Pedrozo-Peñafiel, R. R. Paiva, F. J. Vivanco, V. S. Bagnato, and K. M. Farias
Instituto de Física de São Carlos, Universidade de São Paulo, São Paulo, Brasil

(Received 28 December 2011; published 19 June 2012)

Two-photon cooperative absorption is common in solid-state physics. In a sample of trapped cold atoms, this effect may open up new possibilities for the study of nonlinear effects. The experiment described herein starts with two colliding Na atoms in the S hyperfine ground state. The pair absorb two photons, resulting in both a $P_{1/2}$ and a $P_{3/2}$ atom. This excitation is observed by ionization using an external light source. A simple model that considers only dipole-dipole interactions between the atoms allows us to understand the basic features observed in the experimental results. Both the pair of generated atoms and the photons originating from their decay are correlated and may have interesting applications that remain to be explored.

DOI: 10.1103/PhysRevLett.108.253004 PACS numbers: 32.80.−t, 34.50.Cx, 67.85.−d

In many atomic processes, it is common for a pair of atoms or molecules to absorb a single photon. In fact, such processes were fundamental to the development of the understanding of cold collisions [1] and the determination of scattering length values [1], among others. It is possible, however, that two atoms can be simultaneously excited by a coherent two-photon absorption. This effect was first observed in a mixture of Ba/Tl, where a pair of atoms were simultaneously excited by a cooperative-absorption process [2]. The problem has also been considered theoretically by a few authors [3,4].

While colliding cold atoms have been a test bench for many studies [5], nonlinear optical effects involving two-photon absorption have not been deeply investigated in this system. In a sample of cold atoms, the absence of motion and the long-range part of the interaction guarantee the necessary ingredients for a two-photon cooperative absorption, making this sample adequate for studying cooperative transitions near resonances. In this Letter, we demonstrate the *occurrence of a two-photon cooperative absorption* in a pair of colliding cold Na atoms kept in a magneto-optical trap [6]. Two photons from a *strong* laser having a frequency ω are absorbed by a cooperating pair of atoms producing $3P_{1/2}$ and $3P_{3/2}$ excited atoms when the relationship $2\omega = \omega_{S\rightarrow P_{1/2}} + \omega_{S\rightarrow P_{3/2}}$ between the laser frequency ω and the atomic transition frequencies is satisfied. We start with an overview of this effect followed by a description of the experimental system and the obtained results. Finally, we describe a few possible applications for the observed phenomenon.

Consider two colliding Na atoms. For simplicity, the hyperfine structure will not be included. The relevant levels and transitions of interest are presented in the diagrams in Fig. 1. Single-photon transitions in each individual atom as well as the two-photon transitions considered in this work are represented in the diagrams in Figs. 1(a) and 1(b). Without interaction between the atoms, the transition probability for two-photon absorption by the pair will be the product of the two independent one-photon, one-atom transition probabilities. In this case, the two-photon absorption by the two atoms occurs when the probe laser frequency is resonant with one of the atomic transitions [$3S_{1/2} \rightarrow 3P_{1/2}$ ($\hbar\omega_{P_{1/2}}$) or $3S_{1/2} \rightarrow 3P_{3/2}$ ($\hbar\omega_{P_{3/2}}$)]. When considering a new situation where the atoms can interact, the picture changes; the two-photon absorption by the pair is now possible when $\omega = \frac{\omega_{P_{1/2}}+\omega_{P_{3/2}}}{2}$ once the pair can distribute the energy absorbed and promote each atom to a different excited state.

The ideas for the theoretical basis are presented in Ref. [3], where an electric-dipole interaction is assumed between the incident light and each atom, whereas the interaction between the atoms is considered to be ruled by the dipole-dipole interaction. If we consider the linewidth of both individual transitions as $\hbar\Gamma$ and the dipole

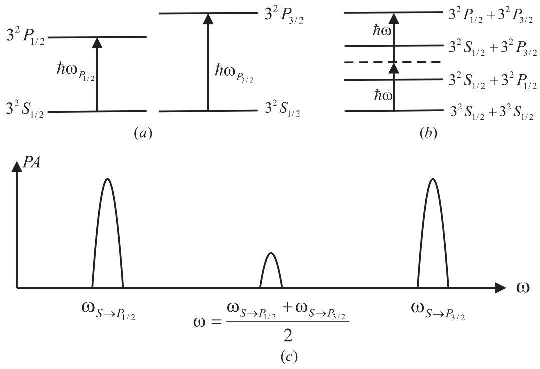

FIG. 1. Diagrammatic representation of the levels and transitions of interest. (a) One-photon transitions in each atom from the ground state to one of the excited states ($3S_{1/2} \rightarrow 3P_{1/2}$ and $3S_{1/2} \rightarrow 3P_{3/2}$). (b) Two-photon cooperative absorption in both atoms from the ground state to the double excited state ($3S_{1/2} + 3S_{1/2} \rightarrow 3P_{1/2} + 3P_{3/2}$). (c) Representation of the probability of absorption (PA) as a function of probe frequency (ω); when ω is equal to $\frac{\omega_{P_{1/2}}+\omega_{P_{3/2}}}{2}$, the presence of atomic interactions makes the transition to the excited states possible.

© 2012 American Physical Society

matrix element of each individual transition as $\mu_{P_{1/2}}$ and $\mu_{P_{3/2}}$, the total probability of absorption (PA) for a system interacting with a laser of frequency ω can be evaluated using second-order perturbation theory in the external field [3]. The final result is that the total absorption probability is

$$
\begin{aligned}
PA(\omega) \propto & \left[\frac{(\mu_{P_{1/2}} E/2\hbar)^2}{(\omega_{P_{1/2}} - \omega)^2 + (\Gamma/2)^2}\right]\left[\frac{(\mu_{P_{3/2}} E/2\hbar)^2}{(\omega_{P_{3/2}} - \omega)^2 + (\Gamma/2)^2}\right] \\
& \times \left[1 + \frac{4\langle H_I\rangle^2/\hbar^2}{(2\omega - \omega_{P_{1/2}} - \omega_{P_{3/2}})^2 + \Gamma^2}\right. \\
& \left. + \frac{4(2\omega - \omega_{P_{1/2}} - \omega_{P_{3/2}})\langle H_I\rangle/\hbar}{(2\omega - \omega_{P_{1/2}} - \omega_{P_{3/2}})^2 + \Gamma^2}\right], \qquad (1)
\end{aligned}
$$

where E is the electromagnetic field amplitude and $\langle H_I\rangle$ is the matrix element describing the interaction [3].

In the absence of interaction between the atoms ($\langle H_I\rangle = 0$), the probability of absorption peaks when the incident photon is resonant with the atomic transition ($\omega = \omega_{P_{1/2}}$ or $\omega = \omega_{P_{3/2}}$), as indicated by the first two brackets of Eq. (1) and represented by the two major peaks in Fig. 1(c). The last two terms of the third bracket in Eq. (1) show that a new absorption peak, which is the evidence of the two-photon cooperative absorption, appears for $\omega = \frac{\omega_{P_{1/2}} + \omega_{P_{3/2}}}{2}$, i.e., halfway between the two atomic transitions, whereas the unit factor reproduces the result for the case when there is no interaction. If we consider the interaction strength ($\langle H_I\rangle$) to be of the order of magnitude of the linewidth ($\hbar\Gamma$), Ref. [3] indicates that the two-photon contribution is estimated to be three orders of magnitude smaller than the one-photon contribution.

To experimentally demonstrate the two-photon cooperative absorption, we have used a magneto-optical trap containing sodium atoms [7]. An overview of the experimental system is presented in Fig. 2. An oven operating at 550 K generates an effusive atomic beam. The beam is decelerated by a Zeeman slowing technique in a spin-flip configuration [8]. Two dye lasers and a solid-state laser are used to produce all of the frequencies required for the experiment: deceleration, trapping, repumper, and probe. The trapping frequency is red-tuned 10 MHz from $3S_{1/2}(F = 2) \rightarrow 3P_{3/2}(F = 3)$ transition [9]. The trapping laser beam passes through an electro-optical modulator, generating a sideband that is resonant with $3S_{1/2}(F=1) \rightarrow 3P_{3/2}(F=2)$ transition and that works as a repumper for atoms ending in the wrong hyperfine ground state during the cooling process. The slowing laser is red-tuned 500 MHz from the $3S_{1/2}(F = 2) \rightarrow 3P_{3/2}(F = 3)$ transition. This laser beam also carries a sideband to allow for optical pumping to $3S_{1/2}(F = 2)$ before the atoms enter the slower magnet. The slowing laser is a solid-state commercial laser (TOPTICA TA-SHG pro), whereas the other two are dye lasers (Coherent 899). The probe laser scans through the transitions by intervals of 30 GHz and has its frequency monitored by a wave meter (HighFinesse WS-U).

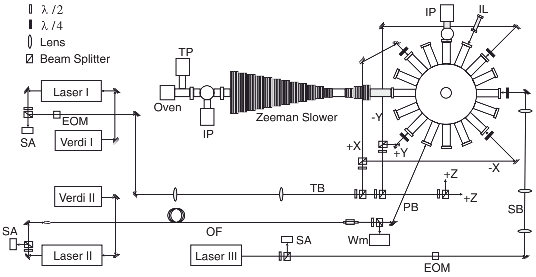

FIG. 2. Schematic representation of the experimental system, where SA denotes saturated absorption; TP, turbo pump; IP, ion pump; Wm, wave meter; IL, ionization laser; EOM, electro-optical modulator; SB, slower beam; PB, probe beam; OF, optical fiber; and TB, trapping beam.

Once the atoms undergo a transition reaching either of the states $3P_{1/2}$ or $3P_{3/2}$, they are detected using ionization caused by a 405 nm laser. The ionization laser reaches the cloud of cold atoms with an intensity of $11\ \mathrm{mW/cm^2}$ and can ionize any population in the $3P_{1/2}$ level and higher. Once ionized, individual ions are detected by a channeltron particle multiplier located near the trapped cloud [7]. A calibrated photodiode collects the fluorescence from the cold atoms to determine the number of trapped atoms, and a CCD camera is used to obtain the atomic cloud image. Both pieces of information allow the determination of the atomic density. The probe and ionization lasers are overlapped and focused into the atomic cloud following the same pathway. Ions detected by the channeltron are processed by an ion counter [10].

The time sequence for this experiment is shown in Fig. 3. Once the magneto-optical trap is filled with approximately 10^9 atoms, the slowing laser is shut down. At this moment, the probe and ionization lasers are released, and after a Δt, ion counting starts. Alternated time intervals detect the signal [Fig. 3(b)] and background [Fig. 3(a)]. The background is subtracted from the signal. Each frequency point is the result of 300 averages. The whole range of frequencies from $\omega_{P_{1/2}}$ to $\omega_{P_{3/2}}$ is contained in the probe laser scan. After a general scan, we have concentrated around the regions of interest. Detectable ion counts were observed for ω around $\omega_{P_{1/2}}$, $\omega_{P_{3/2}}$ and $\omega = \frac{\omega_{P_{1/2}} + \omega_{P_{3/2}}}{2}$ as presented in Fig. 4 and are in agreement with the prediction of Fig. 1.

The intensity balance between the trap and repumper lasers produces a population of atoms in the $3S_{1/2}(F = 2)$ much larger than the $3S_{1/2}(F = 1)$. We make the approximation that most atomic colliding pairs are in the $3S_{1/2}(F = 2) + 3S_{1/2}(F = 2)$ state. This phenomenon was previously investigated in our experimental system [7].

The final registered signal corresponds to the ions produced by the probe laser only, because we subtract signal A from signal B. During window A of the counter, atoms in the magneto-optical trap are naturally promoted to the $3P_{3/2}$ state by the trapping and repumper beams, and these atoms are ionized and counted. During window B, the

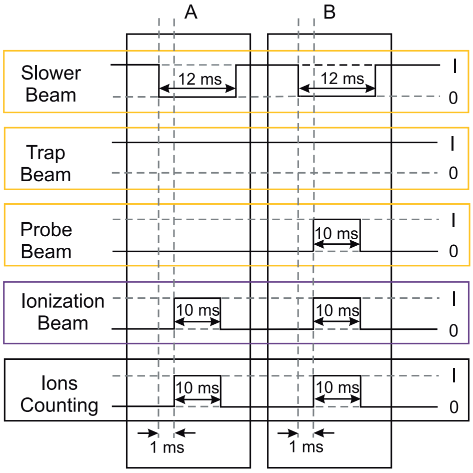

FIG. 3 (color online). The time sequence is divided into two counting windows, *A* and *B*. The first counts the ions formed by the ionization of the atoms in the excited states with energies equal to or higher than the $3P_{1/2}$ state due to absorption of the trap frequencies, i.e., the background ion counts. The second window counts the ions formed due to the absorption of the probe laser and the trap frequencies. The trap frequencies remain on during the whole measurement. The ion counts start 1 ms after the slower beam is shut down. The probe frequency is on during the counts in the second measurement window and off in the background counts.

effect of the probe laser is added. In this case, fluctuations can produce negative overall signals.

The peaks related to the one-photon transitions ($\omega = \omega_{P_{1/2}}$ and $\omega = \omega_{P_{3/2}}$) are much larger than the peak related to the two-photon cooperative absorption at $2\omega = \omega_{P_{1/2}} + \omega_{P_{3/2}}$, and they also present shoulders that are related to the hyperfine states of both ground and excited states. While the single-photon excitation peaks reach values up to 6000/s counts of ions, the two-photon excitation stays below 30/s. This large factor is expected based on calculations [3] for a system where $\langle H_I \rangle$ is on the order of $\hbar\Gamma$. Therefore, our interaction strength must be on the order of the line width.

The central peak in Fig. 4 (two-photon cooperative absorption) presents an evident asymmetry, shown in more detail in the small graph in the center. The asymmetry extending to the red part is a consequence of the attractive part of the interatomic potential.

The two single-photon absorption peaks have a verified linear dependence on the probe laser intensity, whereas the central peak amplitude has a quadratic dependence on the probe laser intensity, demonstrating the two-photon process. Figure 5 shows the observed quadratic intensity dependence.

The overall aspect of the data points presented in Fig. 6 extending more to the red part, reaching a maximum and fast decay on the blue side is a consequence of the compromise of two effects, the number of pairs at smaller internuclear separation and the potential dependence with the atoms' separation. To have a strong two-photon absorption, we need interaction, which can be obtained at the red side of the $\frac{\omega_{P_{1/2}}+\omega_{P_{3/2}}}{2}$ frequency, where the energy levels are curving down due to interaction. In contrast, to the red of resonance, the number of pairs decreases (resonance for pairs at smaller internuclear separation). The combination between those two effects results in the shape observed for the cooperative absorption.

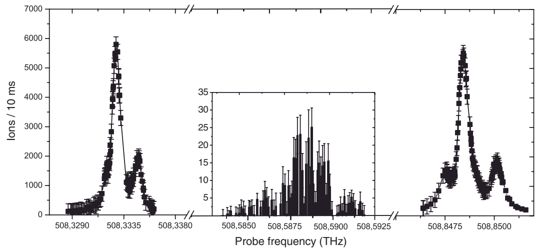

FIG. 4. Ion counts as a function of the probe frequency. From left to right, the first (last) peak is due to the ionization of the atoms excited to the $3P_{1/2}$ ($3P_{3/2}$) state. These peaks have shoulders that are due to hyperfine transitions. The central peak, shown in more detail in the small graph in the center, is evidence of the two-photon cooperative absorption.

In an attempt to better understand the two-photon cooperative absorption line shape, we have produced a simple model equivalent to the photo-associative ionization calculation presented by Gallagher [11]. The ground-state potential depends on the internuclear separation (R) as R^{-6}, whereas the excited-state potentials go as R^{-3}. Therefore, we can consider the ground-state to be constant at long range and the energy levels of the excited states to have a dependence like $\hbar\omega_j - C_j^{(3)}/R^3$ with $j = 1/2$ or $3/2$. Hence, the energy distance decreases as the atoms approach each other, which shifts the resonance frequency to the red.

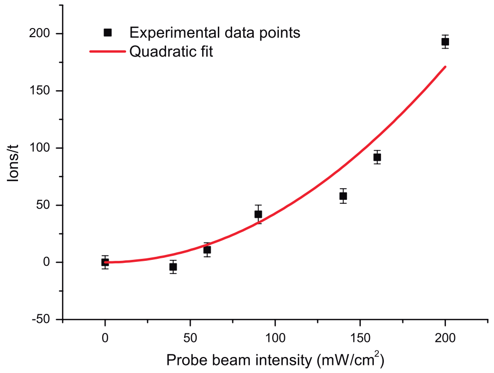

FIG. 5 (color online). Ion counts as a function of the probe intensity. A quadratic fit was plotted to see the expected behavior of two-photon cooperative absorption.

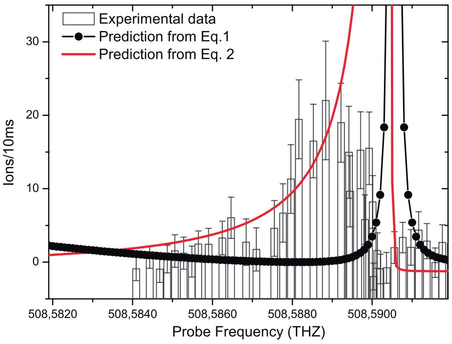

FIG. 6 (color online). Ion counts as a function of the probe laser frequency in the region around the halfway point between the $3P_{1/2}$ and the $3P_{3/2}$ transitions (central peak of Fig. 4). The experimental data are compared with the theoretical curve expected from Eq. (1) (dotted line) and with Eq. (2) (continuous line), which takes into account the R^{-3} dependence of the excited potentials. This finding demonstrates that the peak asymmetry comes from the R^{-3} dependence of the potentials.

Although the number of atoms involved in deeper and deeper collisions goes down for small interatomic distances. We have considered, for the model, that the density of pairs constant as a function of R. Integrating over R [Eq. (2)], we obtain an improvement when compared to Eq. (1). Figure 6 presents, together with experimental data, the models as predicted by Eqs. (1) and (2).

$$
\begin{aligned}
PA(\omega) \propto \int_0^\infty dR \Bigg[& \frac{(\mu_{P_{1/2}} E/2\hbar)^2}{(\omega_{P_{1/2}} - \frac{C^{(3)}_{1/2}}{R^3} - \omega)^2 + (\Gamma/2)^2} \Bigg] \\
\times \Bigg[& \frac{(\mu_{P_{3/2}} E/2\hbar)^2}{(\omega_{P_{3/2}} - \frac{C^{(3)}_{3/2}}{R^3} - \omega)^2 + (\Gamma/2)^2} \Bigg] \\
\times \Bigg[& 1 + \frac{4\langle H_I\rangle^2/\hbar^2}{(2\omega - \omega_{P_{1/2}} - \omega_{P_{3/2}} - \frac{C^{(3)}_{1/2}}{R^3} - \frac{C^{(3)}_{3/2}}{R^3})^2 + \Gamma^2} \\
& + \frac{4(2\omega - \omega_{P_{1/2}} - \omega_{P_{3/2}} - \frac{C^{(3)}_{1/2}}{R^3} - \frac{C^{(3)}_{3/2}}{R^3})\langle H_I\rangle/\hbar}{(2\omega - \omega_{P_{1/2}} - \omega_{P_{3/2}} - \frac{C^{(3)}_{1/2}}{R^3} - \frac{C^{(3)}_{3/2}}{R^3})^2 + \Gamma^2} \Bigg]. \quad (2)
\end{aligned}
$$

This model, presented in Eq. (2), has a good agreement with the behavior of the asymmetric part of the peak, demonstrating that asymmetry comes from the potential dependence on R, and not from hyperfine states, unlike the asymmetry present in the peaks centered at $\omega_{P_{1/2}}$ and $\omega_{P_{3/2}}$.

Although we have good agreement on the red side of the peak, we do not have the same for the maximum of the peak. The constructed model [Eq. (2)] predicts a much faster increase around the peak (factor of 4), and the frequency where the maximum is obtained appears to be displaced further to the blue in the model. In reality, as excitation approaches the peak, we are also approaching both the hyperfine splitting of the ground state (1.7 GHz) and the hyperfine state manifold for the excited states (0.2 GHz). In this region, the combination of the molecular levels produces a complex ‘‘spaghetti’’ of levels [12] already explored in cold atomic collisions. This complex level structure invalidates the simplified level structure considered in the model. To construct a more realistic model, such facts must be taken into account, but such a construction is far beyond the scope of this Letter.

Finally, we should point out that the two-photon cooperative absorption in cold atoms may open up a new, exciting nonlinear type of effect which may allow investigation into the process of cold-atom interactions in classical or quantum degenerate samples. The process is by itself a way to generate entanglement [13] of atoms in the excited state as well as to produce correlated photons with different frequencies [14,15]. Both of those effects may find interesting applications in the future.

We have demonstrated the occurrence of two-photon cooperative absorption in a sample of cold Na atoms. The topic of nonlinearities in colliding cold atoms has potential for many applications, and this first demonstration may stimulate further investigations.

The authors thank Daniel Magalhães, Marcelo Martinelli, and Miled Moussa for fruitful discussions and suggestions, and FAPESP (CEPID), CNPq (INCT), and CAPES for the financial support.

[1] J. Weiner, V. S. Bagnato, S. Zilio, and P. S. Julienne, Rev. Mod. Phys. **71**, 1 (1999).
[2] J. C. White, Opt. Lett. **6**, 242 (1981).
[3] J. R. Rios Leite and C. B. De Araujo, Chem. Phys. Lett. **73**, 71 (1980).
[4] D. L. Andrews and M. J. Harlow, J. Chem. Phys. **78**, 1088 (1983).
[5] J. W. R. Tabosa, S. S. Vianna, and F. A. M. de Oliveira, Phys. Rev. A. **55**, 2968 (1997).
[6] E. L. Raab, M. Prentiss, A. Cable, S. Chu, and D. E. Pritchard, Phys. Rev. Lett. **59**, 2631 (1987).
[7] R. R. de Paiva, R. Muhammad, R. F. Shiozaki, A. L. de Oliveira, D. V. Magalhães, J. Ramirez-Serrano, V. S. Bagnato, and K. M. F. Magalhães, Laser Phys. Lett. **6**, 163 (2009).
[8] D. S. Durfee, Ph.D. thesis, MIT, 1999.
[9] D. M. B. P. Milori, A. M. Tuboy, L. G. Marcassa, R. Habesch, S. C. Zilio, and V. S. Bagnato, Laser Phys. **8**, 1163 (1998).
[10] V. Bagnato, L. Marcassa, C. Tsao, Y. Wang, and J. Weiner, Phys. Rev. Lett. **70**, 3225 (1993).
[11] A. Gallagher, Phys. Rev. A **44**, 4249 (1991).
[12] P. D. Lett, P. S. Julienne, and W. D. Phillips, Annu. Rev. Phys. Chem. **46**, 423 (1995).
[13] A. Einstein, B. Podolsky, and N. Rosen, Phys. Rev. **47**, 777 (1935).
[14] M. D. Reid, P. D. Drummond, W. P. Bowen, E. G. Cavalcanti, P. K. Lam, H. A. Bachor, U. L. Andersen, and G. Leuchs, Rev. Mod. Phys. **81**, 1727 (2009).
[15] M. D. Lukin, Rev. Mod. Phys. **75**, 457 (2003).

IOP Publishing | Astro Ltd Laser Physics Letters

Laser Phys. Lett. **13** (2016) 065501 (10pp) doi:10.1088/1612-2011/13/6/065501

Direct comparison between a two-dimensional magneto-optical trap and a Zeeman slower as sources of cold sodium atoms

E Pedrozo-Peñafiel, F Vivanco, P Castilho, R R Paiva, K M Farias and V S Bagnato

Instituto de Física de São Carlos, Universidade de São Paulo, C.P. 369, 13560-970 São Carlos, SP, Brazil

E-mail: edwinpedrozo@gmail.com

Received 17 March 2016, revised 21 April 2016
Accepted for publication 22 April 2016
Published 12 May 2016

Abstract

The atom source is a relevant component in many atomic molecular optics experiments. The compactness and efficiency of the source are fundamental issues, acquiring more importance as the complexity of the experiments increases. Characterizing new techniques to produce high atom flux is necessary to know the efficiency and peculiarities of each one. This allows choosing the most suitable source for a specific experiment. In this work, we show a direct comparison between a two-dimensional magneto-optical trap (2D-MOT) and a Zeeman slower (ZS) as source of cold sodium atoms to load a standard three-dimensional magneto-optical trap. The optimum parameters for each case are obtained by observing the loading rate and the final number of atoms in the 3D-MOT. We conclude that the 2D-MOT provides a high flux of atoms comparable with that produced by the ZS, but with an enormous advantage with respect to the size of the apparatus.

Keywords: magneto-optical trap, Zeeman slower, 2D-MOT, cold atomic source

(Some figures may appear in colour only in the online journal)

1. Introduction

The physics of cold atoms has expanded dramatically since the original experiments of atomic cooling and trapping [1, 2]. The first deceleration of an atomic beam [1], done with sodium atoms, opened the possibility to capture these atoms in a magneto-optical trap (MOT) [2]. The advantages of cold and ultracold atomic samples are widely recognized and vastly used [3–5], making them a perfect test bench for general physics. Therefore, it is crucial to develop and improve the experimental setup, making it more versatile, efficient, compact, easily constructed and maintained. Usually the first step in every AMO (atomic, molecular and optics) experiment is to load a trap with a source of atoms, molecules or ions. The trap depth sets the maximum energy ($E_{TD} \approx k_B T$) that an atom can have so it can be trapped. This maximum energy is related to the kinetic energy of the particles, and consequently to its temperature. Therefore, to successfully load a shallow trap one must have a good source of cold atoms. Historically the first efforts to cool an atomic beam and load a trap came from the idea of using the radiation pressure from a laser beam to slow down the atoms (laser cooling) [6]. One of the most successful techniques that uses laser cooling to produce this cold atomic beam is the Zeeman-slower (ZS). Designed by Phillips and Metcalf [1] in 1982 it uses the Zeeman shift to compensate the Doppler shift felt by the atoms when they decelerate, keeping them constantly in resonance with the light field.

Other methods use two vacuum chambers in a double-MOT configuration [7] ensuring an ultra-high vacuum (UHV) region at the final trap chamber. Using a hot vapor as the source of atoms, a 3D-MOT is realized in a first chamber and then pushed to the final trap chamber with a laser beam. This makes the vacuum of the final chamber orders of magnitude better due to the fact that only the colder atoms in the first chamber are transferred. A disadvantage of this configuration is the low axial velocity, then—the time to load the 3D-MOT in the UHV vacuum region is relatively long in comparison with a Zeeman slower source. The flux can be increased if

© 2016 Astro Ltd Printed in the UK

one uses a 2D-MOT as a source, instead of the 3D-MOT. This setup, initially developed by Dieckmann *et al* [8] for ^{87}Rb, and expanded to other species like ^{39}K and ^{41}K [9], and ^{7}Li [10], is one of the most recent ways to produce a flux of cold atoms comparable with the Zeeman slower.

For ^{23}Na atoms, the most common source of slow atoms is the ZS. Recently, the first 2D-MOT for ^{23}Na atoms was developed as a source of cold atoms [11], based on the work initially developed for lithium atoms [10]. Therefore, it is interesting to directly compare both sources in the same experimental system. In this work, we used both ZS and 2D-MOT as independent sources of atoms for loading the same 3D-MOT of sodium atoms. We built a 2D-MOT inspired in the design described by Lamporesi *et al* [11] and also used a ZS previously designed using the spin-flip configuration [12, 13] for comparison. We have the advantage that both sources are going to the same science chamber, which means that we directly compared the loading rate, efficiency, and studied other important parameters of each technique in similar conditions. Prior to this work, the work of Dieckmann *et al* [8], showed the comparison realized between a 2D-MOT source of rubidium atoms and a LVIS (Low-velocity Intense Source) [7]. The conclusion was that for Rb atoms the 2D-MOT provided a higher flux of atoms than the LVIS with the advantage of using an overall less laser power.

This letter is divided into four sections. In section 2 we briefly describe the fundamental concepts of both 2D-MOT and ZS. In section 3 we describe the experimental system; in section 4 the results obtained from the characterization giving the optimum parameters found for our system are shown, and finally the conclusions.

2. Main features of the 2D-MOT and ZS

In this section, we give a background of the working principle of both cold atom sources ZS and 2D-MOT.

2.1. Main features of the ZS

ZS sources are designed to decelerate atoms from a maximum initial velocity (v_0) to a velocity (v_{final}) smaller than the trap's capture velocity [14], which is the maximum velocity that the atoms can have in order to be captured in the MOT. ZS consists in using an atomic cycling transition to slow down a beam of atoms via radiation pressure force. This is done by applying a light field counter-propagating to the atomic beam combined with a spatially dependent magnetic field that compensates the Doppler shift of the light with the change in energy due to the Zeeman effect.

When a laser beam with wave vector $\vec{k}$ shines in the opposite direction to an atomic beam and has a frequency close to an atomic resonance (ω_0), the atoms in the ground state will absorb a photon and go to the excited state. In this process they will lose $\hbar k$ of momentum in the $\vec{k}$ direction. After a time (on average) equal to the excited state lifetime, they will spontaneously emit a photon with momentum $\hbar k$ in a random direction. If this transition is cyclic, i.e. the decay occurs directly to the initial ground state, after many cycles the atom will lose a velocity equal to $\hbar k/m$ per cycle in the direction of $\vec{k}$.

In a semi-classical treatment for a two-level atom interacting with a classical light field with frequency ω one can derive the following relation for the force

$$F = \hbar k \frac{\Gamma}{2} \frac{s}{1 + s + \frac{4\delta}{\Gamma^2}} \tag{1}$$

where Γ is the excited state lifetime, $\delta = \omega - \omega_0$ is the slowing light detuning from resonance, and s is the ratio of the laser intensity (I) to the transition saturation intensity (I_s) ($s = I/I_s$). The detuning is strongly dependent on the atom velocity, since atoms with different velocities see a different laser frequency ω due to the Doppler shift. In the rest frame of the atoms, the Doppler effect shifts the slowing light frequency by $\vec{k} \cdot \vec{v}$, where $\vec{v}$ is the atom velocity, so the detuning can be rewritten as $\delta = \omega + \vec{k} \cdot \vec{v} - \omega_0$. In order to compensate this shift, one can use the Zeeman effect to change atomic energy levels.

In the presence of a static magnetic field (B) the hyperfine splitting of the Zeeman sub-levels is given by $\Delta E = \mu' B$, where μ' is the magnetic moment of the cycling transition. Therefore, in the presence of a B field the atomic resonance is equal to $\omega_0 + \mu' B/\hbar$. Combining both the Zeeman and the Doppler effect, in a two-level atom interacting with a classical light field model in the presence of a magnetic field, the slowing light detuning δ is given by

$$\delta = \omega - \omega_0 + \vec{k} \cdot \vec{v} - \frac{\mu' B}{\hbar}. \tag{2}$$

If we have spatially inhomogeneous magnetic field, the light field detuning will be spatially dependent. So we could tailor the magnetic field in order to maintain the maximum deceleration i.e. $\delta = 0$ at each point in space. From (1) we see that if $s \gg 1$ and $\delta = 0$ one can obtain the maximum acceleration for the atoms $a_{\max} = \hbar k \Gamma / 2m$. Considering that the laser beam produces a constant deceleration of the atoms and that it is a fraction of the maximum deceleration ($a = \eta a_{\max}$), the equation for the acceleration can be related to the velocity of the atom at each position by: $(v_{\text{atom}}(z))^2 = v_0^2 - 2az$. Combining all these expressions, we can obtain a magnetic field profile as a function of the position for an optimum cooling condition as

$$B(z) = B_0 - \left(\frac{\hbar k v_0}{\mu'}\right) \sqrt{1 - \left(\frac{z}{z_0}\right)^2} \tag{3}$$

where z_0 is the length of the ZS given by $z_0 = (v_0^2 - v_{\text{final}}^2)/2a$ and B_0 is the magnetic field at the point where the atoms have the initial velocity (v_0).

The initial velocity is set by the Maxwell-Boltzmann distribution of the atom source (usually an oven) and it defines the class of velocities, $v_{\text{initial}} < v_0$, that will be slowed down up to, or smaller than v_{capture} (capture velocity). The v_0 value together with the fraction of the maximum deceleration (η), usually $0.5 < \eta < 0.7$, defines the size of the ZS. There is a balance between the size and the flux of cold atoms, the longer the slower is, the higher the value of v_0—but v_0 also sets the magnitude of the magnetic field. If one chooses to high values of v_0 one might obtain impractical values of $|B(z)|$. The bias field B_0 sets the light field detuning from the cycling transition, usually it is chosen to be of the order of 100 MHz to the red of the transition, by doing so, the Zeeman beam does not create a large unbalancing force at the trap region. Normally one adds at the end a second coil, inverting the field to match the MOT field. Summarizing, the whole process can be seen in the following simple way: the photons satisfying the relation

$$0 = \Delta + \left|\vec{k} \cdot \vec{v}\right| + \frac{\mu' B(z)}{\hbar} \tag{4}$$

will be absorbed by the atoms and in this way the interchange of momentum between light and atoms works to decelerate the atomic beam. Once one atom absorbs a photon it recoils, losing velocity, and after a spontaneous re-emission of the photon, it gains a random momentum, which on average after many absorption–emission processes is zero, thus having a net momentum exchange in the direction contrary to the motion [15].

2.2. Main features of the 2D-MOT

Magneto-optical traps are used for confining neutral atoms in a certain region by combining an inhomogeneous magnetic field and circular polarized light resonant to a cycling transition to create the trapping potential [2]. The MOT working principles can be understood using the one-dimensional case. In 1D, the MOT consists of a pair of counter-propagating laser beams with opposing circular polarization and a linear magnetic field gradient. Usually, the laser frequency is set to the red of an atomic transition.

Because of the Zeeman effect the gradient in the magnetic field creates a position dependence of the hyperfine energy level whose slope depends on the linear product $-\vec{\mu}.\vec{B} = g_F m_F \mu_B B'$. For $m_F > 0$ ($m_F < 0$) the slope is positive (negative). The slightly red-detuned laser has one beam with σ^+ polarization, with respect to the quantization axis created by magnetic field, coming from the x direction and another with σ^- coming from the $-x$ direction. The two opposing dissipative forces are given by

$$F_{\sigma\pm} = \hbar k \frac{\Gamma}{2} \frac{s}{1 + s + \frac{4\delta_{\pm}^2}{\Gamma^2}} (\pm \hat{x}) \tag{5}$$

just like in the case of the ZS, but here, because of the magnetic field gradient, the detuning from the transition δ_+ and δ_- are position dependent. If the atom position (x) is $x > 0$ we have $\delta_- < \delta_+$ and for $x < 0$ we have $\delta_- > \delta_+$.

From that one can see that if the atoms try to escape to the $\hat{x}$ direction the transition with $\Delta m_F < 1$, only possible with σ^- light, will push the atoms more strongly toward the zero position than the σ^+ force is pushing away from zero and vice versa—thus creating a net force that restores the atoms to the zero point of the magnetic field.

The 2D-MOT uses the same principle to cool the atoms in the x and y directions.

Once the atoms are cooled down in the 2D-MOT, they are transferred to a 3D-MOT chamber, where a three-dimensional magneto-optical trap is realized. The atoms are transferred using a laser beam that pushes the atoms from the 2D-MOT to the 3D-MOT chamber. This laser beam is called the push beam. This is the scheme of a double-MOT configuration [11] mentioned before, but with a 2D-MOT as the source of atoms for the 3D-MOT.

3. Experimental apparatus

In this section, we describe the experimental setup and the characterization of both atom sources, ZS and 2D-MOT. The whole experimental apparatus can be seen in detail in figure 1. In the description, the three parts (science chamber, 2D-MOT and ZS) are considered independently; we start with the science chamber where all characterization of both sources took place. Then, we show the ZS characteristics and the 2D-MOT setup.

3.1. Science chamber

The science chamber shown in the center of figure 1 is where the sodium atoms are trapped in a 3D-MOT. It is made of stainless steel with six windows in the lateral face and two deep windows in the bottom and top faces. This chamber is pumped with an ion pump of 75 L s^{-1} and is maintained at a pressure of 8×10^{-10} Torr.

Two coils in anti-Helmholtz configuration mounted along the vertical direction are used to produce the quadrupolar magnetic field. We use a current of 5 A to produce a field gradient of approximately 15 G cm^{-1}.

Three retro-reflected collimated laser beams are used for producing the dissipative and restoring forces in the MOT and are obtained from a Coherent 899 dye laser, that we will call Dye laser 1 from now on. Each arm of the beam has a diameter of 2.0 cm and intensities of 15.9 mW cm$^{-2} \approx 2.5 I_s$, with I_s being the saturation intensity for the $D2$ line of sodium.

For producing the 3D-MOT we use two frequencies: the transition $3^2S_{1/2}(F = 2) \rightarrow 3^2P_{3/2}(F' = 3)$ as cooling frequency, and the transition $3^2S_{1/2}(F = 1) \rightarrow 3^2P_{3/2}(F' = 2)$ as the repumper [2]. The laser is locked to the cooling transition observed in the saturation absorption spectroscopy, and the MOT frequency is then red-detuned by 23 MHz. The repumper frequency is obtained by using an Electro-optical modulator, EOM, (Newport) of 1.7 GHz. Its intensity is about 49% the intensity of the cooling frequency or 7.8 mW cm^{-2} ($I = 1.2 I_s$). This is observed in a Fabry-Perot interferometer used to measured the intensity ratio between cooling and repumper beams.

The characterization of the atom sources was based on the number of trapped atoms in the 3D-MOT. This number was obtained through the measurement of the atomic fluorescence with a calibrated photodetector (PD). The total power scattered by the cloud can be given by [16] $P_{\text{total}} = N_{\text{MOT}} \hbar \omega_0 \Gamma \rho_{ee}$, where N_{MOT} is the total number of atoms, $\hbar \omega_0$ is the energy of the transition in question (cooling transition), $\Gamma \rho_{ee}$ is the total

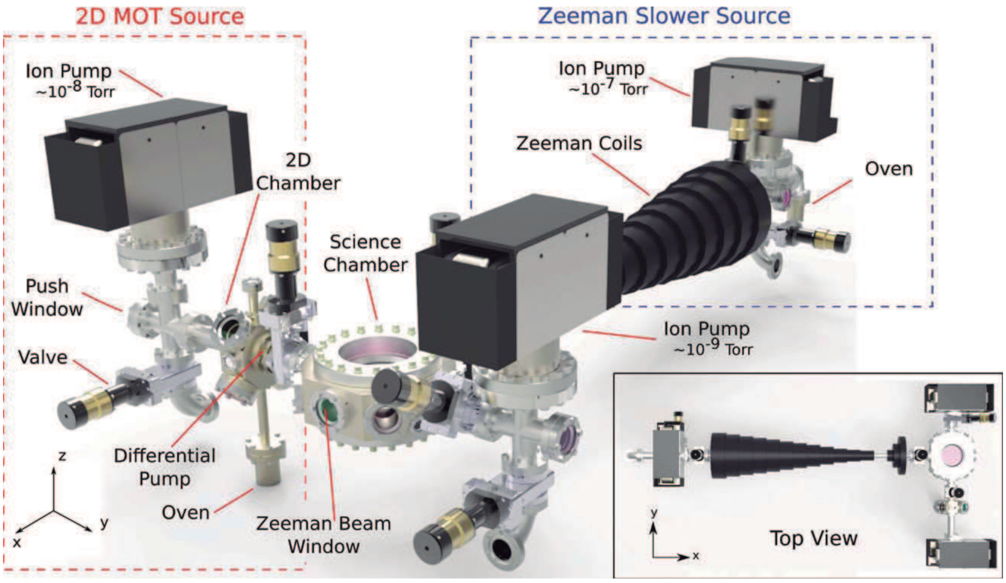

Figure 1. Experimental system. On the left is the 2D-MOT chamber with the corresponding ionic pump to produce the necessary vacuum to trap the atoms coming out from the oven. On the top right is the ZS. It is possible to notice the compactness of the 2D-MOT chamber with respect to the ZS apparatus. In the central region is the science chamber.

decay rate the from the excited state, $\Gamma = 2\pi \times 10$ MHz, the linewidth of the $D2$ sodium line, and $\rho_{ee} = \frac{1}{2}s\left[1+s+\left(\frac{2\delta}{\Gamma}\right)^2\right]^{-1}$ is the density matrix element for the excite state population, and s is the saturation parameter [17].

The atomic cloud scatters light isotropically, but with the PD we are able to collect just a portion of this light so that the power on the PD obeys the ratio $P_{\mathrm{PD}}/P_{\mathrm{total}} = \mathrm{d}\Omega/4\pi = \pi r^2/4\pi f^2$. Here, f and r are the focus and radius of the lens used to focus the fluorescence of the MOT onto the PD. Also, the relation between the power of the light emitted by the atomic cloud and the voltage measured by the PD is given by the proportionality factor α ($P_{\mathrm{PD}} = \alpha V_{\mathrm{PD}}$), which is obtained from the calibration of the PD, and has units of Watts Volts^{-1}. Combining all these relations, the number of atoms is given by, $N_{\mathrm{MOT}} = 4\alpha f^2(\hbar\omega_0\Gamma\rho_{ee}r^2)^{-1}V_{\mathrm{PD}}$.

3.2. ZS as a source of atoms and main characteristics

The ZS is a cylindrical stainless steel tube of 2.39 cm of internal diameter, 2.55 cm of external diameter and 100 cm length covered with a set of coils which generate the ZS magnetic field.

We use an ion pump of 75 L s^{-1} to maintain a pressure of about 10^{-8} Torr. A six-way connects to the oven, shown in figure 1, and which we will call oven$_{\mathrm{ZS}}$ from now on. Between the ZS tube and the oven$_{\mathrm{ZS}}$, there is a gate valve that allows separating these two regions. Also, there is a differential pumping tube that maintains a difference in the pressure of 10^{-1} between these two parts of the system in order to avoid the excess of pressure in the ZS tube caused by the oven$_{\mathrm{ZS}}$.

The top window of the six-way is used to connect the ion pump and the side-windows are used as observation windows, in which it is possible to see directly by eye, or camera, the fluorescence of the atomic beam while interacting with the decelerating light.

The oven$_{\mathrm{ZS}}$ is connected to an elbow shaped tube with a gasket at the end. This gasket has a nozzle of 4 mm diameter and is attached to the output of the elbow tube in order to produce an effusive collimated atomic beam when the oven$_{\mathrm{ZS}}$ is heated. The differential pumping tube also helps to collimate the atomic beam, leaving in the beam only the atoms whose trajectory is almost horizontal, i.e. in the axial direction of the ZS tube, which in this way can then reach the science chamber. Also, between these two regions we place a gate valve in order to separate the two regions while using only the 3D-MOT with the 2D-MOT as the source of atoms, among other technical reasons, like independent maintenance.

The magnetic field of the ZS is produced by a set of coils placed with axial symmetry. We use a spin-flip configuration [12, 13] in which the magnetic field at the beginning of the ZS, i.e. at the output of the oven$_{\mathrm{ZS}}$ is very high and slowly decreases with distance, reaching a part of zero magnetic field and afterwards an increasing small magnetic field, as expressed by (3) and shown in figure 2. Figure 2 also shows the magnetic field profile together with the ZS for comparison.

The counter-propagating laser beam used to decelerate the atomic beam enters by the opposite window of the ZS tube and is focused onto the nozzle, i.e. the output of the oven in order to compensate the solid angle in which the effusive atomic beam is opening. The beam in the entrance window, where the intensity is measured, has a diameter of 3 cm

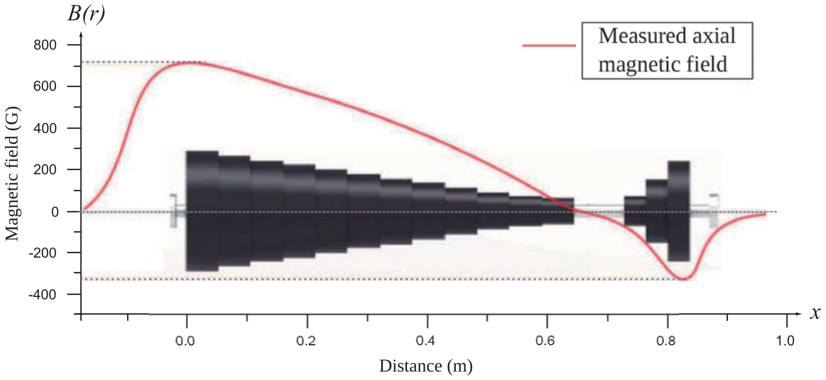

Figure 2. Magnetic field profile of the ZS. Solid line represents the theoretical profile given by (3) and the experimental data are represented by dots. The current used to generate this magnetic field is 12 A.

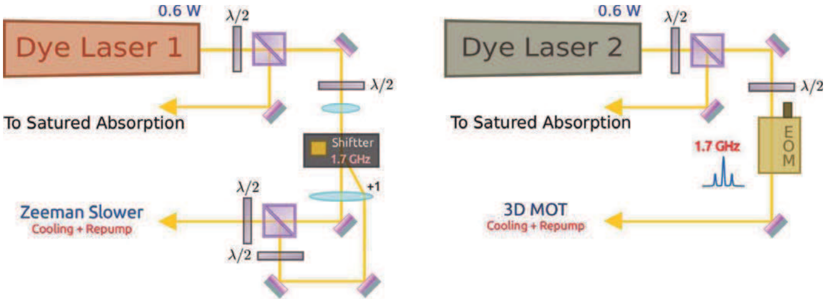

Figure 3. Optical system used for 3D-MOT and ZS as a source of atoms.

and is the combination of the two frequencies, cooling and repumper, with intensities of $4.5I_s$ and $1.1I_s$ respectively. The repumper frequency is used to maintain the atom flux in the state $3^2S_{1/2}(F = 2)$. At the nozzle, where the atoms come out from the oven, the beam has a diameter of 0.6 cm. The frequency of the deceleration laser beam, which we will call ZS laser beam from now on, is red-detuned about 180 MHz relative to the cooling transition.

To obtain the repumper frequency we use an acoustic-optical modulator, AOM (Brimrose), with an input radio-frequency (RF) around 1.712 GHz. The optical setup for producing the frequencies for decelerating the atom flux and the frequencies for trapping the atoms in the 3D-MOT chamber are depicted in figure 3.

To characterize the ZS performance we vary the parameters around those projected in the design, as the temperature of the oven$_{ZS}$, current of the ZS coils, frequency and power of the cooling and repumper light. When each parameter is changed we look at the number of trapped atoms in the science chamber.

We also started optimizing the 3D-MOT in order to obtain the best configuration of frequencies, intensities and alignment of the laser beams. The results of this characterization are shown below.

The optimum value for the temperature of the oven is 300 °C and the best value for the current of ZS coils is 12 A. Figure 4 shows that the best detuning for the ZS laser beam is about -180 MHz with respect to the cooling frequency. Also, from figure 4 it is possible to notice that the frequency detuning allows several tens of MHz of scan and still have a good number of trapped atoms in the 3D-MOT. In this figure, it is possible to see that the number of trapped atoms is of the order of 10^{10} with a relatively low intensity of $\sim 1.7I_s$.

With respect to the repumper light of the Zeeman slower we see from figure 5 that the best frequency is about -150 MHz with respect to the repumping frequency. We obtain a good number of atoms with an intensity around $\sim I = 1.1I_s$.

3.3. 2D-MOT as a source of cold atoms and its characteristics

The 2D-MOT system is composed of a stainless steel chamber with four windows (2.75″ CF flanges) aligned in a cross geometry 45° rotated from the gravitational axis. These windows are used for the trapping light, while the gravitational axis defines the ZS (ZS$_{2D}$) and oven (oven$_{2D}$). In the top of the 2D chamber, the small window is used as the entrance of the laser that decelerates the atomic beam coming out from the oven, which is placed at the bottom and attached to the 2D chamber through a tube of diameter 1.71 cm and a length of 10 cm (see figure 6). This tube also helps to collimate the atomic beam coming out from the oven$_{2D}$. Then, the 2D-MOT also has a

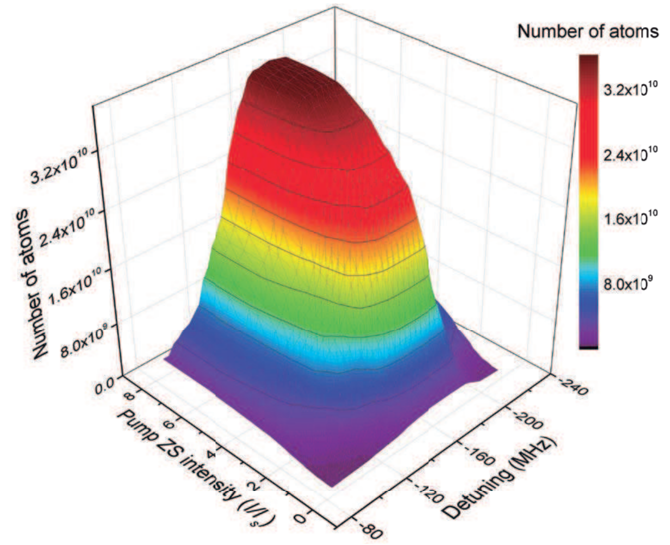

Figure 4. Number of trapped atoms as a function of the intensity and detuning of the counter-propagating cooling laser beam which decelerates the atoms coming from the oven$_{ZS}$.

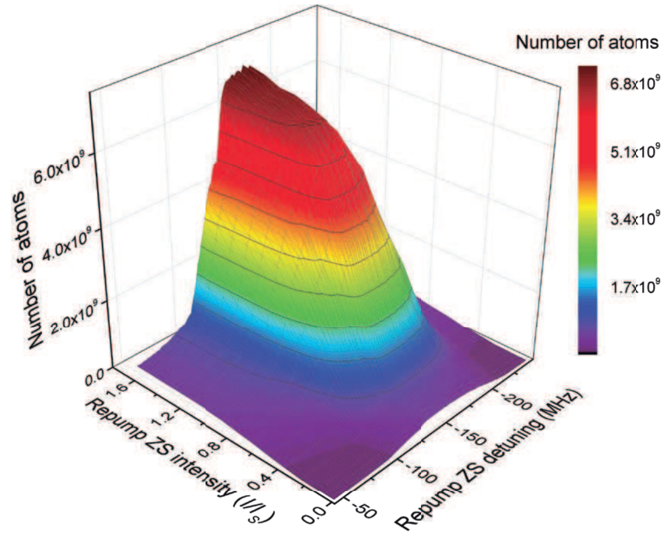

Figure 5. Number of trapped atoms as a function of the intensity and detuning of the repumper laser beam. This beam is combined with the decelerating cooling beam and acts on the atom flux coming from the oven$_{ZS}$ in order to recover the atoms that fall into the state $3^2S_{1/2}(F = 1)$ state. This detuning is measured with respect to the repumper transition frequency. In this case, the decelerating pumping beam was fixed with a value of $4.5I_s$ of intensity and -180 MHz with respect to the cooling transition.

ZS-like magnetic filed profile produced by the remaining field of the 2D-MOT as it will be briefly explained.

To produce the magnetic field of the 2D-MOT of ^{23}Na four sets of nine permanent magnets arranged in a rectangular shape are used. The geometrical center of this arrangement is exactly the center of the 2D-MOT chamber as shown in figure 6. The center of the magnets has a horizontal separation of 9.0 cm and a 10.0 cm vertical separation. They have a magnetization of 1.0×10^6 A m^{-1} and a dipole unit vector perpendicular to both the push and gravitational axes. The magnets are N42 grade Nb with dimensions of $1'' \times 3/8'' \times 1/8''$, produced by K&J magnetics.

For the 2D-MOT, the field gradient along the $\hat{z}$-direction is calculated and measured to be 49 G cm^{-1}. Additionally, the

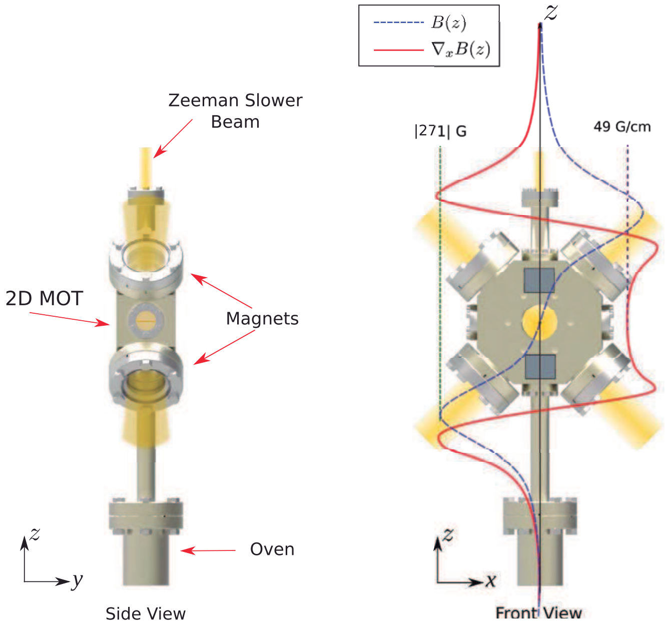
Zeeman Slower Beam
2D MOT
Magnets
Oven
z
y
Side View
B(z)
∇xB(z)
z
|271| G
49 G/cm
z
x
Front View

Figure 6. 2D-MOT chamber and magnetic field profile generated by the four sets of nine permanent magnets. The magnetic field along the z-axis is shown. The atom transfer between the 2D-MOT and 3D-MOT is realized in the y-direction. With this configuration the magnetic field is null along the y-direction around the center of the chamber ($x = 0,\ z = 0$). The curve for the magnetic field represents the experimental magnetic field and the gradient of this field is calculated from this curve.

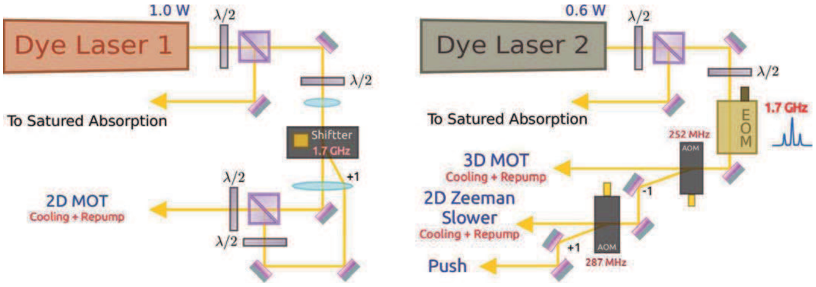
1.0 W
λ/2
Dye Laser 1
λ/2
To Satured Absorption
Shiftter
1.7 GHz
+1
λ/2
2D MOT
Cooling + Repump
λ/2
0.6 W
λ/2
Dye Laser 2
λ/2
To Satured Absorption
1.7 GHz
EOM
252 MHz
AOM
3D MOT
Cooling + Repump
-1
2D Zeeman Slower
Cooling + Repump
+1
AOM
287 MHz
Push

Figure 7. Optical setup used for the 3D-MOT and 2D-MOT.

arrangement of the magnets ensures that the magnetic field and its derivative along the $\hat{y}$-axis is zero (figure 6). The field profile along the gravitational axis is also simulated and used as an effective Zeeman decelerator (ZS_{2D}). The profile of the magnetic field and the respective gradient is shown in figure 6.

A Coherent 699 dye laser (Dye laser 2) is used for generating the cooling and repumper frequencies required for the 2D-MOT. To produce the necessary frequencies for the ZS_{2D} (cooling and repumper) we use a portion of the light generated by Dye laser 1, which is used for the 3D-MOT. This light, which comes from an EOM (around 1.712 GHz), passed through an AOM to generate the correct detuning (see figure 7), then containing the cooling and the repumper transitions. The optical setup for the 2D-MOT is depicted in figure 7.

The 2D-MOT and science chamber are joined through a differential pumping tube of 0.2 cm diameter and 2.3 cm length which maintain a difference in pressure between these two chambers of the order of 10^{-3} ($P_{sc} = 10^{-3}P_{2D}$). The cooled atoms in the 2D-MOT are transferred to the 3D-MOT chamber using the push beam whose frequency is 12 MHz blue-detuned from the cooling transition of the 2D-MOT—we found this optimum frequency by scanning it and observing the number of trapped atoms in the science chamber, as shown in figure 8.

Figure 1 shows the 2D-MOT chamber attached to the science chamber and all the parts that compose it. The pressure in this chamber when operating the oven_{2D} is about 9×10^{-9} Torr to 1×10^{-8} Torr.

From the description of the 2D-MOT principle of operation and looking at the experimental apparatus we can

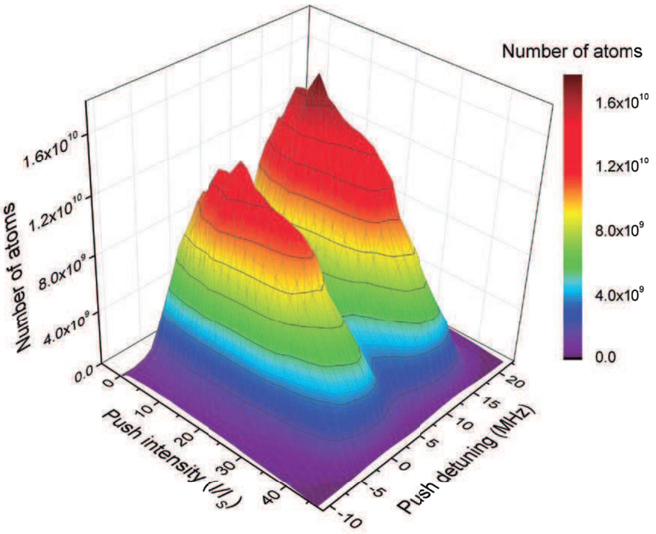

Figure 8. Number of trapped atoms as a function of the push beam intensity and detuning.

resume the overall operation as follows: the atoms are heated in the oven at approximately 210 °C producing an effusive vapor of atoms that travels through the tube connecting the oven$_{2D}$ and the 2D-MOT chamber. The tube works as a collimator creating an atomic beam which will reach the 2D-MOT chamber. On the way to the chamber, the atomic beam is decelerated by a counter-propagating laser beam and the remaining magnetic field produced by the permanent magnets. When the atoms reach the center of the chamber they feel the dissipative force of the light beams and the magnetic field, being cooled in this way in the axial direction in the center of the chamber. Due to the absence of magnetic field and cooling light in the longitudinal direction (y-axis) the 2D-MOT exhibits an elongated geometry in this direction, similar to that of a cigarette. Once the atoms are in the 2D-MOT region, a push beam propagating in the $+\hat{y}$-direction is turned on, i.e. pushing the atoms in the 2D-MOT to the capture volume of the 3D-MOT, where they are finally captured. We again measured the fluorescence of the 3D-MOT, as for the ZS characterization, in order to determine the number of trapped atoms in the 3D-MOT.

The frequency and intensity of the push laser beam were varied. We found in figure 8 that ~12.2I_s is the best intensity for transferring the atoms. We used a collimated beam with a diameter of ~1 mm. We observe that when the detuning is zero there is a good transfer of atoms from the 2D to the 3D-MOT, but the push beam affects also the 3D-MOT itself, changing its shape and position and possibly limiting its number of trapped atoms. At +12 MHz, the fluorescence signal of the 3D-MOT slightly increases and we could not see any direct effect of the push beam on the final MOT, so we chose to continue with this configuration. The value of this parameter is in total agreement with the value reported in [11] for ^{23}Na.

Figure 9 shows the number of trapped atoms as a function of the frequency of the repumper beam and its intensity. This beam has a diameter of 2.0 cm, and it is noted from the curve that with an intensity of ~4.3I_s we start to have a number of trapped atoms of the order of 10^{10}.

In figure 10 is shown the intensity and detuning for the ZS cooling light of the 2D-MOT. With a detuning of −275 MHz and an intensity of $I = 31.8I_s$ a number of atoms of the order of 10^{10} is obtained. The diameter of this beam is about 1 cm.

With all these parameters fixed we vary the temperature of the oven, which was found to be optimum at 210 °C.

For the 2D trapping frequency the best detuning is −13 MHz and this value was used in all the processes described above. Taking into account that the linewidth for this transition is $\Gamma = 10$ MHz we obtained that the frequency is red-detuned approximately 1.3Γ. The intensity of each retro-reflected arm of the 2D-MOT trapping beam is ~5.1I_s.

4. Overall comparison between the two atom sources

The characterization of a loading source involves mostly the determination of its loading rate (L). It is worth recalling that for comparing the two sources of atoms to load the 3D-MOT we attached the 2D-MOT and the ZS together with the science chamber. We first realized the loading with the ZS, obtaining the main features of the loading process, and afterwards we did the same for the 2D-MOT loading.

All the parameters were optimized looking for the largest number of trapped atoms of the 3D-MOT in the main chamber. With all the optimized parameters for the ZS and 2D-MOT, separately, we obtained the loading curve in the 3D-MOT in

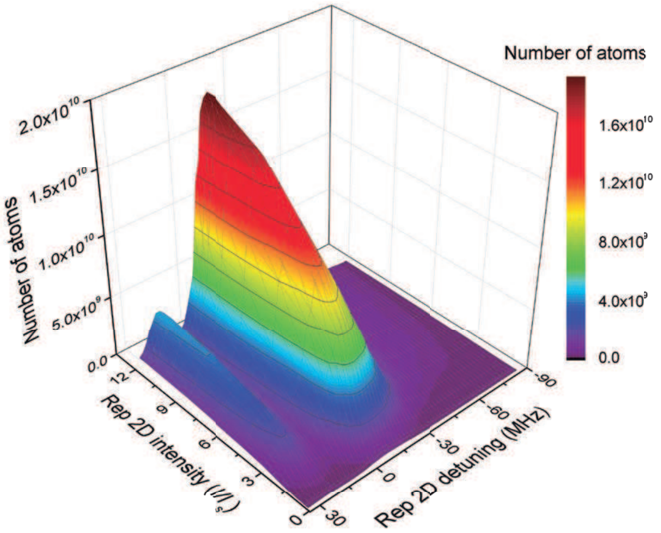

Figure 9. Number of trapped atoms as a function of the repumper beam intensity and detuning of the 2D-MOT. The detuning is measured with respect to the repumper frequency transition.

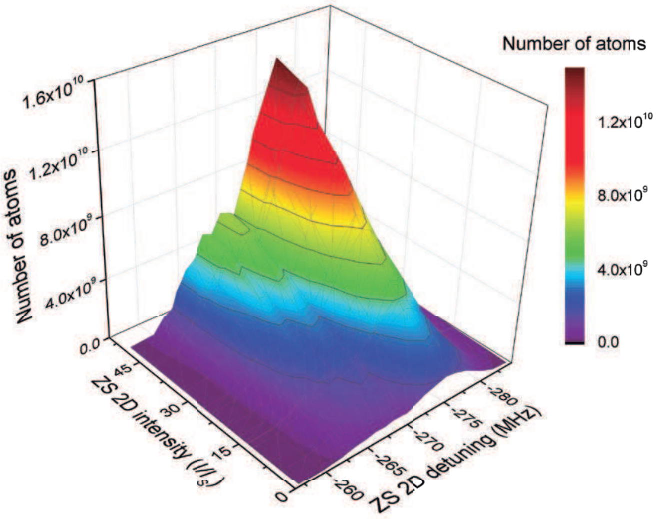

Figure 10. Number of trapped atoms as a function of the detuning and intensity of the ZS cooling beam of the 2D-MOT.

order to evaluate the loading rate of the 3D-MOT when used with each source of atoms at a time.

To compute the loading rate of the 3D-MOT from the ZS and 2D-MOT, we fit the linear part of the loading curve and take its slope. This is valid because in this initial loading we can neglect the losses due to collisions with other trapped. This collisions, and then the losses, increases with the density.

The optimal values for the parameters used in these experiments are shown in table 1. It is important to recall that the parameters for the 2D-MOT are similar to those reported by Lamporesi *et al* [11], with the exception of the ZS beam for the 2D-MOT, for which we use around 6 times higher intensity in order to decelerate the atoms in the atomic beam. Also, the values for the ZS are typical values in this kind of system for ^{23}Na atoms [12, 13].

Table 1. Comparison between the optimal values of the parameters of the ZS and 2D-MOT as source of atoms.

2D-MOT	Zeeman slower
$T_{\mathrm{Oven}_{2D}} = 210$ °C	$T_{\mathrm{Oven}_{ZS}} = 300$ °C
—	$\mathrm{Current}_{ZS-\mathrm{coils}} = 12$ A
$\Delta\mathrm{Cool}_{2D} = -13$ MHz	$\Delta\mathrm{Cool}_{ZS} = -180$ MHz
$I_{\mathrm{Cool}_{2D}} = 5.1\, I_s$	$I_{\mathrm{Cool}_{ZS}} = 1.7\, I_s$
$\Delta\mathrm{Rep}_{2D} = -8$ MHz	$\Delta\mathrm{Rep}_{ZS} = -150$ MHz
$I_{\mathrm{Rep}_{2D}} = 4.3\, I_s$	$I_{\mathrm{Rep}_{ZS}} = 1.12\, I_s$
$\Delta\mathrm{Cool}_{2D}^{ZS} = -275$ MHz	—
$I_{\mathrm{Cool}_{2D}^{ZS}} = 31.8\, I_s$	—
$\Delta\mathrm{Rep}_{2D}^{ZS} = -250$ MHz	—
$I_{\mathrm{Rep}_{2D}^{ZS}} = 10.3\, I_s$	—
$\Delta\mathrm{Push} = +12$ MHz	—
$I_{\mathrm{Push}} = 12.2\, I_s$	—
$N = 2.0 \times 10^{10}$	$N = 3.0 \times 10^{10}$
$\mathrm{L} = 1.8 \times 10^{10}$ atoms s^{-1}	$\mathrm{L} = 4.1 \times 10^{10}$ atoms s^{-1}

Note: ΔCool and ΔRep denotes the detuning of the cooling and repumper beams with respect to the cooling and repumper transition frequencies, respectively. $I_s = 6.26$ mW cm^{-2}.

5. Conclusions

We show the comparison between a well established and a relatively novel experimental tool for producing cold atomic beam sources. This comparison gives us the grounds to build state-of-the-art setups and to tailor them to fit our experimental needs. The ZS, as was shown by the data presented here, is well known for its robustness and high atom flux of trappable atoms. In comparison with the 2D-MOT, it is a simple setup, requiring fewer laser frequencies and total power to achieve similar results. The 2D-MOT, on the other hand, has proven to be as good as the ZS. When comparing the optimum parameters, we could reach an atom flux comparable with that of a ZS. The construction is a little more tricky but the upside is that it is a more compact and clean system, in the sense of less background pressure. Unlike the ZS, the atoms coming from the 2D-MOT have lower axial velocity, and due to the differential pumping stage, the axial velocity profile of the atoms that reach the science chamber has lower components than the ZS, once the ZS does not prevent the hot atoms from reaching the 3D-MOT chamber. This feature makes the 2D-MOT ideal for BEC experiments, were a high flux of atoms is needed to decrease the experimental sequence time, but the vacuum in the trap region should be as low as possible in order to reach quantum degeneracy.

Acknowledgments

The authors thank A Kruger, A Silva and V Monteiro for help in some part of the experimental setup and measurements, and FAPESP (CEPID), CNPq (INCT), and CAPES for the financial support.

References

[1] Phillips W D and Metcalf H 1982 *Phys. Rev. Lett.* **48** 596
[2] Raab E L, Pretiss M, Cable A, Chu S and Pritchard D E 1987 *Phys. Rev. Lett.* **59** 2631
[3] Dalfovo F, Giorgini S, Pitaevskii L P and Stringari S 1999 *Rev. Mod. Phys.* **71** 463
[4] Bloch I, Dalibard J and Zwerger W 2008 *Rev. Mod. Phys.* **80** 885
[5] Bloch I, Dalibard J and Nascimbene S 2012 *Nat. Phys.* **8** 267
[6] Phillips W D 1998 *Rev. Mod. Phys.* **70** 721
[7] Lu Z T, Corwin K L, Renn M J, Anderson M H, Cornell E A and Wieman C E 1996 *Phys. Rev. Lett.* **77** 3331
[8] Dieckmann K, Spreeuw R J C, Weidemuller M and Walraven J T M 1998 *Phys. Rev.* A **58** 3891
[9] Catani J, Maioli P, De Sarlo L, Minardi F and Inguscio M 2006 *Phys. Rev.* A **73** 033415
[10] Tiecke T G, Gensemer S D, Ludewig A and Walraven J T M 2009 *Phys. Rev.* A **80** 013409
[11] Lamporesi G, Donadello S, Serafini S and Ferrari G 2013 *Rev. Sci. Instrum.* **84** 063102
[12] Durfee D S 1999 *Dynamic Properties of Dilute Bose–Einstein Condensates* (Massachusetts Institute of Technology, Department of Physics) (http://cua.mit.edu/ketterle_group/Theses/DSDThesis.pdf)
[13] Naik D S 2006 *Bose–Einstein Condensation: Building The Testbeds to Study Superfluidity* (Georgia Institute of Technology, School of Physics) https://smartech.gatech.edu/handle/1853/13991
[14] Muniz S R, Magalhães K M F, Courteille Ph W, Perez M A, Marcassa L G and Bagnato V S 2001 *Phys. Rev.* A **65** 015402
[15] Foot C J 2005 *Atomic Physics* (New York: Oxford University Press)
[16] Seman J A 2011 *Study of Excitations in a Bose–Einstein Condensate* (Universidade de São Paulo, Instituto de Física de São Carlos) www.teses.usp.br/teses/disponiveis/76/76131/tde-24102011-140439/pt-br.php
[17] Metcalf H J and van der Straten P 1990 *Laser Cooling and Trapping* (New York: Springer)